THE UNIVERSITY OF QUEENSLAND

AUSTRALIA

The role of the adipose tissue microenvironment in kidney cancer

Kunyu Shen

Master of Medicine (Chinese medicine)
Bachelor of Medicine (Chinese medicine)

A thesis submitted for the degree of Doctor of Philosophy at

The University of Queensland in 2019

School of Biomedical Sciences

Faculty of medicine

Abstract

Obesity increases the risk of tumourigenesis, but paradoxically may predict better prognosis after cancer has been diagnosed. There is a general lack of understanding of interactions between cancer cells and adipose tissue. Obesity is characterised by activated endoplasmic reticulum (ER) stress and increased infiltration of macrophages in the adipose tissue. Little is known about the connection between the ER stress and infiltration of macrophages in the adipose tissue. Additionally, the impact of each characteristic on the biology of cancer cells is unclear. This PhD project attempted to define the adipose tissue microenvironment in the setting of cancer, in particular, kidney cancer. The thesis adds knowledge that helps to define the heterogeneous adipose tissue microenvironment and its functions in cancer development.

The thesis is presented as a literature review (**Chapter 1**) followed by four original research sections **(Chapters 2-5**) that have, in some cases, been published (**Chapter 2**) or submitted (**Chapters 3** and **4**).

The literature review (**Chapter 1**) will initially introduce the epidemiology, pathophysiology and prognostic factors for kidney cancer, followed by a summary of the advances in biomarker discovery in renal cell carcinoma (RCC). The literature review then introduces the structure, function and signaling pathways of the ER, followed by a discussion of the involvement of ER stress in cancer. The crosstalk between obesity, cancer and ER stress is also discussed. Finally, the role of macrophages in the tumour microenvironment is summarised.

Chapter 2 is an immunohistochemistry-based retrospective cross-sectional study. Software-assisted quantification of staining intensity and proportion of positive pixels was applied to measure expression of glucose-regulated-protein-78/GRP78 (an ER stress marker) in archived specimens of renal tumour tissues (n=114), adjacent non-neoplastic renal tissues (n=68), and perinephric adipose tissues (n=60) in participants diagnosed with clear cell RCC (ccRCC), the commonest subtype of the RCC. Results demonstrated that GRP78 was not an optimal risk stratification marker for ccRCC. However, upregulated GRP78 in perinephric adipose tissue may be linked with a lower chance of metastasis.

Chapter 3 introduces a liquid-overlay based method to generate reproducible and functional mature adipocyte spheroids using human perinephric adipose tissue-derived mesenchymal stem cells and the murine 3T3-L1 cell line. The established adipocyte spheroids were responsive to the ER stress activator, tunicamycin. and could secrete adiponectin, monocyte chemoattractant protein-1 (MCP-1) and interleukin/IL-8. Hence, the three-dimensional culture platform was able to serve as an adipose tissue microenvironment that could be applied in *in vitro* experiments.

In **Chapter 4**, macrophage behaviour in the adipose tissue microenvironment was investigated using the 3D culture platform introduced in **Chapter 3**. Co-culture experiments were performed to measure the polarisation, migration and invasion of murine and human macrophages. Results demonstrated that mature adipocyte spheroids caused an MCP-1 independent recruitment of Raw 264.7 cells (murine macrophage cell line), which was abolished by tunicamycin treatment. The normal adipose tissue microenvironment induced the unpolarised macrophages to shift into an M2 macrophage phenotype. M1 and M2 macrophages exhibited distinct invasion capacity towards adipocyte spheroids. The presence of M1 macrophages inhibited the invasion of Kirsten mouse sarcoma virus-transformed non-producer human osteosarcoma (KHOS) cell line and 786-0 cancer cells (human kidney cancer cell line).

In **Chapter 5**, the association of macrophage immunophenotyping of perinephric adipose tissue with aggressiveness of ccRCC was investigated, particularly with regard to distant metastasis. Multiplex immunofluorescence was applied to stain CD68, CD163 and CD206 in the perinephric adipose tissue. Three pixel-based algorithms, based on either individually optimised thresholding or consistent maximal and minimal thresholding, were applied to quantify the positivity of the cluster of differentiation (CD) markers across the whole image and in the segmented cytoplasm compartment. Results demonstrated that the most aggressiveness subtype, ccRCC with distant metastasis, exhibited higher expression of CD206 and CD163 compared to the non-metastatic ccRCC and oncocytoma.

Finally, a general discussion of the results and an outlook of future directions are presented in **Chapter 6**.

Declaration by author

This thesis is composed of my original work, and contains no material previously published or written by another person except where due reference has been made in the text. I have clearly stated the contribution by others to jointly-authored works that I have included in my thesis.

I have clearly stated the contribution of others to my thesis as a whole, including statistical assistance, survey design, data analysis, significant technical procedures, professional editorial advice, financial support and any other original research work used or reported in my thesis. The content of my thesis is the result of work I have carried out since the commencement of my higher degree by research candidature and does not include a substantial part of work that has been submitted to qualify for the award of any other degree or diploma in any university or other tertiary institution. I have clearly stated which parts of my thesis, if any, have been submitted to qualify for another award.

I acknowledge that an electronic copy of my thesis must be lodged with the University Library and, subject to the policy and procedures of The University of Queensland, the thesis be made available for research and study in accordance with the Copyright Act 1968 unless a period of embargo has been approved by the Dean of the Graduate School.

I acknowledge that copyright of all material contained in my thesis resides with the copyright holder(s) of that material. Where appropriate, I have obtained copyright permission from the copyright holder to reproduce material in this thesis and have sought permission from co-authors for any jointly authored works included in the thesis.

Publications included in this thesis

1. **Shen K**, Johnson DW, Vesey DA, McGuckin MA, Gobe GC. Role of the unfolded protein response in determining the fate of tumor cells and the promise of multi-targeted therapies. *Cell Stress Chaperones*. 2018;23(3):317–334. doi:10.1007/s12192-017-0844-3

2. **Shen K**, Vesey DA, Ellis RJ, Del Vecchio SJ, Cho Y, Teixeira-Pinto A, McGuckin MA, Johnson WJ, Gobe GC. (2019) GRP78 expression in tumour and perinephric adipose tissue is not an optimal risk stratification marker for clear cell renal cell carcinoma. *PLOS ONE* 14(1): e0210246. https://doi.org/10.1371/journal.pone.0210246

3. **Shen K**, Vesey DA, Hasnain SZ, Zhao KN, Wang H, Saunders N, Burgess M, Johnson DW, Gobe GC. A cost-effective three-dimensional culture platform functionally mimics the adipose tissue microenvironment surrounding the kidney. BBRC. 2020; 522 (3):736-742. https://doi.org/10.1016/j.bbrc.2019.11.119

Other publications during candidature

Shen K, Vesey DA, Johnson DV, Gobe GC. Generation of adipocyte spheroids to study the effect of the ER stress-activated microenvironment on macrophage migration. Poster presented at Keystone Symposia-Obesity and Adipose Tissue Biology; Banff, Canada, Feb 7-13, 2019

Shen K, Vesey DA, Johnson DV, Gobe GC. Studying the macrophage behaviour in the adipose tissue microenvironment using the 3D culture. Poster presented at Tsinghua-RIKEN Summer Program 2019; Tsinghua University, Beijing; China, June 9-12, 2019.

Contributions by others to the thesis

Significant contributions by others to this thesis were predominantly related to the data analysis, which is presented in **Chapter 2,** and the idea of multiplex immunofluorescent staining in perinephric adipose tissue which was undertaken in **Chapter 5.** In particular, thanks go to Prof David Johnson, Dr Robert Ellis (Centre for Kidney Disease Research, University of Queensland) and A/Prof Armando Teixeira-Pinto (School of Public Health, Faculty of Medicine and Health, The University of Sydney) who guided me to perform the multiple regression analysis and create receiver operating characteristic curves to check the logistic regression models. I also thank A/Prof Nicholas Saunders and Dr Melinda Lea Burgess (The University of Queensland Diamantina Institute) who shared their precious successful experience in designing the 3-plex immunofluorescent staining panel.

I also need to acknowledge Dr Debra Black (Microscopy core facility, Translational Research Institute) who performed the automatic multiplex staining with the Ventana system. Thanks also goes to Mrs Yitian Ding and Mrs Dalia Khalil (Flow cytometry core facility, TRI) who performed all the fluorescence-activated cell sorting.

Acknowledgement goes to Dr Keng Lim Ng, Ms Sharon Del Vecchio and Dr Robert Ellis (Centre for Kidney Disease Research, University of Queensland), for their roles in collecting tissue and blood samples and recording clinical information of participants, which constitute the basic materials of the thesis.

Finally, I acknowledge all my co-authors who have not been named above who made contributions to published and submitted manuscripts included in this thesis.

Statement of parts of the thesis submitted to qualify for the award of another degree

No works submitted towards another degree have been included in this thesis.

Research involving human or animal subjects

Metro South Human Research Ethics Committee

(Approval No. HREC/05/QPAH/95)

Metro South Human Research Ethics Committee

(Approval No. HREC/16/QPAH/353)

No animal subject was involved in this research.

Acknowledgements

I have always been expecting to write this section because it means this ascetic journey nears an end. I believe like what most people feel, the experience of pursuing a doctoral degree does not always feel fulfilling and enjoyable. In most cases, to be honest, I must fight with my own resistance, frustration and fears of failure. Luckily, there have been so many professionals, peers and friends who provided me with help and support unselfishly. I thank you all for shinning a light on my life of PhD.

First and foremost, I wish to thank my amazing team of advisors. In particular, A/Prof Glenda Gobe who served as my principal supervisor. Until today, I still remember your words "Kunyu, just go!" which encouraged me to step on the stage to present my work for the first time in a foreign country. You have given me your most support for a lot of my unfeasible ideas. I cannot say thank you enough for your patience to help improve my writing and communication skills. Without your encouragement and enthusiasm, those unfeasible ideas cannot turn into figures and graphs in the thesis. Thank you.

To A/Prof David Vesey, who is a passionate, hard-working and most importantly a serious scientist, your spirit of questioning everything and your enthusiasm for science have made me consider about what the goals of doing research really are. Thank you for always willing to discuss with me in detail about my project. You were always saying that you are not a specialist in this filed, though you were able to point to the most fatal flaws in my experimental design and data interpretation. Thank you for sending me those interesting papers, and your time spent with me inside the lab. Thank you for all the skills you taught me and all the warm encouragement you sent to me. It was so nice to have you in my advisory team. Thank you.

To Prof David Johnson, I have always appreciated you for giving me the chance to visit your team in 2015 and introducing me to Glenda. If it were not for the short chat over a tea break during a conference held in Guangzhou, I would not be sitting here to write the acknowledgements for my PhD thesis in English. I thank you for your careful editing and constructive suggestions for all my manuscripts included in the thesis. I have always admired your highly efficient way of working and your kindness to people, which has influenced me throughout my PhD studies and will serve as a role model in my future career. Thank you.

To Dr Sumaira Hasnain, the last but not the least addition to my advisory panel, the advice you have given along the way has been very constructive—mostly relating to proof reading of the protocol I wrote for *in vitro* studies using your specialities in ER stress and adipose tissue biology. Your quick manuscript turnaround time and excellent suggestions have greatly improved my data interpretation and figure formatting. Thank you.

I would also like to thank the other members of the Centre for Kidney Disease Research, who have provided support over the years. In particular, Ms Sharon Del Vecchio, who had been sitting by my side for two years and assisted my sample collection. Your friendship has meant a lot to me. Thanks to Dr Robert Ellis who has given me many valuable suggestions and handy help for my project. I feel lucky to learn from you. Thanks to Mr Evan Owens who is always around and glad to help no matter whether it was for software trouble-shooting or freezer defrosting. Your easy-going personality always makes me feel happy to work in the lab. Thanks also to Dr Vishal Diwan and Mr Hossam Kamli who were always willing to have a chat and share all the happenings in life and lab.

I would like to thank Dr Jeffrey Grice for chairing my milestone panels. I also show appreciation for Dr Christudas Morais, A/Prof Nicholas Saunders and A/Prof Rick Sturm for examining my milestone documents.

Apart from my formal advisory team and immediate research group, there have been a number of individuals who have taken the time to provide me with advice and support, despite having enormous workloads of their own. First, I would like to thank TRI for providing the excellent research facilities which are managed by excellent technicians and officers who have provided technique support for my project. Particular thanks go to Dr David Sester, Mrs Yitian Ding and Mrs Dalia Khalil from the Flow Cytometry Core facility; Ali Ju from the Microscopy Core facility; Dr Justin Large and Dr Debra Black from the Microscopy Core facility. Next, I acknowledge Ms Gency Gunasingh and Ms Yashu Balalle who shared the techniques of spheroid generation, embedding and cryosectioning. I acknowledge Dr Ruzhi Zhang who shared the technique of stem cell cultivation. I acknowledge Dr Katharine Irvine and Dr Abdullah Tarique who shared their experience in culturing primary macrophages.

Finally, I would like to sincerely thank my family and friends back in China. I know I skipped a lot of important moments in your life, some of which will be my life-long regrets. My dear partner Jiulong, I cannot find anyone else in the world who is more patient with me than you. Thanks for your company over the past few years.

Financial support

The candidate was supported by a UQ-CSC joint scholarship, with The University of Queensland waiving the PhD tuition fee and The Chinese Scholarship Council providing a PhD stipend (File No. 2016008440278).

The University of Queensland Faculty of Medicine and Tsinghua University Institution of Immunology provided financial support for conference travel.

The studies received funding from the Nephrology Department Princess Alexandra Hospital and The University of Queensland School of Biomedical Sciences.

Keywords

kidney cancer; clear cell renal cell carcinoma; endoplasmic reticulum stress; adipose tissue microenvironment; macrophage behaviour; three-dimensional co-culture; immunohistochemistry; multiplex immunofluorescence

Australian and New Zealand Standard Research Classifications (ANZSRC)

ANZSRC code: 060199, Biochemistry and Cell Biology not elsewhere classified, 70%

ANZSRC code: 110709, Tumour immunology, 20%

ANZSRC code: 060101, Cancer cell biology, 10%

Fields of Research (FoR) Classification

FoR code: 0601, Biochemistry and Cell Biology, 55%

FoR code: 1107, Immunology, 40%

FoR code: 1103, Clinical Sciences, 5%

Table of contents

List of tables

List of figures

List of abbreviations

All abbreviations are listed in alphabetical order.

aOR	Adjusted odds ratio
αSMA	Alpha-smooth muscle actin
ASC	Adipose tissue derived mesenchymal stem cells
ATF	Activating transcription factor
ANOVA	Analysis of variance
AUC	Area under the receiver operating characteristic curve
AMPK	AMP activated protein kinase
BAT	Brown adipose tissue
BMI	Body mass index
CAF	Cancer-associated fibroblasts
CCL2	The chemokine C-C motif gland 2
ccRCC	Clear cell renal cell carcinoma
CCR2	C-C chemokine receptor 2
CD	Cluster of differentiation
CHIP	Chromatin immunoprecipitation assay
CHOP	C/EBP homologous protein
CI	Confidence interval
CLS	Crown-like structure
CPT1A	Carnitine palmitoyltransferase 1A
CSF-1	Colony stimulating factor 1
CXCL8	Chemokine CXC motif ligand 8
CY	Cyanine
C/EBPα	CCAAT/enhancer-binding protein alpha
DAB	Diaminobenzidine hydrochloride chromogen
DMEM-F12	Dulbecco's Modified Eagle Medium: Nutrient Mixture F-12
ECM	Extra cellular matrix
eIF2α	Eukaryotic translation initiation factor 2α
EMT	Epithelial-mesenchymal transition
ER	Endoplasmic reticulum
ERAD	ER-associated degradation
E2F1	E2F transcription factor 1
FBS	Fetal bovine serum
FACS	Fluorescence-activated cell sorting
FFPE	Formalin-fixed, paraffin-embedded
FGF	Fibroblast growth factor
FISH	Fluorescence in situ hybridization
FMO	Fluorescence minus one
GADD	Growth arrest and DNA-damage-inducible protein
GFP	Green fluorescence protein

GM-CSF	Granulocyte-macrophage colony stimulating factor
GP130	Glycoprotein 130
GRP78	Glucose-regulated protein-78
GTP	Guanosine triphosphate
HBBS	Hank's Balanced Salt Solution
H&E	Haematoxylin and eosin
HIF	Hypoxia-inducible factor
HO-1	Heme oxygenase-1
HR	Hazards ratio
HRP	Horseradish peroxidase
HSC	Heamatopoietic stem cells
Hsp	Heat shock protein
H_2O_2	Hydrogen peroxide
IBMX	3-Isobutyl-1-methylxanthine
IBTK	Inhibitor of Bruton's tyrosine kinase
Interferon-gamma	IFN-γ
IHC	Immunohistochemistry
IGF	Insulin-like growth factor
IL	Interleukin
IQR	Interquartile range
IRE	Inositol-regulating enzyme
IRS	Immunoreactivity score
JAK	Janus Kinase
JNK	C-Jun amino-terminal kinase
LDH	Lactate dehydrogenase
LPS	Lipopolysaccharide
mAb	Monoclonal antibody
MAPK	Mitogen activated protein kinase
MCP-1	Monocyte chemoattractant protein-1
MFI	Mean fluorescence intensity
MMP	Matrix metalloproteinases
MSC	Mesenchymal stem cells
mTORC1	Mammalian target of rapamycin complex 1
NFκB	Nuclear factor κB
OD	Optical density
OPN	Osteopontin
OS	Overall survival
OS-9	Osteosarcoma amplified 9
P/S	Penicillin-streptomycin
q-rtPCR	Quantitative reverse transcription polymerase chain reaction
pAb	Polyclonal antibody
PBMC	Peripheral blood mononuclear cells

PBS	Phosphate-buffered saline
PDGF-β	Platelet-derived growth factor-β
PD-L1	Programmed cell death ligand-1
PERK	Double-stranded RNA-activated protein kinase/PKR-like ER kinase
PI3K	Phosphoinositide 3-kinase
PKC	Protein kinase C
PMN	Pre-metastatic niches
PPAR	Peroxisome proliferator-activated receptor
RBC	Red blood cell
RGB	Red-green-blue
pVHL	Protein of *Von Hippel Lindau*
pSTAT	Phosphorylated signal transducer and activator of transcription
ROC	Receiver operating characteristic
SCF	Stem cell factor
SFRP	Secreted frizzled-related protein
STAT	Signal transducer and activator of transcription
SVF	Stromal vascular fraction
sXBP1	Spliced X-box binding protein 1
REDD1	Regulated in development and DNA damage response 1
TAM	Tumour-associated macrophages
TBE	Tris/Borate/Ethylenediaminetetraacetic acid
TGF	Transforming growth factor
TLR	Toll like receptors
TNF	Tumour necrosis factor
TNM	Tumour-node-metastasis
Trem2	Triggering receptor expressed on myeloid cells 2
TSA	Tyramide signal amplification
UCP-1	Uncoupling protein-1
UPR	Unfolded protein response
VEGF	Vascular endothelial growth factor
VEGFR	Vascular endothelial growth factor receptor
VHL	*Von Hippel Lindau*
WAT	White adipose tissue
3D	Three-dimensional

Chapter 1

Introduction

1.1 Included Publications

Aspects of Section 2.2 of this chapter were adapted from a narrative review published in the Cell Stress and Chaperones.

Shen K, Johnson DW, Vesey DA, McGuckin MA, Gobe GC. Role of the unfolded protein response in determining the fate of tumor cells and the promise of multi-targeted therapies. Cell Stress Chaperones. 2018;23(3):317–334. doi:10.1007/s12192-017-0844-3

The candidate was the lead author of this narrative review. She contributed significantly to the conception and design of this review (80 %) and analysis and interpretation of the literature (70 %), and drafted the majority of the manuscript (90 %).

1.2 General introduction

There is increasing interest in understanding the interaction of tumour cells with the surrounding stromal structure, including adipose tissue, with a long-term aim to target the tumour microenvironment to inhibit the proliferation and metastasis of tumour cells [1]. Renal cell carcinoma (RCC) is among the five cancer types that have achieved the most attention regarding the association between obesity and the increased incidence of cancer, other types being colon, oesophagus, breast and corpus uteri cancers [2]. However, recent findings suggest that, at the time of RCC diagnosis, being overweight might be associated with a better prognosis [3, 4]. The obesity paradox in RCC highlights the importance of crosstalk between adipose tissue and carcinomas in the progression of kidney cancer.

An association between increased body mass index (BMI) and increased ER stress levels in adipose tissue has also been reported in healthy populations [5]. Obesity-induced ER stress is responsible for the pro-inflammatory microenvironment in adipose tissue [6]. It is classically accepted that cancer is a chronic inflammatory and metabolic disease, and obesity-associated adipose tissue inflammation and oxidative stress are pathogenetic for cancer [1]. However, little is known about obesity-associated ER stress levels in perinephric adipose tissue and its influence on RCC progression. Understanding the effects of obesity-associated ER stress on cancer development may deepen our understanding of the heterogeneous tumour microenvironment.

We have recently found through immunohistochemistry (IHC) that the perinephric adipose tissue from patients diagnosed with renal tumours who had higher BMI had more chances to express higher level of an ER stress marker (as demonstrated by lower average gray value), glucose-regulated-protein-78 (GRP78) (Spearman correlation coefficient=-0.23, p=0.04). Simultaneously, a trend that the downregulated expression of GRP78 in perinephric adipose tissue might be associated with a poor prognosis of kidney cancer was found, with the downregulation of GRP78 correlating with increased probability of metastasis (95 % confidence interval [CI] of OR: 0.99 to 1.38, p=0.07). The results suggested that the activated ER stress under an obese microenvironment may exert a protective role for patients diagnosed with kidney cancer. Coincidently, this result was consistent with the obesity paradox in RCC [3, 4].

The focus of interaction between obesity and cancer has long been the tumour-promoting role of obesity-associated chronic inflammation. What has been largely ignored is that the inflammatory reaction also functions as a crucial tumour-eliminating mechanism in immune-surveillance [7]. However, evidence from our one-point IHC study is insufficient to deduce that activated ER stress in the obese perinephric microenvironment impedes RCC progression. Hence, research was undertaken

based on cell culture to mimic the ER stress-activated obese microenvironment of adipose tissue and reflect the *in vivo* interaction among carcinomas, adipose tissue and surrounding immune cells.

The literature review will initially introduce the epidemiology, pathophysiology and prognostic factors for kidney cancer, followed by a summary of the advances in biomarker discovery in RCC. The commonest form of RCC is clear cell RCC (ccRCC) and this subtype became the focus of the thesis. The literature review introduces the structure, function and signaling pathways of the ER, followed by a discussion of the involvement of ER stress in cancer. The crosstalk between obesity and cancer is also discussed. Finally, the role of macrophages in the tumour microenvironment is summarised.

1.3 Literature review

1.3.1 Epidemiology, pathophysiology and prognostic factors of kidney cancer

1.3.1.1 Epidemiology of kidney cancer

Kidney cancer is a silent killer disease which develops without specific symptoms in its early stages and is often found incidentally in imaging screening for other indications [8]. The median age at diagnosis is around 64 years of age [9]. As per a recent report from the World Cancer Research Fund International [10], kidney cancer is the 14th most common cancer in the world, with 403,262 of new cases and 175,098 of deaths in 2018. It is estimated that there will be 184,416 deaths in 2020 and the number will reach 310,968 in 2040. A gender disparity in the incidence for kidney cancer is distinct, with men being nearly twice as likely as women to develop kidney cancer (age standardised incidence rates per 100,000: 6.0 versus 3.1, respectively). The distribution of kidney cancer incidence varies by geographic area, with the highest age standardised incidence rates found in North American and Europe, and the lowest incidence in Africa (**Fig 1.1**) [10].

1.3.1.2 Histopathological classification of kidney cancer

The most common kidney cancer, at around 90 %, is RCC. RCC are classified as ccRCC (75-85 %), papillary RCC (type 1 and type 2) (10-15 %), chromophobe RCC (5-10 %), collecting duct RCC which is very rare, and unclassified RCC at less than 5 %. Some of the renal neoplasms are benign, with very low or no malignant potential, such as papillary renal adenoma, oncocytoma (3-7 % of kidney neoplasms), and angiomyolipoma [11]. In histological appearance, the most common subtype ccRCC is characterised by compact alveolar or acinar-like nests interspersed with arborizing vasculature. The malignant epithelial cells clustered in the nests have transparent cytoplasm [12]. This is due to the dissolving of the lipid and glycogen-rich cytoplasmic deposits during histological processing [13].

1.3.1.3 Pathogenesis of RCC

Genomic analysis has found 16 significantly mutated genes across ccRCC, papillary RCC and chromophobe RCC and the mutation feature in each subtype is distinct [14]. As per the report from a group of Chinese scientists who applied rigorous bioinformatics analysis, 50 % of the 98 Chinese ccRCC patients carried altered gene expression (including but not limited to mutations in the Von Hippel Lindau gene/*VHL*) that are involved in the ubiquitin-mediated proteolysis pathways which regulate the degradation of proteins [15]. As the most common altered gene in ccRCC, *VHL* encodes

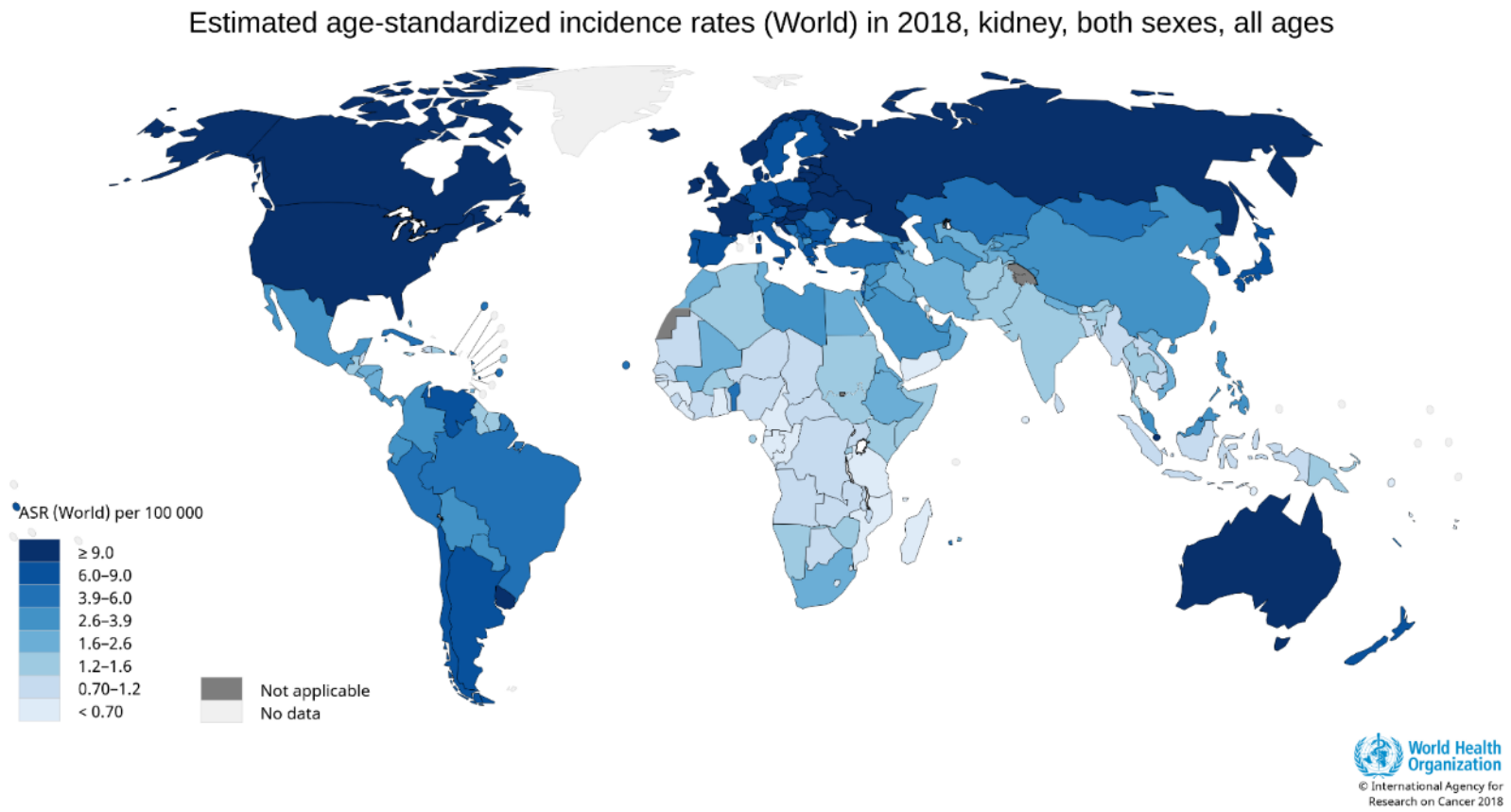

Fig 1.1 Estimated age-standardised incidence rates in 2018 for kidney cancer

The heatmap demonstrates the heterogeneous geographic distribution of kidney cancer incidence (age standardised risk/ASR per 100,000 people). The 10 top-ranking countries are Belarus, Latvia, Lithuania, Czech Republic, Estonia, Slovakia, France, Hungary, Iceland and Croatia. In 2018, Australia ranked 19th with ASR being 9.8. The figure was created using the online data visualisation tool provided by International Agency for Research on Cancer, World Health Organization (http://gco.iarc.fr).

the protein of VHL (pVHL), which binds to elongin B, elongin C or cellulin 2 to form complexes that are essential for the degradation of intracellular proteins, such as hypoxia-inducible factor (HIF) 1α and 2α. Accumulated HIF1α and HIF2α bind to HIFβ and the complex transports into the nucleus, acting as a transcription factor. Alterations in *VHL* result in the upregulation of mRNA that codes for proteins which contribute to tumour development, including vascular endothelial growth factor (VEGF), transforming growth factor α (TGF α), platelet-derived growth factor-β (PDGF-β) and matrix metalloproteinase protein (MMP) [16]. The *VHL* mutation is also responsible for the altered lipid metabolism in ccRCC. It was reported recently that the mitochondrial fatty acid transporter carnitine palmitoyltransferase 1A (CPT1A) is suppressed by HIF1 and HIF2, thus forcing the accumulation of lipid droplets in the cytoplasm of ccRCC [17].

1.3.1.4 Prognostic factors for RCC

To date, various prognostic factors have been identified for RCC, including clinical and biomedical features, histological subtypes and pathological diagnosis [18]. For example, severe anaemia and upregulated lactate dehydrogenase (LDH) after RCC diagnosis indicate short overall survival (OS) [19, 20]. By histological subtype, the OS of metastatic non-ccRCC patients (12.8 months) was significantly poorer than that of ccRCC patients (22.3 months) when treated with targeted therapies (hazards ratio/HR for death = 1.41, $P<0.0001$) [21]. The OS (5 to 12 months) and treatment response for RCC with sarcomatoid differentiation is the poorest [22]. Overexpression of the prevalent programmed cell death ligand-1 (PD-LI) and active epithelial-mesenchymal transition (EMT) contribute to the escape of antitumour immunity and metastasis for sarcomatoid RCC [23].

Tumour-node-metastasis (TNM) staging is the most widely applied risk stratification system for predicting RCC prognosis: T indicates tumour size and whether it has grown into a nearby area; N describes the presence of regional lymph nodes invasion; and M indicates whether the cancer has metastasised [24]. The numbers 0 through 4 appearing after T, N and M, and the letter “a” or “b” after the numbers, indicate increasing severity. Once the categories have been assigned, patients will be classified into an overall stage of I, II, III, or IV [25]. According to data reported by the American Cancer Society, approximately 65 % of the patients have tumours confined to the kidney at diagnosis. For this group, the 5-year survival rate is 93 % (stage I, II). If kidney cancer has spread to surrounding tissues or the regional lymph nodes (stage III), the 5-year survival rate is 69 %. If the cancer has distant metastasis (stage IV), the 5-year survival rate is 12 % [26].

1.3.1.5 Obesity is an uncertain predictive factor for RCC

Although being overweight is an established risk factor for developing kidney cancer [2, 27], renal tumours growing in an obese microenvironment may exhibit less aggressiveness. A meta-analysis involving retrospective data from 20 cohort studies reported an improved recurrence-free survival in RCC patients with BMI ≥25 kg/m^2 prior to nephrectomy compared with those with BMI <23 kg/m^2 (HR = 0.49, p = 0.14) [3]. Consistently, a prospective multi-centre randomised controlled trial reported that there was an insignificant prolongation of the disease-free survival, and a decrease of lymphatic spread with increasing BMI, for patients who were diagnosed with high risk ccRCC [28]. However, there are discrepancies regarding the prognostic influence of being overweight on specific histological subtypes of non-metastatic RCC. For example, as was shown by a large cohort study using multivariate analyses, increased BMI was significantly associated with higher recurrence-free survival and cancer-specific survival rates in patients diagnosed with ccRCC (HR = 0.94 and 0.875, respectively). In contrast, in patients with chromophobe RCC, increased BMI was associated with poor prognosis, whereas no significant correlation was found between the prognosis of papillary RCC and BMI [29].

The promising prognostic role of obesity was reconfirmed when visceral fat instead of BMI was measured to reflect the degree of obesity. For example, retrospective data from 2187 patients diagnosed with RCC between 1994 and 2012 in Korea demonstrated that a larger visceral fat area was predictive of better prognosis, as the median cancer-specific survival length for patients with visceral obesity was 26.1 months longer than those with smaller visceral fat area (p=0.006) [30]. The promising predictive role of preoperative visceral obesity was consistent with results from two studies in Japan with smaller sample size. In the earlier retrospective study, the RCC five-year recurrence-free survival was higher in patients with larger visceral fat area compared those with smaller area (HR = 1.974, p = 0.042) [31]. In the other study, a large visceral fat area (≥100 cm^2) demonstrated a significant correlation with the better prognosis of metastatic RCC (HR = 0.625, p = 0.029) [32]. However, data from another retrospective study in Korea including 706 RCC patients who underwent nephrectomy showed that both the highest and the lowest visceral adipose/total adipose ratios were correlated with a high chance of recurrence, with significant HR values being 4.760 and 3.198, respectively. Additionally, a high visceral adipose/total adipose ratio was associated with high grade of tumours at diagnosis (HR = 1.023, p = 0.037), further challenging the promising prognostic role of visceral obesity [33].

1.3.1.6 Advances in biomarker discovery in RCC

The first-line therapies for advanced ccRCC target the VHL-HIF-VEGF signaling pathway [34]. However, responses to the targeted agents vary between individuals. Understanding the association of altered gene/protein expression with aggressiveness of cancer and treatment responses advances targeted therapy. For example, Choueiri *et al.* found that outcomes of metastatic ccRCC patients treated with targeted tyrosine kinase inhibitors sunitinib and pazopanib worsened with increased PD-L1 expression in tumour tissues [35]. The finding boosted a series of clinical trials to further evaluate the effects of systematic treatment for ccRCC by including PD-L1 inhibitors [36].

Research into other histological biomarkers is also underway to further improve the accuracy of diagnosis and treatment responses. For example, results from IHC indicate that GRP78, an ER stress resident protein, is a promising prognostic marker for ccRCC. Fu and colleagues tested GRP78 expression in renal tumour tissues and adjacent non-tumourous renal tissues from 42 Chinese ccRCC patients and found GRP78 expression was significantly higher in renal tumour tissues than in the adjacent non-tumourous renal tissues. Moreover, they found the level of GRP78 expression was positively correlated with later TNM stages and larger tumour sizes [37]. Targeting ER stress by turning on its pro-apoptotic signaling may compromise the failed anti-tumour effect of other treatments. For example, mutation of *p53* (the tumour guardian gene) is a shared feature for ccRCC, papillary RCC and chromophobe RCC [14]. Research by Schwarzenberg *et al*. identified that the proteasome inhibitor bortezomib could overcome the resistance of RCC against troglitazone, which targets apoptosis mediated by the peroxisome proliferator-activated receptor γ (PPARγ)-*p53* signaling pathway [38].

1.3.2 ER stress and cancer

1.3.2.1 A brief introduction to the structure and function of the ER

The ER network is a continuous lipid double-layered system comprising a nuclear envelope, peripheral ER and cortical ER. The peripheral ER comprises two sub-domains which are functionally and morphologically different: peripheral ER sheets and peripheral ER tubules. The primary difference in structure is that ER sheets are flat and studded with ribosomes while ER tubules are highly curved and largely lack ribosomes. Hence, ER sheets and ER tubules are often termed rough ER and smooth ER, respectively. Having partly flat and rough, or partly high curved and smooth surfaces, the cortical ER is tethered to the plasma membrane and works as a mediator of Ca^{2+} concentration between the ER lumen and the extracellular environment, which regulates muscle contraction [39]. This elaborate internal membrane system has a series of specialized functions: (1) secretory protein synthesis, modification, quality control and transportation; (2) lipid synthesis and

distribution; (3) sterol synthesis; (4) Ca^{2+} storage and regulation; and (5) interior compartmentalisation and interconnection within cells [40]. The variation of the abundance of the ER is likely related to the heterogeneity in functions of different cells. For example, the ER structure is rare in cells of the thin limb of Henle's loop in the kidney, which plays a non-significant role in electrolyte transport [41]. However, in podocytes in Bowman's capsule of the glomeruli, where there is active Ca^{2+} flow, the ER is abundant [42].

1.3.2.2 ER quality control mechanism

The protein folding process is inherently error-prone [43]. Environmental stress such as ultraviolet light exposure, depletion of Ca^{2+}, osmotic stress, oxidative stress, and deprivation of nutrients in pathological conditions such as malignancy, increase the accumulation of improperly folded polypeptides [44]. If they are not removed from the ER via a process known as ER-associated degradation (ERAD), the partially folded or misfolded polypeptides are susceptible to aggregation in disordered structures, which are toxic to the cell [45]. Providentially, the ER has an orchestrated quality-control system to facilitate the processes of protein folding and misfolded protein degradation, in which adenosine triphosphate (ATP)-dependent chaperones, also known as heat shock proteins (Hsps), play a crucial role [46, 47]. For example, GRP78, a 70 kDa protein which binds to the hydrophobic surface of the non-native proteins and cooperates with Hsp110, is capable of interfering with protein aggregation [48], assisting the unfolding and refolding of misfolded protein [49, 50]. GRP78 also keeps the stability of unfolded proteins until they are competent for the correct folding process under normal conditions [51]. Despite the support offered for primary quality control by all of the above factors, many newly synthesized proteins end up misfolded. The unwanted misfolded proteins are recognised and then retro-translocated to the cytosol for ultimate degradation by the ubiquitin-proteasome pathway, as a secondary quality control [52]. Misfolded proteins are flagged by glycosylation with a specific oligosaccharide structure ($Man_7GlcNAc_2$ with α 1, 6-linked mannosyl residual) [53]. The mannose-6-phosphate receptor homology domain of osteosarcoma amplified 9 (OS-9), an ER-resident lectin, recognises α 1, 6-linked terminal mannose [54, 55]. OS-9 interacts with the 3-hydroxyl-3-methylglutaryl-coenzymeA reductase degradation ligase for ubiquitination [56]. Finally, ubiquitinated proteins are recognised and degraded by the 26S proteasome [57].

If the ERAD is insufficient, the ER will be congested with immature proteins in a process known as ER stress, initiating a complicated and dynamic signaling network which enhances the resistance of cells to ER stress and is collectively known as the unfolded protein response (UPR) [58] (**Fig 1.2**).

1.3.2.3 Signaling cascades elicited by UPR

There are three ER stress proximal transducers: activating transcription factor-6 (ATF6), double-stranded RNA-activated protein kinase/PKR-like ER kinase (PERK), and inositol-requiring enzyme 1 (IRE-1), which all have binding sites for GRP78. In unstressed cells, the stress transducers are maintained in an inactivated state by GRP78 so as to block their activity. Under ER stress, GRP78 dissociates from these ER-residential proteins to initiate downstream cascades [59] (**Fig 1.2**). ATF6 is the only transducer that departs the ER via translocation in the membrane of the Golgi [60]. ATF6 signaling functions to enhance protein folding and degradation capacity. Upon translocation from the ER to the Golgi apparatus, ATF6 undergoes structural modifications which release a cytosolic fragment, pATF6 (N) [61]. PATF6(N) then moves into the nucleus to activate the transcription of genes encoding most ER chaperones and some ERAD components [62].

PERK signaling decides the cell fate after exposure to ER stress. Upon ER stress, PERK phosphorylates eIF2α (eukaryotic translation initiation factor 2α) and consequently deactivates eIF2B. This results in blocking guanosine triphosphate (GTP)-dependent transportation of the initiator Met-$tRNA_i^{Met}$ to the rough ER, which consequently downregulates global translation. Activated eIF2 also inhibits the influx of nascent polypeptides into the ER [63]. The immediate result of this translation inhibition is a reduction in the rates of global protein synthesis, which saves energy consumption when oxygen and ATP levels are low. Although PERK signaling reduces the synthesis of most proteins, it preferentially increases the biosynthesis of some proteins that can help cells survive in stressed conditions, for example, inhibitor of Bruton's tyrosine kinase α (IBTKα), growth arrest and DNA-damage-inducible protein (GADD34) and Gcn4p. Alternatively, PERK signaling may increase the biosynthesis of some proteins that induce cell death (e.g. ATF4) if the stress is irreversible. IBTKα can protect cells from caspase3/7-dependent cell death [64]. Activated ATF4 induces the expression of C/EBP homologous protein (CHOP), also known as growth arrest and DNA-damage-inducible protein 153 (GADD 153), which can induce the apoptotic pathway [65]. In contrast, activated ATF4 and CHOP also conjointly target genes, such as GADD 34, that relieve translation attenuation for recovering cells from stress [66]. Similarly, Gcn4p enhances biosynthesis of amino acids, which helps cells withstand starvation [67]. In addition, PERK inhibits the synthesis of cell cycle regulators, such as cyclin D1, resulting in cell cycle arrest in the G1 phase [68]. Consequently, if the UPR is transient, these adaptive responses promote cell survival. However, if the UPR is prolonged, overconsumption of nutrients and energy during protein synthesis causes oxidative stress which can further enhance protein misfolding by interfering with disulphide bond formation during protein folding [68]. This effect is enhanced by the pro-apoptotic influence of CHOP that, together with a prolonged UPR, pass the molecular thresholds for induction of apoptosis.

In the case of inositol-regulating enzyme 1 (IRE1), dissociation from GRP78 initiates the phosphorylation and dimerization of IRE1. This in turn results in removal of a 26 nucleotide intron from X-box binding protein 1 (XBP1) mRNA, leading to the synthesis of the isoform XBP1(S), which translocates into the nucleus to induce the upregulation of its target genes. The protein products of these genes facilitate every aspect of the secretory pathway ranging from protein folding and entry of

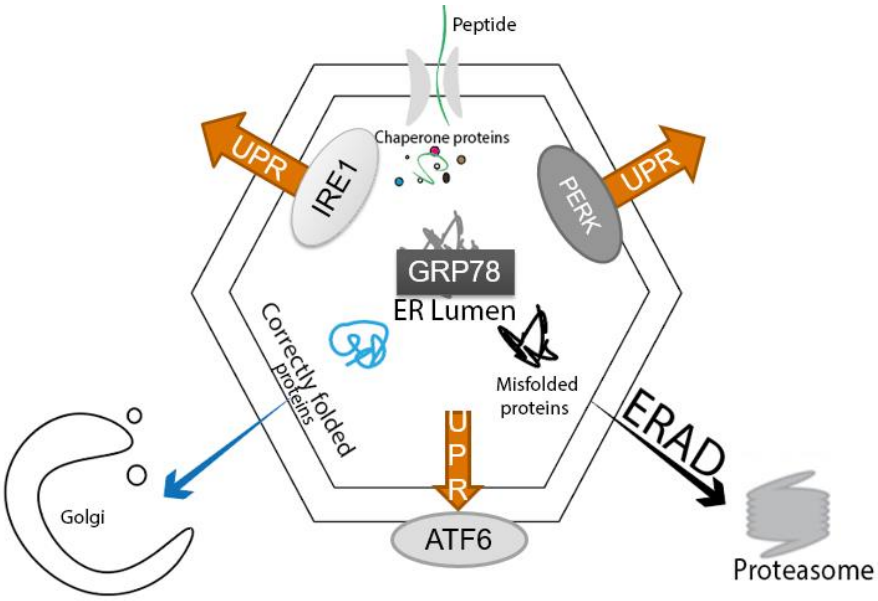

Fig 1.2 ER stress and UPR

When newly synthesized proteins translocate into the ER lumen, they rapidly associate with chaperone proteins that facilitate protein folding. Upon adopting the native state, proteins are released from the ER to pass down the secretory pathway via the Golgi. Proteins that fail to adopt their native conformation are eventually degraded by the proteasome. This process is called ERAD. The protein folding process is error prone. Approximately 70 % of the nascent polypeptides end up misfolded even with the assistance of ER chaperones. If the loading of the misfolded proteins exceeds the capacity of ERAD, the ER lumen will be crowded with misfolded proteins, and this situation is called ER stress. Under ER stress, three signaling molecules IRE1, ATF6 and PERK are released from the core ER stress protein GRP78, thereby initiating the UPR, which inhibits translation, blocks the entrance of nascence polypeptides, helps the processes of protein folding and ERAD, and ultimately relieves ER stress and maintains cell survival. However, if the ER stress is irreversible and becomes chronic, UPR can trigger signaling pathways that induce cell death.

Abbreviations: ATF, activating transcription factor; ER, endoplasmic reticulum; ERAD, ER-associated degradation; GRP, glucose-regulated protein; IRE, inositol-regulating enzyme; PERK, double-stranded RNA-activated protein kinase/PKR-like ER kinase, UPR, unfolded protein response

proteins into the ER to ERAD [44, 69]. IER1α is another branch of the UPR that can convert pro-survival ER stress to pro-apoptotic ER stress, depending on the activation of c-Jun amino-terminal kinase (JNK) [70]. The prolonged activation of JNK is known to induce tissue and stimulus-specific apoptosis through mitochondrial-dependent caspase activation [71]. Unlike the broad expression of IRE1α, IRE1β is exclusively expressed in intestinal and bronchial epithelial cells [71]. In contrast with the high cleavage activity of IRE1α against XBP1 mRNA, the RNase domain of IRE1β has higher cleavage potential against 28S ribosome RNA, which may cause apoptosis [72]. Regarding the cell protective role, IRE1β is required for the production of mucins (Muc5b and Muc5ac) in the respiratory tract [73] and Muc2 in the goblet cells in the colon [74]. Consistent with the dual functions of the PERK branch of the UPR, the existence of IRE1 signaling further indicates that the UPR, which had been thought to be pro-survival under ER stress, could also induce cell death when ER stress is persistent and harmful. Hence, targeting apoptotic ER-stress induced pathways might be effective in eliminating unwanted cells, such as tumour cells.

1.3.2.4 Activation of ER stress as an adaptive behaviour of cancer cells

Due to uncontrolled proliferation, cancer cells often live in a condition with insufficient oxygen and nutrition accompanied by an upregulation of HIF-1. As discussed previously, HIF-1 promotes tumourigenesis. Additionally, HIF-1 decreases ATP consumption during glycolysis via stimulating the gene expression of pyruvate dehydrogenase kinase, which inhibits pyruvate dehydrogenase [75]. Hence, cancer is known to inherently maintain a highly efficient proliferation rate when confronting hypoxia [76]. Apart from assisting the pro-survival signaling in tumourigenesis, the hypoxic stress also activates the IRE1 and PERK arms of the UPR, which launches downstream cascades to increase insensitivity of tumour cells towards pro-apoptotic signaling [77] (**Fig 1.3**). The activation of ER stress in response to oxygen-glucose deprivation has been reported in previous studies. For example, in primary cultures of mixed rat brain cortical cells which were deprived of oxygen and glucose, the PERK-eIF2α and IRE1-XBP1 branches of the UPR were stimulated [78]. In the context of tumours, the upregulation of GRP78 was also related to glucose depletion [79].

1.3.2.5 ER stress levels in cancers

It has now become clear that the activation of ER stress is a common phenomenon in tumourigenesis [80-82]. The altered expression of ER stress proteins has been observed in various cancer types, including lung [83], breast [84], colon [85], gastric [86], pancreatic [87], liver [88, 89], prostate [90, 91], kidney [37], skin [92], uterine [93], and ovarian cancers [94], leukaemia [95], myeloma [96] and glioblastoma [97].

GRP78 is the common UPR component that has upregulated expression in most of the tumour tissues as mentioned previously. The activation of GRP78 correlates with the severity and prognosis of cancer. For example, the activation of a rarely known splicing variant of GRP78, GRP78va, as a result of unleashing PERK signaling, is associated with enhanced viability of leukaemic cells [98]. The cancer supporting role of PERK signaling has been revalidated in other research. Meixia *et al.* found that xenograft tumours grown from Ki-RasV12 and Ha-RasV12-transformed mouse fibroblasts with wild-type PERK-eIF2α-ATF4 were 6 times larger than tumours with a compromised PERK-eIF2α-ATF4 pathway, suggesting that inhibiting PERK-eIF2α-ATF4 activity inhibits the growth of tumours [82]. The silencing of IRE1β, however, may contribute to the carcinogenesis of colorectal cancer, which is characterised by a dysregulated expression of mucins [99], because the integrity of IRE1β is crucial for the normal characterisation of Muc2 in the colon [74]. Consistently, it has been found that there was a downregulated IRE1β expression in colorectal adenocarcinomas compared with normal colon [100]. Clinical studies based on archived tumour tissues demonstrate that the expression levels of specific ER stress markers can work as predictors of cancer (summarised in **Table 1.1**).

1.3.2.6 The immune-surveillance sabotage mediated by hyperactive XBP1 signaling

Blunted anti-cancer immunity is an underlying process of cancer development. By means of utilizing ER stress, tumours may successfully suppress or evade immune scavenging [76]. In physiological conditions, tumour-irrelevant $CD8^+$ dendritic cells constitutively activate the IRE1-α/XBP1 axis without triggering the UPR cascades, and so regulate the gene expression that maintains ER homeostasis and the phenotype of dendritic cells. Furthermore, intact IRE1-α/XBP1 signaling plays a significant role in the cross-presentation by $CD8^+$ dendritic cells [101]. Overexpression of XBP1 has been discovered in tumour-associated dendritic cells in aggressive cancers. This overexpression has negative effects on the function of dendritic cells in the tumour microenvironment [102]. For example, Cubillos-Ruiz *et al.* [94] found that the expression of the spliced XBP1 was positively correlated with the volume and weight of ovarian tumours in murine models. They further found the lipid peroxidation product 4-hydroxy-trans-2-nonenal in ovarian cancer-associated dendritic cells stimulated the production of XBP1. The dendritic cells which were devoid of XBP1 demonstrated significant suppression of genes, such as *Agpat6*, *Fasn*, *Scd2*, and *Lpar1*, which are involved in lipid metabolism pathways, and genes such as *ATF6*, *Sec61α1*, *Pdia4*, *Sec24*, which are involved in the ER stress response. Large intracellular lipid bodies were only found in the XBP1-sufficient dendritic cells but not in the XBP1-deficient cells. The accumulation of triglyceride in bone-marrow derived dendritic cells decreased the surface expression of the major histocompatibility complex-1 (MHC-1) which was loaded with ovalbumin-derived peptide epitope, thus hindering the activation of CD^{8+} T cells. The immune sabotage of XBP1 is revalidated in XBP1 deficient mice where the T cells

exhibited enhanced capacity to hamper tumour growth. Moreover, silencing IRE1α/XBP1 signaling prolonged survival of mice bearing aggressive orthotopic ovarian tumours. These results collectively indicate that the XBP1-dependent turbulence of lipid metabolism contributes to the dysfunction of dendritic cells, which weakens the T-cell mediated anti-tumour responses (**Fig 1.3**).

1.3.2.7 Cancer killing potential of the UPR by interfering with the cell cycle

The presence of cell cycle-mediated cancer resistance is a great challenge for antitumour therapies [103]. The UPR facilitates the tumouricidal treatment by blocking cell cycling of cancer cells. Upregulation of the G1/S phase regulator, cyclin D1, in G1 phase is found in various malignant neoplasms [104-109]. As is shown by Brewer *et al*., PERK-eIF2-ATF4 signaling activated by tunicamycin (an ER stress inducer) inhibits the translation of cyclin D1, thereby inhibiting cyclin D1 forming a complex with cyclin dependent kinase (CDK). Thus, the retinoblastoma protein is not able to be phosphorylated, which results in cell-cycle arrest in G1 phase [68]. It is worth noting that the G1 phase arrest mediated by the UPR may lead to resistance to agents that target the succeeding phases of cell cycle, indicating the importance of selecting the appropriate therapy when the intact cell cycle is interfered by the UPR.

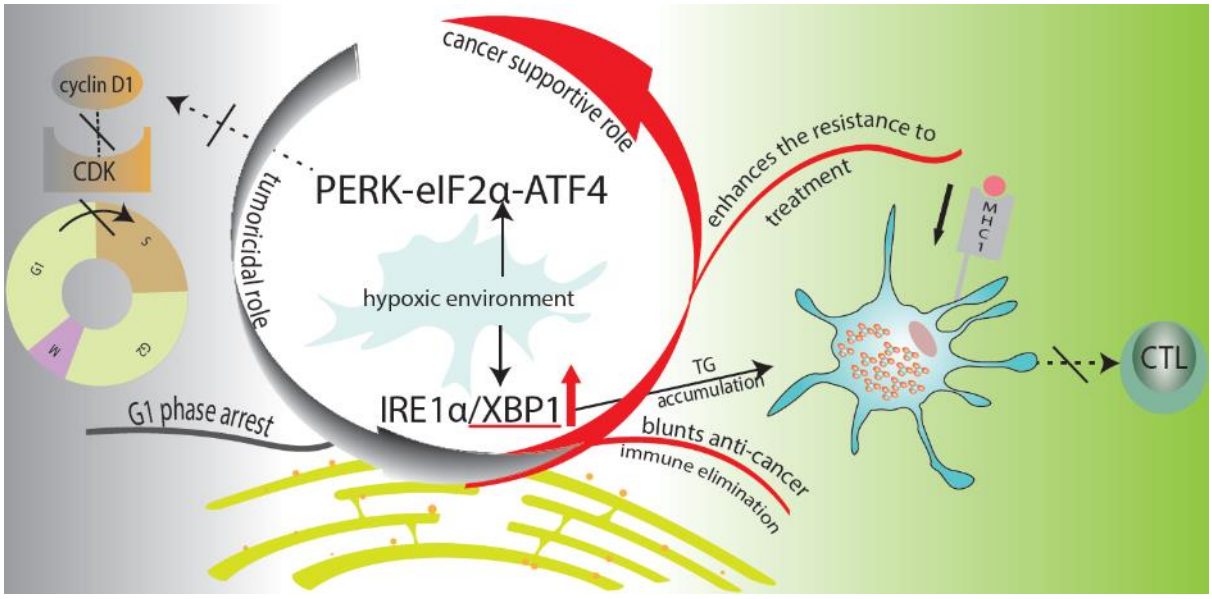

Fig 1.3 Dual roles of UPR in cancer

Cancer cells often live under hypoxic conditions which activate the IRE1 and PERK branches of the UPR to support cancer growth. On the one hand, cancer cells exploit the prosurvival UPR signaling to conquer the lethal effect of treatments. On the other hand, upregulated XBP1 induces the accumulation of TG in dendritic cells, which decreases the expression of the MHC1, thereby hindering the activation of $CD8^+$ T cells. The immune sabotage of XBP1 contributes to a blunted immune elimination of cancer cells. In contrast, the G1 phase arrest of cancer cells is also related to the activation of the PERK branch of the UPR, suggesting that UPR has dual roles in determining the fate of cancer cells.

Abbreviations: ATF, activating transcription factor; CDK, cyclin dependent kinase; CTL, cytotoxic T lymphocyte; eIF2α, eukaryotic translation initiation factor 2α; IRE, inositol-regulating enzyme; MCH1, major histocompatibility complex1; PERK, double-stranded RNA-activated protein kinase/PKR-like ER kinase; TG, triglyceride; XBP1: X-box binding protein 1

Table 1.1 Summary of the upregulation of ER stress markers in different human tumour types and the association with aggressiveness and prognosis of cancer

	Cancers	Markers	Methods	Sample size	Results
Poor prognostic role of the up-regulated ER stress markers	Endometrial adenocar-cinoma [110]	GRP78 CHOP	IHC	246	1. CHOP expression paralleled the GRP78 expression in adipocytes and in the tumour. 2. High visceral adipocyte GRP78 expression positively correlated with advanced-stage disease and deep myometrial invasion. 3. High visceral adipocyte GRP78 expression was significantly associated with decreased disease-free survival.
	RCC [37]	GRP78	IHC PCR	42	1. GRP78 expression was significantly higher in RCC tissues compared with nontumourous renal tissues. 2. The high levels of GRP78 mRNA expression and protein expression were related to the large tumour size and high clinical stage.
	OSCC [111]	GRP78	IHC	46	1. Patients with OSCC exhibited an upregulation of the expression of GRP78 than the health control. 2. GRP78 expression was positively correlated with tumour size, stage, grade, lymphatic invasion and distant metastasis. 3. Positive GRP78 expression was inversely correlated with survival.
	Prostate cancer [112]	GRP78	IHC	153	1. The intensity of the GRP78 expression was markedly higher in the primary tumour compared with areas of benign epithelium. 2. Patients with strong GRP78 expression had higher risk of death and recurrence than patients with weak expression.
	Hepatitis B virus-related-hepato-cellular cancer [113]	HSP27 HSP60 HSP70 HSP90 GRP78 and GRP94	IHC wester n blot	52	1. Expression of HSP27, HSP70, HSP90, GRP78, and GRP94 increased along with the stepwise progression of hepatocarcinogenesis. 2. There was a positive correlation between the expression of GRP78, GRP94, HSP90, and HSP70 and prognostic factors of hepatocellular. 3. Strong correlation was found only in GRP78.

	Lung cancer [114]	GRP78 GRP94	IHC PCR	54	1. There was a significant overexpression of GRP94 and GRP78 in cancer tissues as compared to normal tissues. 2. The overexpression of GRP94 and GRP78 was correlated with poor differentiation and late stage.
	Melanoma [115]	GRP78	IHC	171	1. The IRS of GRP78 increased with the progression of melanoma. 2. The IRS of GRP78 increased with increasing tumour thickness and with increasing dermal tumour mitotic index. 3. Compared with patients whose IRS<25, patients with IRS≥25 had shorter disease-free survival and OS. 4. The overexpression of GRP78 was not an independent predictor of disease-free survival or OS.
Promising prognostic role of the up-regulated ER stress markers	Adenocar-cinomas of the oesophagus [116]	GRP78, GRP94	IHC PCR	137	1. Significant higher mRNA levels of GRP78 were found in the well differentiated tumours as compared to moderately and poorly differentiated tumours. 2. A strong GRP78 IHC staining was correlated with early tumour stage. 3. A weak GRP94 IHC staining was correlated with early tumour stage and less lymph node involvement. 4. A trend towards better prognosis was found in patients with high GRP78 and GRP94 mRNA levels.
	Urothelial carcinoma of the upper urinary tract [117]	GRP78	IHC	126	1. There was a significantly higher incidence of GRP78 expression in low-grade invasive tumours than in high-grade invasive tumours. 2. The overexpression of GRP78 was associated with the improved disease free survival.
	Colorectal adenocar-cinoma [100]	IRE1β	IHC PCR wester n blot	42	1. IRE1β expression was significantly lower in cancer tissues compared with nontumourous colorectal tissues. 2. The low levels of IRE1β expression, RNA and protein expression were related to the presence of lymph node metastasis and high clinical stage.

Abbreviations: ER, endoplasmic reticulum; GRP, glucose regulated protein; HSP, heat shock protein; CHOP, C/EBP homologous protein; IHC, immunohistochemical; FFPE, formalin-fixed, paraffin-embedded; RCC, renal cell carcinoma; RT-PCR, reverse transcription polymerase chain reaction; IRS: immunoreactivity score; OSCC, oral squamous cell carcinoma; OS, overall survival

1.3.3 Crosstalk between adipose tissue and cancer

1.3.3.1 Characteristics of general and kidney tissue-specific adipose tissue

Distributed throughout the body, adipose tissue is mainly stored subcutaneously and around large organs, such as the lungs, kidneys, heart, liver, stomach and intestines. It is also found in the bone marrow and surrounding the vascular adventitia [118]. Adipose tissue is composed mostly of adipocytes and includes stromal vascular fraction (SVF). The SVF constitutes pre-adipocytes, fibroblasts, immune cells, endothelial cells and vascular smooth muscle cells [119]. Factors secreted by these cellular components (known as adipokines) are crucial for adipose tissue to exert its functions as an endocrine organ. The cellular origin and functions of adipokines have been extensively reviewed previously [119]. The counterbalance between the anti-inflammatory and pro-inflammatory adipokines is crucial for maintaining the metabolic homeostasis. The changed secretory profile of adipose tissue under obesity can cause systemic metabolic disorder. For example, the secretion of the anti-inflammatory adipokine, adiponectin, is suppressed under obesity, which decreases insulin sensitivity and is correlated with greater risk of ischemic heart disease [120]. Insulin resistance is also observed when the secretion of another anti-inflammatory protein, secreted frizzled-related protein 5 (SFRP5), is decreased in the obese adipose tissue [121].

Except for sharing the above common features of white adipose tissue (WAT), brown adipose tissue (BAT) has a special morphological phenotype and subcellular microstructure. These characteristics of BAT correspond to their functional state. Early research in mammals discovered that there was a type of the brown-coloured adipose tissue existing for the lifetime of rodents and hibernating animals, which was catabolically active during exposure to the conditions of alarm or stress [122]. Aherne and Hull reported the distribution and morphology of BAT in human infants: occurring around the adrenals, kidneys, thyroid, thymus and oesophagus, BAT had rich capillaries and showed various amount of lipid locules in the cytoplasm of adipocytes. Moreover, they discovered that there were abundant mitochondria in cytoplasm where the lipid was depleted [123]. A later retrospective study based in Japan using samples from human perinephric adipose tissue demonstrated that brown adipocytes are located centrally in the fat lobules, surrounded by a layer of unilocular white adipocytes. Moreover, the content of BAT decreased with aging, as characterised by the multilocular brown adipocytes gradually being replaced by the unilocular white adipocytes [124, 125].

The adipokine secretory profile of BAT is distinct from that of WAT. Although there has not been a confirmed factor that is exclusively produced by BAT, the brown fat adipokines are crucial for BAT to exert its metabolic functions [126]. For example, BAT is known to produce the active thyroid hormone, triiodothyronine, which contributes to the thermogenesis of brown adipocytes after

exposure to noradrenaline and cold [127]. Fibroblast growth factor 21 (FGF-21) is another upregulated brown fat adipokine during exposure to cold, which is responsible for promoting glucose oxidation and improving dyslipidaemia [128]. The thermogenic activation in BAT also favours an anti-inflammatory phenotype shift of the adipose tissue macrophages via an IL-4 dependent manner [129]. This change will potentially influence the immunomodulation of adipose tissue. Although the secretory pattern of brown perinephric adipocytes is unknown, data indicate that the specificities of the kidney-specific adipose tissue may affect the progression and prognosis of kidney-related diseases. For example, it was recently found that the secretion of neuregulin 4, a healthy metabolic modulator, was decreased in BAT under chronic kidney disease [130, 131]. The secretory profile of BAT remains elusive in cases of kidney cancer, however data is available that the content of peri-adrenal BAT was positively correlated with high incidence of cancer-induced cachexia [132]. Future research is warranted to detect the possible relationship between the secretory pattern within the kidney tissue-specific adipose tissue and progression of the kidney cancer.

1.3.3.2 Nutritional status and survival of cancer

Due to the growing awareness of the metabolic functional change after weight gain and weight loss, there is an increasing interest in studying the interplay between tumour-associated adipose tissue and tumour progression. In the real-world setting, the “obesity paradox” is not limited to kidney cancer. Growing evidence suggests that malnutrition can increase risk of cancer-associated mortality [133, 134]. For example, results from a retrospective study including 1,762 participants diagnosed with various types of cancer (including colon/rectal, respiratory, pancreatic, oesophageal, stomach and kidney cancer) demonstrated that low total adipose tissue index was an independent mortality risk factor (adjusted HR=1.26, $p<0.001$) [135]. To date, most research has focused on the catabolic effect (e.g. lipolysis) of cancer-associated cachexia on adipose tissue and on the contributory roles of adipose tissue in tumour development [136]. However, there appears to be an antagonistic feedback from adipose tissue to cancer cells under an obese microenvironment, which remains elusive.

1.3.3.3 Link between obesity and cancer

There is strong evidence supporting cancer as an obesity-associated complication [137]. Multiple mechanisms (for example, inflammation, lipid metabolism and macrophage biology) bridge obesity and cancer. Firstly, chronic low-grade systemic inflammation is probably the most well-known player linking obesity and cancer. The secretion of pro-inflammatory adipokines, such as C-reactive protein, IL-6, tumour necrosis factor/TNF and IL-17 are increased under obese conditions [119, 138]. Results of a recent meta-analysis demonstrate that the circulatory upregulation of IL-6, TNF α and leptin is positively associated with aggressiveness of various types of cancer, including breast, endometrial, ovarian, kidney and colorectal cancer and multiple myeloma [139]. The pro-proliferative effect of

inflammation facilitates cancer development via promotion of angiogenesis and survival of cancer cells. The mechanism is related to the activation of signaling pathways that can support cell proliferation and angiogenesis or inhibit apoptosis. Such pathways include the IL-6/signal transducer and activator of transcription 3 (STAT3) and TNF α/nuclear factor κB (NFκB) signaling pathways [140]. Moreover, obesity-associated inflammation can induce genomic instability and interfere with DNA repair, therefore favouring tumourigenesis [141]. Secondly, obesity-associated inflammation provides connections between energy metabolism and cancer development. For example, the proinflammatory cytokine, IL-17A favours the uptake of palmitic acid by ovarian cancer cells, therefore promoting their proliferation [142]. Finally, obesity and cancer are also linked through the immune mechanism. For example, obesity reconstitutes the mammary adipose tissue, characterised by an increased density of myofibroblasts (labelled by α–smooth muscle actin/α-SMA) [143]. *In vivo* immune phenotype detection uncovered that the obesity-mediated ECM remodelling was causally associated with an increased infiltration of M2 macrophages which demonstrated an upregulated expression of angiogenic genes [144].

1.3.3.4 Characteristics of tumour-associated adipose tissue

Adipose tissue has high plasticity in response to different pathophysiological conditions, including cancer [118]. As an important component of the tumour stroma, adipose tissue grown in proximity to cancer cells undergoes dramatic changes in morphology, lipid metabolism and secretory profile [145]. Such alterations shape the tumour-modified adipocytes into a specific phenotype, which is named as cancer-associated adipocytes [146]. The close coordination between adipocytes and cancer cells is crucial for mediating the progression of cancer, resulting in significant adipose tissue remodelling in cancer-associated cachexia (**Fig 1.4**).

The tumour microenvironment could induce the dedifferentiation of adipocytes. In the invasive edge of breast cancer, the size and lipid content of adipocytes were less than which was seen distant from the tumour [147]. Using an *in vitro* model, the process of delipidation was reconfirmed when the expression of adipocyte markers (for example, FABP4 and adiponectin) was decreased in adipocytes co-cultured with breast cancer cells [148]. The liberated lipids can fuel the growth of cancer cells. The free fatty acids released by adipocytes can be translocated into nearby cancer cells where the gene expression involved in lipogenesis is upregulated [149]. Huang and colleagues have found a mechanism that may explain the reverse lipid metabolism in cancer cells and adipocytes [150]. Huang *et al.* found adipogenesis and lipid metabolism related genes, for example, genes coding for mammalian target of rapamycin receptor complex 1 (mTORC1) and peroxisome proliferator-activated receptor α (PPARα), were suppressed in adipocytes but upregulated in cancer cells. This change, favoured energy utilisation of cancer cells while saving energy consumption in the adipose

tissue. They further found the lipid metabolic remodelling aggravated the invasive capacity of prostate cancer cells in a mouse model, which was dependent on the activation of the CPT1A (a PPARα target gene)-osteopontin/*Spp1* signaling pathway when the upstream gene *P62* was silent. Moreover, the macrophages infiltrated in *P62* ablated adipose tissue were reprogrammed from M1 to M2, which may synergise the metastasis of tumour cells [151].

Cancer-associated adipocytes exhibit a fibroblast-like phenotype, promoting invasiveness of cancer through regulating the secretion of both soluble factors and extra-cellular matrix (ECM) molecules. Muller and her team found both the gene and protein expression of IL-6 and matrix metalloproteinases-11 (MMP-11) was significantly higher in the breast cancer-associated adipose tissue compared with those from healthy donors [148]. In their research, the adipose stroma-derived IL-6 exerted a pro-invasive effect on cancer cells. The ECM protease MMP may synergise the pro-invasive effect of IL-6 by facilitating cancer cells to overcome the ECM barrier [152, 153].

Loss of WAT during cachexia is a common comorbidity in late stage of malignant cancer [154]. Treatment with IL-6 receptor antibody rescued the atrophy of adipocytes, decreased the serum free fatty acid levels and downregulated the expression of uncoupling protein-1 (UCP-1) in the WAT of the colon cancer cachexia mice model, indicating the lipolysis and browning of adipose tissue in late stage of cachexia might be IL-6 signaling pathway dependent [155]. Cancer cachexia also activates the fibrotic remodelling of adipose tissue. For example, Alves and colleagues found using IHC that the ECM proteins, for example, collagen, fibronectin and elastin, were upregulated in the subcutaneous adipose tissue from cachectic patients with gastrointestinal cancer compared with weight-stable controls. αSMA staining and fibroblast-specific protein 1 (FSP1) expression showed in cachectic patients that there were more myofibroblasts around the adipocytes, which contributed to the activation of the TGF β signaling pathway [156]. The increased ECM promotes the M2 polarisation of macrophages, which further aggravates adipose tissue remodelling and cancer metastasis [157].

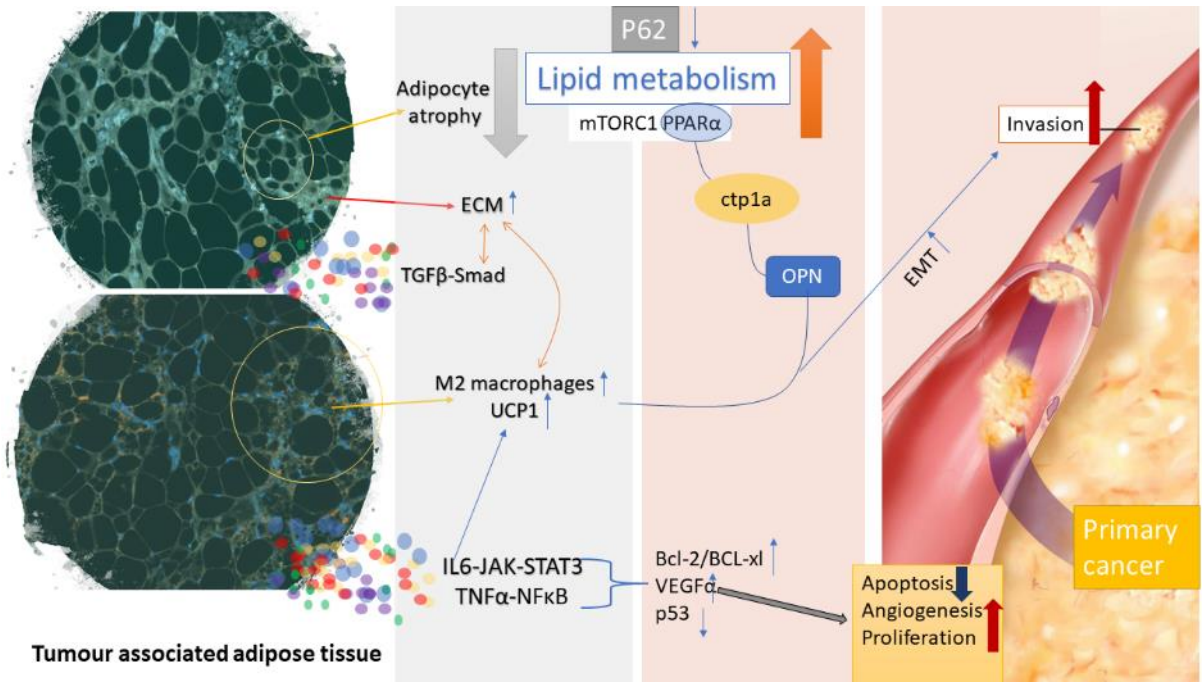

Fig 1.4 Characteristics of tumour associated adipose tissue in cancer cachexia

In the adipose tissue at late stage of cachexia, adipocytes with atrophic morphology have an active browning process, as demonstrated by an upregulated UCP-1. Tumour associated adipose tissue and the tumour exhibit opposite profiles of lipid metabolism: the adipogenesis and lipogenesis is suppressed in the adipose tissue whereas the catabolic process is activated in cancer cells. This change is dependent on downregulation of an autophagy adaptor P62 in the adipose tissue and related to a reverse modulation of mTROC1 and PPAR α: downregulation in adipocytes and upregulation in cancer cells. The downstream cascades of PPAR α promote cancer metastasis through a PPAR α-CPT1A signaling pathway, which increases synthesis of OPN. Tumour-associated adipose tissue accumulates increased ECM components as a result of an activated TGF β-smad signaling pathway. The remodelling of tumour associated adipose tissue is also characterised by an increased infiltration of M2 macrophages, which may facilitate invasion of the tumour through activating EMT. The proinflammatory adipokines (e.g IL-6 and TNF α) activate IL-6-JAK-STAT3 and TNF α-NFκB signaling pathways, and collectively exert pro-tumourigenic and anti-apoptotic effects.

Abbreviations: ECM, extra cellular matrix; EMT, epithelial mesenchymal transition; JAK, Janus Kinase; mTORC, mammalian target of rapamycin receptor complex; NFκB, nuclear factor κB; OPN, osteopontin; PPAR, peroxisome proliferator-activated receptor; STAT, signal transducer and activator of transcription; TGF, transforming growth factor; TNF, tumour necrosis factor; UCP, uncoupling protein; VEGF, vascular endothelial growth factor

1.3.3.5 Adipose derived stem cells promote cancer metastasis

Mesenchymal stem cells (MSC) are known to support the migration of endothelial cells *in vitro* via a paracrine manner [158]. The increased migration capacity of endothelial cells in tumour stroma is a proangiogenic feature, which facilitates intravasation [159]. Hence, there is an increasing interest in investigating the role of adipose tissue derived mesenchymal stem cells (ASC) in promoting the invasion of cancer cells [160]. For example, a group of Chinese scientists recently reported that conditioned medium from murine ASC promoted the invasiveness of breast cancer cell lines, accompanied by the upregulation of VEGF. Moreover, they found the stem cell factor (SCF) secreted by ASC caused the downregulation of microRNA 20b (miR 20b), known to display tumour suppressor gene characteristics. Chromatin immunoprecipitation (Chip) assay showed that the promoter region of miR 20b had a binding site to E2F transcription factor 1 (E2F1) which was exported from the nucleus after activation of the SCF-mitogen activated protein kinase (MAPK)-P38 signaling pathway. Silencing of P38 or upregulating miR 20b blocked the SCF-induced invasion of cancer cells [161].

1.3.3.6 Adipocytes impede the metabolism of chemotherapeutic agents

Recently, there has been recognition that adipose tissue is involved in drug catabolism [162]. For example, a promising anti-cardiovascular disease agent, anacetrapib, was retained in the adipose tissue, inducing a prolonged and unwanted half-life. The drug was, therefore, banned from entering the market [163]. In the case of cancer chemotherapy, adipocytes were able to quickly absorb and catabolise daunorubicin into daunorubicinol which had less cytotoxicity [164]. The researchers demonstrated the abundant expression of daunorubicin-metabolising enzymes (e.g. aldo-keto reductases and carbonyl reductases) in adipocytes compared with other cell types, however they did not compare these enzymes in adipocytes derived from obese and lean donors. Hence, deductions could not be made regarding whether the distinct anti-cancer drug responses between the obese and lean individuals were directly related to the different distribution of drug metabolising enzymes in adipocytes [165]. Future research is warranted to investigate the crosstalk between adipose tissue and cancer prognosis from the angle of drug metabolism.

1.3.4 The role of macrophages in the tumour microenvironment

1.3.4.1 Tumour-associated macrophages - the allies of tumour cells

Macrophages can constitute up to 50 % of the solid tumour mass [166]. Most evidence suggests that the number of macrophages in tumour tissue is associated with poor cancer prognosis [167]. Typically, however, macrophages are responsible for cell killing [168]. As efficient phagocytic leukocytes in the innate immune response, monocytes migrate across vascular walls, then activate to

macrophages to engulf invading pathogens in infected tissue mediated by a system of receptors on macrophages [169]. Upon binding to the helper T lymphocytes (Th1, CD4+), the interferon-gamma (IFN-γ) receptors on macrophages are activated, which enables the macrophages to release lysosomal enzymes and nitric oxide to destroy microorganisms within the phagolysosome [170]. However, in the case of cancer, tumour-associated macrophages (TAM) do not phagocytose cancer cells. Instead, they are disguised as allies of tumour cells, hampering the anti-tumour effects of CD8+ cytotoxic T lymphocytes [171] and promoting angiogenesis both in the primary site of tumour and in the pre-metastatic niches (PMN) [172].

1.3.4.2 The subtypes and origin of macrophages

The application of flow cytometry and fate-mapping techniques enables us to better distinguish the individual components of the macrophage system. In a broad sense, macrophages compromise two subsets: infiltrating macrophages; and tissue-resident macrophages. Macrophage infiltration only happens at the site of pathologies, such as plaques in atherosclerosis [173] and adipose tissue in obesity [174]. Those infiltrating macrophages originate from circulating monocytes [168]. Tissue-resident macrophages are located throughout all tissues and they are often named specifically based on their location (e.g. mesangial cells in the glomeruli of kidneys, osteoclasts in bone, Kupffer cells in liver) [175]. The tissue-resident macrophages are crucial for the organogenesis and homeostasis of different organs [176, 177].

There has long been a dogma that all macrophages are derived from monocytes and originate from adult heamatopoietic stem cells (HSC) [178]. In fact, only the circulating monocytes originated entirely from HSC; most tissue resident macrophages originate from yolk sac-derived erythro-myeloid progenitors. They are minimally replaced by HSC-derived cells at different stages after birth in mice [179]. The maturation of fetal macrophages does not require the transcription factor, Myb, which regulates the proliferation of HSC [180]. Tissue-resident macrophages have life-long *in situ* self-renewing capacity, which is CSF dependent but IL-4 independent [168]. Hence, tissue-resident macrophages and infiltrating macrophages have distinct lineages. Studies exploring the origin of human TAM are limited. Using immunofluorescent staining for three cases of invasive secondary tumours (including breast, liver and oral mucosal cancer) after sex-mismatched bone marrow transplantation, Kurashige *et al.* found CD163+ TAM are originated from bone marrow (mainly contributed by the donor) [181]. Additionally, they found the macrophages in non-tumour tissue are completely replaced by bone marrow-derived cells, which is different from the findings in mice [179]. The discrepancy may be due to the longer life span of humans and a disruption of homeostasis by radiation therapy in their experiments.

1.3.4.3 Macrophage reprogramming in the tumour microenvironment

Macrophages have strong plasticity in response to different tumour microenvironment as demonstrated by a reprogramming of their immune phenotype (M1 or known as classically-activated macrophages and M2 or known as alternatively-activated macrophages) [182]. Although being criticised for its oversimplification, educating macrophages with specific chemokines (e.g. INFγ and lipopolysaccharide, LPS for M1; IL-4 and IL-13 for M2) is still widely applied and accepted to generate polarised macrophages *in vitro* to mimic the *in vivo* macrophage reprogramming [183]. The immune phenotype of macrophages in the tumour microenvironment is orchestrated by complicated signaling pathways and interaction with stromal cells.

As a downstream product of many cancer gene mutants (e.g. *p53*), the level of IL-6 is often high in the tumour microenvironment [184]. IL-6 exerts tumourigenic effects mainly through the IL-6-STAT signaling pathways [185] Additionally, IL-6 induces macrophage differentiation from monocytes and is also a product of differentiated macrophages [186]. IL-6 is also an important mediator of macrophage polarisation. For example, IL-6 activates the alternative macrophage polarisation through upregulating IL-4 receptors in mice and sensitising the IL-4-pSTAT6 effects on macrophages, causing an upregulation of genes associated with M2 macrophages, including *Mrc1*, *Arg 1*, *IL-10* and *Retnla* [187]. The upregulation of these M2 macrophage-associated genes was also observed in the murine macrophages bearing *JNK1* and *JNK2* mutations. The M1 macrophage-associated genes, including *cd11c*, *IL-1β*, *Il6*, *Nos2* and *TNF α*, were downregulated in this situation, indicating the JNK signaling pathway is crucial for M1 macrophage polarisation [188]. However, the mTOR signal may be indispensable for M2 macrophage polarisation, as demonstrated by a more significant M1-like shift for both immune phenotype and cytokine secretory profile in LPS-stimulated human peripheral blood mononuclear cells (PBMC) after rapamycin (an mTOR inhibitor) treatment [189].

Tumour stromal cells accelerate recruitment of macrophages in tumour tissues and modify the configuration of macrophages in the tumour microenvironment [190]. It was reported that co-culture of follicular lymphoma-associated MSC with CSF 1-activated monocytes for 7 days upregulated mRNA expression of IL-10, VEGF and IL-6 in macrophages, which facilitated angiogenesis. However, it blunted the sensitivity of macrophages following exposure to LPS, as demonstrated by a mild upregulation of TNF α, IL-10 and IL-12 compared with the culture without MSC [191]. Mutations of genes associated with lipid (e.g. *SQSTM1)* and glucose (e.g. *Sirtuin 6*) metabolism are frequent in many cancers [192]. As was discussed in a previous section, macrophages were driven into a M2 phenotype in P62 (coded by *SQSTM1*)-ablated adipose tissue [151]. Similarly, the M2

configuration of macrophages was present in *Sirtuin 6* ablated adipose tissue of mice in an IL-4-dependent manner [193].

1.3.4.4 Prognostic value of infiltrating M2 macrophages in tumour

Increased infiltration of M2 macrophages in tumour tissue has significant prognostic value for poor cancer outcome. Results from a transcriptomic analysis investigating immune cell profiles from 21,000 breast cancer samples demonstrated distinct prognostic potency for M1 and M2 macrophages, with upregulation of M2 but downregulation of M1 macrophages predicting poor cancer outcomes in most cases [194]. Additionally, high expression of M2 macrophage-associated genes was significantly associated with low response for chemotherapy (odds ratio [OR] = 0.78, p = 0.003) for both oestrogen receptor positive and negative breast cancer in that study. The last decade has seen an emerging interest in investigating the prognostic value of macrophage infiltration in tumour tissue, especially in the field of breast cancer (**Table 1.2**). Most evidence supports the lethal effect of high infiltration of M2 macrophages (CD163+, specifically). However, the prognostic implications were often different according to the cancer subtypes, the aggressiveness of the cancer, cancer therapy, the markers being detected and whether univariant or a multivariant statistics were applied.

Targeting of tumour-infiltrating M2 macrophages is promising in cancer therapy. For example, blocking the chemokine C-C motif ligand 2 (CCL2)/ C-C chemokine receptor 2 (CCR2) signals decreased the number of tumour infiltrating macrophages and suppressed the polarisation of macrophages to a M2 phenotype in a mouse hepatocellular carcinoma model. The mRNA expression of M2 macrophages and cytokines secreted by M2 macrophages were downregulated after CCR2 knockdown or blockade. The postsurgical recurrence of tumours was decreased in a CD8+ T cell-dependent manner, indicating blocking the CCL2/CCR2 signals can release the M2 macrophage-mediated immune-suppression in the tumour microenvironment [195].

1.3.4.5 The protumoural role of TAM

The popular gene profile to distinguish M1 and M2 macrophages is a result of an *in vitro* experiment using specific cytokine stimulation on monocytes [196]. TAM in the real tumour microenvironment often have a more complicated profile of gene expression and cytokine secretion [197]. The high expression of M2 macrophage markers (e.g. CD163) can independently predict poor cancer prognosis, though it is now more acceptable to refer to them as TAM from a functional point of view. The protumoural role of TAM will be discussed in this section in three aspects: immunosuppression, angiogenesis and metastasis (**Fig 1.5**).

Transcriptomic analysis has demonstrated that numbers of tumour-infiltrated macrophages and regulatory T (Treg) cells increase while CD8+ T cells and Th cells decrease with aging, in cancers which have an aging-associated poor prognosis. These data indicate that macrophage infiltration in tumour tissue may favour an immune-suppressive tumour microenvironment [198]. The upregulation of IL-4 receptor α (IL-4Rα) is seen in M2-polarised macrophages and in CD14+ PBMC isolated from cancer patients [199]. IL-4Rα expressed on macrophages is important for maintaining the T-cell immune suppression in tumour microenvironment, because knock-out of the gene coding IL-4Rα in macrophages completely rescued the inhibited anti-tumour immunity after CD8+ T cell supplementation in mice. Although the CD11b+ myeloid cells had a M2-like gene expression profile (e.g. *Arg, mrc1, IL-10, TGF-β*), the high expression of IL-4Rα was collectively induced by IL-13 and TNF-α rather than by IL-13 alone [200]. Granulocyte-macrophage colony stimulating factor (GM-CSF) overexpression in the setting of cancer is responsible for the recruitment of myeloid-suppressor cells [201]. It was recently reported that GM-CSF supported the secretion of IL-8 by macrophages, which is necessary for the upregulation of PD-L1 on macrophages. This autonomous PD-L1 expression suppressed the anti-tumour immunity of CD8+ T cells [202].

Altered macrophage metabolism favours the formation of abnormal vasculature in the tumour microenvironment [203]. The infiltration of CD163+ cells is correlated with the density of vasculature in the tumour stroma, indicating macrophages may promote cancer progression through supporting angiogenesis [204]. Upregulation of the development and DNA damage response 1 (REDD1), a suppressor for mTORC1, in hypoxic TAM inhibited glucose uptake and glycolysis in TAM, supporting the usage of glucose in surrounding endothelial cells. Knockdown of REDD1 in hypoxic TAM recovered the pericyte coverage and cadherin junctions between endothelial cells in the highly permeabilised vasculature, therefore preventing metastasis [205].

TAM support metastasis of tumours [206]. MMP is a family of enzymes that can degrade components constituting ECM and is important in tumour invasion [207]. In an estrogen receptor negative breast cancer cohort (n = 89), the high expression of MMP-9 in CD163 and CD68 double positive cells was associated with a worse OS ($p<0.001$), indicating TAM may support tumour metastasis through secreting MMP-9 [208]. Hiratsuka *et al.* found that cancer cell lines injected through the tail vein of mice were preferably metastasised to lung in a VEGF receptor 1 (VEGFR 1)-dependent manner. Moreover, MMP-9 expression was higher in lung than other organs which did not show metastasis. They further proved that the interaction between endothelial cells and TAM is necessary for MMP-9 expression in both endothelial cells and macrophages. These results suggest that TAM are important inducers for distant metastasis and relevant mechanism is related to the MMP 9-VEGR 1 signaling

Table 1.2 Prognostic value of macrophage infiltration in tumour tissue

Macrophage (mc) markers/ statistics/annotation (if any)	Prognostic significance	Sample size	Type of cancer	Year	Country	Ref
CD68, CD163, CD11c/ Multivariant Cox regression analysis	1. Infiltration of higher number of CD163+mc in TN was correlated with shorter DFS. (HR=1.86*). 2. Infiltration of higher number of CD11c+ mc in TS was correlated with longer DFS. (HR=0.32**).	367	Invasive breast cancer	2019	South Korea	[209]
CD68, CD163/ Cox proportional hazards model/ No adjustment for covariant	1. Infiltration of higher number of CD163+mc in adipose stroma was associated with shorter DFS in node-negative breast cancer (n=42*). 2. High presence of CD68+ CLS was associated with shorter DSF in node-positive breast cancer (n=56*).	140	Breast cancer tissue harbouring>50 % of the adipose stroma	2018	South Korea	[210]
CD68, CD163/ Spearman correlation and simple linear regression analysis/ No adjustment for covariant	1. High CD163 expression in ER negative and triple negative cohorts was associated with longer OS*. 2. High CD68 expression in ER negative cohort was associated with shorter OS*.	558	Breast cancer	2018	United States	[208]
CD68, CD163/ Multivariant Cox regression model	Infiltration of higher number of CD163+ mc in TS was associated with short OS (HR=2.9**).	371	Invasive breast cancer	2018	United States	[211]
CD68 CLS/ Multivariant cox regression analysis	High density of CD68+ CLS (>5 per tissue) was associated with high chance to develop malignant cancer (HR=6.8*).	172	Adipose stroma of benign breast tumour	2018	United States	[212]
CD68/ Multivariant cox regression analysis	High infiltration of CD68+ mc was significantly associated with shorter OS.	58	Invasive breast cancer	2017	United States	[213]

CD163/ Cox regression analysis/ No adjustment for covariant	1. Overall, high CD163 positive did not show prognostic significance for DFS. 2. Only in the cohort accepting radiation therapy (n=40), high CD163 positivity was correlated with short DFS*.	83	Breast cancer treated by conserving surgery showing no evidence of metastasis	2018	Sweden	[214]
CD163/ Multivariant Cox regression analysis	Infiltration of higher number of CD163+ mc was associated with shorter recurrence free survival (HR=2.2*) and increased lymph node metastasis (HR=4.4***).	282	Invasive breast cancer	2017	Norway	[215]
CD163/ Multivariant Cox regression analysis	1. Infiltration of higher number of CD163+ mc was associated with shorter OS (HR=4.15***). 2. Infiltration of higher number of CD163+ mc was associated with shorter DFS (HR=3.83***).	278	Triple negative breast cancer	2018	China	[216]
CD68, CD163, CD204/ Multivariant Cox regression analysis	1. Infiltration of higher number of CD204+ cells was associated with shorter recurrence free survival (HR=4.61**), distant recurrence free survival (HR=8.57**) and breast cancer specific survival (HR=15.87***). 2. No significant prognostic value was found for CD68 and CD163.	149	Breast cancer including luminal-like, Her2 positive and triple negative subtypes	2017	Japan	[215]
CD68, CD206 and CD11c/ Multivariant Cox regression analysis	1. Combined CD206/CD11c signature (CD206 low and CD11c high) was an independent prognostic variable for longer DFS (HR=0.65*). 2. No significant prognostic value was found when CD68, CD206 or CD11c was evaluated singly as an independent variable.	185	ccRCC	2014	China	[217]
CD163/ Multivariant Cox regression analysis	Infiltration of higher number of CD163+ cells was associated with shorter DFS. (HR=2.5*).	75	Colorectal cancer	2014	Sweden	[193]

CD163/ Multivariant Cox regression analysis	1. Infiltration of higher number of CD163+ cells was associated with shorter progression free survival (HR=2.68**) and OS (HR=2.30**). 2. No significant prognostic value was found for CD68.	110	Stage 3 and 4 epithelial ovarian cancer	2013	China	[218]
CD163/ Multivariant Cox regression analysis	1. The number of CD163+ cells are more in pancreatic undifferentiated carcinoma with osteoclast-like giant cells than in anaplastic carcinomas of pancreas, without osteoclast-like giant cells. 2. CD163 expression did not show prognostic significance for OS.	27	Pancreatic undifferentiated carcinoma with osteoclast-like giant cells	2018	Italy and United States	[219]
CD163/ Student t test/ Direct prognostic value is unavailable.	CD163 positivity was higher in the high atypical score group than in the low atypical score group**.	50	Meningioma	2013	Japan	[193]

Abbreviations: ccRCC, clear cell renal cell carcinoma; CLS, crown-like structure; DFS, disease free survival; ER, estrogen receptor; HR, hazard ratio; mc, macrophages; OS, overall survival; TN, tumour nest; TS, tumour stroma; *p<0.05, **p<0.01, *** p<0.001

pathway [220]. The activated downstream phosphoinositide 3-kinase (PI3K)-AKT signaling may favour the tumour progression both in the primary and metastatic sites [221].

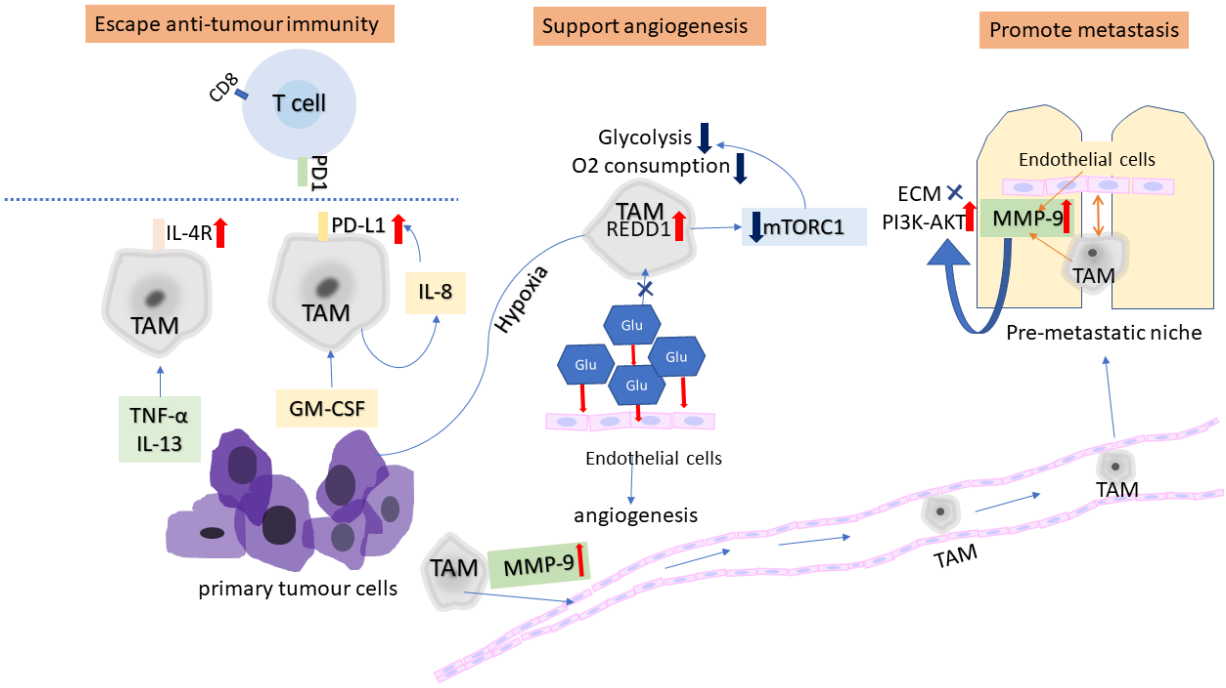

Fig 1.5 The protumoural role of TAM

In the tumour microenvironment, GM-CSF activates TAM to secrete IL-8, which upregulates the expression of PD-L1 on TAM; TNF-α and IL-3 activate TAM in cooperation, which upregulates the expression of IL-4R on TAM. These changes collectively impede the CD8+ T cell mediated anti-tumour immunity. The hypoxic microenvironment upregulated REDD1 on TAM, which is an inhibitor of mTORC1. Consequently, the uptake of glucose and glycolysis was suppressed in TAM. The saved O_2 and glucose were exploited by neighbouring endothelial cells, therefore favouring the formation of the abnormal vasculature which is leaky. MMP-9, the protease for degrading ECM, is upregulated on TAM, which facilitates the tumour invasion at primary site and translocation of TAM at pre-metastatic niches. The interaction between TAM and endothelial cells at pre-metastatic niches further upregulates the MMP-9 expression on both TAM and endothelial cells in an auto-stimulatory manner. The normal ECM was disrupted. Cooperating with the activated PIK3-AKT signaling pathway, this change prepares the pre-metastatic niche for tumour seeding and progression.

Abbreviation: ECM, extra cellular matrix; Glu, glucose; GM-CSF, granulocyte-macrophage colony stimulating factor; IL-4R, IL-4 receptor; MMP-9, matrix metalloproteinases 9; mTORC1, mammalian target of rapamycin complex 1; PD-L1, Programmed cell death ligand 1; PI3K, phosphoinositide 3-kinase; O_2, oxygen; REDD1, regulated in development and DNA damage response 1; TAM, tumour-associated macrophages; TNF, tumour necrosis factor

1.3.4.6 Macrophages – a link between adipose tissue and cancer

The importance of macrophages that reside in adipose tissue in driving cancer progression has been highlighted, but the molecular mechanisms underlying their regulation of the crosstalk between adipocytes and cancer cells have not been well established.

There is a reverse regulation of energy metabolism between cancer cells and the proximal adipose tissue [150]. Additionally, adipose tissue resident macrophages are important in maintaining the metabolic homeostasis of adipose tissue, highlighting the pivotal role that macrophages play in connecting adipocyte and cancer cell metabolism [222]. M2 macrophages, the predominant cancer-associated macrophages, have a distinct metabolic profile, as characterised by a high level of fatty acid oxidation as a response of the IL-4/PPAR-ϫ-coactivator-1β/STAT6 signal activation [223]. It was reported in Nature that the activation of M2 macrophages was indispensable in the process of WAT browning in exposure to cold [129]. The lipid metabolic profile in this process resembles that in cancer-associated cachexia where WAT lipolysis is increased, indicating M2 macrophages may fuel cancer cells through facilitating the lipolysis of cancer associated adipose tissue [136]. M2 macrophage derived exosomal apoprotein E is known to contribute to the invasion of gastric cancer cells through the PI3-AKT signaling pathway [224]. The lipid transport protein, apoprotein E, is crucial for maintaining the homeostasis of lipid metabolism in adipose tissue [225]. Hence, apoprotein E may be an important molecular regulator in the orchestration of adipose tissue remodelling in the context of cancer progression through both non-lipid and lipid functions.

Obesity-associated macrophages also increases stemness of cancer cells. Single-cell technologies have shown that tumour tissue compromises non-malignant stromal compartments (for example, fibroblasts, endothelial cells and immune cells), stem cell-like populations and differentiated cancer cells [226]. Aggressive cancer cells often exhibit profiles shared by stem cells, such as stem-like transcriptional features and uncontrolled proliferative ability [227, 228]. It was recently reported that infiltrating macrophages from obesity-associated mammary fat promote the stem-like properties of breast cancer cell lines [229]. Payal *et al.* found a predominant phenotype of macrophages in mammary fat tissue under a pre-existing obese microenvironment, which expressed CD36 and Plin2 in mice, and ABCA1 and CD36 in humans. These proinflammatory and metabolically activated macrophages, or their conditioned medium, facilitated the formation of tumour spheroids, accompanied by an upregulated stem-like mRNA expression in cancer cells. The mechanism was dependent on the activation of the IL-6-glycoprotein 130-phosphorylated STAT 3 (IL-6-GP130-pSTAT3) signaling pathway.

1.4 Knowledge gaps

Based on the literature review and the research interest, the following knowledge gaps have been recognised:

1. The ER stress expression level in the perinephric adipose tissue and relevant association with the prognosis of kidney cancer have not been studied.
2. The precise mechanism which can explain "obesity paradox" in kidney cancer is largely unknown.
3. There has not been a cost-effective *in vitro* model to mimic the functional perinephric adipose tissue microenvironment.
4. Whether an ER stress-activated adipose tissue microenvironment will impact the macrophage behaviour and whether the "obesity paradox" in kidney cancer can be partially explained through related mechanisms are unclear.
5. The macrophage phenotype in kidney cancer-associated adipose tissue has not been mapped in human samples.
6. The invasive capacity of kidney cancer cells towards adipocytes in the presence of different macrophages has not been compared *in vitro*.

1.5 Aims

The hypothesis of this thesis was that the heterogeneous adipose tissue microenvironment had a role in cancer development, especially for kidney cancer.

The primary aims of this thesis were to:

i Evaluate the risk stratification potential of an ER stress marker GRP78 in the perinephric adipose tissue of ccRCC (**Chapter 2**);

ii Establish a three-dimensional (3D) *in vitro* culture platform to mimic the functional adipose tissue microenvironment (**Chapter 3**);

iii Investigate macrophage behaviour in the adipose tissue microenvironment (**Chapter 4**), in particular to:

a. Evaluate polarisation of macrophages;
b. Evaluate the migration and invasion of macrophages;
c. Evaluate the different invasion capacity of cancer cells in the presence of different macrophage phenotypes;

iv Evaluate the association of immunophenotyping of adipose tissue with aggressiveness of ccRCC, with particular regard to distant metastasis (**Chapter 5**).

Chapter 2

GRP78 expression in tumour and perinephric adipose tissue is not an optimal risk stratification marker for ccRCC

2.1 Included Publications

This chapter is adapted from an original research article published in *PLOS ONE*.

Shen K, Vesey DA, Ellis RJ, Del Vecchio SJ, Cho Y, Teixeira-Pinto A, McGuckin MA, Johnson WJ, Gobe GC. (2019) GRP78 expression in tumour and perinephric adipose tissue is not an optimal risk stratification marker for clear cell renal cell carcinoma. *PLOS ONE* 14(1): e0210246. https://doi.org/10.1371/journal.pone.0210246

The candidate was the lead author of this original research article. She contributed significantly to the conception and design of this study (80 %) and analysis and interpretation of the literature (70 %), and drafted the majority of the manuscript (90 %).

2.2 Overview

Objective: ccRCC is the most common subtype of kidney cancer, which is difficult to treat and lacks a reliable prognostic marker. A previous study showed that the ER stress marker, GRP78, is a potential prognostic marker for ccRCC. The present study aimed to: (1) examine whether GRP78 was upregulated in ccRCC compared with matched non-neoplastic renal tissue; and (2) investigate whether GRP78 expression in ccRCC tissue or perinephric adipose tissue has any association with ccRCC aggressiveness.

Methods: A retrospective cross-sectional study of 267 patients who underwent nephrectomy for renal tumours between June 2013 and October 2017 was conducted at Princess Alexandra Hospital, Brisbane, Australia. Software-assisted quantification of average grey value of staining (staining intensity method) and proportion of positive pixels (positive pixel method) was applied to measure expression of GRP78 in archived specimens of renal tumour tissues (n = 114), adjacent non-neoplastic renal tissues (n = 68), and perinephric adipose tissues (n = 60) in participants diagnosed with ccRCC.

Results: GRP78 was not upregulated in renal tumour tissue compared with paired normal renal tissue. In tumour tissue, GRP78 expression did not show any association with ccRCC aggressiveness using either quantification method. In adipose tissue, downregulation of GRP78 demonstrated poor correlation with increased probability of metastasis, with one unit increase in average grey value of GRP78 staining weakly correlating with a 17 % increase in the OR of metastasis (95 % CI: 0.99 to 1.38, p = 0.07).

Conclusion: GRP78 expression in tumour tissue is not valuable as a risk stratification marker for ccRCC.

2.3 Introduction

The kidney is the 14th most common site for primary malignancy worldwide [8]. Approximately 90 % of kidney cancers are RCC, of which ccRCC is the most common variety, constituting approximately 75 % of all RCC diagnoses [230]. The next most common RCC variants are papillary and chromophobe RCCs, which have a lower rate of metastasis compared with ccRCC. Common benign renal tumours include papillary adenoma, renal oncocytoma, and angiomyolipoma [231]. Although imaging modalities, such as computerised tomography, are able to differentiate between malignant and benign renal tumours, this process is not completely reliable, and approximately 5-8 % of lesions remain indeterminate [232]. Identification of molecular markers which are better able to identify tumours expected to have worse patient outcomes would therefore be of great value to patients and clinicians.

ER stress markers show promising risk stratification potential for ccRCC [37]. The ER is responsible for the quality control of protein folding. Accumulation of misfolded proteins causes ER stress, which is correlated with tumourigenesis [233]. GRP78 is a chaperone of the heat shock protein 70 family and is one of the best-recognised ER stress markers [96]. Fu and colleagues first reported the upregulation of GRP78 in the renal tumour tissue from 42 Chinese ccRCC patients, where they showed association between GRP78 expression with clinicopathological features [37]. There was a significantly higher expression of GRP78 in renal tumours compared to the adjacent non-neoplastic kidney, and the level of GRP78 expression was positively correlated with advanced TNM stages and larger tumour size. However, the conclusions that could be drawn from this study were limited by lack of adjustment for confounders (e.g. BMI, diagnosis of hypertension and smoking history), possible observer bias due to the subjective nature of semi-quantitative measurement, small sample size and limited generalisability with respect to race. Moreover, the clinical translation of the finding was restricted due to its dependence on renal biopsy, which is not consistently performed in the diagnosis of kidney cancer considering the low diagnostic accuracy and various complications [234].

The biopsy of perinephric adipose tissue poses less risk for patients than renal biopsy if we could find a marker which can predict aggressiveness of ccRCC. Expression of ER stress markers in adipose tissue has been shown to be a potent prognostic marker for endometrial cancer. In a retrospective study (n = 179), Koji *et al*. [110] investigated the correlation between clinical outcomes of endometrial cancer and expression of ER stress markers in visceral adipose tissue. They found that the proportion of positive staining for GRP78 and CHOP was positively correlated with higher tumour stage ($p = 0.005$) and negatively associated with disease-free survival ($HR = 2.88$, $p = 0.005$). Similar to the contributing role of obesity for endometrial cancer, being overweight ($BMI \geq 25 kg/m^2$) is an established risk factor for developing ccRCC, with the observed relative risk being 1.5 times

higher than that of patients with a normal BMI [235]. Paradoxically, overweight patients appear to have a lower risk of dying from kidney cancer (HR = 0.49) [3]. Little is known about the expression of GRP78 in perinephric adipose tissue and its potential prognostic role for ccRCC.

To further elucidate the relationship between ER stress, obesity and kidney cancer, we applied IHC staining to investigate GRP78 expression in renal tumour, non-neoplastic renal tissue and perinephric adipose tissue. The study hypotheses included that, 1) GRP78 expression is upregulated in tumour tissue compared with matched normal renal tissue; and 2) the expression levels of GRP78 in both tumour tissue and perinephric adipose tissue are positively associated with ccRCC aggressiveness. Understanding the expression patterns of the ER stress marker GRP78 in renal samples and perinephric adipose tissue may prove to be translationally meaningful, by allowing risk stratification of ccRCC patients and development of effective therapies which modulate ER stress levels. Moreover, exploring the prognostic role of GRP78 expression in perinephric adipose tissue would help to better understand the roles of tumour-associated adipose tissue in the pathogenesis of ccRCC.

2.4 **Methods**

2.4.1 Sample and data collection

This study received ethics approval from the Metro South Human Research Ethics Committee (HREC/05/QPAH/95; HREC/16/QPAH/353) and utilised archived formalin-fixed, paraffin-embedded (FFPE) specimens from consenting patients who underwent nephrectomy for renal tumours at the Princess Alexandra Hospital, Brisbane, Australia between June 2013 and September 2017 [236]. Inclusion criteria include that, 1) aged over 18 years old; 2) did not accept treatment for kidney cancer before surgery and 3) diagnosis of ccRCC. Following nephrectomy, samples of tumour tissue, distal non-neoplastic cortical tissue, and tumour-adjacent perinephric adipose tissue were excised, fixed in 4 % formaldehyde for 24 hours, and stored at 4°C prior to being blocked in paraffin. Clinical data were recorded in a database. Demographic data, medical and smoking history were collected from structured interviews and corroborated through chart review. Pathological diagnosis was recorded from the pathology report. Tumours were staged according to the 7th TNM Classification of Malignant Tumours [237] and graded according to the International Society for Urological Pathology (ISUP) grading system for RCC by two pathologists [238]. Work flow of study participation is summarised in **Fig 2.1**.

2.4.2 IHC staining

Sections of 4 μm thickness were cut onto Superfrost Plus slides. Paraffin was removed by xylene and the tissue was rehydrated through graded washes of ethanol in water, ending in a final rinse in water. Endogenous peroxidase activity was quenched by incubation in 3 % hydrogen peroxide/H_2O_2 (H-1009, Sigma) for 10 min. A microwave (Whirlpool, 850W) was used for antigen retrieval. Slides were put into a lidded glass container which was filled with 250 mL of Tris-EDTA solution (10mM Tris Base, 1mM EDTA solution, 0.05 % Tween 20, pH=9). Two cycles of antigen retrieval (first cycle: power of 10 for 2 min and 20s; second cycle: power of 2 for 15 min) were applied. Non-specific binding was blocked by Background Sniper (BS966, Biocare Medical) for 15 min, followed by an incubation with the primary antibody (GRP78, 1:50, SANTSC-376768, Santa Cruz Biotechnology) at room temperature for one hour. MACH 1 Universal HRP-Polymer detection kit (901-M1U539-082914, Biocare Medical) containing anti-mouse secondary antibody (incubated for 15 min), signal amplification reagent (incubated for 30 min) and diaminobenzidine hydrochloride chromogen (DAB) (incubated for 5 min), was used per manufacturer's instructions followed by counterstaining with haematoxylin (AHH-1L ProSciTech). A section of liver tissue (gifted by Clay Winterford, Berghofer Medical Research Institute, Brisbane) known to express GRP78, as indicated by the primary antibody datasheet, was used as the positive control. The negative control was done by eliminating the primary antibody prior to adding the secondary antibody. The specificity of the

GRP78 antibody was tested by mixing the primary antibody with a blocking peptide (GL Biochem/Shanghai-687830, amino acid sequence: ee edkkedvgtv vgidlgttys cvgvfkngrv) at a concentration ten times of the primary antibody. The mixture was left at room temperature for one hour before being added to the slides (**Fig 2.2**). Staining of slides was carried out blinded to the medical records.

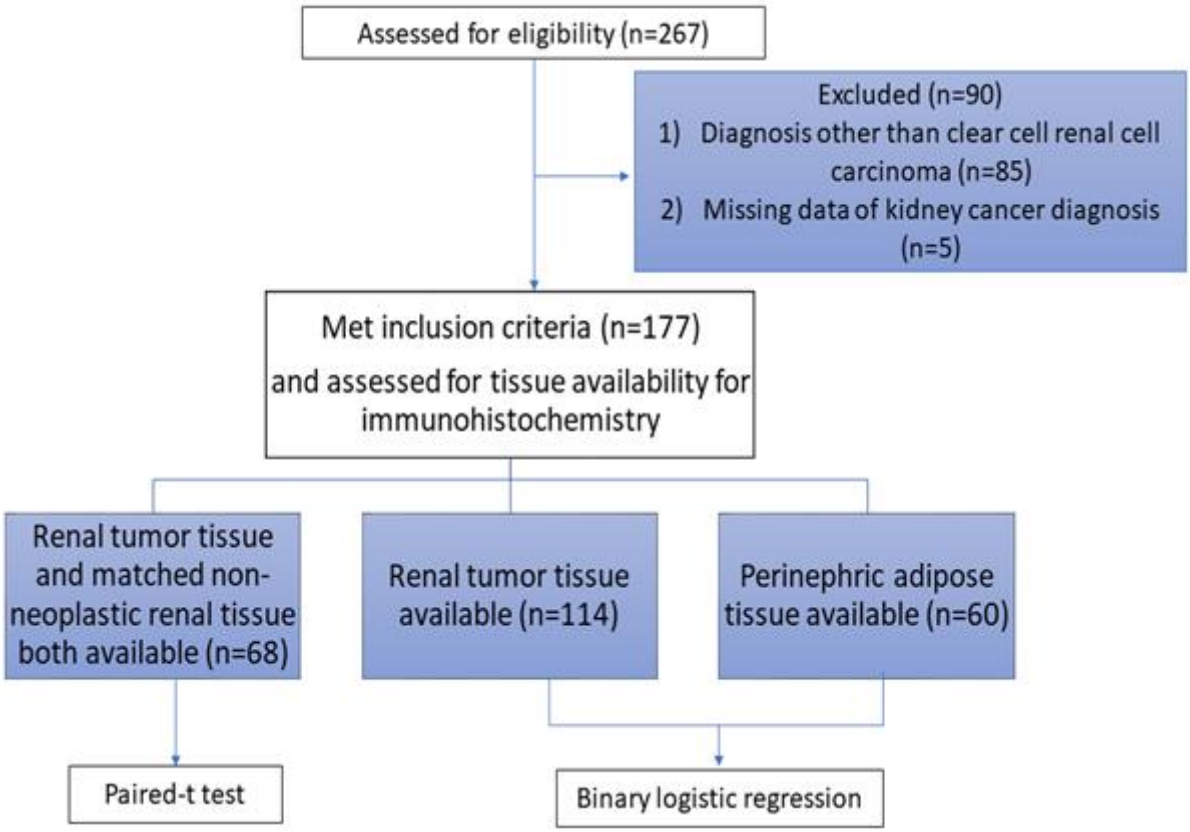

Fig 2.1 Flow chart of participation in the study

267 participants recorded in the database were assessed for eligibility. 90 participants who did not meet the inclusion criteria were excluded. Included 177 participants were further assessed for tissue availability for immunohistochemistry staining. Finally, 68 participants with both tumour and non-neoplastic renal tissue available were included in the paired-t test. Participants with the tumour tissue available (n = 114) or with the perinephric adipose tissue available (n = 60) were included in the binary logistic regression analysis.

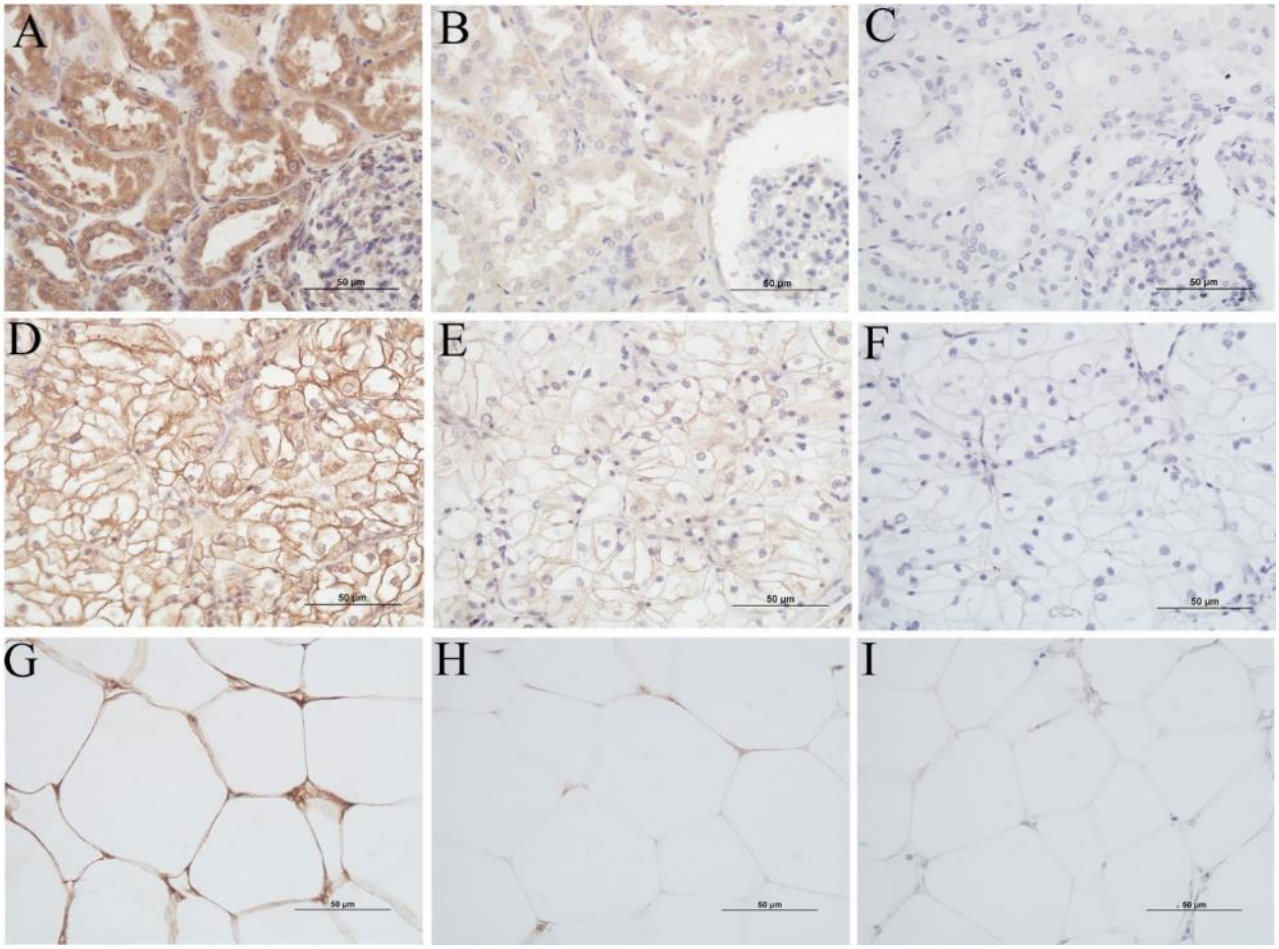

Fig 2.2 Staining patterns of GRP78 in different tissues

Images were captured at x40 using Nikon Brightfield microscopy. (A) Non-neoplastic renal tissue; (B) Negative control of non-neoplastic renal tissue (blocking peptide mixed with primary antibody); (C) Negative control of non-neoplastic renal tissue (eliminating primary antibody); (D) Clear cell renal cell carcinoma; (E) Negative control of clear cell renal cell carcinoma (blocking peptide mixed with primary antibody); (F) Negative control of clear cell renal cell carcinoma (eliminating primary antibody); (G) Perinephric adipose tissue; (H) Negative control of perinephric adipose tissue (blocking peptide mixed with primary antibody); (I) Negative control of perinephric adipose tissue (eliminating primary antibody).

2.4.3 Image capture and analysis

The stained slides were scanned with Olympus Slide Scanner VS120 (rm4026,) using the x20 objective. The scanned images were viewed using the OlyVia image reading software. Three to five snapshots were captured randomly at 50 % view size from each original image. The cropped images were saved in TIFF format and exported into the software Fiji for analysis [239]. Firstly, a statistical model was built using IHC toolbox to detect the DAB-stained colour in renal tissues and adipose tissues [240]. Secondly, images were manually edited by deleting glomeruli, large blank areas, vessels and fibrosis. Macro language was written for processing series of commands. Colour threshold was set to “0-254” prior to measuring average grey value and proportion of positive pixels. Methods used

for measuring the proportion of positive pixels were based on previous studies [241]. Average grey value was used to measure staining intensity of DAB. The more chromogen presented in stained areas, the darker the brown colour appeared macroscopically. However, as measured by the standard intensity function of Fiji, standard red-green-blue (RGB) colour images acquired from bright field microscopy had the lowest average grey value of 0 for a black, dark-stained area and the highest average grey value of 250 for a white, unstained area [242]. This resulted in an inverse correlation between average grey value and staining intensity.

2.4.4 Statistical analysis

Categorical data were reported as count (percentage). Continuous data were reported as mean (95 % CI or standard deviation) or median (interquartile range [IQR]), depending on whether or not the data were normally distributed. Outcome variables regarding ccRCC aggressiveness were dichotomised as follows: tumour grade: low [1-2] and high [3-4]; tumour stage: low [1-2] and high [3-4]; tumour size: [≤70mm] and [>70mm]; metastases: [presence] and [absence]. A paired-t test was used to compare GRP78 expression (measured by both average grey value of staining intensity and proportion of positively stained pixels) between renal tumour tissue and adjacent non-neoplastic renal tissue. Binary logistic regression was applied to model ccRCC aggressiveness based on the expression value of GRP78, adjusting for potential covariates, including BMI, history of smoking and diagnosis of hypertension. To evaluate the predictive ability of the logistic models, receiver operating characteristic (ROC) curves were fitted to the logistic models and the area under the ROC curve (AUC) reported. Differences in GRP78 expression between benign tumour and ccRCC, and distribution of GRP78 between different outcome variables were displayed descriptively. P-values<0.05 were considered statistically significant. Statistical analysis was performed using Stata 14 (StataCorp, College Station, TX, USA).

2.5 Results

2.5.1 Patient characteristics

267 participants recorded in the database were assessed for eligibility. After excluding 90 participants who did not meet the inclusion criteria (missing data about kidney cancer diagnosis n = 5, diagnosis other than ccRCC n = 85), 177 participants were further assessed for tissue availability when included in specific statistical analysis. 68 participants with both tumour and non-neoplastic renal tissue available for IHC were included in the paired-t test when comparing the GRP78 expression between the tumour tissue and the matched non-neoplastic renal tissue. Participants with the tumour tissue available (n = 114) or with the perinephric adipose tissue available (n = 60) for IHC were included in the binary logistic regression analysis when predicting ccRCC aggressiveness based on the expression value of GRP78 in either tissue type (**Fig 2.1**). Demographic and clinicopathological characteristics of 68 participants for whom both tumour tissue and normal renal tissue were available for IHC analysis are displayed in **Table 2.1**.

2.5.2 Staining patterns of GRP78 in tumour tissue and non-neoplastic renal tissue

In ccRCC tissue, the expression of GRP78 was mainly observed in areas close to the cell membrane. The cytoplasm of some ccRCC cells was unstained due to the lipid-rich cytoplasmic deposits being washed away during tissue processing **(Fig 2.3A)**. In non-neoplastic renal tissue, GRP78 is positive in all tubules with no distinctive difference of staining intensity between proximal renal tubule and distal renal tubule epithelial cells. However, in the capillary bundles of glomeruli, the GRP78 expression is much lower (**Fig 2.3B**).

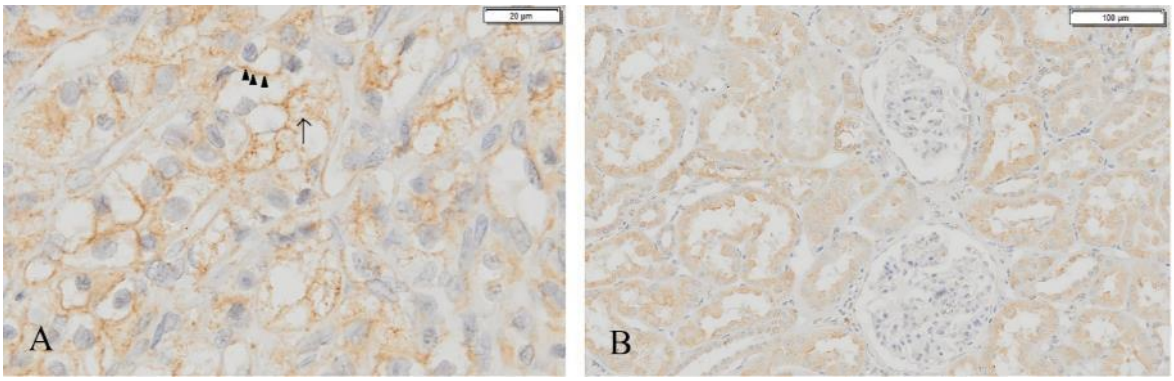

Fig 2.3 Staining patterns of GRP78 in ccRCC tumour tissue and non-neoplastic renal tissue

(A) Image was captured at x40 under 100 % view for clear cell renal cell carcinoma tumour tissue. Scale bars=20 µm. Arrow: staining on the cytoplasm; arrow heads: staining close to the cell membrane; (B) Image was captured at x10 under 25 % view for non-neoplastic renal tissue

Table 2.1 Characteristics of the study population with both renal tumour and non-neoplastic renal tissue available for IHC

Variables	Study cohort(n=68)
Age (years), mean (sd)	61 (11)
Age <60 years	32 (47 %)
Female	27 (40 %)
White race[a]	65 (98 %)
Diabetes[a]	13 (19 %)
Hypertension[a]	43 (65 %)
Smoking history[a]	
Former and current	37 (57 %)
Never	28 (43 %)
BMI (kg/m^2)[a], mean (sd)	30 (7)
BMI category[a]	
Underweight (<18.5 kg/m^2)	2 (3 %)
Normal weight (18.5-24.9 kg/m^2)	11 (17 %)
Overweight (25-29.9 kg/m^2)	27 (42 %)
Obese (≥30 kg/m^2)	25 (38 %)
eGFR ($ml/min/1.72m^2$), mean (sd)	77 (18)
CKD stage	
1 (eGFR >90 mL/min/1.73 m^2)	14 (21 %)
2 (eGFR 60-90 mL/min/1.73 m^2)	43 (63 %)
3 (eGFR 30-59.9 mL/min/1.73 m^2)	11 (16 %)
4 or 5 (eGFR <30 mL/min/1.73 m^2)	0
Tumour size (mm), median [IQR]	50 [36, 74]
Tumour size >70 mm	18 (26 %)
Tumour stage[a]	
1	32 (48 %)
2	4 (6 %)
3	29 (43 %)
4	2 (3 %)
Tumour grade	
1	3 (4 %)
2	24 (35 %)
3	29 (43 %)
4	12 (18 %)
Presence of metastasis[a]	9 (13 %)
Proportion of positive pixels in tumour tissues, mean (sd)	0.47 (0.12)
Proportion of positive pixels in normal tubules, mean (sd)	0.44 (0.10)
Staining intensity in tumour tissues, mean (sd)	202.0 (3.6)
Staining intensity in normal tubules, mean (sd)	202.8 (4.0)

[a]Missing data ≤4 %

Abbreviations: BMI, body mass index; CKD, chronic kidney disease; eGFR, estimated glomerular filtration rate; sd, standard deviation

2.5.3 Difference of GRP78 expression in tumour tissue and non-neoplastic renal tissue

Under both quantification methods, the difference in GRP78 expression between tumour and paired non-neoplastic renal tissue was modest (staining intensity method: mean difference = - 0.74, 95 % CI:-1.67 to 0.19, p = 0.12; positive pixel method: mean difference = 0.03, 95 % CI: - 0.003 to 0.06, p = 0.07; **Table 2.2**).

Table 2.2 Difference of GRP78 expression between tumour tissues and adjacent non-neoplastic renal tissues. (n=68)

	Tumour tissues	Adjacent non-neoplastic renal tissues	95 % CI for mean difference	p-value
	mean (sd)	mean (sd)		
Average grey value	202.04 (3.64)	202.78 (3.85)	-1.67 to 0.19	0.12
Proportion of positive pixels	0.47	0.44	-0.003 to 0.06	0.07

There was a statistically insignificant smaller average grey value (interpreted as stronger staining intensity) (mean difference = -0.74) in renal tumour tissues when it was compared with a paired non-neoplastic renal tissues (p = 0.12). There was a higher proportion (mean difference = 0.03) of positive pixels in renal tumour tissues when it was compared with a paired non-neoplastic renal tissues, which did not reach statistical significance (p = 0.07).

2.5.4 Association of GRP78 expression in tumour tissue with ccRCC aggressiveness

Distribution of GRP78 expression in tumour tissue among different categories of the outcome variables is summarised in **Table 2.3**. When adjusting for BMI, hypertension and history of smoking, we did not find any tumour grading categorising potential for either staining intensity measurement (adjusted odds ratio [aOR] = 0.99, 95 % CI: 0.88 to 1.12, AUC = 0.55, **Fig 2.4A**) or proportion of positive pixel measurement (aOR = 0.56, 95 % CI: 0.02 to 17, AUC = 0.50, **Fig 2.4B**). Since high tumour stage was largely ascribed by large tumour size (aOR = 16.6, 95 % CI: 5.3 to 52.0) and presence of metastasis (aOR = 2.5, 95 % CI: 0.36 to 17.5), tumour size and metastasis were set as two separate outcome variables to describe ccRCC aggressiveness. Neither staining intensity (aOR=0.98, 95 % CI: 0.84 to 1.14) nor proportion of positive pixels (aOR = 3.8, 95 % CI: 0.07 to 217.9) was found to have any predictive potential for tumour size with ROC curves showing poor discrimination ability (AUC < 0.54, **Figs 2.4C** and **2.4D**). Similar results were observed for metastasis for both staining intensity (aOR = 1.12, 95 % CI: 0.88 to 1.41**, Fig 2.4E**) and proportion of positive pixels (aOR = 1.39, 95 % CI: 0.00 to 814.4, **Fig 2.4F**).

Table 2.3 Distribution of GRP78 expression in tumour tissue (N=114) among different categories of ccRCC aggressiveness

Aggressiveness categories	N	Staining intensity	95 % CI	Proportion of positive pixels	95 % CI
Tumour grade					
Grade1	13	202.6	[201.2, 204.0]	0.49	[0.42, 0.56]
Grade2	43	202.5	[201.6, 203.3]	0.47	[0.44, 0.51]
Grade3	42	201.8	[200.7, 202.9]	0.49	[0.45, 0.53]
Grade4	16	202.9	[200.7, 205.0]	0.45	[0.39, 0.51]
Tumour stage[a]					
Stage 1	64	202.4	[201.7, 203.1]	0.47	[0.44, 0.50]
Stage 2	7	201.8	[199.7, 203.9]	0.47	[0.40, 0.53]
Stage 3	39	202.6	[201.5, 203.8]	0.48	[0.44, 0.52]
Stage 4	3	196.3	[183.7, 208.8]	0.53	[0.26, 0.84]
Tumour size					
≤70mm	86	202.3	[201.7, 203.0]	0.47	[0.45, 0.50]
>70mm	28	202.2	[200.8, 203.5]	0.49	[0.45, 0.54]
Metastasis[a]					
No metastasis	104	202.22	[201.7, 202.8]	0.48	[0.45, 0.50]
Presence of metastasis	9	203.1	[198.3, 207.8]	0.49	[0.38, 0.59]

[a]Missing data <1 %

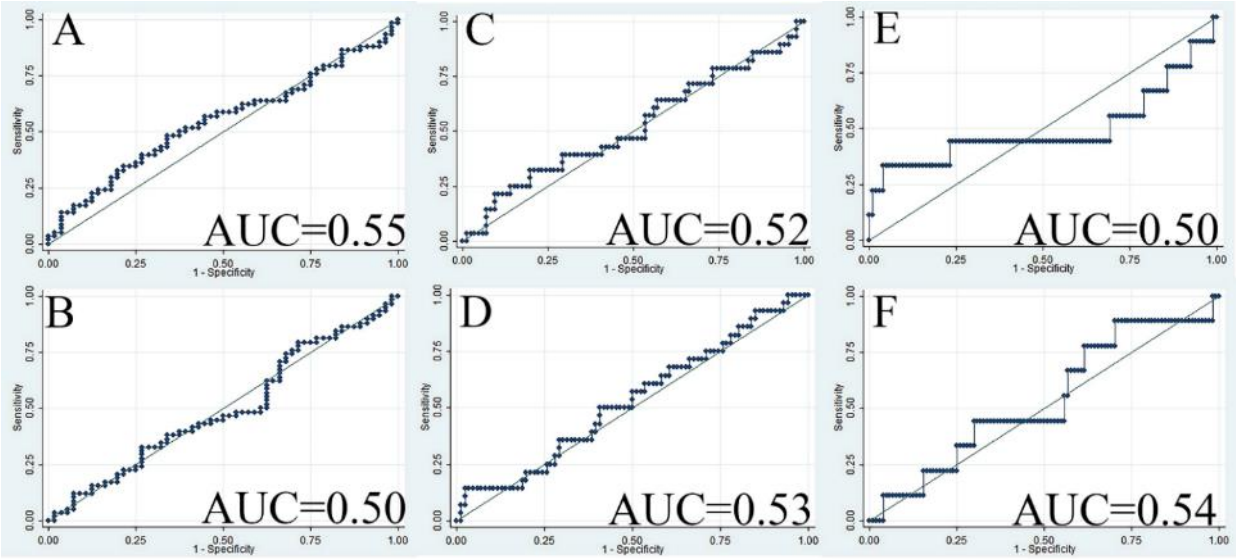

Fig 2.4 ROC curves with GRP78 expression in ccRCC tumour tissue

GRP78 expression in ccRCC tumour tissue was applied to predict ccRCC aggressiveness, using receiver operating characteristic (ROC) curves. (A) ROC curve when staining intensity in tumour tissue was applied to predict tumour grade (OR = 0.96, AUC = 0.55); (B) ROC curve when proportion of positive GRP78 staining in tumour tissue was applied to predict tumour grade (OR = 0.95, AUC = 0.50); (C) ROC curve when staining intensity in tumour tissue was applied to predict tumour size (OR = 0.99, AUC = 0.52); (D) ROC curve when proportion of positive GRP78 staining in tumour tissue was applied to predict tumour size (OR = 4.26, AUC = 0.53); (E) ROC curve when staining intensity in tumour tissue was applied to predict whether there is a presence of metastasis (OR = 1.08, AUC = 0.50); (F) ROC curve when proportion of positive GRP78 staining in tumour tissue was applied to predict whether there is a presence of metastasis (OR = 1.93, AUC = 0.54). Abbreviations: AUC, area under the curve; ccRCC, clear cell renal cell carcinoma; OR, odds ratio; ROC, receiver operating characteristics.

2.5.5 Association of GRP78 expression in adipose tissue with ccRCC aggressiveness

Distribution of GRP78 expression in perinephric adipose tissue among different categories of the outcome variables is summarised in **Table 2.4**. Similar to the results in the tumour tissue, neither staining intensity measurement (aOR = 1.00, 95 % CI: 0.91 to 1.11, AUC = 0.57, **Fig 2.5A**) nor proportion of positive pixel measurement (aOR = 0.95, 95 % CI: 0.84 to 1.08, AUC = 0.52, **Fig 2.5B**) in the perinephric adipose tissue was found to have any tumour grading categorising potential. Similarly, neither staining intensity (aOR = 1.00, 95 % CI: 0.79 to 1.25, AUC = 0.63, **Fig 2.5C**) nor proportion of positive pixels (aOR = 0.95, 95 % CI: 0.84 to 1.07, AUC = 0.49, **Fig 2.5D**) was found to have any predictive potential for tumour size. Regarding the metastatic discrimination potential, for one unit increase in average grey value of GRP78 staining intensity in perinephric adipose tissue, the odds of ccRCC being diagnosed with metastasis increased by 17 % (95 % CI: 0.99 to 1.38,

AUC=0.73, **Fig 2.5E**). However, no metastatic discrimination potential was found for proportion of positive pixels (OR = 1.06, 95 % CI: 0.91 to 1.23, AUC = 0.55, **Fig 2.5F**).

Table 2.4 Distribution of GRP78 expression in paranephric adipose tissue (N=60) among different categories of ccRCC aggressiveness

Aggressiveness categories	N	Staining intensity	95 % CI	Proportion of positive pixels	95 % CI
Tumour grade					
Grade 1	1	190.7	-	0.07	-
Grade 2	25	185.2	[183.4, 187.0]	0.13	[0.10, 0.15]
Grade 3	21	183.8	[180.1, 187.5]	0.13	[0.11, 0.15]
Grade 4	13	189.3	[187.5, 191.1]	0.12	[0.09, 0.14]
Tumour stage					
Stage 1	28	184.2	[181.9, 186.6]	0.13	[0.11, 0.15]
Stage 2	3	187.2	[173.7, 200.7]	0.16	[0.05, 0.27]
Stage 3	27	187.1	[184.6, 189.6]	0.11	[0.10, 0.13]
Stage 4	2	185.1	[164.3, 205.8]	0.14	[-0.09, 0.37]
Tumour size					
≤70 mm	38	184.8	[182.9, 186.7]	0.13	[0.11, 0.14]
>70 mm	22	187.3	[184.4, 190.1]	0.12	[0.11, 0.14]
Metastasis					
No metastasis	52	185.1	[183.4, 186.8]	0.12	[0.11, 0.14]
Presence of metastasis	8	189.3	[186.0, 192.7]	0.14	[0.09, 0.19]

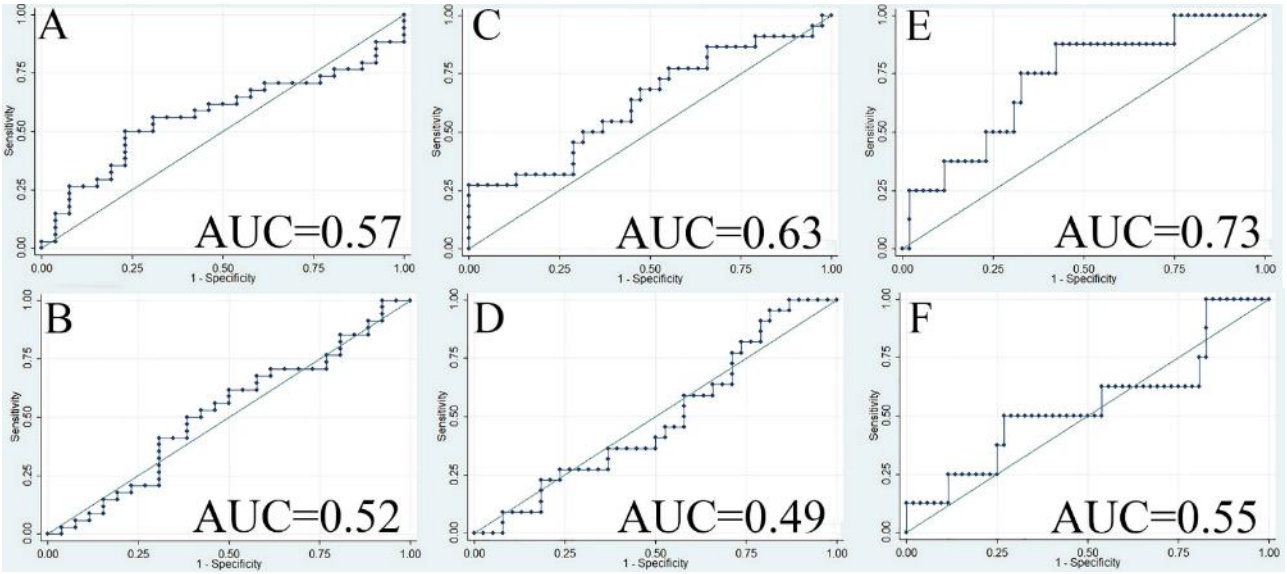

Fig 2.5 ROC curve when GRP78 expression in perinephric adipose tissue was applied to predict the presence of metastasis

GRP78 expression in ccRCC perinephric adipose tissue was applied to predict ccRCC aggressiveness, using ROC curves (A) ROC curve when staining intensity in adipose tissue was applied to predict tumour grade (OR = 1.01, AUC = 0.57); (B) ROC curve when proportion of positive GRP78 staining in adipose tissue was applied to predict tumour grade (OR = 1.00, AUC = 0.52); (C) ROC curve when staining intensity in adipose tissue was applied to predict tumour size (OR = 1.08, AUC = 0.63); (D) ROC curve when proportion of positive GRP78 staining in adipose tissue was applied to predict tumour size (OR = 0.99, AUC = 0.49); (E) ROC curve when staining intensity in adipose tissue was applied to predict whether there is a presence of metastasis (OR = 1.17, AUC = 0.73); (F) ROC curve when proportion of positive GRP78 staining in adipose tissue was applied to predict whether there is a presence of metastasis (OR = 1.06, AUC = 0.55). Abbreviations: AUC, area under the curve; ccRCC, clear cell renal cell carcinoma; OR, odds ratio; ROC, receiver operating characteristics.

2.5.6 Difference of GRP78 staining intensity in ccRCC associated adipose tissues and benign tumour associated adipose tissues

The GRP78 staining intensity between ccRCC and benign tumour associated adipose tissues were compared to examine the risk stratifying potential of GRP78 expression in fat tissue (**Fig 2.6**). There was no statistically significant difference in expression of GRP78 between ccRCC-associated (N=60) and benign tumour-associated adipose tissue (N = 7) (mean difference of average grey value = -3.26, p = 0.17). The distribution of GRP78 staining intensities in tumour-associated adipose tissues among benign tumours and different grades of ccRCC were further explored (**Table 2.5**). The box plot (**Fig 2.7**) demonstrated that, compared with grade 2 and grade 3 ccRCC, grade4 ccRCC and benign tumours exhibited a lower expression of GRP78 with higher every grey values.

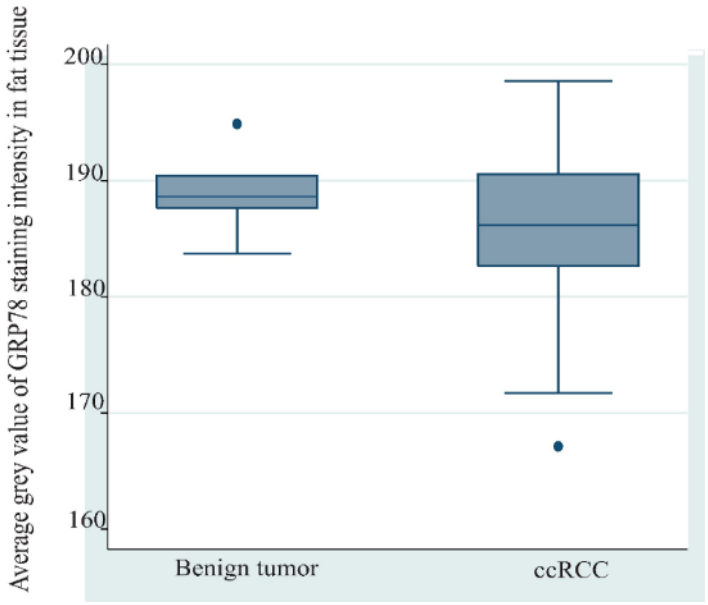

Fig 2.6 Difference of GRP78 staining intensity between benign tumour associated adipose tissue and ccRCC associated adipose tissue

There was a higher expression of GRP78 in ccRCC-associated adipose tissue (N = 60) compared with that in benign tumour-associated adipose tissue (N = 7), as indicated by a lower average grey value in ccRCC tumour associated adipose tissue than benign tumour-associated adipose tissue (mean difference of average grey value = -3.26, P = 0.17). Abbreviation: ccRCC, clear cell renal cell carcinoma

Table 2.5 Distribution of GRP78 staining intensity in benign tumour-associated adipose tissue and ccRCC associated paranephric adipose tissue

	N	Staining intensity	95 % CI
ccRCC tumour grade			
Grade 1	1	190.7	-
Grade 2	25	185.2	[183.4, 187.0]
Grade 3	21	183.8	[180.1, 187.5]
Grade 4	13	189.3	[187.5, 191.1]
Benign tumour[a]	7	188.9	[185.8, 192.0]

[a] Five oncocytoma and two non-neoplastic cystic benign tumours were combined into “benign tumour”.

Abbreviation: ccRCC, clear cell renal cell carcinoma

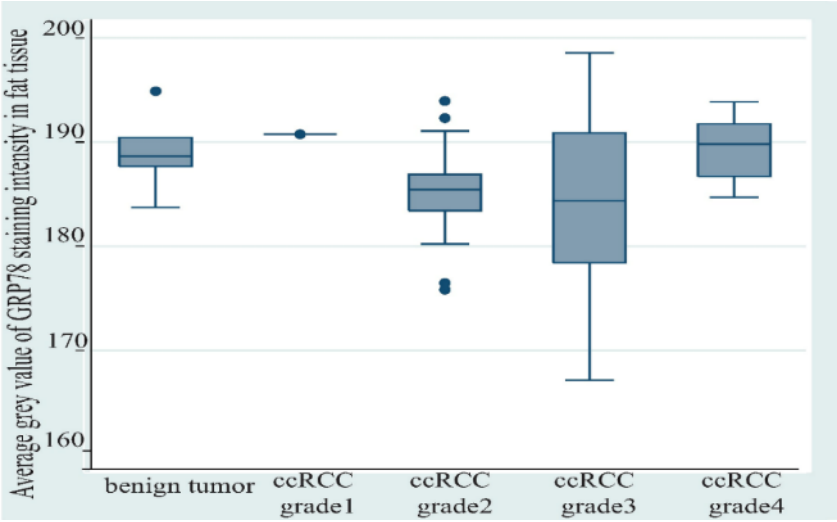

Fig 2.7 Distribution of GRP78 staining intensity in tumour associated adipose tissue among benign tumour and different ccRCC grades

Compared with grade 2 (N = 25) and grade 3 (N = 21) ccRCC, grade 4 ccRCC (N = 13) and benign tumour (N = 7) exhibited a lower expression of GRP78, as indicated by greater average grey values. Abbreviation: ccRCC, clear cell renal cell carcinoma.

2.6 Discussion

In this study, the GRP78 expression was not upregulated in ccRCC tumour tissue compared with paired non-neoplastic renal tissue. Moreover, GRP78 expression levels in both renal tumour tissue and tumour-associated perinephric adipose tissue were not associated with grade or size of ccRCC tumours, except for a weak metastatic predictive potential that was found for GRP78 staining intensity in ccRCC tumour-associated perinephric adipose tissue. However, due to the number (N = 8) in the least frequent outcome variable (presence with metastasis) being less than 10, no covariate was introduced in the model to adjust bias. Moreover, this finding was not supported when proportion of positive pixels was applied to measure GRP78 expression. Although descriptive analysis found benign tumour-associated perinephric adipose tissue exhibited higher average grey value of GRP78 staining intensity than ccRCC-associated perinephric adipose tissue, it is not reasonable to deduce weak GRP78 staining intensity (as demonstrated by higher average grey value) is related to a better prognosis, due to an even weaker GRP78 staining intensity that was found in grade 4 ccRCC tumour-associated perinephric adipose tissue.

Contrary to the findings by Fu *et al*. [37], upregulation of GRP78 expression was not found in renal tumour tissue. This apparent disparity may be explained by methodologic differences in the approach to accounting for tissue heterogeneity. Compared with ccRCC tumour tissue, the normal nephron has much greater tissue heterogeneity, being composed of glomeruli and tubules with lumens of various size [243]. Obviously, the tubular lumen will remain unstained in IHC. Theoretically, glomeruli, the major components of which are capillary bundles, will be more weakly stained by GRP78 than the rest of the nephron structure, because the ER does not exist in erythrocytes [244]. Hence, failure to appropriately account for tissue heterogeneity may introduce bias when comparing the proportion of positively stained areas between renal tumour tissue and paired normal renal tissue. However, the previous publication did not use a method that mitigated the risk of the bias of tissue heterogeneity. On the other hand, in the present study, tubular lumens and glomeruli were manually eliminated prior to comparing the proportions of GRP78 positively stained areas between tumour and adjacent non-neoplastic renal tissue. Similarly, the conflicting results between staining intensity and proportion of positive pixels may be partially explained by adipose tissue heterogeneity as a result of variation in size of adipocytes. For example, larger adipocytes for participants with higher BMI may leave the cellular stainable area smaller (lipid being washed from cells during processing) (**Figs 2.8A** and **2.8B**), which was consistent with the statistically significant inverse association observed between BMI and proportion of positive pixels (correlation coefficient = - 0.20, p = 0.02) (**Fig 2.8C**). However, we did not find any significant association between BMI and staining intensity (correlation coefficient = - 0.16, p = 0.15) (**Fig 2.8D**).

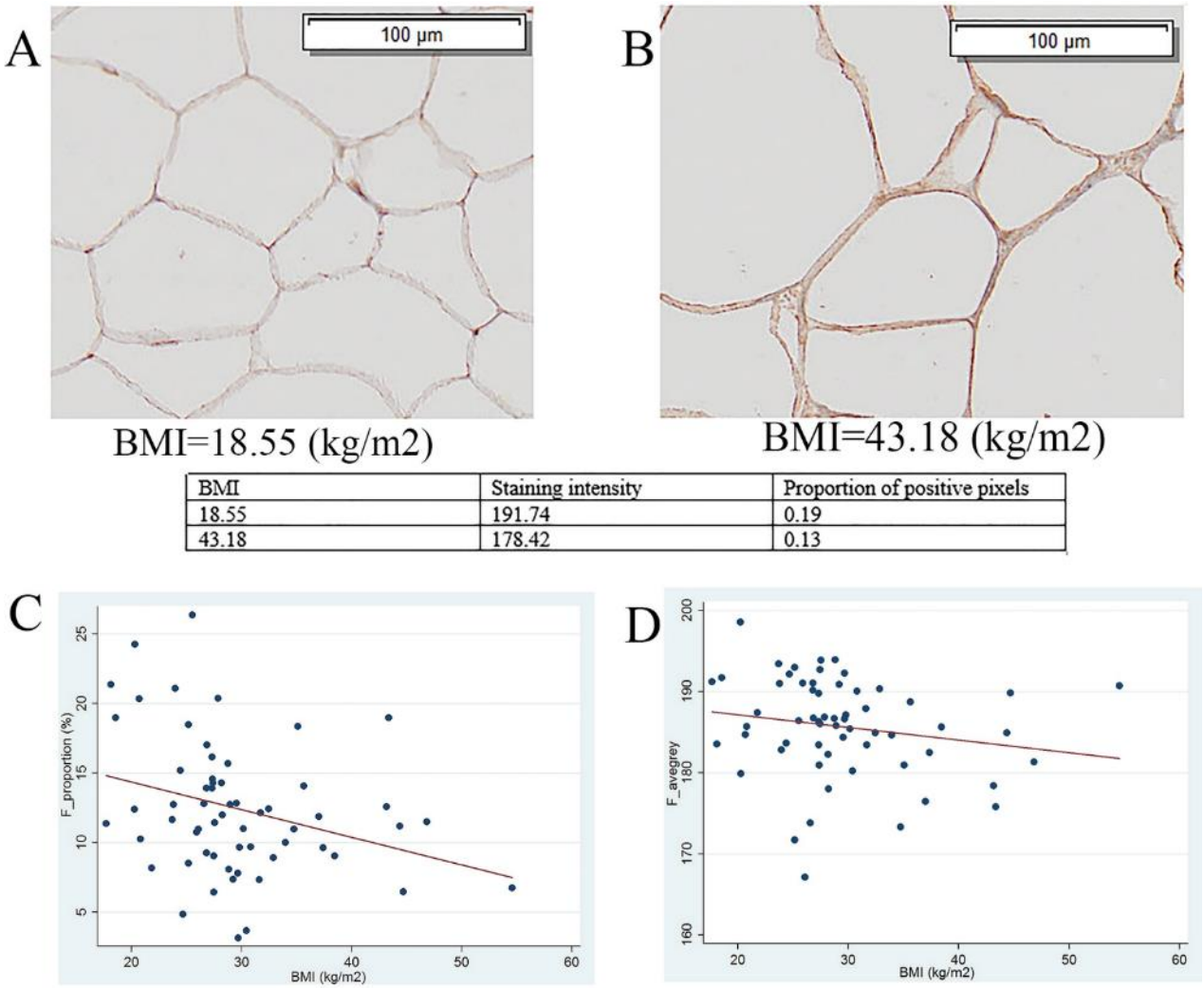

BMI	Staining intensity	Proportion of positive pixels
18.55	191.74	0.19
43.18	178.42	0.13

Fig 2.8 The impact of adipose tissue heterogeneity on proportion of positive pixels

(A) Images were captured at ×10 under 50 % view. Scale bar = 100 μm. BMI = 18.55; Average grey value = 191.74; Proportion of positive pixels = 0.19; (B) Images were captured at ×10 under 50 % view. Scale bar = 100 μm. BMI = 43.18; Average grey value = 178.42; Proportion of positive pixels = 0.13; (C) Scatter plot of BMI versus proportion of positive GRP78 stained pixels in adipose tissue. Coefficient = - 0.20, p = 0.02; (D) Scatter plot of BMI versus average grey value of GRP78 staining in adipose tissue. Coefficient = - 0.16, p = 0.15.

Abbreviation: BMI, body mass index; F_avegrey, average grey value of GRP78 staining in adipose tissue; F_proportion, proportion of positive GRP78 stained pixels in adipose tissue.

The hypoxic cancer microenvironment suppresses the differentiation of tumour cells. Likewise, undifferentiated tumour cells tend to grow faster, exacerbating hypoxia within the cancer microenvironent [245]. The activation of ER stress is an adaptive behavior in response to such a suboptimal microenvironment [246]. The observed adipose tissue GRP78 staining intensity generally met with this supposition, showing a gradually increasing staining intensity from grade 0 to grade 3. Opposite to an expected over expression of GRP78, the GRP78 staining intensity was the lowest in grade 4 ccRCC. It is difficult to interpret the result further, due to small sample size and the lack of examination of the whole ER stress signaling network.

This study has the largest sample size to date and was based on the investigation of a different race population compared with the previously published study by Fu *et al*.. Other strengths of this study include use of appropriate statistical tests and software-assisted DAB chromogen quantification of both proportion of positive pixels and average grey value of GRP78 staining intensity. On the other hand, the findings in this study are subjected to two major limitations. Firstly, this study only examined the expression of one ER stress marker, GRP78. Although the activation of GRP78 is considered as an initial sign of ER stress, the one time-point assessment of GRP78 expression cannot reflect the full-course status of ER stress [247], because ER stress involves mutiple downstream signaling pathways that are mediated by different signaling proteins [248]. Secondly, quantifying DAB chromogen intensity in IHC has long been a controversial issue, because the brightness of a DAB-stained region is not directly proportional to the concentration of localized antigen [247]. However, this is an inherent limitation of the IHC stainining. In the process of image analysis, it was found that the result of average grey value fit with the intuitive impression of the staining intensity.

Collectively, the findings failed to demonstrate any utility of GRP78 as a risk stratifying marker for ccRCC. This does not necessarily refute a role for activated ER stress as a potential therapeutic target for kidney cancer, because the peak expression of different ER stress markers may vary with different stages in cancer development [249]. Further studies in this area are warranted.

2.7 Conclusion

GRP78 is not upregulated in renal tumour tissue compared with paired normal renal tissue. Thus, for the purpose of risk stratification of ccRCC, GRP78 would not appear to be a useful marker. Since the predictive value of GRP78 expression in adipose tissue is uncertain due to the presence of conflicting findings according to methodologic approach, it is important to eastablish an adipose tissue microenvironment *in vitro* to study the role of ER stress activated obese microenvironment in kidney cancer.

Chapter 3

Generation of a 3D culture platform to mimic the functional adipose tissue microenvironment

3.1 Included publications

This chapter included contents from an original research article published in the journal of *Biochemical and Biophysical Research Communications*.

Shen K, Vesey DA, Hasnain SZ, Zhao KN, Wang H, Saunders N, Burgess M, Johnson DW, Gobe GC. A cost-effective three-dimensional culture platform functionally mimics the adipose tissue microenvironment surrounding the kidney. BBRC. 2020; 522 (3):736-742. https://doi.org/10.1016/j.bbrc.2019.11.119

The candidate was the lead author of this original research article. She contributed significantly to the conception and design of this study (80 %) and analysis and interpretation of the literature (70 %), and drafted the majority of the manuscript (90 %).

3.2 Overview

Obesity is an established risk factor for developing RCC. However, recent findings suggest that obese patients with RCC may have better prognosis. This obesity paradox highlights the uncertain roles played by adipose tissue in RCC progression. Activation of ER stress has been observed in human disease associated with obesity and multiple animal models. Using IHC and a patient cohort, **Chapter 2** of this thesis describes how GRP78, an ER stress marker, was upregulated in the perinephric adipose tissue of RCC patients who had higher BMI (Spearman correlation coefficient= - 0.16, $p = 0.15$). The upregulation of GRP78 was related to a lower metastatic rate (95 % CI of OR: 0.72 to 1.01, $p = 0.07$), which is in agreement with obese RCC patients having better prognosis, within the obesity paradox. However, evidence from this one-point IHC study is insufficient to deduce that activated ER stress in the obese perinephric microenvironment modulates RCC progression. Hence, a cell culture-based study to mimic the ER stress-activated obese microenvironment of adipose tissue was initiated. The adipogenic differentiation of the primary stromal vascular fraction isolated from human perinephric adipose tissue was induced in a scaffold-free 3D culture environment simply by coating 96-well plates with 1 % agarose. As evidenced by accumulation of adiponectin in the culture medium and enhancement of Nile red fluorescence staining over the time of adipogenic differentiation, this method can be used to produce reproducible and functional adipocyte spheroids. A co-culture platform including the adipocyte spheroids will be applied to study the macrophage behaviour in the kidney cancer-associated adipose tissue microenvironment in the succeeding chapter.

3.3 Introduction

The increased economic burden from obesity-associated comorbidities, such as cancer, has boosted the research interest in the adipose tissue microenvironment [162]. Since adipose tissue is universally distributed across the human body, many solid tumours grow closely to the adipose tissue or directly in the adipose tissue stroma, such as breast cancer. The role of the interaction between adipose tissue and cancer cells in the tumour development is complicated. Adipose tissue is an active endocrine organ, secreting many adipokines and cytokines, such as leptin, adiponectin, monocyte chemoattractant protein-1 (MCP-1, also known as CCL2), IL-6, IL-8, IL-10 and TNF α, exerting either pro-tumourigenic or anti-tumourigenic functions [118]. Additionally, the lipid metabolism and morphology of adipose tissue are altered to adapt to the cancer development, promoting tumour growth and causing cachexia [250]. However, the prognostic role of obesity in predicting mortality of cancer remains uncertain. On one hand, increased BMI is a known risk factor for developing cancers. On the other hand, increased adiposity after cancer diagnosis is a favourable prognostic factor for many cancers, including RCC [251].

The structure and function of adipose tissue vary with distribution. More sensitive to insulin, subcutaneous adipose tissue with smaller adipocytes is better at buffering the lipid flux in circulation [252]. Rich in vasculature, immune cell infiltration and large adipocytes, visceral adipose tissue is more active in lipolysis but more susceptible to insulin resistance [251]. Additionally, the pattern of adipose tissue distribution in the human body carries prognostic information for cancers. For example, a high visceral fat index was reported to be associated with shorter OS for metastatic colorectal cancer after bevacizumab treatment [253]. However, subcutaneous adiposity was a favourable prognostic factor for OS in renal, pancreatic, oesophageal, stomach and respiratory cancers [135]. To determine whether, or not, adipocyte-cancer cell interactions mediate cancer progression, it is crucial to establish an *in vitro* model which reproduces the microenvironment and crosstalk between adipose tissue and cancer cells.

Mainly obtained from the procedure of liposuction, subcutaneous adipose tissue has been widely used to isolate primary adipocytes in preclinical research [254] Since the role of the adipose tissue microenvironment in cancer development and progression has gained common recognition, adipocytes directly isolated from the tumour microenvironment are needed to investigate their interactions with cancer cells. For example, breast cancer-related research has extensively applied adipocytes isolated from the adipose stroma of breast cancer [135]. As a clinical waste of radical nephrectomy surgery, perinephric adipose tissue (adipose tissue between renal capsule and Gerota's Fascia) is an easily obtained visceral adipose tissue, which exerts little ethical concern when applied in preclinical research [255]. Separated from the paranephric fat by the Gerota's Fascia, perinephric

fat has direct anatomical interaction with the kidney. Sharing common lymphatic vessels with the kidney, the host or infiltrating cells or cytokines secreted in the perinephric adipose tissue may affect tumour metastasis [256, 257]. Hence, the value of adipocytes isolated from perinephric adipose tissue should be noted, though publications about relevant applications are limited in the field of the kidney cancer-associated microenvironment.

Using 3D culture to reproduce the tumour microenvironment is a trend in cancer research. 3D culture of adipocytes has shown advantages over traditional two-dimensional cell culture in a recent publication [258]. First, adipocytes grown under a 3D culture environment develop large unilocular lipid droplets in the cytoplasm. The lipid droplets have a similar morphology to those found in mature adipocytes under physiological conditions. Second, adipocyte spheroids were more sensitive to the stimulation of uremic toxins, as evidenced by a significant downregulation of adiponectin and upregulation of IL-8 observed in adipocyte spheroids after exposure to indoxyl sulphate, than in general adipocytes. Third, the 3D cell aggregates are flexible to manipulate in constructing the co-culture system by changing the density or location of the spheroids according to the requirement of experiments [258].

It has been reported that human ASC could form 3D cell aggregates using the hanging drop technique [259] or special culture dishes with an ultra-low attachment surface [260]. However, these methods depend on a difficult handing technique and/or expensive laboratory consumables. The liquid overlay technique, simply using a thin coating of agarose, has successfully generated more homogeneous and reproducible cancer cell aggregates compared with the hanging drop technique [261]. However, its application in generating human adipocyte spheroids has not been reported. The culture dish produced for adherent cell culture is normally gas-plasma treated, the surface of which is more hydrophilic and negatively charged than untreated polystyrene material [262]. Agarose is a neutrally charged hydrophilic material, which cannot bind to cell attachment proteins present in the culture medium. Lacking any embedded or bond fibrous proteins, such as collagen, the agarose coated surface cannot form cell-matrix junctions, forcing cells into a suspended status, enabling 3D spheroid formation through cell-cell interactions [263].

The core idea of the present chapter is to build a 3D culture platform using the liquid overlay technique to culture the adipocytes derived from human perinephric adipose tissue. The hypotheses include: 1) the technique can reproducibly produce functional adipocyte spheroids which are responsive to ER stress; 2) increasing seeding density of adipocyte spheroids can make a pro-inflammatory adipose tissue microenvironment; and 3) increasing seeding density of adipocyte spheroids can mimic an ER stress-activated adipose tissue microenvironment in kidney cancer.

3.4 Methods

3.4.1 Isolation and culture of human perinephric stromal vascular fraction

This study received ethics approval from the Metro South Human Research Ethics Committee (HREC/16/QPAH/353). Perinephric adipose tissue was obtained after radical nephrectomy surgery from consented participants diagnosed with renal tumours. Demographic and pathological characteristics of the study participants are described in **Table 3.1**. The excised perinephric adipose tissue was submerged in ice-cold Hank's Balanced Salt Solution (HBBS) (ThermoFisher 14025076) containing 400 U/mL of penicillin and 400 µg/mL streptomycin (4 % P/S) (Gibco 15070063) immediately after nephrectomy. SVF was isolated according to the methods described by Naderi *et al.* [264] and Lee *et al.* [265].

Collagenase type I (Gibco 15070063) solution (2 mg/mL) was prepared by dissolving the collagenase in fetal bovine serum (FBS)-free HBBS and filtering the solution through a strainer (pore size 0.2 µm). The adipose tissue was minced in a sterilised petri dish which was placed on ice and then was transferred to the collagenase type I solution at a ratio of 3 g of tissue per 10 mL of the solution. After gentle shaking (150 RPM) for 1.5 h at 37 ˚C, the "fat cake" in the top layer was removed and the aqueous phase was filtered through a cell strainer (pore size 100 µm) and centrifuged at 500 g for 5 min. Erythrocytes were removed by adding a red blood cell (RBC) lysis buffer with gentle shaking for 10 min at room temperature (Roche 11814389001). Cell pellets were then suspended in MSC culture medium (ScienCell 7501) at a density of 4×10^4/mL and grown in 75 cm^2 flasks which had been coated with 15 µg/mL of L-lysine (ScienCell 0403). When reaching 70-80 % confluence, cells were sub-cultured with a 1-4 split using accutase (Gibco A1110501) **(Fig 3.1**). Images showing the morphology of SVF prior to adipogenic differentiation are displayed in **Fig 3.2**.

3.4.2 Culture of 3T3-L1 cell line

The 3T3-L1 cell line was a kind gift from Dr Sumaira Hasnain (Mater Research Institute-The University of Queensland). Dulbecco's Modified Eagle Medium/Nutrient Mixture F-12 (DMEM-F12) (Gibco 11320033) containing 10 % FBS and 1 % P/S (Gibco 15070063) was applied as the growth medium for the 3T3-L1 cells and the base medium for adipogenic differentiation medium. The adipogenic differentiation medium was prepared freshly and contained 0.5 mM of 3-isobutyl-1-methylxanthine (IBMX) (Sigma I5879), 1 µM of dexamethasone (Sigma D4902) and 10 µg/mL of human recombinant insulin (Sigma 91077c). The recipe was adapted from the article published by Lane *et al.* [266]. Images showing the morphology of 3T3-L1 cells prior to adipogenic differentiation are displayed in **Fig 3.3**.

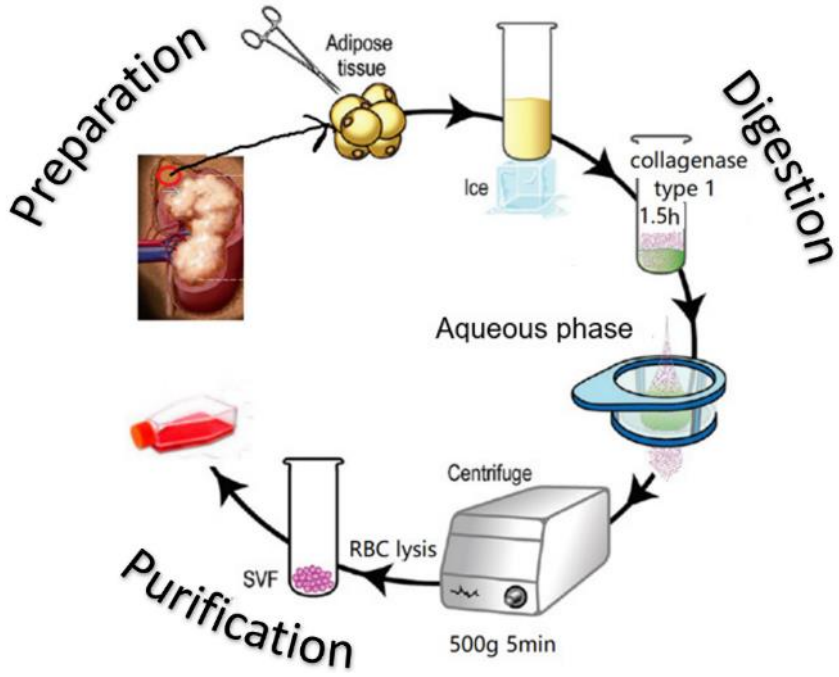

Fig 3.1 Workflow of isolating SVF

Preparation: 1) 10 mL of collagenase type I solution per 3 g of tissue was prepared by dissolving collagenase in HBBS (2 mg/mL) and filtering through a 0.2 µm strainer. 2) The adipose tissue was minced in a petri dish placed on ice. Digestion: 1) After several washes with HBBS, the adipose tissue was transferred into to the collagenase solution and incubated at 37 ˚C for 1.5 h with gentle shaking. 2) The aqueous phase was filtered through a 70 µm cell strainer then flow through was centrifuged at 500×G for 5min. Purification: 1) The RBC lysis buffer was warmed to room temperature, then the cell pellets were incubated for 10 min with 2 mL of the RBC lysis buffer with gentle shaking. 2) After centrifuging at 500×G for 5 min and removing the supernatant, the purified cell pellets were suspended in growth medium.

Abbreviations: HBBS, Hank's Balanced Salt Solution; RBC, red blood cell; SVF, stroma vascular fraction

3.4.3 Flow cytometry analysis

Flow cytometry analysis was performed to identify MSC. Cells were harvested with human Fc block solution (BD 564220) to block non-specific Fc receptor binding and were incubated with specific antibody for 30 min on ice. Live and dead cell discrimination was performed by adding DAPI before sample analysis. Details on antibodies and live/dead cell dye are summarised in **Appendix 1**. If not specified, 1×10^6 cells were suspended in 100 µL of the staining solution per sample. The samples were analysed using the instrument BD LSR Fortessa X-20. Non-stained cells were used to set the voltage of the instruments. If not specified, non-stained cells were used to gate the positive population. However, a fluorescence minus one (FMO) control was used to gate the positive population for the rare event. Flow cytometry data were analysed using the FlowJo Software.

3.4.4 Adipogenic differentiation of MSC and 3T3-L1 cells using a liquid overlay technique-based 3D culture environment

The inner 60 wells of a 96 well plate were coated with 70 µL of sterilised 1 % agarose and solidified at 37 ˚C for 2 h. Sterilised phosphate-buffered saline (PBS) solution containing 1 % P/S was filled into the outer 36 wells to avoid the edge effect. MSC and 3T3-L1 cells were seeded at a density of 5,000 per well in 100 µL of MSC culture medium and DMEM/F12 growth medium, respectively. 24 h later (day 0), the old medium was replaced with 150 µL of MSC adipogenic differentiation medium (ScienCell 7541) for MSC and the freshly made adipogenic differentiation medium for 3T3-L1 cells. For MSC, the medium was changed on day 6 and day 12. The supernatant was collected on day 0, 6, 12 and 18 to measure the concentration of total adiponectin by enzyme-linked immune-sorbent assay (ELISA) (R&D DY1065). For 3T3-L1 cells, the medium was changed on day 7. The supernatant was collected on day 0, 7 and 14 to measure the concentration of total adiponectin by ELISA (R&D DY1119).

3.4.5 Staining and imaging of adipocyte spheroids

On day 0, 6, 12 and 18 (or on day 0, 7, 14 and 21 for 3T3-L1 cells), harvested spheroids were fixed with 4 % paraformaldehyde (Sigma F8775) for 15 min and were embedded in tissue freezing medium (GeneralData TFM-5). The solidified blocks were sectioned using a Leica CM 1950 cryostat at a thickness of 12 µm at -20˚C. After permeabilisation with 0.1 % Tween 20 for 5 min, the slides were incubated in a Nile red (Sigma 72458) and DAPI (Invitrogen D1306) dual staining solution (1 µg/mL in PBS) for 10 min. Images were photographed with a FV3000 confocal microscope at ×20 magnification using the laser 561 and 405 under the same brightness and background settings. The protocol of oil red O staining was adapted from the method published by Lillie *et al.* [267]. In this method, the slides were rinsed in water and then in 60 % isopropyl alcohol (a few seconds for both washes) before being stained with oil red O solution. The oil red O staining solution was freshly made by diluting 6 mL of the saturated oil red O stock solution (0.5 % in isopropyl alcohol, Sigma O1391) with 4 mL of distilled water. After centrifuging, the clear supernatant was filtered directly onto the section. After differentiation with 60 % isopropyl alcohol (a few seconds) and haematoxylin counter staining, slides were mounted using Kaiser's glycerine-jelly (recipe see **Appendix 2**). The agarose spheroid blocks were prepared for haematoxylin and eosin (H&E) staining using an internal protocol introduced by Dr Justin Large (Histology Core Facility, Translational Research Institute, Brisbane). Briefly, the paraformaldehyde-fixed spheroids were embedded in 2 % agarose at 37 ˚C in a pre-warmed microcentrifuge tube. The solidified block was removed by carefully cutting off the bottom of the tube and then transferred in a cassette filled with foam pads prior to routine histological

processing. Slides with Oil red O and H&E staining were scanned with an Olympus slide scanner VS120 using the ×20 objective.

3.4.6 Quantitative real-time polymerase chain reaction

Three technique replicates were applied in quantitative reverse transcription polymerase chain reaction (q-rtPCR) to measure the mRNA expression. Spheroids were collected in RNAlater (ThermoFisher AM7020). Total RNA was extracted using a TRIzol reagent (Invitrogen 15596026). DNA was eliminated by a DNA removal kit with DNase 1 (Invitrogen AM1906). cDNA was generated using a cDNA reverse transcription kit (Applied Biosystems 4368813). q-rtPCR data were obtained using the instrument LightCycler480, Roche LifeScience with SensiFast SYBR low-Rox mix (Bioline BIO-94005) added to 1 µg of cDNA. Results were normalised to mean expression of the housekeeping gene (18S ribosomal RNA for human and β-actin for mouse) and expressed as a fold change compared to the control group. Initial real-time amplification was examined by electrophoresis to confirm the size of the products, by referring to the Ultra Low Range DNA Ladder (Invitrogen 10597012). SYBR Safe DNA gel stain (Invitrogen S33102) was used to stain the 4 % agarose Tris/Borate/Ethylenediaminetetraacetic acid (TBE) buffer. The voltage was set to be 10 V per cm and the running time was 1 h 15 min. After PCR amplification, a melting curve was generated to check the specificity of the product. Primer sequences are listed in **Appendix 3**. Images of electrophoretic gels demonstrating the specificity of the PCR products are displayed in **Appendix 4**.

3.4.7 Statistical analysis

Comparisons between groups were made using the analysis of variance (ANOVA), paired or unpaired t-test when appropriate. When there was a statistically significant difference in ordinary ANOVA, post hoc testings were performed to determine where the difference occurred between groups. When there was a statistically-significant difference in one-way repeated measures ANOVA, Tukey's multiple comparisons were performed to determine the difference occurring between groups. $p<0.05$ was considered statistically significant. Statistical analysis was performed using GraphPad Prism 7.0.

3.5 Results

3.5.1 Morphologic observation of human perinephric adipose tissue isolated SVF and 3T3-L1 cells prior to adipogenic differentiation

Undifferentiated SVF isolated from the adipose tissue started adhering at 20 h after seeding, exhibiting a polygonal morphology (10-25 μm) (**Fig 3.2a**). Cells elongated over the amplification period, exhibiting heterogeneous morphological patterns, such as spindle, polygon and "string of beads" (**Figs 3.2b** and **3.2c**). It took approximately 6 days for cells to reach 70 % confluence and become homogeneous in shape (80-100 μm in diameter) (**Fig 3.2d**). The morphologic characteristics of 3T3-L1 cell line are displayed in **Fig 3.3**.

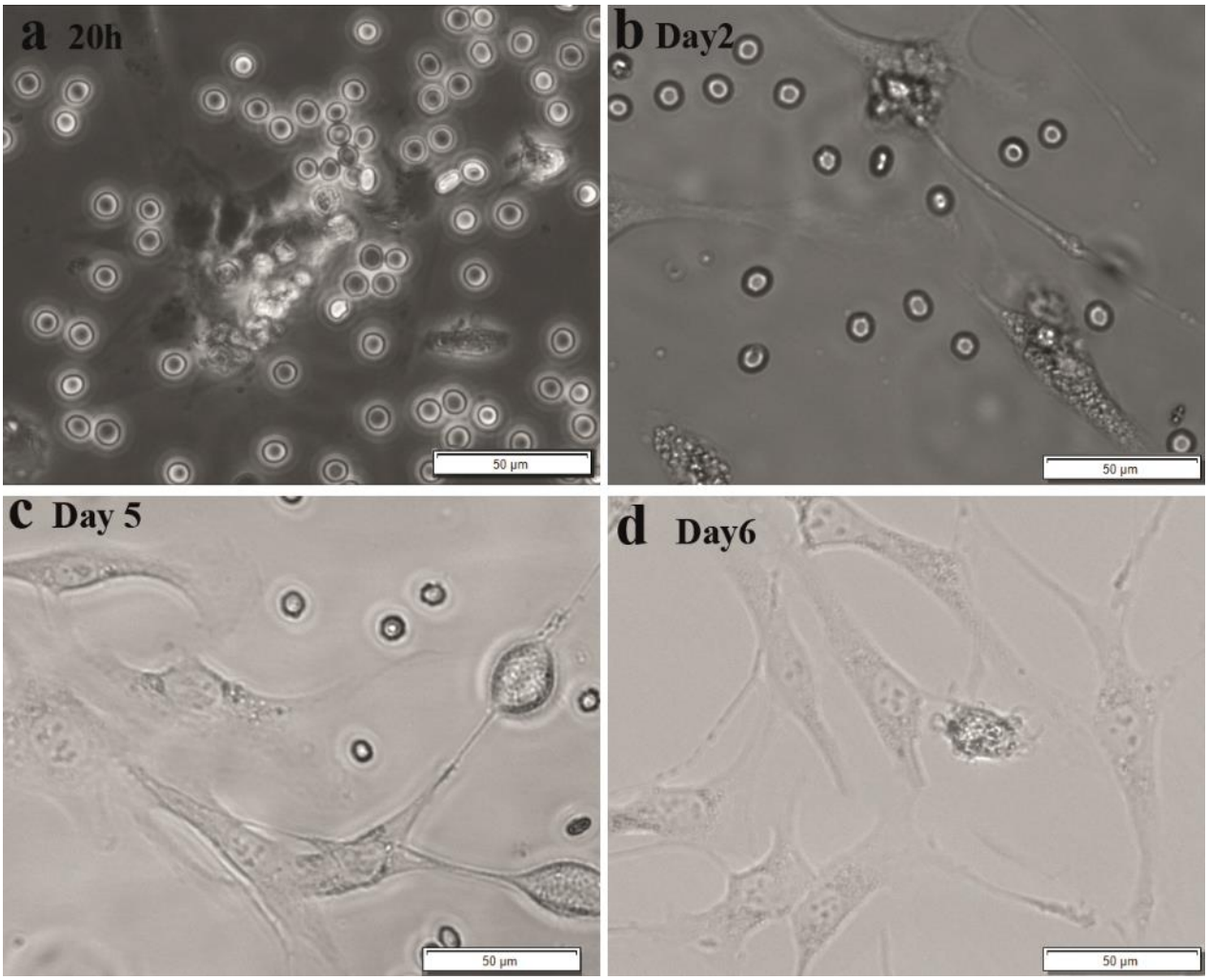

Fig 3.2 Morphologic characteristics of stromal vascular fraction

a Cell attachment started from 20 h after seeding (×40). **b, c** Heterogeneous morphological patterns were observed during the amplification period. **b** was photographed on the day 2 (×40). **c** was photographed on the day 5 (×40). **d** On day 6, cells reached approximately 70 % confluence and were homogeneous in shape (×40). Scale bars = 50 μm.

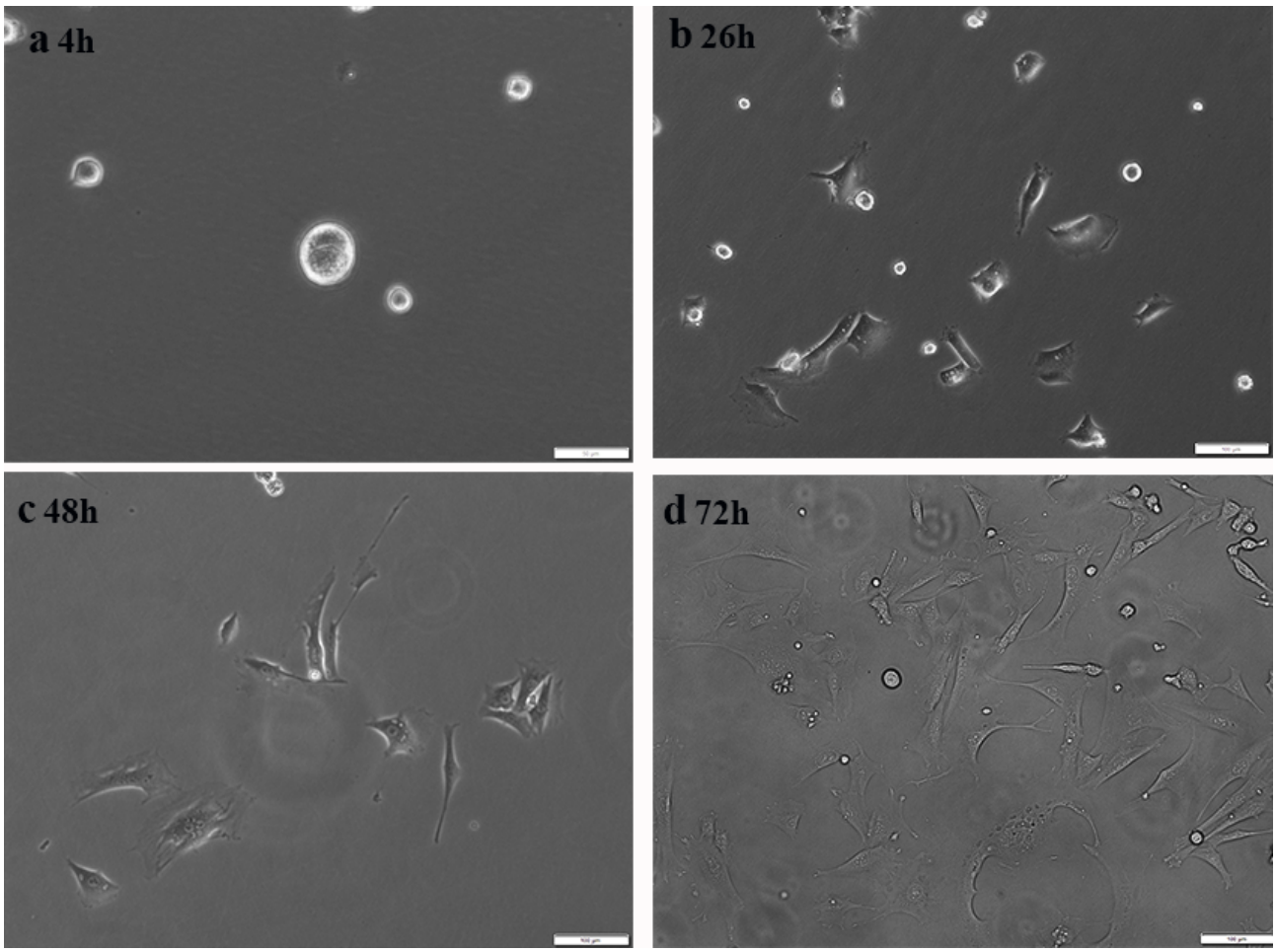

Fig 3.3 Morphologic characteristics of 3T3-L1 cells

Cells were seeded at a density of 10^4/ml. Cells were growing in adherent and exhibited fibroblast-like morphology. It took 72 h for cells to reach approximately 70 % confluent. **a** 4 h, scale bar = 50 μm (×40); **b** 26 h, scale bar = 100 μm (×10); **c** 48 h, scale bar = 100 μm (×10); **d** 72 h, scale bar = 100 μm (×10).

3.5.2 SVF was double positive for CD105 and CD90 but were negative for CD14

CD105 and CD90 are positive markers for mesodermal stem cells. They have been widely tested for MSC identification [268]. Flow cytometry results demonstrated that 93.2 % of SVF was double positive for CD105 and CD90 after the cells had been sub-cultured 3 times (**Fig 3.4c**). For assessing the purity of the stem cells, the cell surface expression of CD14 which is one of the key late differentiation markers of myeloid lineage cells was tested [269].

Flow cytometry results demonstrated that the stem cells were negative for CD14 (**Fig 3.4h**). It has also been reported that adipose tissue is a source of pluripotent stem cells [270]. Hence, the expression of the pluripotency marker, stage-specific embryonic antigen-3 (SSEA-3), was tested. Flow cytometry results demonstrated that 0.96 % of SVF was positive for SSEA-3 (**Fig 3.4f**). FMO control was used to gate the positive population for SSEA-3 (**Fig 3.4e**) and CD14 (**Fig 3.4g**).

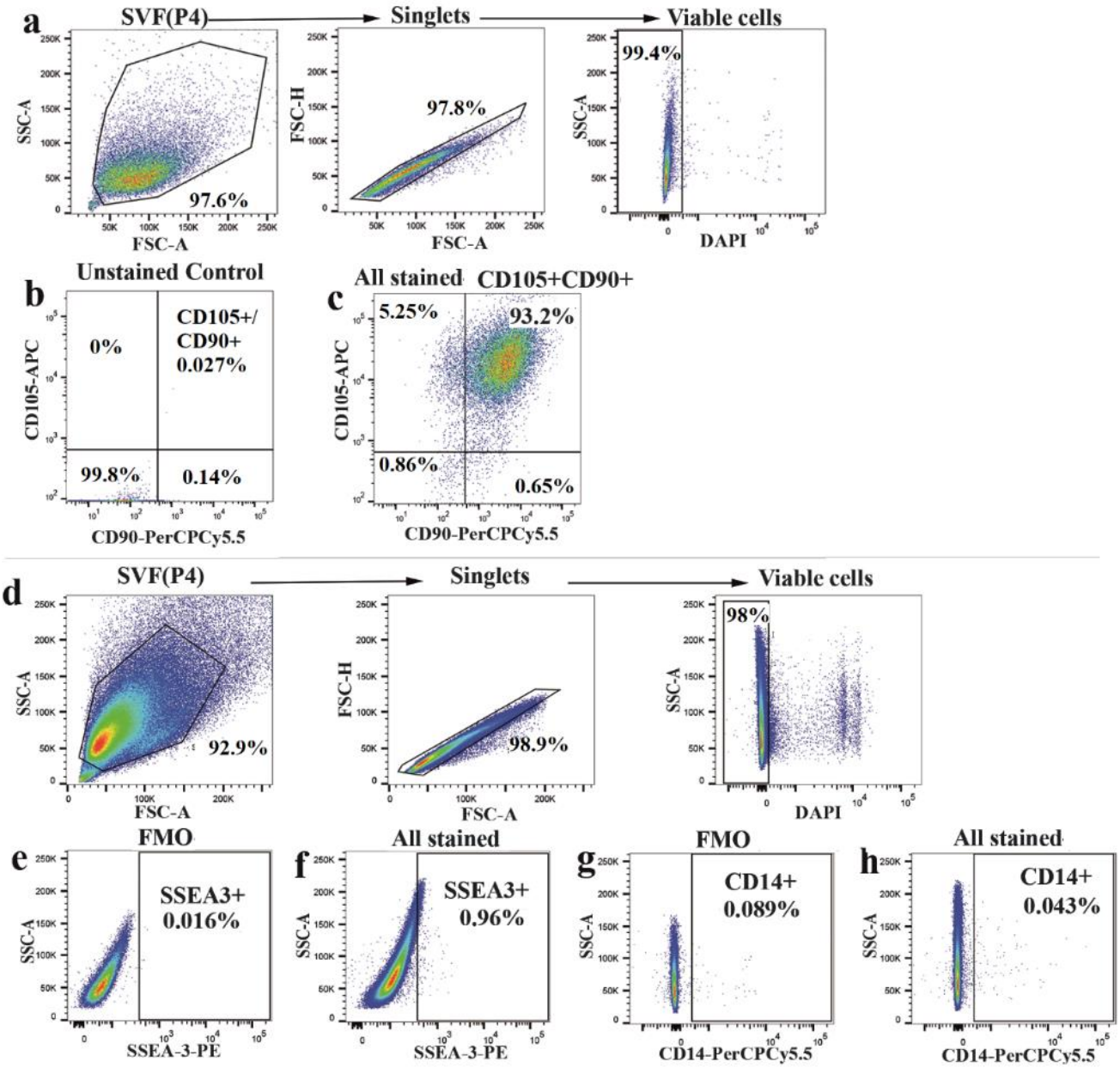

Fig 3.4 SVF was double positive for CD105 and CD90 but were negative for CD14.

a and **d** demonstrate the gating strategy to identify live cells. Demonstrated in **b**, the location of the positive population was gated using the unstained control. **c** demonstrates that 93.2 % of the stromal vascular fraction (SVF) was $CD105^{+}/CD90^{+}$. Demonstrated in **e** and **g**, the location of the positive population was gated using the fluorescence minus one (FMO) control. **f** demonstrates that 0.96 % of the SVF was positive for SSEA-3, and in **h**, the SVF was negative for CD14.

3.5.3 Homogeneous adipocyte spheroids were generated using the liquid overlay technique-based 3D culture.

H&E staining demonstrated that on day 18, large unilocular lipid droplets had formed in the cytoplasm (**Fig 3.5**). Spheroids increased in size with adipogenic differentiation of MSC (**Fig 3.6a**). On day 18, adipocyte spheroids were floating above the medium. Nile red and Oil red O staining revealed that the lipid gradually accumulated in the cytoplasm (**Figs 3.6b and 3.6c**). Consistently, ELISA results showed the concentration of the total adiponectin was gradually increased in the culture medium over adipogenic differentiation when spheroids were plated singly in 96 well plates (**Fig 3.6d**). Consistently, the lipid droplets gradually accumulated, and the total adiponectin was gradually increased with adipogenic differentiation of 3T3-L1 cells (**Fig 3.7**). Adipocyte spheroids were differentiated from MSC isolated from 3 donors (**Table 3.1**).

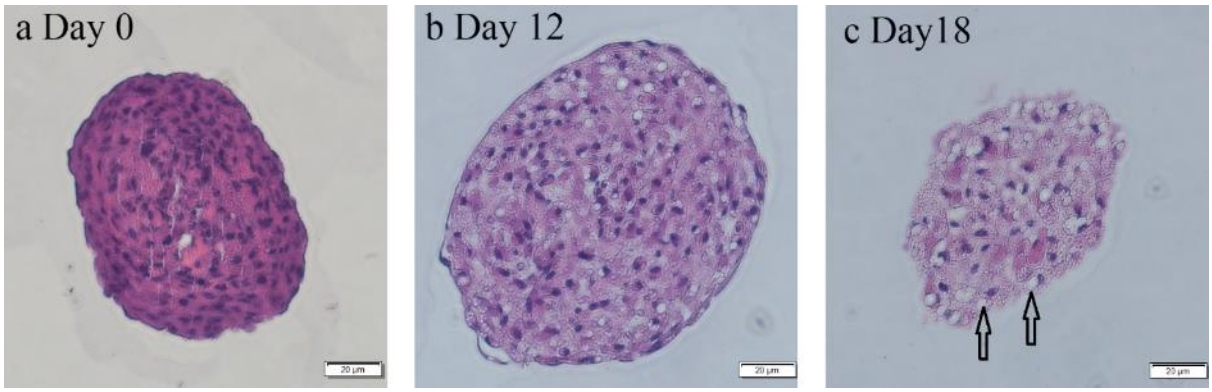

Fig 3.5 H&E staining of MSC-derived adipocyte spheroids

Images were scanned with Olympus slide scanner VS120 using the ×20 objective. Scale bars = 20 μm. **a** Day 0; **b** Day 6; **c** Day 18; Arrows indicate unilocular lipid droplet formed in cytoplasm.

Table 3.1 Characteristics of the study population

De-identified participant number	Date of birth	Sex	BMI (kg/m^2)	Diagnosis	Tumour size	Tumour grade	Tumour stage
Patient 1	29-Jan-1961	Female	30.5	Oncocytoma	80mm	#	#
Patient 2	10-Aug-1967	Male	31.4	ccRCC	120mm	2	3
Patient 3	1-Apr-1963	Female	35	ccRCC	65mm	3	3

Tumours were staged according to the 7th TNM Classification of malignant tumours and graded according to the International Society for Urological Pathology (ISUP) grading system for renal cell carcinoma, which is not applicable for oncocytoma. Abbreviations: BMI, body mass index; ccRCC, clear cell renal cell carcinoma.

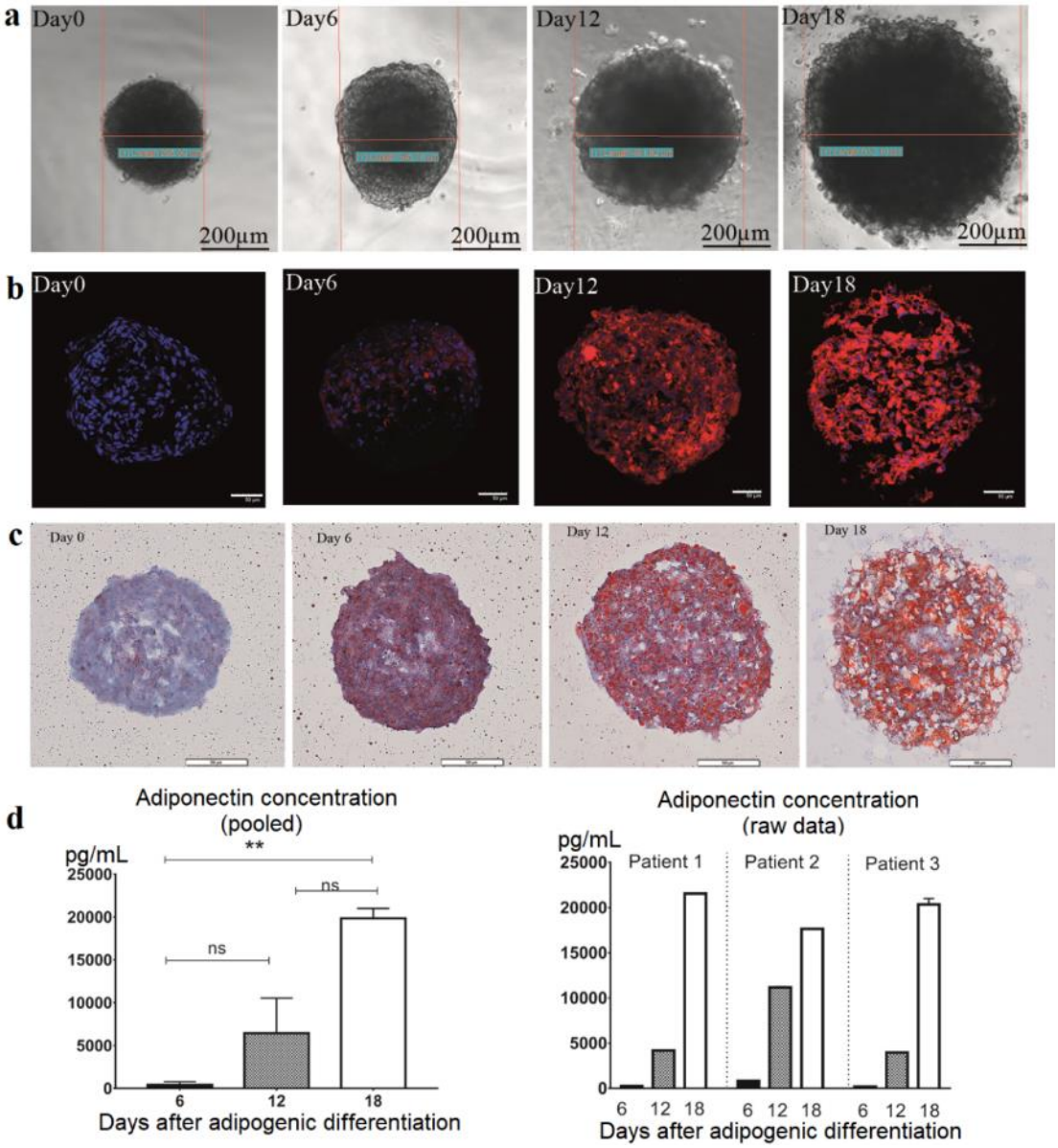

Fig 3.6 Adipogenic differentiation of MSC

a Increase in size of spheroids over 18 days of adipogenic differentiation is demonstrated in the bright field images. **b** Images of Nile red staining (scale bars = 50 µm) photographed with a FV3000 confocal microscope at ×20 magnification using the 561 and 405 nm lasers under the same brightness and background settings demonstrated that the lipid (red fluorescence) increasingly accumulated in the spheroids. **c** The result was confirmed by images of Oil red O staining (scale bars = 100 µm) which were scanned with Olympus slide scanner VS120 using the ×20 objective. **d** Results in ELISA demonstrated an increasing adiponectin concentration in the culture medium with differentiation. Of note, the concentration of adiponectin on day 0 was below the lower limit of assay sensitivity. **$p<0.01$, ns, $p>0.05$, Tukey's multiple comparisons after repeated measures one-way ANOVA, error bars represent estimated standard errors of the mean. Data were pooled from 3 independent experiments using MSC derived from 3 donors (see **Table 3.1**). Error bars in raw data indicate the standard deviation of the technique duplicates in ELISA.

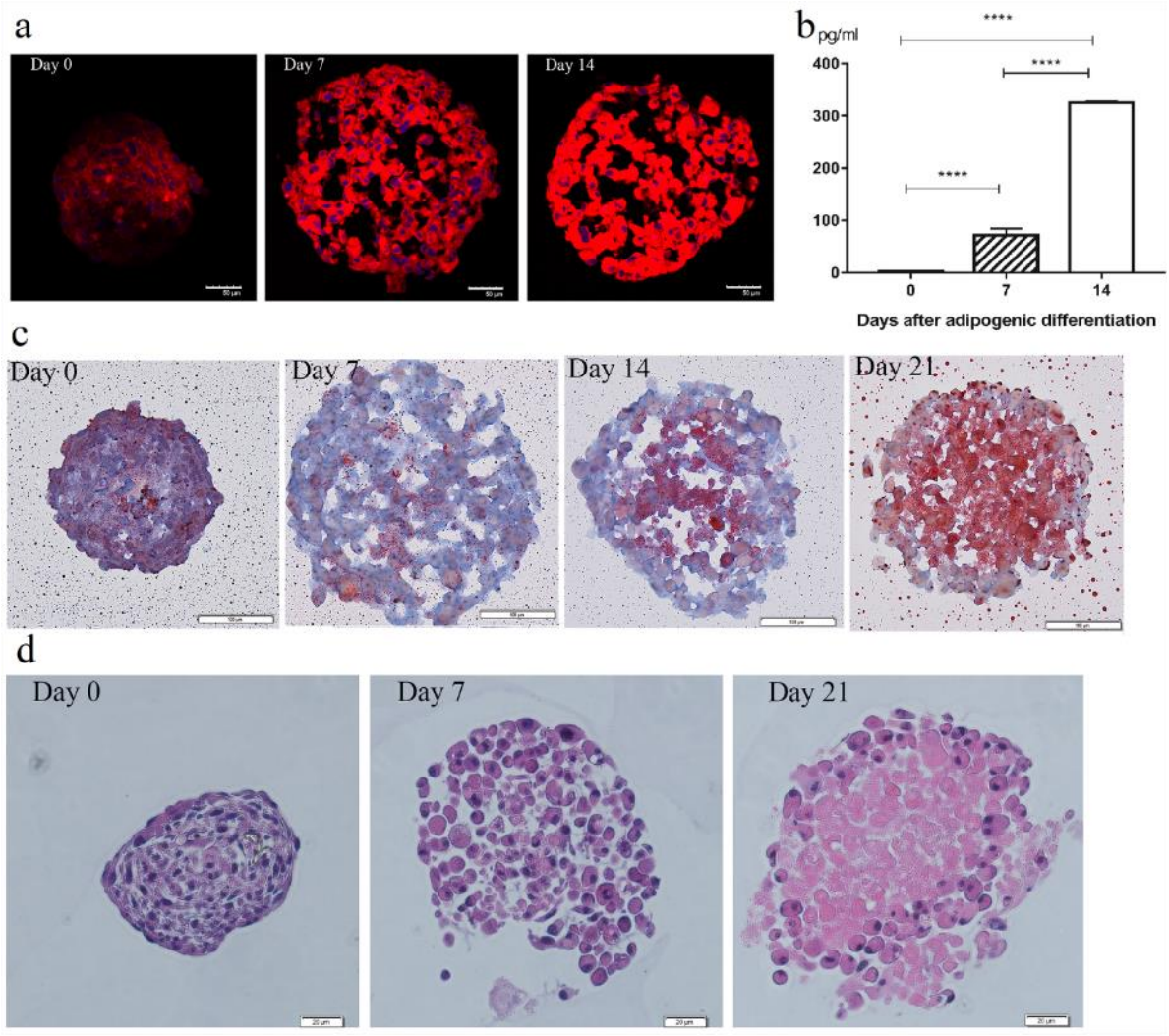

Fig 3.7 Adipogenic differentiation of 3T3-L1 cells

a. Images were photographed with a FV3000 confocal microscope at ×20 magnification using the lasers of 561 and 405 nm under the same brightness and background settings. Scale bars = 50 μm. Nile red staining revealed that the lipid accumulated in the cytoplasm over time. **b**. ELISA results demonstrated the concentration of the total adiponectin was gradually increased in the culture medium with adipogenic differentiation when spheroids were plated singly in 96 well plates. Data were pooled from three independent experiments. ****$p<0.0001$, post hoc testing after one-way ANOVA, error bars indicate standard estimated errors of the mean. **c.** Scale bars = 100 μm. The Oil red O staining confirmed that the lipid gradually accumulated in the cytoplasm. **d**. Scale bars = 20 μm. Examples of H&E staining demonstrated that necrosis may be appeared in the core of the spheroid on Day 21.

3.5.4 ER stress affected adiponectin and MCP-1 secretion in adipocyte spheroids.

Mature adipocyte spheroids were collected and placed in a 24-well plate at a density of 5 spheroids per well at the end of the adipogenic differentiation period (18 days). Spheroids were maintained in the FBS-free medium containing 5 µg/mL of tunicamycin for 24 h. Tunicamycin is a drug which inhibits N-linked glycosylation, thereby blocking protein folding and causing ER stress [271].q-rtPCR results demonstrated that mRNA expression of *GRP78* and spliced X-box binding protein 1 (*sXBP1*, another ER stress protein) was upregulated. In contrast, with the increase in ER stress, the expression of abundant transcript 1 (*APM-1*) and *MCP-1* was downregulated (**Fig 3.8a**). These results were confirmed by ELISA for adiponectin (**Fig 3.8b**) and MCP-1 (**Fig 3.8c**). However, the effect of tunicamycin on mRNA expression and cytokine secretion of IL-8 was uncertain, due to insignificant changes being observed after the treatment (**Figs 3.8a** and **3.8d**). Consistently, 3T3-L1-derived adipocyte spheroids were responsive to ER stress as demonstrated by an upregulation of mRNA expression of *GRP78* and *sXBP1* after exposure to tunicamycin (**Fig 3.9a**). ER stress also affected adiponectin secretion by adipocyte spheroids derived from 3T3-L1 cells (**Fig 3.9b**).

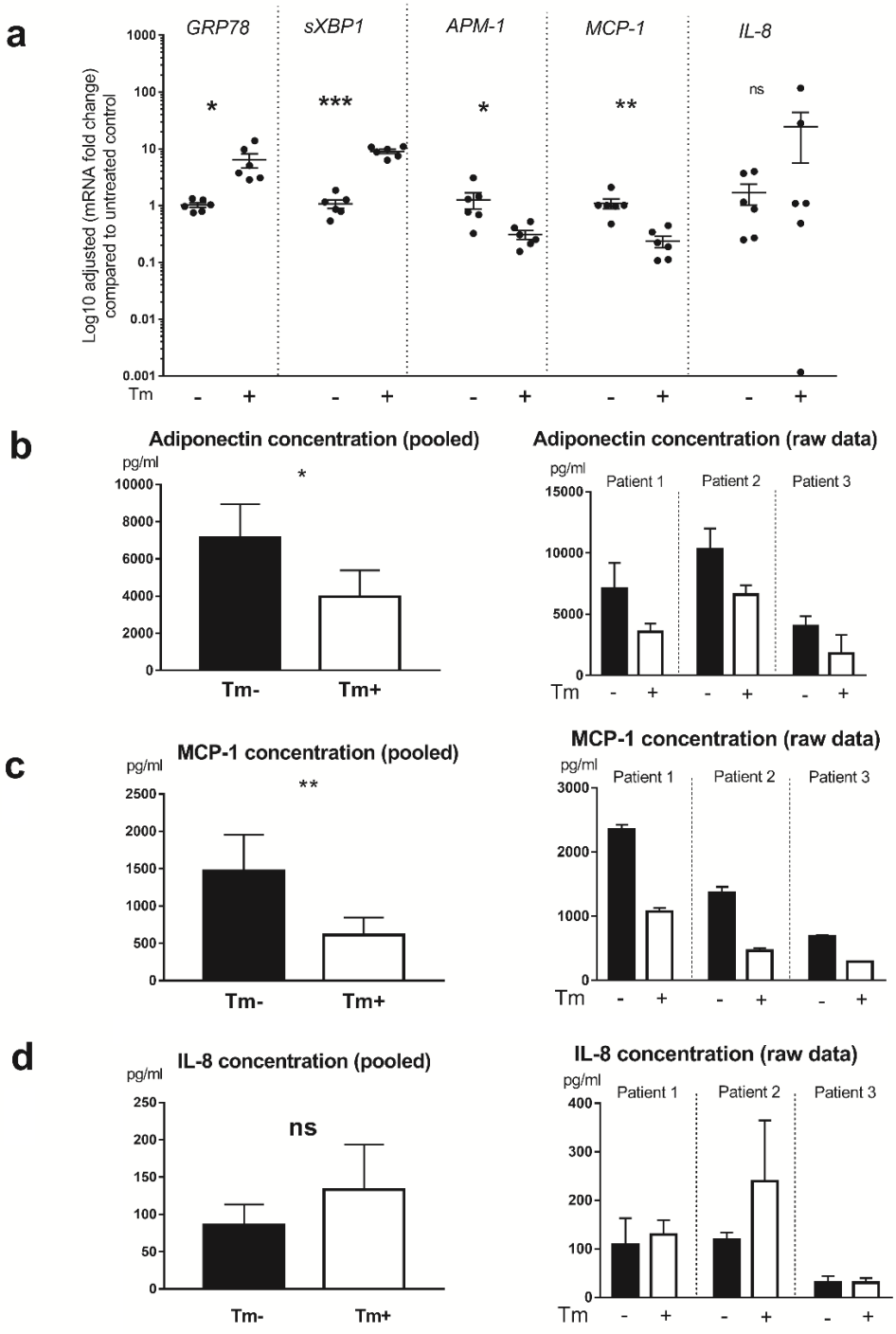

Fig 3.8 ER stress affected mRNA expression and cytokine secretion of APM-1 and MCP-1.

a demonstrates mRNA expression of *GRP78, sXBP1, APM-1 MCP*-1 and IL-*8* in adipocyte spheroids cultured in the medium with or without tunicamycin (Tm) (5 µg/mL) for 24 h. The fold change represents the gene expression in experimental vs control conditions. *p<0.05, **p<0.01, ***p<0.001, ns, p>0.05, unpaired t-test. Error bars indicate estimated standard errors of the mean. **b, c** and **d** demonstrate adiponectin (**b**), MCP-1 (**c**) and IL-8 (**d**) concentration in the culture supernatant maintaining 5 adipocyte spheroids. Error bars indicate estimated standard errors of the mean. *p<0.05, **p<0.01, ns, p>0.05, paired ratio t test. Results were pooled from 3 independent experiments using mesenchymal stem cells derived from 3 donors (see **Table 3.1**). Error bars in raw data indicate the standard deviation of the technique duplicates in ELISA.

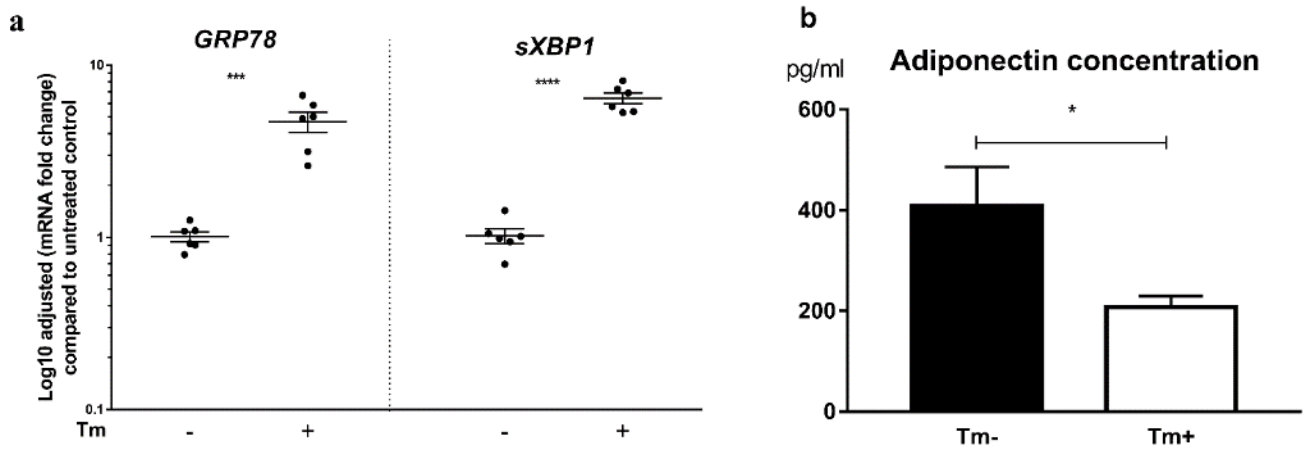

Fig 3.9 ER stress affected adiponectin secretion by 3T3-L1-derived adipocyte spheroids.

Adipocyte spheroids were collected and placed in a 24-well plate at a density of 20 spheroids per well at the end of the adipogenic differentiation (14 days). Spheroids were maintained in the FBS-free medium containing 5 µg/mL of tunicamycin (Tm) for 24 h. **a** demonstrates that mRNA expression of *GRP78* and *sXBP1* was upregulated in adipocyte spheroids after exposure to Tm. The fold change represents the gene expression in experimental vs control conditions. ***p<0.001, **** p<0.0001, unpaired t-test. Error bars represent estimated standard errors of the mean. **b** demonstrates that ER stress interferes the adiponectin secretion by adipocyte spheroids. Error bars indicate estimated standard errors of the mean. *p<0.05, paired ratio t test. Results were pooled from 3 independent experiments.

3.5.5 Increasing density of adipocyte spheroids did not disrupt the secretion of adiponectin.

As was reported by Klingelhutz *et al.* [258], increasing the number of adipocyte spheroids (differentiated for 10 days) maintained in a single well of 24-well plates skewed the adipocyte associated microenvironment to produce a pro-inflammatory phenotype. For example, the concentration of adiponectin in the culture medium decreased when increasing the number of spheroids from 5 to 20. However, the direction of change was opposite to that for IL-8, which was increasingly secreted with the increment of the seeding density. The reproducibility of this finding was tested in this project under the same conditions using the human ASC-derived adipocyte spheroids (differentiated for 18 days). Unexpectedly, the level of adiponectin increased with the seeding density from 5 to 20 rather than decreasing (**Fig 3.10a1**). In the normalised result showing adiponectin secretion per 5 spheroids, the adiponectin level did not differ among groups maintaining varying numbers of spheroids (**Fig 3.10a2**). This finding was confirmed in another experiment using the 3T3-L1-derived adipocyte spheroids (differentiated for 14 days) which were seeded at varying densities (**Figs 3.10b1** and **3.10b2**). Consistent with published results, the level of IL-8 was positively associated with the number of spheroids (**Fig 3.10c1**) [258]. However, the difference among groups

diminished in the normalised result demonstrating the IL-8 secretion by every 5 spheroids (**Fig 3.10c2**). Collectively, the increment of cytokine levels with increasing numbers of spheroids was mainly due to an accumulating effect rather than a cellular response to the changes in the microenvironment.

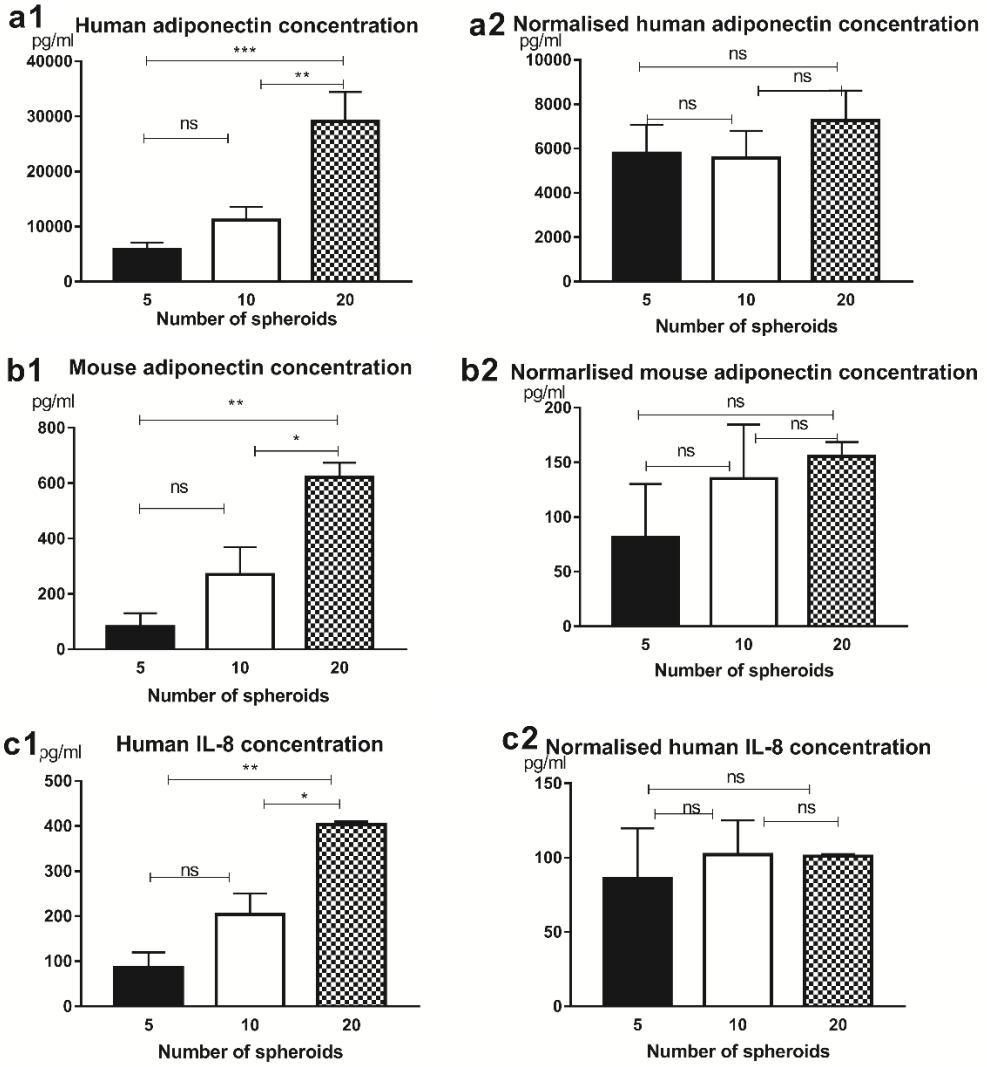

Fig 3.10 Total secretion of adiponectin and IL-8 upregulated with addition of spheroids

Maintained in the FBS-free DMEM-F12 medium, adipocyte spheroids were seeded in a 24-well plate with varying numbers of spheroids (from 5 to 20) in each well. The concentration of adiponectin and IL-8 was measured in the conditioned medium after 24 . **a1** and **b1** demonstrate the level of adiponectin increased with the increment of numbers of adipocyte spheroids derived from human mesenchymal stem cells and 3T3-L1 cells, respectively. **c1** demonstrates IL-8 secretion increases with addition of spheroids. The normalised concentration of human adiponectin, mouse adiponectin and human IL-8 produced by every 5 spheroids is respectively displayed in **a2**, **b2** and **c2**, demonstrating no significant difference among groups. *$p<0.05$; **$p<0.01$; ***$p<0.001$; ns, $p>0.05$, post-hoc test after ordinary one-way ANOVA, error bars indicate standard estimated errors of the mean.

3.5.6 Increasing density of spheroids might protect adipocytes against ER stress.

It was hypothesised that increasing the number of adipocyte spheroids maintained in a single well could generate a stressed microenvironment due to a rapid consumption of nutrients [258]. Nutrient starvation renders cells vulnerable to ER stress [272]. Hence, the ER stress sensitivity of the adipocyte spheroids was measured in response to the change of spheroid seeding density. Contrary to this hypothesis, q-rtPCR results did not show significant differences of *GRP78* (**Fig 3.11a1)** and *sXBP1* (**Fig 3.11b1**) mRNA expression in human ASC-derived adipocyte spheroids with change of number of spheroids. Surprisingly, in the normalised results showing the average mRNA expression by 5 spheroids in various conditions there was a significantly lower mRNA expression of *GRP78* (**Fig 3.11a2)** and *sXBP1* (**Fig 3.11b2**) when 20 spheroids were maintained than 5. There was a trend that *GRP78* mRNA expression upregulated with the increment of 3T3-L1-derived spheroids seeding density. However, the difference between groups was not significant in both unnormalised (**Fig 3.11c1**) and normalised (**Fig 3.11c2)** results. In contrast, in both unnormalised (**Fig 3.11d1**) and normalised (**Fig 3.11d2**) results, *sXBP1* mRNA expression upregulated with increasing number of spheroids derived from 3T3-L1 cells.

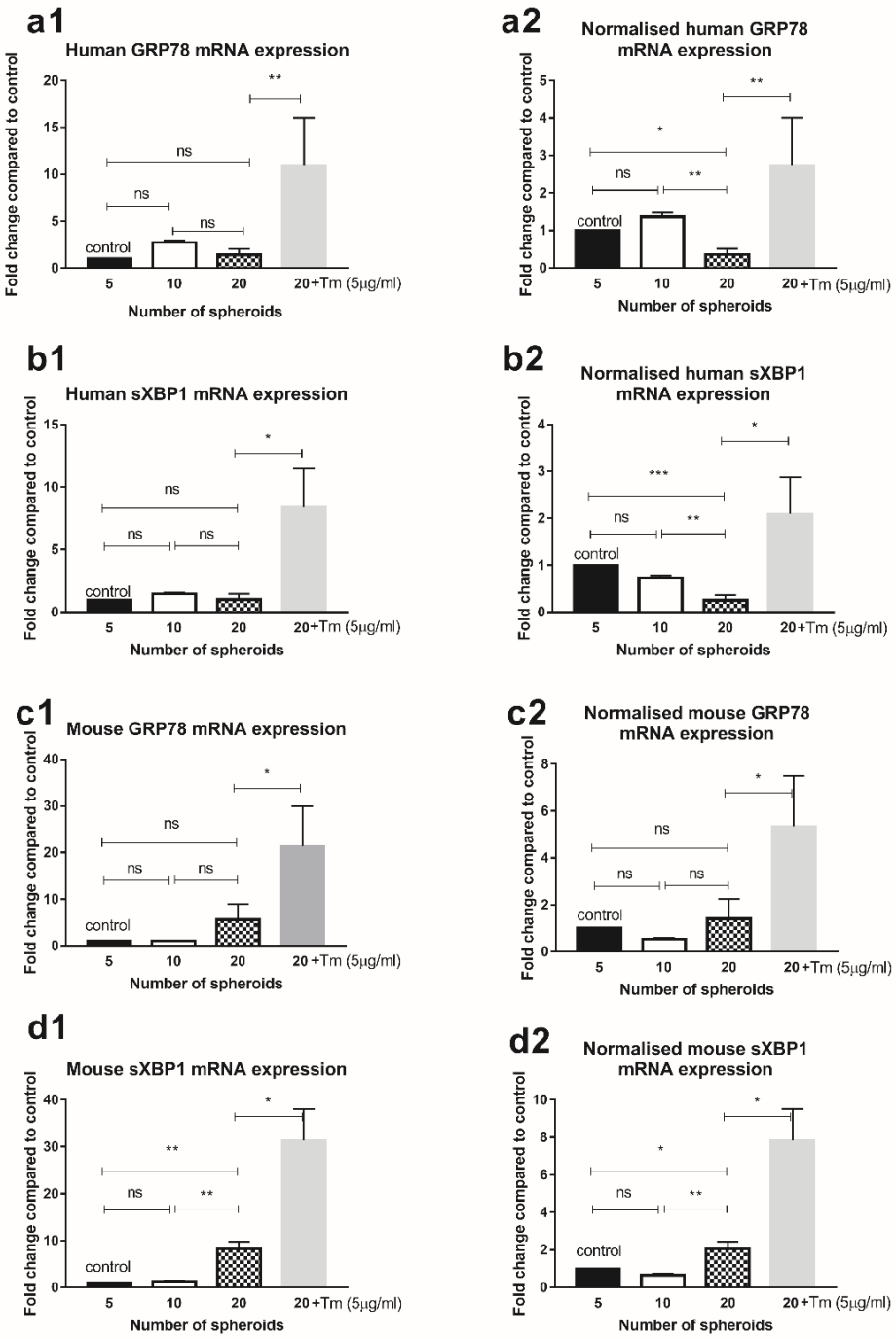

Fig 3.11 *GRP78* and *sXBP1* mRNA expression in response to change of spheroids number

Human mesenchymal stem cells and mouse 3T3-L1-derived adipocyte spheroids were maintained at a density from 5 to 20 for 24 h. Human *GRP78* (**a1**), human *sXBP1* (**b1**), mouse *GRP78* (**c1**) and mouse *sXBP1* (**d1**) mRNA expression are displayed as a fold change compared to the control (5 spheroids maintained in a single well). Normalised results (**a2**, **b2**, **c2** and **d2**) demonstrate the average mRNA expression by 5 spheroids in various conditions. *p<0.05, **p<0.01, ***p<0.001, ns, p>0.05, post-hoc test after one-way ANOVA. Positive control was 20 spheroids treated by tunicamycin (Tm). 20 vs 20+Tm, paired ratio t test. Error bars represent estimated standard errors of the mean. Data were pooled from 3 independent experiments.

3.6 Discussion

The results demonstrate that the liquid overlay technique can cost-effectively generate reproducible mature adipocyte spheroids, which can functionally produce adiponectin, MCP-1 and IL-8. Human ASC and 3T3-L1 cells grown in the 3D culture environment exhibited strong capacity for adipogenic differentiation, indicating the liquid overlay technique can be applied to generate a platform for *in vitro* studies requiring an adipose tissue microenvironment.

To the best of my knowledge, the liquid overlay-based 3D culture has never been reported to generate human adipocyte spheroids. It has been published recently that this technique was able to successfully generate 3T3-L1-derived murine adipocyte spheroids in a spontaneous manner, indicating that applying this model has gained increasing value [273]. Applying a 3D co-culture technique is a mainstream in research associated with the tumour microenvironment, which can reflect cell-cell and cell-matrix interactions. The ECM based hydrogel is widely applied in building the scaffolds in 3D culture [274]. However, the challenge is to put cells in the same co-culture system, simultaneously, especially when including mature adipocytes that normally require longer induction time than other cell types (e.g. macrophages). In this study, spheroids were maintained in the agarose coated plate over a period long enough required for adipogenic differentiation, providing a platform to prepare mature adipocyte spheroids before incorporating them into a co-culture system to interact with other cells. The scaffold-free property of the adipocyte spheroids makes them easy to be transferred between culture dish and medium, meeting with the design of experiments as required.

Adipocyte spheroids established in the study were able to produce adiponectin, MCP-1 and IL-8. As adipocyte secretions, these cytokines are key mediators in maintaining physiological homeostasis or contributing to adipose tissue dysfunction in diseases [275]. Adiponectin is exclusively secreted by adipose tissue, exerting protective anti-inflammatory, anti-atherosclerotic functions and increasing insulin sensitivity [120]. MCP-1 (also known as CCL2) exerts monocyte/macrophage recruiting functions by interacting with its receptor CCR2 [276]. The abundance of MCP-1 in adipose tissue and circulation is related to macrophage infiltration in the adipose tissue and development of metabolic disorders, such as insulin resistance and hepatic steatosis [277]. IL-8 (also known as chemokine C-X-C motif ligand 8, CXCL8) is a chemoattractant which recruits neutrophils and macrophages, contributing to self-defence or tissue damage in inflammation [278]. The mRNA expression of IL-8 in human adipocytes is upregulated upon exposure to proinflammatory cytokines (e.g. IL-1beta and TNF α) but downregulated by dexamethasone [279].

q-rtPCR results showing treatment of tunicamycin decreased the expression of *APM-1* (human gene encoding adiponectin) and *MCP-1* were consistent with previous studies. In other research, treatment

of human adipocytes with tunicamycin impaired the multimerisation of adiponectin to form the most bioactive isoform which has high molecular weight (>300KD) [280]. Similarly, the mRNA expression of *MCP-1* was reported to be downregulated after exposure to tunicamycin in adipocytes differentiated from 3T3-L1 cells [281]. Marjon *et al*. reported that IL-8 secretion was upregulated in exposure to tunicamycin at a concentration of 5 μg/ml for 24 h [282]. In the present study, there was a non-significant trend for tunicamycin to upregulate IL-8 secretion. The published data from others only reflected the average result from technique triplicates in a single experiment. It should be noted that great variance within groups present in primary cell culture may blunt the statistical power to detect variance between groups when the sample size is small, which was the situation in the present study when data pooled from three independent experiments using adipocytes from different donors being analysed [283]. Hence, even the statistical result did not show a significant upregulation of IL-8 upon tunicamycin treatment, it is insufficient to conclude that tunicamycin has no effect on IL-8 expression in reality.

In a similar 3D culture platform established by hanging-drop technique, Klingelhutz *et al.* found that increasing the density of adipocyte spheroids could mimic a pro-inflammatory microenvironment as demonstrated by an upregulation of IL-8 with downregulation of adiponectin [258]. In the present study, the concentration of both IL-8 and adiponectin has always been increased with increment of spheroids numbers. However, it was unclear in the previous publication whether the total concentration of cytokines or the average concentration normalised by number of spheroids was measured. Hence, the production of IL-8 and adiponectin by 5 spheroids was further analysed when different numbers of spheroids were maintained in the same space. The normalised results did not show any significant difference among groups, indicating the increment of cytokine levels with increasing numbers of spheroids was mainly due to an accumulating effect rather than a cellular response to the changes in the microenvironment.

Similarly, discrepancies existed between unnormalised and normalised results regarding the mRNA expression of ER stress-related genes in response to changes in spheroid density. For human ASC-derived adipocyte spheroids, increasing spheroid density did not aggravate ER stress as predicted. In contrast, a significantly lower mRNA expression of both *GRP78* and s*XBP1* was observed when there were more spheroids maintained (20 vs 5) in the normalised results. However, the results were not consistent with the findings in 3T3-L1-derived adipocyte spheroids as demonstrated by a positive association between s*XBP1* mRNA expression and number of spheroids in the normalised results. Considering the human ASC-derived adipocyte spheroids have stronger adiponectin secreting capacity than 3T3-L1-derived adipocyte spheroids, the inverse trend of change might be related to a protective role of adiponectin against ER stress [284, 285]. However, the mechanism is uncertain

without further investigating the change of signaling pathways that are possibly involved. Compared to a significant and consistent upregulation of s*XBP1* and *GRP78* mediated by tunicamycin, manipulating the density of adipocyte spheroids is not an ideal technique to create an ER stress-activated microenvironment.

3.7 Conclusion

Taken together, the liquid overlay technique cost-effectively generates reproducible mature and functional adipocyte spheroids that secrete adiponectin, MCP-1 and IL-8, and are responsive to the ER stress inducer, tunicamycin. This technique can be applied to establish a platform for studies requiring either a healthy or stressed adipose tissue microenvironment, though manipulating spheroid density singly may not modulate adipose tissue microenvironment to a certain direction as desired.

Chapter 4

Studying macrophage behaviour in an adipose tissue microenvironment

4.1 Included publications

This chapter included contents from an original research article published in the journal of *Biochemical and Biophysical Research Communications*.

Shen K, Vesey DA, Hasnain SZ, Zhao KN, Wang H, Saunders N, Burgess M, Johnson DW, Gobe GC. A cost-effective three-dimensional culture platform functionally mimics the adipose tissue microenvironment surrounding the kidney. BBRC. 2020; 522 (3):736-742. https://doi.org/10.1016/j.bbrc.2019.11.119

The candidate was the lead author of this original research article. She contributed significantly to the conception and design of this study (80 %) and analysis and interpretation of the literature (70 %), and drafted the majority of the manuscript (90 %).

4.2 Overview

Adipose tissue is associated with many chronic inflammatory diseases, including cancer. Within the SVF of adipose tissue, the recruitment of pro-inflammatory (M1) macrophages plays a negative role in maintaining adipose tissue homeostasis, therefore initiating tumourigenesis. However, TAM exhibit a tissue-remodelling phenotype (M2), therefore facilitating tumour metastasis. Investigating the macrophage behaviour in the adipose tissue microenvironment assists in understanding the fat-cancer interplay from the view of immune modulation. Applying a novel 3D culture technique, we co-cultured adipocyte spheroids and macrophages to investigate the invasion capacity of macrophages towards adipocyte spheroids and the polarisation effect of the adipose tissue microenvironment on macrophage phenotype. Simultaneously, we applied the same co-culture system to study the invasion capacity of cancer cells towards adipocyte spheroids in the presence of different macrophages. We discovered that the mature adipocyte spheroids caused an MCP-1 independent, but CCR2 dependent recruitment of Raw 264.7 cells. The migration was abolished by tunicamycin treatment, which is an inducer for ER stress. Unpolarised macrophages shifted into an M2 macrophage phenotype when co-cultured with adipocyte spheroids. M1 and M2 macrophages exhibited distinct invasion capacity through the Matrigel coated trans-well membrane. The presence of M1 macrophages inhibited the invasive capacity of Kirsten mouse sarcoma virus-transformed non-producer human osteosarcoma (KHOS) and 786-0 kidney cancer cells. Reprogramming the macrophage phenotype into M1 in the tumour microenvironment may be promising in preventing cancer metastasis.

4.3 Introduction

Adipose tissue is found in proximity to the primary site of many cancers and could be the invasive site in early stages of cancer metastasis. The interactions of malignant cells with the normal cell types in the adipose tissue may have impact on cancer prognosis [286]. For example, the infiltration of macrophages (CD68+) in the adipose stroma of benign breast tumour is an independent risk factor of developing malignant breast cancer [212]. Investigating the dynamic interactions of macrophages with adipocytes is crucial for comprehensively understanding the role of adipose tissue microenvironment in cancer development.

The macrophage is a cell type characterised by a high level of plasticity in terms of phenotype, function and motility [287]. Adipose tissue macrophages have been identified as the primary source of cytokines produced by adipose tissue [288]. The phenotype switching of macrophages is often observed in obesity-associated adipose tissue as demonstrated by M1 macrophage aggregation and increased secretion of pro-inflammatory cytokines, such as MCP-1 [277]. Adiponectin produced by adipose tissue is known to maintain the anti-inflammatory profile of macrophages [289]. However, it has been recently found that under obese conditions, overexpression of microRNA-34a in adipose tissue inhibited the M2 polarisation of macrophages [161]. The skew of M2 macrophages into M1 in obesity aggravates metabolic disorders and inflammation, and therefore could be a mechanism underlying the increased risk of tumourigenesis [290, 291]. However, in the breast cancer tumour-associated adipose tissue sampled from patients who had a high metastatic rate and poor cancer survival, the predominant macrophages observed were M2 macrophages [210]. The negative impacts of M2 macrophages on cancer prognosis are associated with inhibited T cell anti-tumour immunity, enhanced extravasation of cancer cells and angiogenetic effects [292].

Chapter 2 introduced a finding through IHC that GRP78 (an ER stress marker) was upregulated in the perinephric adipose tissue of ccRCC from patients with high BMI. Regression analysis revealed that the upregulated GRP78 expression might be associated with decreased cancer metastasis [293]. It would be of interest to know the effects of activated ER stress in perinephric adipose tissue on macrophage migration and polarisation, considering the interplay between macrophages and cancer prognosis.

In this chapter, a co-culture system including cancer cells, macrophages and adipocyte spheroids (the modelling technique introduced in **Chapter 3**) was applied to measure the polarisation, migration and invasion of murine and human macrophages in an ER stress-activated or a normal adipose tissue microenvironment. Moreover, the invasion capacity of cancer cells towards adipocyte spheroids in the presence of either M1 or M2 macrophages was compared.

4.4 Methods

4.4.1 Purifying monocytes from peripheral blood mononuclear cells

This study received ethics approval from the Metro South Human Research Ethics Committee (HREC/16/QPAH/353). Whole peripheral blood was obtained prior to radical nephrectomy surgery from consented participants diagnosed with renal tumours. Peripheral blood mononuclear cells (PBMC) were isolated by density gradient centrifugation following the Histopaque manual (Sigma 10771) [277]. The expression of CD16 in human blood monocytes is increased during the course of inflammation, as demonstrated using CSF-1 treatment [294]. To make sure all the monocytes used in the experiments were initially homogeneous, only the classic monocytes (CD14+/CD16-) were purified using fluorescence-activated cell sorting (FACS) with the Beckman Coulter MoFlo Astrios EQ sorter. Gating strategy to purify monocytes from PBMC is displayed in **Fig 4.1**.

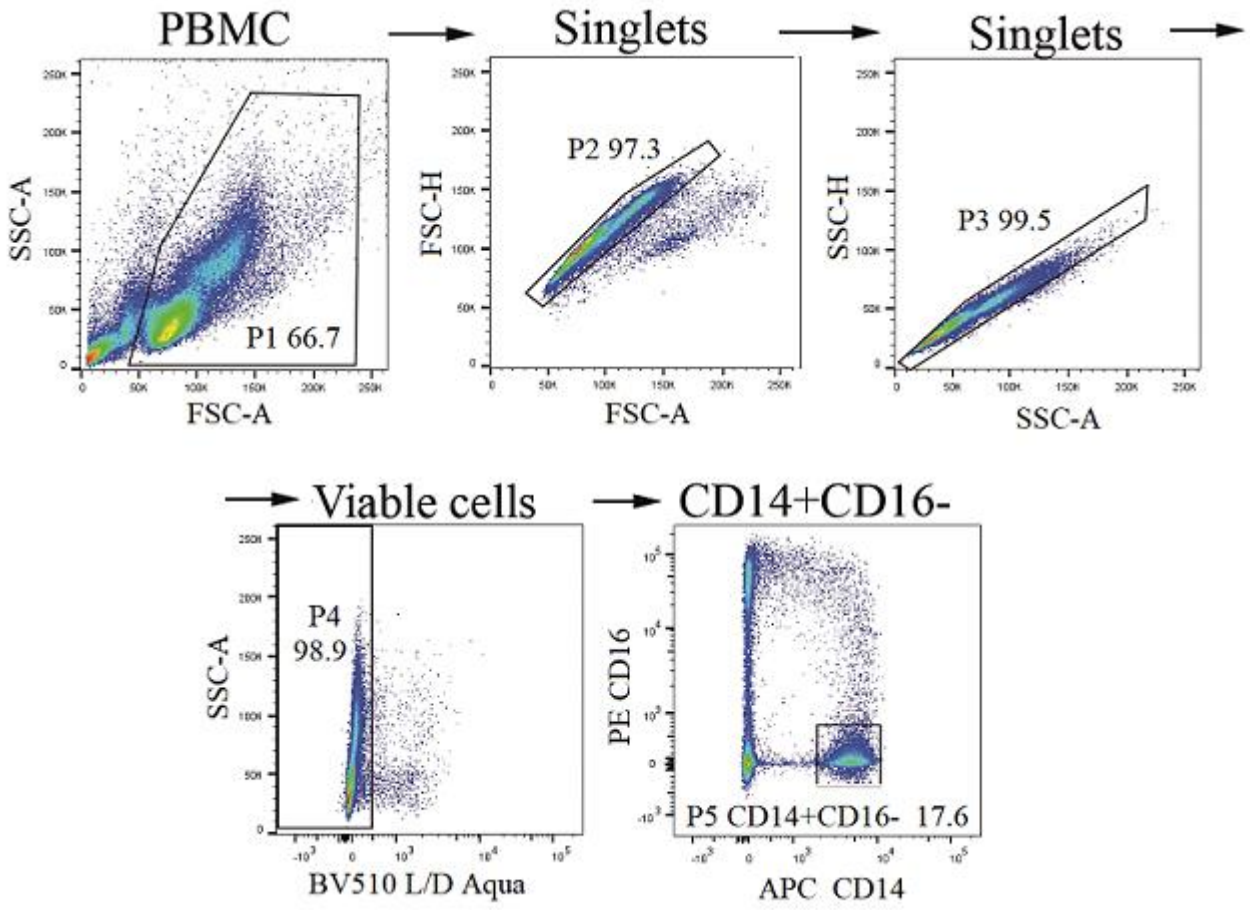

Fig 4.1 Gating strategy to purify monocytes from PBMC

Classic monocytes (CD14+/CD16-) were purified using fluorescence-activated cell sorting. Live/dead aqua was used to discriminate live cells from dead cells.

4.4.2 Differentiation of M1/M2 macrophages from monocytes

M1 and M2 macrophages were generated based on the method introduced by Tarique *et al.* with modification [295]. The ingredients supplemented in culture medium have been summarised in **Appendix 5**. Briefly, purified monocytes were seeded in 6 well culture plates at a density of 500,000 per well and maintained in the macrophage differentiation medium for 6 days. Then, cells were maintained in the M1 or M2 induction medium, or still in the macrophage differentiation medium (M0) for 2 days (**Fig 4.2**). At the end of the induction, cells were collected to check the expression of macrophage phenotype markers (CD80, CD86, CD163, CD206, CD209 and CD200R) by flow cytometry analysis.

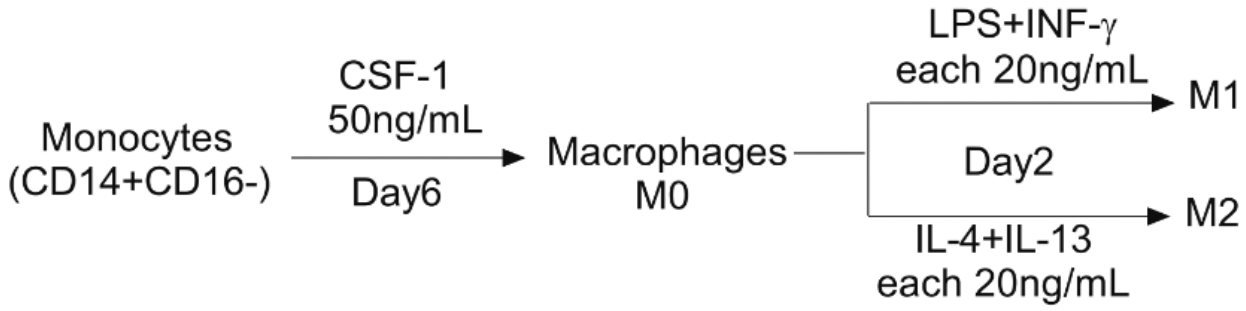

Fig 4.2 Paradigm of differentiating M1 and M2 macrophages from PBMC

CD14+/CD16- monocytes sorted from donors diagnosed with renal tumours were cultured with colony stimulating factor (CSF)-1 containing medium for 6 days. Then, M1 macrophages were generated by stimulating with lipopolysaccharide (LPS) and interferon (INF)-γ; M2 macrophages were generated by stimulating with interleukin (IL)-4 and IL-13.

4.4.3 Flow cytometry analysis

Flow cytometry analysis was performed to quantify the expression of different surface markers on classically and alternatively activated macrophages. Cells were harvested with human Fc block solution (BD 564220) to block non-specific Fc receptor binding and were incubated with specific antibody for 30 min on ice. Live and dead cell discrimination was performed by adding viability dye before sample analysis. Details on antibodies and live/dead cell dye are summarised in **Appendix 1**. If not specified, 1×10^6 cells were suspended in 100 µL of the staining solution per sample. The samples were analysed using the instrument BD LSR Fortessa X-20. Non-stained cells were used to set the voltage of the instruments. Flow cytometry data were analysed using the FlowJo Software.

4.4.4 Culture of cell lines

The human RCC cell line, 786-0 (ATCC CRL-1932^{TM}), the human osteosarcoma cell line, KHOS (ATCC CRL-1544 ^{TM}), and the mouse macrophage, Raw 264.7 cell line (ATCC TIB-71 ^{TM}) were

cultured in DMEM-F12 medium supplemented with 10 % FBS, 1 % P/S, and maintained at 37 ˚C atmosphere containing 5 % CO_2. The KHOS cells used in this experiment were green fluorescence protein (GFP)-transfected and were a kind gift from Dr Liliana Endo-Munoz (The University of Queensland Diamantina Institute, Brisbane, Australia).

4.4.5 Trans-well invasion and migration assay

A pre-set of five mature adipocyte spheroids (adipogenic differentiation for 18 days) were placed in each well of the 24-well plates in DMEM-F12 culture medium (FBS-free) for 24 h before placing in the trans-well inserts. DMEM-F12 culture medium (FBS and adipocyte spheroid free) was used as negative control. The 6.5 mm inserts with 5 µm pores and polycarbonate membrane (Corning 3421) were applied in the invasion assay in which the induced M1/M2 macrophages were placed at a density of 20,000 per 100 µL in the DMEM-F12 culture medium (FBS-free). The inserts were pre-coated with 100 µL of the Corning Matrigel Growth Factor Reduced (lactose dehydrogenase elevating virus/LDEV free) Basement Membrane MatMatrix (Corning BDAA354230) at a concentration of 250 µg/mL for 1.5 h at 37 ˚C, after which the Matrigel was removed. Cells placed in the inserts were allowed 24 h for the invasion assay. The setting of the migration assay for Raw 264.7 macrophages was the same as the invasion assay except that the membrane was not coated with Matrigel. The 6.5 mm FluoroBlock inserts with 8 µm pores and dyed polyethylene terephthalate membrane (Corning 35112) were applied in the invasion assay in which cancer cells were co-cultured with either M1 or M2 macrophages in DMEM-F12 FBS-free medium. Cancer cells were seeded at a density of 20,000 per 100 µL; macrophages were seeded at a density of 10,000 per 100 µL. All cells were starved for 8 h by replacing the full culture medium (containing 10 % FBS) with FBS-free culture medium prior to seeding in the inserts, except for M1 and M2 macrophages, for the purpose of maintaining their polarisation.

4.4.6 Processing, staining, imaging and quantification of migrated/invaded macrophages

The non-migrating/invading cells from the upper surface of the membrane were removed by a cotton tipped swab after the migration/invasion assay. Then, the cells on the bottom surface were fixed in 4 % paraformaldehyde for 15 min, stained with 1 % crystal violet (Sigma C6158) for 10 min, washed with water, and mounted on glass slides with the bottom side down. Images for quantification were photographed using the Nikon Brightfield Manual Microscope using a ×40 objective for the migration assay and a ×20 objective for the invasion assay. Five imaging points were chosen for each sample. The points were located at the centre of the membrane and four midpoints of the radii which split the membrane in four equal sectors. The mean number of cells counted manually in the five fields of view represented the migrated/invaded macrophages for each sample.

4.4.7 Live cell staining of macrophages and cancer cells

M1/M2 macrophages were stained with the CellTracker Red CMTPX Dye (Invitrogen C34552) at a concentration of 7 μg/mL (diluted in FBS-free DMEM-F12 medium) for 30 min at 37 ˚C. After two washes with PBS, cells were rested in M1/M2 induction medium for 8 h prior to co-culture. 786-0 cancer cells were stained with the CellTrace Violet dye (Invitrogen C34557) at a concentration of 10 μg/mL (diluted in PBS) for 30 min at 37 ˚C. After two washes with the full culture medium, cells were starved in FBS-free culture medium for 8 h prior to co-culture.

4.4.8 Imaging and quantification of invaded cancer cells in the presence of macrophages

The membrane housing on the FluoroBlock inserts can block the fluorescently-labelled cells in the top chamber of the inserts, thereby eliminating the processing steps prior to imaging [296]. Images for quantification were photographed using a ×10 objective with the Olympus IX73 Inverted Manual Microscope. Images (16 bit) were acquired in greyscale output at a display resolution of 1376×1038 using the cellSens Software. The gain and exposure were optimised in each independent experiment based on the signal intensity and were kept consistent when taking photos. The method of choosing the imaging fields of view was the same as imaging of the migrated/invaded macrophages. Macrophages, KHOS cells and 786-0 cells were imaged under the CY3, GFP and DAPI excitation filters, respectively. The area of the invaded cells was quantified using the software FIJI. Thresholds of images were adjusted manually with the setting above the background noise while leaving all the invaded cells visible. The mean area in the five fields of view represented the area of invaded cells for each of the sample.

4.4.9 Statistical analysis

Comparisons between groups were made using the ANOVA, paired or unpaired t-test when appropriate. When there was a statistically significant difference in ordinary ANOVA, post hoc testings were performed to determine where the difference occurred between groups. When there was a statistically significant difference in one-way repeated measures ANOVA, Tukey's multiple comparisons were performed to determine the difference occurred between groups. $P<0.05$ was considered statistically significant. Statistical analysis was performed using GraphPad Prism 7.0.

4.5 Results

4.5.1 Morphologic observation of M0, M1 and M2 macrophages

Over the 6 days of differentiation, purified monocytes elongated and became adherent. Mature macrophages (M0) are heterogeneous in size and shape. Some cells were rounded and flatted. Others had stretched pseudopodia (**Fig 4.3a**). After 2 days of polarisation, M1 macrophages became more rounded, and less tightly adherent to the well surface (**Fig 4.3b**). However, some M2 macrophages had more stretched pseudopodia and others further increased their size with more flatly outspread cytoplasm (**Fig 4.3c**).

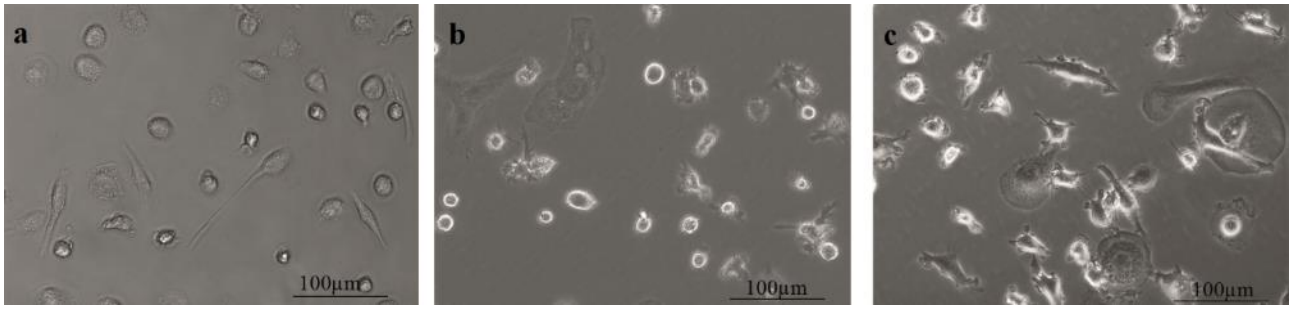

Fig 4.3 Morphologic characteristics of M0, M1 and M2 macrophages

Images were photographed using the ×20 objective with the Olympus IX73 Inverted Manual microscope. Scale bars = 100 μm.

a. M0 macrophages; **b**. M1 macrophages; **c**. M2 macrophages

4.5.2 M1 and M2 macrophages exhibited distinct phenotypic characterisation.

After 2 days of polarisation with M1 and M2 differentiation media (**Fig 4.2**), the expression of a panel of surface markers was investigated on M0, M1 and M2 macrophages. M2 macrophages exhibited significantly higher expression of CD200R and CD206 than M1 macrophages. Similarly, the expression of CD163 and CD209 was higher in M2 macrophages than M1 macrophages. However, the differences were not statistically significant. There was a trend that the expression of CD80 and CD86 was higher in M1 macrophages than M2 macrophages. However, the differences were not statistically significant. The raw data of the mean fluorescence intensity (MFI) of the 6 CD markers measured in 5 independent experiments are displayed in **Fig 4.4**.

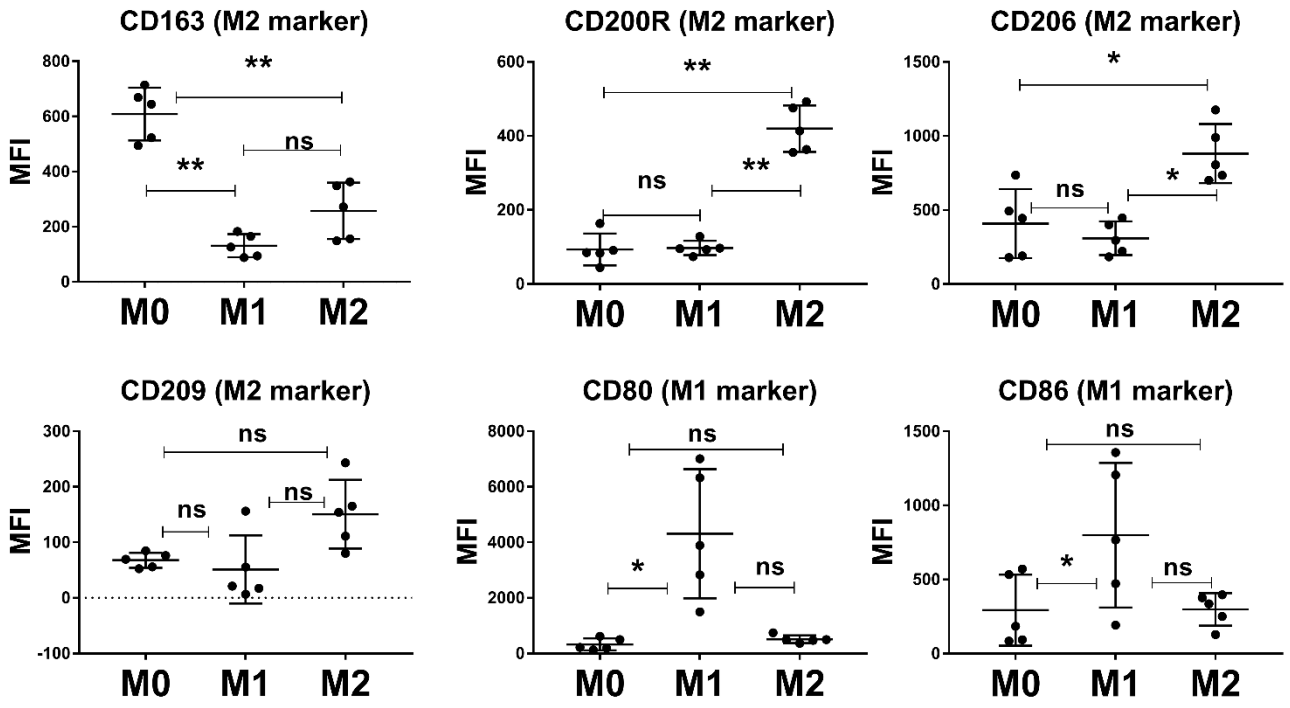

Fig 4.4 Phenotypic characteristics of the M1 and M2 macrophages

M2 macrophages exhibited high expression of CD163, CD200R, CD206 and CD209; M1 macrophages exhibited high expression of CD80 and CD86 in flow cytometry analysis. Dot plots represent the mean fluorescence intensity (MFI) of a specific CD marker measured in one out of the five independent experiments using pooled peripheral blood mononuclear cells derived from at least 3 donors. *p<0.05, **p<0.01, ns, p>0.05, Tukey's multiple comparison after repeated measures one-way ANOVA. Error bars represent estimated standard errors of the mean.

4.5.3 The expression of CD163 and CD209 in M0 macrophages was upregulated when co-cultured with adipocyte spheroids.

Based on published data, co-culture of human PBMC with pre-adipocytes upregulated the expression of CD163. Moreover, the expression level was increased over the period of adipogenic differentiation [297]. However, it has not been confirmed in the 3D culture system that co-culture with mature adipocyte spheroids could induce the unpolarised macrophages to shift into M2 macrophages. Hence, the M0 macrophages (100,000 cells in 100 µL of the FBS-free control medium) were seeded in the trans-well inserts (pore size = 0.4 µm, Corning CLS3413), which were placed above the 10 adipocyte spheroids, and allowed to co-culture for 24 h. Results from the flow cytometry analysis demonstrated that the expression of CD163 and CD209 was significantly higher in M0 macrophages co-cultured with the adipocyte spheroids than in M0 macrophages grown on their own. No significant difference was observed for the expression of other macrophage phenotype markers, including CD200R, CD206, CD80 and CD86 (**Fig 4.5**).

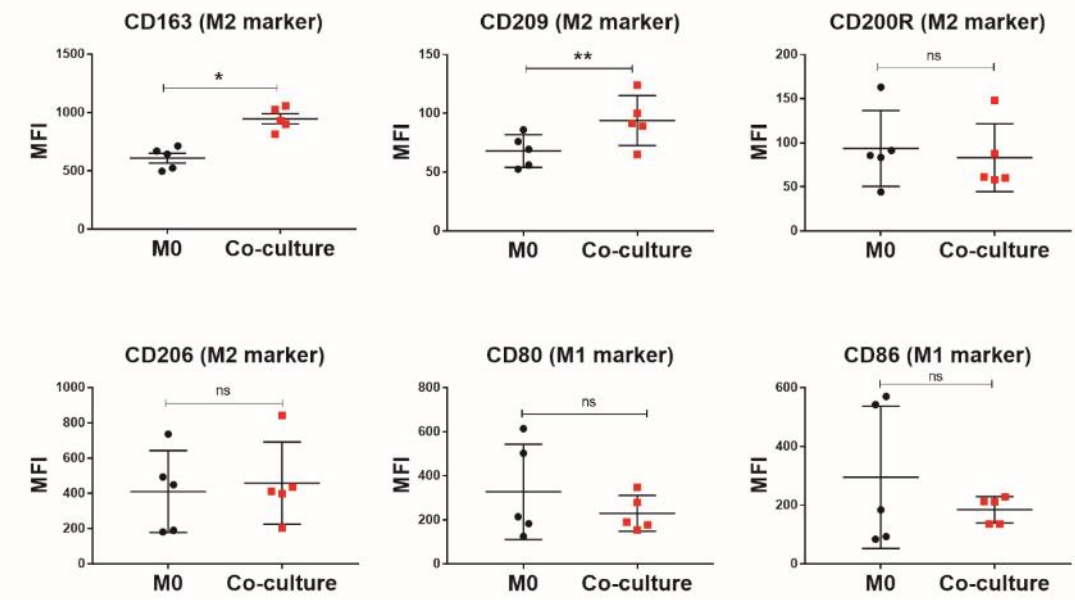

Fig 4.5 CD163 and CD209 were upregulated when M0 macrophages were co-cultured with the mature adipocyte spheroids.

Co-culture of M0 macrophages with ten adipocyte spheroids for 24 h significantly upregulated expression of CD163 and CD209 in macrophages. However, no significant change was observed for other macrophage phenotype markers. Data reflect 5 independent experiments and each experiment was using the pooled peripheral blood mononuclear cells isolated from at least 3 donors. *$p<0.05$, **$p<0.01$, ns, $p>0.05$, paired t-test. Error bars represent estimated standard errors. Abbreviation: MFI, mean fluorescence intensity.

4.5.4 Exposure to tunicamycin did not shift M2 macrophages into M1.

Since a negative association between ER stress level and kidney cancer metastatic rate was found previously and M2 macrophages in the tumour microenvironment may facilitate metastasis [293, 298], the effect of ER stress on the M1 phenotype skew to M2 macrophages was investigated. However, neither an upregulation of M1 markers nor a downregulation of M2 markers was observed in M2 macrophages upon tunicamycin treatment at the concentration of 2 to 4 μg/mL in the flow cytometry analysis, indicating ER stress and macrophage polarisation may not be directly linked in the setting of cancer metastasis (**Fig 4.6**). Tunicamycin is a drug which inhibits N-linked glycosylation, thereby blocking protein folding and causing ER stress [271].

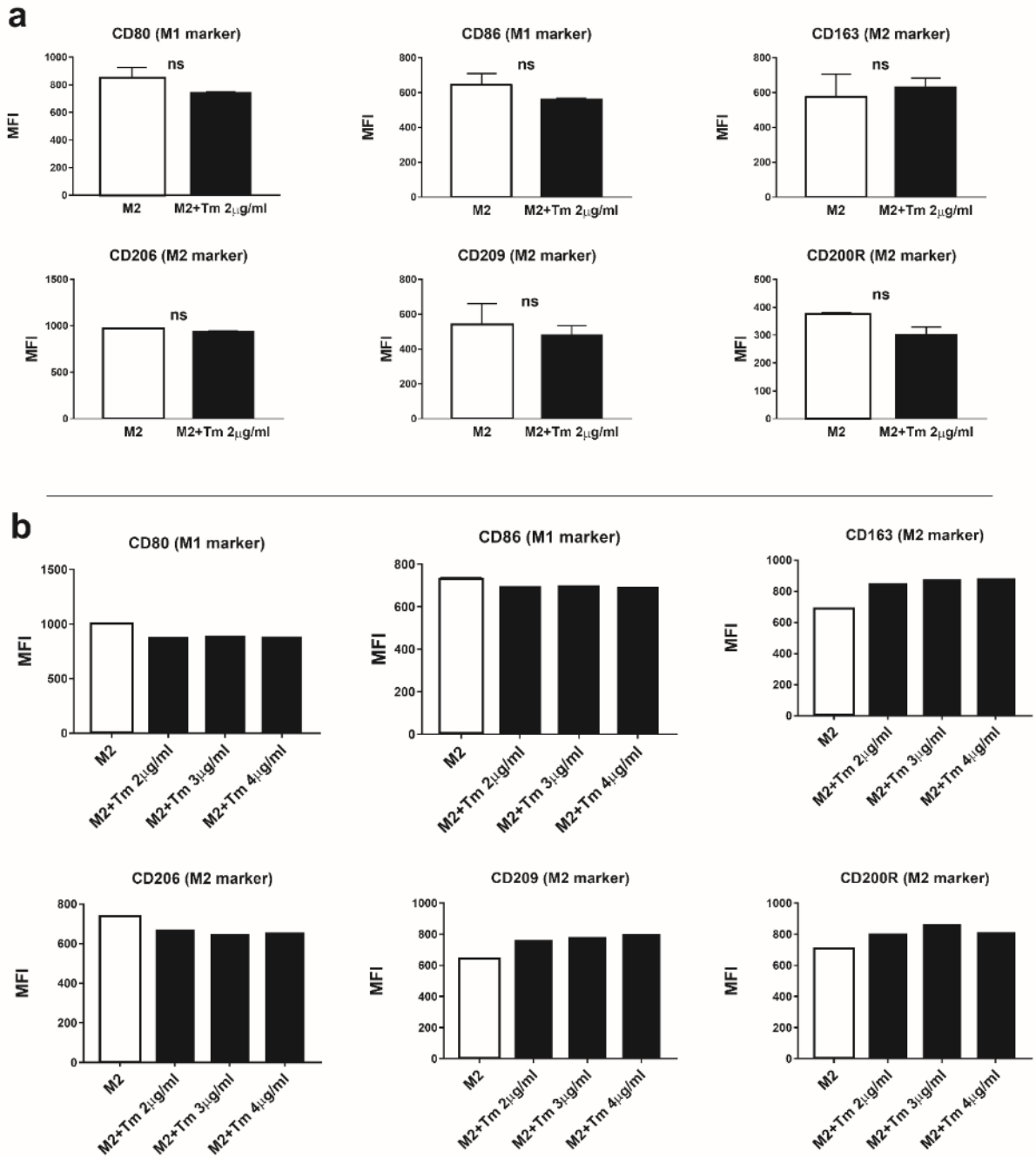

Fig 4.6 Treatment with tunicamycin did not cause an M1 phenotype switch to M2 macrophages. **a.** Macrophage phenotype markers were tested by flow cytometry analysis in M2 macrophages treated with or without tunicamycin (Tm) at a concentration of 2 μg/mL for 24 h. No MFI (mean fluorescence intensity) of the markers exhibited significant difference under the two conditions. Data were pooled from two independent experiments with technique duplicates. ns, $p>0.05$, paired ratio t test. **b.** To confirm that Tm has no direct effect on phenotypes of macrophages, the experiment was repeated by treating M2 macrophages with increasing concentrations of Tm from 2 to 4 μg/mL. For all the markers, the variance of MFI was very small in response to different concentrations of Tm.

4.5.5 Tunicamycin diminished the migration of Raw 264.7 cells towards adipocyte spheroids.

Trans-well migration results demonstrated that, compared with the control medium, medium maintaining 5 adipocyte spheroids caused a significant migration of Raw 264.7 cells. The migration was diminished when spheroids were pre-treated with tunicamycin (5 µg/mL) for 24 h (**Fig 4.7a**). Graphs of the migrated cell number pooled from 3 independent experiments and raw data are displayed in **Fig 4.7b**. Demographic information of participants has been displayed in **Table 3.1** (**Chapter 3**). Trypan blue exclusion assay and MTT assay results demonstrated that tunicamycin at the concentration of 2 µg/mL had less impact on cell proliferation and viability **(Table 4.1 and Fig 4.8**). To exclude that the diminished migration reflected inhibited cell viability caused by tunicamycin, the migration assay by treating adipocyte spheroids with tunicamycin at the concentration of 2 µg/mL was repeated. Consistently, the migration of macrophages was blocked, with the 95 % CI of the difference between group means of migrated cell number being -79.7 to 236.2 (**Fig 4.9, Groups 1-2**).

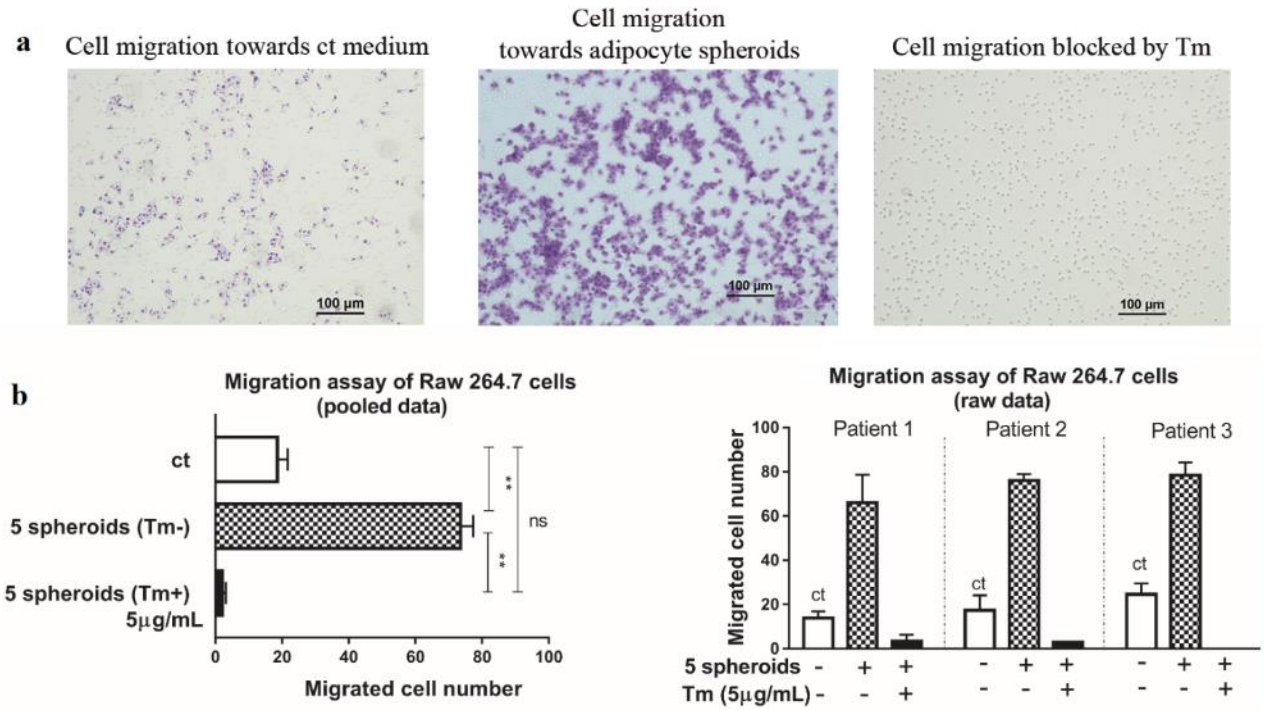

Fig 4.7 Tunicamycin blocked the migration of Raw 264.7 cells.

a. Images were photographed using the ×10 objective and cell numbers were quantified under the ×40 objective. Scale bar=100 µm. **b.** Compared with the control (ct) medium, a significant migration was caused in the presence of adipocyte spheroids [ct vs 5 spheroids (Tm-)], which was blocked when the spheroids were treated with tunicamycin (Tm) at a concentration of 5 µg/ml [5 spheroids (Tm-) vs 5 spheroids (Tm+)]. Data reflect 3 independent experiments including technique duplicates. **p<0.01, ns, p>0.05, Tukey's multiple comparisons after one-way repeated measures ANOVA. Error bars indicate estimated standard errors of the mean in pooled data and standard deviation of the mean in raw data.

Table 4.1 Results of Trypan blue exclusion and MTT assays when Raw 264.7 cells were treated with tunicamycin at different concentrations

Concentration of tunicamycin	Live/Live+Dead ratio	Cell count	OD value/ OD value for control ×100%
5 μg/mL	88 %	1.35×10^5/mL	39.74 %
2.5 μg/mL	88 %	2.23×10^5/mL	44.04 %
1.25 μg/mL	79 %	2.64×10^5/mL	52.58 %
0.625 μg/mL	72 %	2.82×10^5/mL	56.98 %
0 μg/mL	85 %	3.22×10^5/mL	100 %

Raw 264.7 cells were seeded at a density of 5,000 per well in a 96 well plate and treated with tunicamycin at serially diluted concentrations for 24 h. Cell count and MTT assay results demonstrated that the proliferation of macrophages was inhibited dramatically in response to tunicamycin at the concentration of 5 μg/mL. OD = optical density.

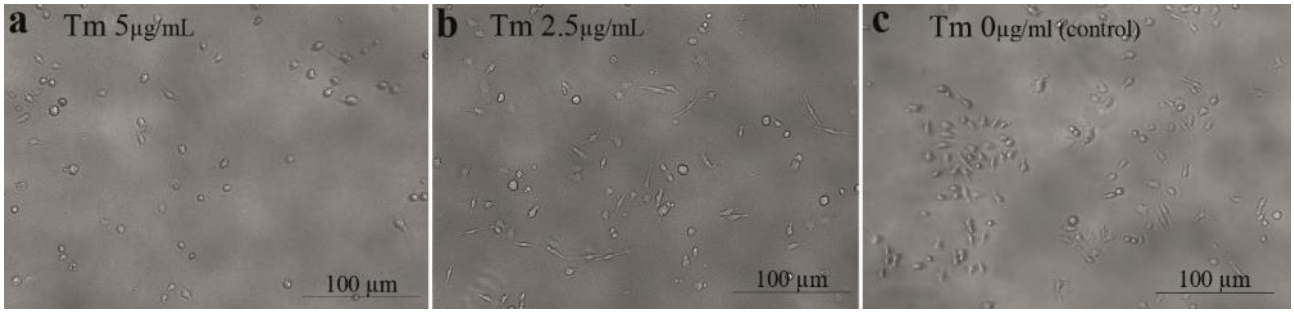

Fig 4.8 Morphology of Raw 264.7 cells in exposure to Tunicamycin at various concentrations

Live cell images demonstrated the cells became more rounded with less protuberance in response to tunicamycin (Tm) at the concentration of 5 μg/mL. Images were photographed using a ×10 objective with the Olympus IX73 Inverted Manual microscope. Scale bars = 100 μm. **a.** 5μg/mL; **b.** 2.5 μg/mL; **c.** control.

4.5.6 The diminished migration effect was not mediated by low secretion of MCP-1.

MCP-1 is a potent chemokine for recruiting macrophages [299]. ELISA and q-rtPCR results demonstrated that the MCP-1 secreted by adipocyte spheroids was decreased by the treatment of tunicamycin at the concentration of 5 μg/mL (**Figs 3.8a** and **3.8c**, **Chapter 3**). The possible mechanism underlying the diminished migration caused by tunicamycin was then further investigated. 24 h prior to placing Raw 264.7 cells in the trans-well inserts above the 5 adipocyte spheroids, culture medium maintaining adipocyte spheroids was replaced with FBS-free medium containing 90 nM of the CCR2 antagonist, INCB3344 (MCE HY-50674), or 2 μg/mL of the MCP-1 neutralising antibody (R&D MAB679), or both reagents. Then, Raw 264.7 cells were allowed to migrate in such medium or the control medium for another 24 h. No migration blocking effect was observed in the presence of MCP-1 neutralising antibody alone (**Fig 4.9**, Groups 1-3). A trend of blocking effect was shown in the presence of CCR2 antagonist (**Fig 4.9**, Groups 1-4), especially when

both the antagonist and the neutralising antibody were added (**Fig 4.9**, Groups 1-5), however the differences were insignificant.

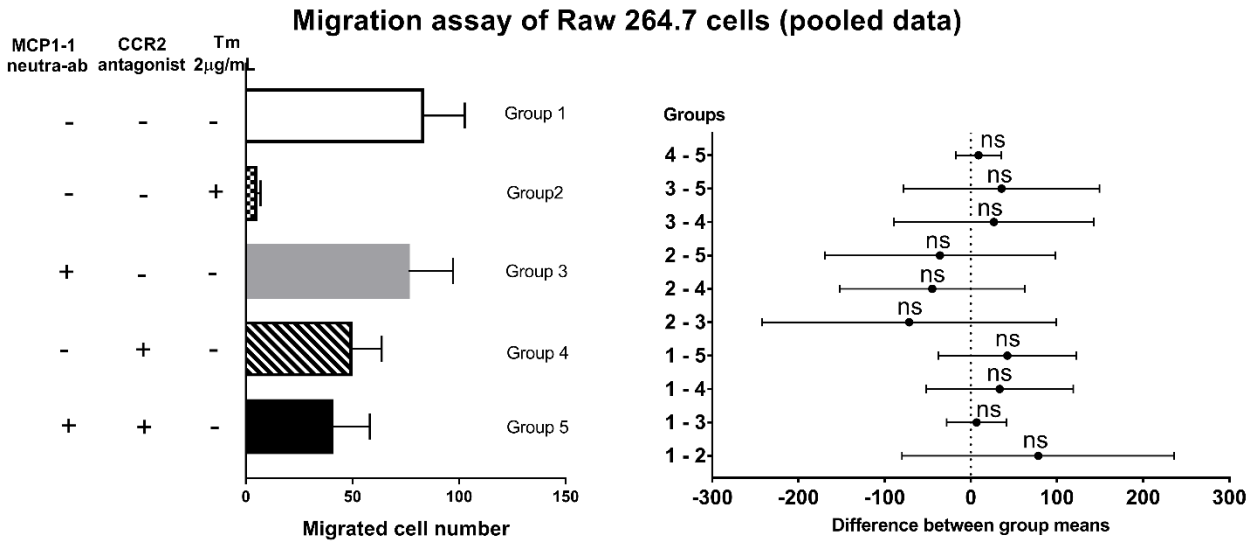

Fig 4.9 Low concentration of MCP-1 was not the major mechanism underlying the blocked migration effect mediated by tunicamycin.

Migration of Raw 264.7 cells towards the adipocyte spheroids was measured in the following microenvironment: Group 1, no treatment; Group 2, supplemented with 2 μg/mL of the tunicamycin (Tm); Group 3, supplemented with 2 μg/mL of the MCP-1 neutralising antibody (neutra-ab); Group 4, supplemented with 90 nM of the CCR2 antagonist, INCB3344; Group 5, supplemented with both MCP-1 neutralising antibody and CCR2 antagonist. The migration of Raw 264.7 cells was decreased dramatically when adipocyte spheroids was pre-treated with 2 μg/mL of Tm (Groups 1-2). No migration blocking effect was observed in the presence of MCP-1 neutralising antibody alone (Groups 1-3). However, a trend of blocking was shown in the presence of CCR2 antagonist (Groups 1-4), especially when both the antagonist and the neutralising antibody were added, with 95 % confidence intervals of the difference between group means being -37.5 to 122.5 (Groups 1-5). Data reflect 3 independent experiments including technique duplicates. ns, $p>0.05$, Tukey's multiple comparisons after the one-way repeated measures ANOVA. Error bars indicate estimated standard errors of the mean.

4.5.7 M1 and M2 macrophages exhibited distinct invasion capacity.

Similar to the result of Raw 264.7 cell migration, medium maintaining 5 adipocyte spheroids demonstrated a significantly stronger recruiting capacity for primary M2 macrophages compared with the control medium in the invasion assay. M1 macrophages did not invade through the Matrigel coated (250 μg/mL) trans-well inserts (**Figs 4.10a** and **4.10b**).

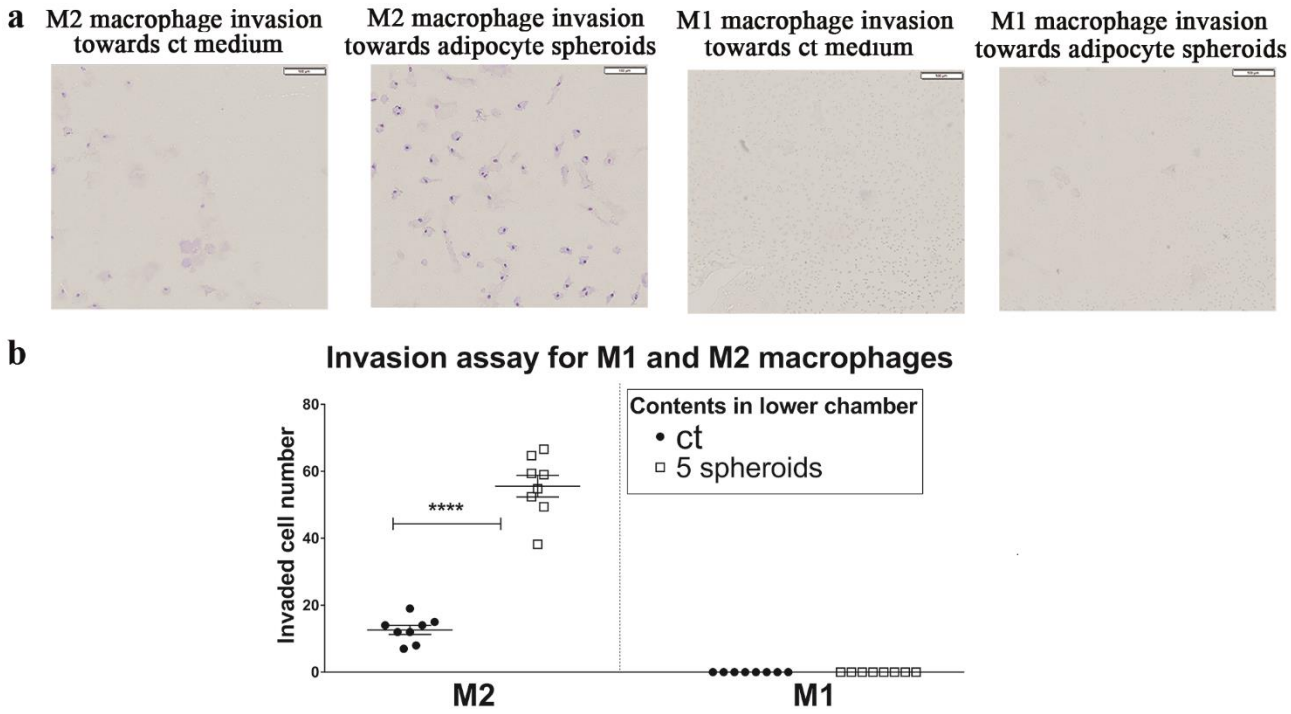

Fig 4.10 Distinct invasion capacity between M1 and M2 macrophages

a. M1 and M2 macrophages were seeded in the trans-well inserts (coated with Matrigel at 250 μg/mL), which were placed above the 5 adipocyte spheroids or above the control (ct) medium. Images of crystal violet-stained macrophages were photographed using the ×10 objective and cell number was quantified under the ×20 objective. Scale bars = 100 μm. **b**. Compared with the ct medium, a significant invasion for M2 macrophages was caused in the presence of adipocyte spheroids. However, M1 macrophages did not invade through the Matrigel coated trans-well inserts. Data were compiled from 2 independent experiments, with each experiment including 4 technique replicates. The square dots represent the number of invaded macrophages towards the medium maintaining 5 adipocyte spheroids; the circle dots represent the number of invaded macrophages towards the ct medium. ****<0.0001, unpaired t test. Error bars represent estimated standard deviation of the mean.

4.5.8 M1 and M2 macrophages exhibited distinct expression levels of integrin $\alpha_M\beta_2$.

Being one of the most important cell adhesive receptors, integrin $\alpha_M\beta_2$ (CD18/CD11b) is abundant on the macrophage surface, which shares many ligands with ECM [300]. To evaluate whether the distinct invasion capacity between M1 and M2 macrophages may be associated with the different expression level of integrin $\alpha_M\beta_2$, the expression of CD18 and CD11b was measured using flow cytometry analysis. M2 macrophages demonstrated higher expression levels of both CD18 and CD11b (**Fig 4.11**). Demographic information of patients has been summarised in **Table 4.2**.

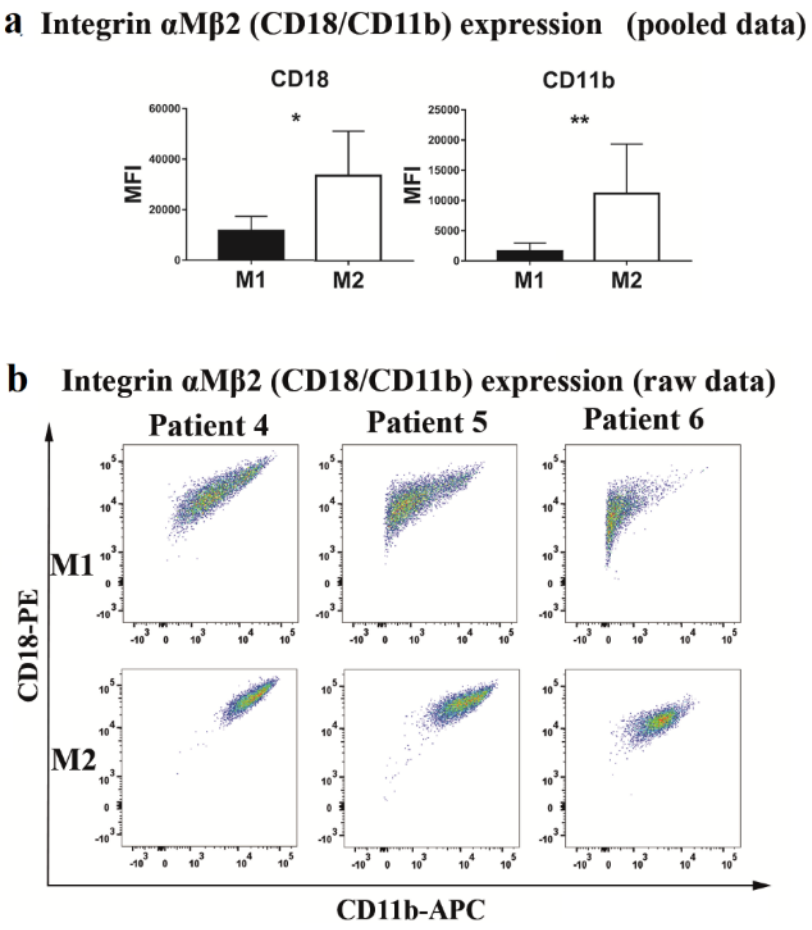

Fig 4.11 Distinct integrin expression levels between M1 and M2 macrophages

a. Results of mean fluorescence intensity (MFI) measured by flow cytometry analysis demonstrate that the expression of both CD18 and CD11b was significantly higher in M2 macrophages compared with M1 macrophages. *p<0.05, **p<0.01, ratio paired t test. Error bars represent estimated standard deviation of the mean. Data were pooled from 3 independent experiments, each of which was using peripheral blood mononuclear cells from a single participant. **b**. Compared with M1 macrophages, MFI of M2 macrophages demonstrates a positive shift along the CD18-axis and CD11b-axis for all samples in raw data.

Table 4.2 Characteristics of the study population

De-identified participant number	Date of birth	Sex	BMI (kg/m^2)	Diagnosis	Tumour size	Tumour grade	Tumour stage
Patient 4	16-Sep-1955	Male	27	ccRCC	38mm	2	3
Patient 5	15-June-1960	Male	42	ccRCC	90 mm	3	3
Patient 6	21-May-1963	Male	38	ccRCC	45mm	2	3

Tumours were staged according to the 7th TNM Classification of malignant tumours and graded according to the International Society for Urological Pathology (ISUP) grading system for renal cell carcinoma. Abbreviation: BMI, body mass index; ccRCC, clear cell renal cell carcinoma.

4.5.9 The presence of M1 macrophages inhibited the invasion capacity of cancer cells.

To evaluate whether the presence of different macrophages would influence the invasion capacity of cancer cells, the invasion was measured of KHOS osteosarcoma cancer cells (**Fig 4.12**) and 786-0 kidney cancer cells (**Fig 4.13**) towards the adipocyte spheroids or control medium when the cancer cells were co-cultured with different macrophage phenotypes. Adipocytes are important components in the bone marrow microenvironment [301]. The crosstalk between adipocytes and tumour cells may influence the bone metastasis of osteosarcoma [302]. Likewise, the spread of tumour cells into the perinephric adipose tissue is a marker of early metastasis for kidney cancer [303]. First, our data confirmed the results that M2 macrophages exhibited a significantly more active motility capacity through the Matrigel coated trans-well membrane when co-cultured with both KHOS (**Fig 4.12b**) and 786-0 cancer cells (**Fig 4.13b**). Excitingly, KHOS cancer cells exhibited significantly weaker invasion capacity in the presence of M1 macrophages. However, the presence of M2 macrophages did not significantly enhance or weaken the invasion capacity of cancer cells (**Figs 4.12a** and **4.12c**). Unexpectedly, the invasion capacity of 786-0 cancer cells did not show significant difference in the co-culture system in the presence of either M1 or M2 macrophages. However, 786-0 cancer cells exhibited significantly stronger invasion capacity when only cancer cells were placed above the adipocyte spheroids (**Figs 4.13a** and **4.13c**).

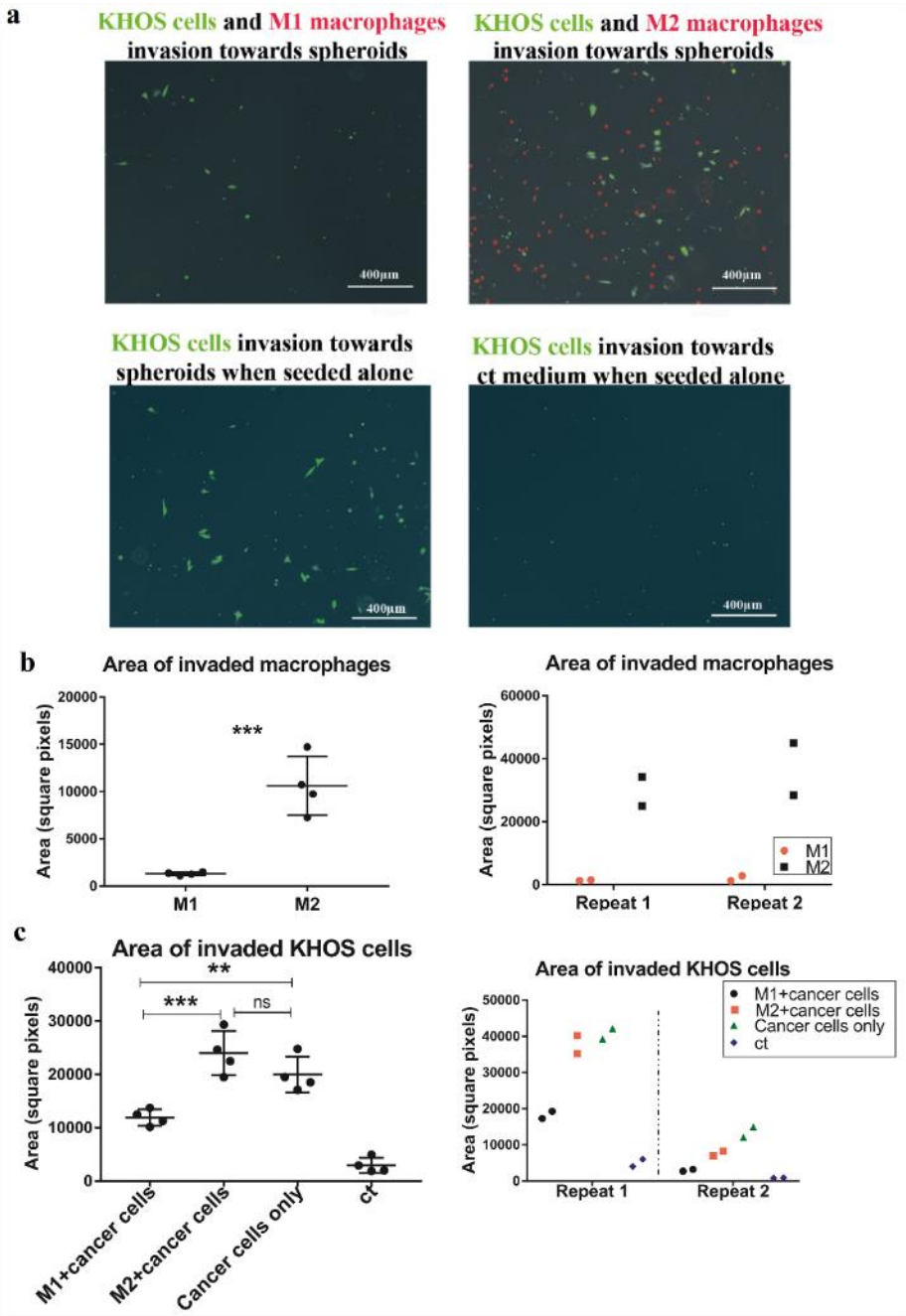

Fig 4.12 Invasion assay of KHOS cells in the co-culture system with or without macrophages

a. Images were acquired using the ×4 objective, by combining the GFP (green) and CY3 (red) channels. KHOS cells are green in colour. Macrophages (both M1 and M2) are red in colour. Scale bars = 400 μm. **b.** M1 macrophages exhibited a significantly weaker invasion capacity than M2 macrophages when co-cultured with KHOS cancer cells. ***p<0.001, unpaired t-test. **c.** In the presence of M1 macrophages, the area of the invaded KHOS cancer cells was significantly less than the invasion area when KHOS cancer cells were placed alone in the trans-well inserts. There were significantly more invading KHOS cancer cells when co-cultured with M2 macrophages than with M1 macrophages. **p<0.01, ***p<0.001, ns, p>0.05, post hoc testing after ordinary one-way ANOVA. Results were derived from a pilot experiment followed by two repeats (repeat 1 and 2). Each dot represents data from a single replicate. Error bars represent standard deviation. Abbreviation: ct, FBS-free DMEM-F12 control medium.

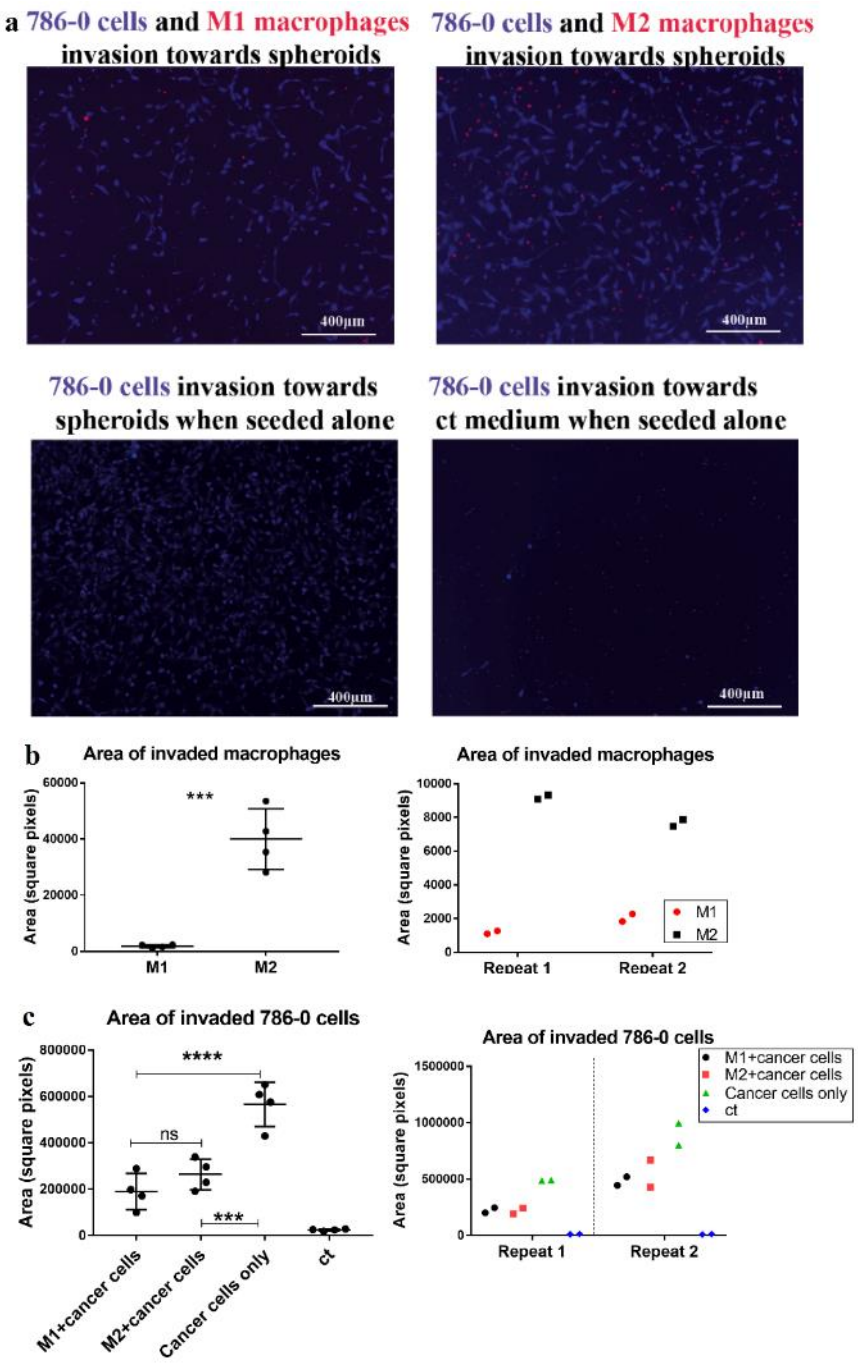

Fig 4.13 Invasion assay of 786-0 cells in the co-culture system with or without macrophages

a. Images were acquired using the ×4 objective, by combining the DAPI (blue) and CY3 (red) channels. 786-0 cells are blue in colour. Macrophages (both M1 and M2) are red in colour. Scale bars = 400 μm. **b.** M1 macrophages exhibited a significantly weaker invasion capacity than M2 macrophages when co-cultured with 786-0 cancer cells. ***p<0.001, unpaired t-test. **c**. 786-0 cancer cells exhibited significantly stronger invasion capacity when placed alone. No significant difference of invasive capacity was observed between 786-0 cancer cells co-cultured with M1 macrophages and 786-0 cancer cells co-cultured with M2 macrophages. ***p<0.001, ****p<0.0001, ns, p>0.05, post hoc testing after ordinary one-way ANOVA. Results were derived from a pilot experiment followed by two repeats (repeat 1 and 2). Each dot represents data from a single replicate. Error bars represent standard deviation. Abbreviation: ct, FBS-free DMEM-F12 control medium.

4.6 Discussion

To the best of our knowledge, this is the first study using the liquid overlay-based 3D culture technique to establish a co-culture system to study the macrophage behaviour in the human adipose tissue microenvironment. It was found that the adipocyte spheroids caused an MCP-1 independent, but CCR2 dependent migration of Raw 264.7 cells, which could be blocked by the ER stress inducer, tunicamycin. Co-culture with the adipocyte spheroids shifted the unpolarised M0 macrophages into an M2 phenotype, as demonstrated by an upregulation of CD163 and CD209. Of note, M1 and M2 macrophages demonstrated distinct invasion capacity with only M2 macrophages invading through the Matrigel-coated trans-well membrane towards the adipocyte spheroids. In addition, M2 macrophages expressed a higher level of integrin $\alpha_M\beta_2$ (CD11b/CD18) than M1 macrophages, indicating the different expression level of integrin $\alpha_M\beta_2$ may be associated with the distinct invasion capacity between M1 and M2 macrophages. Both M1 and M2 macrophages suppressed the invasion of kidney cancer 786-0 cells in the trans-well assay. However, only the presence of M1 macrophages suppressed the invasion of osteosarcoma KHOS cells. The variation suggests the effects of TAM on metastases may be dependent on certain tumour microenvironment.

Widely applied as a monocyte/macrophage migration inducer in experiments, MCP-1 (also known as CCL2) is a well-known chemoattractant for monocytes and macrophages. Administration of NOX-E36 (an MCP-1 neutralising reagent) alleviated proteinuria and restored glomerular endothelial integrity in a diabetic nephropathy mouse model, however did not interfere with the absolute macrophage number in the nephron [304]. Coincidently, supplementation with MCP-1 neutralising antibody at the concentration of 2 µg/mL did not ablate or attenuate the migration of Raw 264.7 cells in this present study. It was recommended by the manufacturer that 0.5-2 µg/mL of the neutralising antibody can block 75 ng/mL of MCP-1 which was far beyond the concentration (approximately 2 ng/mL) measured in the supernatant maintaining 5 adipocyte spheroids for 24 h. The blocked macrophage migratory effect potentially caused by totally or partially neutralising MCP-1 may be compensated by other chemokines secreted by the mature adipocyte spheroids, such as IL-8, CCL7, CCL8, CCL10, CCL13, CCL19, CCL21 [305]. Hence, the interfered MCP-1 secretion induced by tunicamycin must not be the major mechanism underlying the blocked macrophage migration effect observed in the study. Except for being the MCP-1 receptor, CCR2 can also bind to CCL7 and CCL12 in mice [306]. This may be an explanation for the nearly significant migration-suppressing effect for Raw 264.7 cells mediated by the CCR2 antagonist. The N-glycosylation of CCR2 is functionally important for ligand binding and chemotaxis, indicating the diminished migration effect might be linked with an impaired post-translational modification of CCR2 mediated by tunicamycin [307].

Blocking MCP-1 in the culture medium did not interfere with the recruitment of Raw264.7 cells. Conversely, the migration of this immortalised macrophage cell line was diminished in the presence of the ER stress inducer, tunicamycin. The cell count assay (**Table 4.1** and **Fig 4.8**) demonstrated that the cell number of Raw264.7 cells treated by 5 μg/mL tunicamycin was lower than Raw264.7 cells treated with tunicamycin at a concentration of 2 μg/mL (1.35×10^5/mL vs 2.23×10^5/mL). Even though showing such a different impact on cell proliferation, the migration blocking effect induced by tunicamycin at these two concentrations was very similar (**Fig 4.9**). Hence, the result was interpreted as a blocking effect that might be ER stress relevant. It would be very interesting to compare the result using PBMC derived macrophages and this could be a future direction of the study.

This study reconfirmed the finding that the normal adipose tissue microenvironment favours the M2 phenotype shift of macrophages, using both macrophages and adipocytes isolated from human samples. The mechanism is related to the activation of the full length adiponectin-IL-4-signal transducer and activator of transcription 6 (STAT 6) signaling pathway, which supports the high demand of glucose oxidation for M2 macrophages [308, 309]. Since a negative association between ER stress level and kidney cancer metastatic rate was found previously and M2 macrophages in the tumour microenvironment may facilitate metastasis [293, 298], we hypothesised that tunicamycin could induce the M1 phenotype skew for M2 macrophages. However, neither an upregulation of M1 markers nor a downregulation of M2 markers was observed in M2 macrophages upon tunicamycin treatment, indicating ER stress and macrophage polarisation may not be directly linked in the setting of cancer metastasis.

The distinct invasion capacity between M1 and M2 human macrophages that we observed resembles that reported by Cui *et al.* where the distinct invasion capacity between M1 and M2 mouse macrophages and relevant mechanisms were systematically investigated both *in vitro* and *in vivo* [310]. Unlike an upregulated protein level of integrin $\alpha_M\beta_2$ being observed in M2 human macrophages in our study, the integrin $\alpha_M\beta_2$ gene expression was reported to be lower in M2 than M1 mouse macrophages. However, the M2 macrophage motility promoting role of integrin $\alpha_M\beta_2$ demonstrated in their publication was consistent with our finding because the knock-down of integrin $\alpha_M\beta_2$ inhibited the migration of M2 macrophages. Of note, Cui *et al.* discovered that the integrin α_D deficiency decreased the recruitment of M1 macrophages in inflamed mouse adipose tissue and improved insulin sensitivity and glucose tolerance. It will be important in future studies to evaluate the expression and function of integrin α_D in human macrophages, which may provide a novel treatment for diabetes.

The pro-metastatic role of M2 macrophages is partially ascribed to pro-angiogenic signaling pathways activated under a tumour-associated hypoxic microenvironment, which has been extensively reviewed [311]. Live imaging of tumour cell intravasation using animal models has also

confirmed that the motility of tumour cells occurred in close proximity to perivascular macrophages in the tumours [312]. Hence, we hypothesised that more cancer cells could invade through the Matrigel-coated trans-well membrane accompanied by M2 macrophages, considering the distinct invasion capacity between M1 and M2 macrophages observed in our study. Surprisingly, increased invasion of KHOS osteosarcoma cancer cells was observed in the presence of M2 macrophages compared with M1 macrophages. It would be questionable to conclude here that M2 macrophages facilitate the invasion of KHOS cells without comparing the invasion of KHOS cells in the absence of M2 macrophages. However, no significant difference was shown in this comparison. Unexpectedly, the greatest invasive capacity for kidney cancer 786-0 cells was shown when the cancer cell itself was placed in the top of the trans-well membrane, with no significant difference of invaded cancer cell number observed between the presence of M1 and M2 macrophages. The only common finding from these results is that M1 macrophages inhibit the invasion of cancer cells, however it is uncertain whether the mechanism is related to direct interaction or paracrine effects. Monitoring the metastasis-preventing effect by reprogramming tumour resident macrophage phenotypes using *in vivo* models is a future endeavour.

4.7 Conclusion

Overall, these findings expand our understanding about how the adipose tissue microenvironment (healthy or stressed) may influence macrophage polarisation and migration/invasion *in vitro*. An understanding of how ER stress interferes with macrophage filtration and how the interaction of M1 macrophages with cancer cells affects tumour invasion will be essential for targeting macrophages in preventing cancer metastasis.

Chapter 5

Macrophage profiling in perinephric adipose tissue using multiplex immunofluorescence and digital analysis approaches

5.1 Included publications

This chapter included contents from an original research article published in the journal of *Biochemical and Biophysical Research Communications*.

Shen K, Vesey DA, Hasnain SZ, Zhao KN, Wang H, Saunders N, Burgess M, Johnson DW, Gobe GC. A cost-effective three-dimensional culture platform functionally mimics the adipose tissue microenvironment surrounding the kidney. BBRC. 2020; 522 (3):736-742. https://doi.org/10.1016/j.bbrc.2019.11.119

The candidate was the lead author of this original research article. She contributed significantly to the conception and design of this study (80 %) and analysis and interpretation of the literature (70 %), and drafted the majority of the manuscript (90 %).

5.2 Overview

Quantitative image analysis using multiplex IHC is an important tool to identify the association between tissue-specific immune profiles and cancer aggressiveness. It was previously reported that the M2 phenotype skew for macrophages in breast cancer-associated adipose tissue predicted poor cancer prognosis. However, macrophage phenotypes and relevant prognostic value in human perinephric adipose tissue have never been reported in the setting of kidney cancer. **Chapter 5** aimed to characterise the macrophage-associated immune profiles in perinephric adipose tissue and to explore the potential prognostic value of macrophage phenotypes in predicting distant metastases in ccRCC. A multiplex immunofluorescence panel was established to label the expression of macrophage phenotype markers, including CD163, CD206 and CD68, in archived FFPE human perinephric adipose tissue. Simultaneous detection of the three CD markers in the same tissue sample was processed using Vectra III multispectral microscopy and Inform 2.2.1 image analysis software. Compared to the perinephric adipose tissue derived from participants diagnosed with non-metastatic ccRCC and oncocytoma, the perinephric adipose tissue samples from metastatic ccRCC, considered the most aggressive of these groups, exhibited the highest expression of CD163 and CD206, which are commonly used M2 macrophage markers.

5.3 Introduction

Orchestrated within the tumour microenvironment, TAM exert protumoural functions through inhibiting anti-tumour immunity, assisting angiogenesis and promoting metastasis (**Fig 1.5, Chapter 1**). The protumoural functions of TAM have been demonstrated in an increasing number of clinical trials that found a positive correlation between high expression of M2 macrophages in tumour tissue and poor cancer prognosis (**Table 1.2, Chapter 1**). Adipose tissue is also an important depository of macrophages, with the proportion of macrophages increasing when obesity exists [313]. Obesity-associated macrophage infiltration in adipose tissue is believed to contribute to increased risk of tumourigenesis through activating proinflammatory signaling pathways [1], although in the case of kidney cancer, this association has not been proven. There is some evidence that obesity-associated adipose tissue macrophages contribute to the stem-like properties of cancer cells, and thereby have a protumoural role [229]. The macrophage-associated immune phenotypes in adipose tissue may also be linked with cancer prognosis. For example, an M2 phenotype skew for macrophages was observed in mice within the tumour-associated adipose tissue experiencing changes of lipid metabolism, which were favourable for cancer cell development [150]. Relevant research in humans is limited to the field of breast cancer with findings supporting that high M2 macrophage expression in adipose stroma of breast tumours predicted poor cancer prognosis [210, 211]. As discussed previously, perinephric adipose tissue which is easily obtained after radical nephrectomy is an important but often ignored tumour-associated adipose tissue for kidney cancer [257]. Investigating the macrophage phenotypes in perinephric adipose tissue may help better understand roles of the heterogeneous adipose tissue in kidney cancer progression. The macrophage phenotypes may be identified using several CD antibodies, described in the following paragraphs.

CD68 antibody has been widely used for identifying macrophages in the field of tumour microenvironment (**Table 1.2**, **Chapter 1**). CD68 is mainly expressed on the lysosomal membrane, with a small proportion of CD68 present on the cell membrane [314]. However, the belief that CD68 positivity is indicative of phagocytosis rather than a specific marker for macrophages suggests that the current use of CD68 to identify circulating and tissue macrophages may be incorrect [315]. The new paradigm for use of CD68 to identify cellular function, rather than simply macrophage presence, is based on observations that CD68 antibodies have cross-reactions with fibroblasts and endothelial cells [316], and muscle cells phagocytosing lipids were CD68 positive [317].

CD163 is predominately used as an M2 macrophage marker whose upregulation is associated with an unfavourable cancer prognosis (**Table 1.2, Chapter 1**). The transmembrane CD163 protein is a transmembrane scavenger receptor for haptoglobin-haemoglobin complexes. These complexes are mainly expressed on, but not limited to, monocytes and macrophages [318]. For example, a

significant portion of malignant bladder cancer cells is known to express CD163 [319]. CD163 expressed on tissue-resident macrophages can recognise bacteria, therefore maintaining tissue homeostasis by innate immunity [320]. CD163 expression was also found to be upregulated upon stimulation of IL-4 and IL-13 in *in vitro* studies mimicking the M2-polarisation of macrophages (**Fig 4.4, Chapter 4**). CD163-heme oxygenase-1 (HO-1) signaling is crucial for protecting against inflammatory injury by upregulating the anti-inflammatory cytokine IL-10 upon LPS stimulus [321].

Consistent with CD163, expression of CD206 was upregulated in monocyte-derived macrophages after exposure to IL-4 and IL-13 (**Fig 4.4, Chapter 4**). The transmembrane pattern recognition protein CD206, also known as mannose receptor, is primarily expressed on macrophages and immature dendritic cells [322, 323]. As an M2 macrophage marker, the poor prognostic value of CD206 was reported in ccRCC tumour tissue [217]. It was also reported that CD206-positive macrophages may be located tightly bound to the endothelial cells of capillaries, providing VEGF to endothelial cells and therefore promoting tumour growth [324].

Simultaneous detection of multiple epitopes in the same tissue section, known as multiplex IHC, has become a powerful tool in exploring the complex tumour microenvironment [325]. The technique enables detection of multiple markers using fewer samples without disrupting the tissue integrity. Compared to an image labelled with only one epitope, multiplexed images contain more useful information, such as colocalisation of markers, and distribution of markers relative to one another. When imaging multiplex immunofluorescent staining, each fluorophore-labelled target of interest is excited by one pre-setting wavelength. The emitted fluorescence only goes through one filter in the imaging collecting instrument [326]. The spectral unmixing for multiplex immunofluorescence is therefore more accurate than the colour deconvolution tool which is applied in analysing brightfield chromogen IHC. Development of the tyramide signal amplification (TSA) technique promotes the widespread application of multiplex immunofluorescent detection. TSA is an enzyme-mediated detection method that utilises the catalytic activity of horseradish peroxidase (HRP) which is conjugated to the secondary antibody [327]. Briefly, the fluorophore-labelled tyramide derivatives are converted to an active form that covalently binds to protein residues when H_2O_2 is catalysed by HRP. The tyramine-fluorophore is therefore deposited in proximity to the sites of epitope-antibody interactions. However, the primary and secondary antibodies are washed away prior to the next round of staining. Hence, use of TSA technique overcomes the limitation of choosing secondary antibodies from distinct animal species, which also must be linked with different signal reporters.

In this chapter, a multiplex immunofluorescence panel was optimised to detect simultaneously the expression of CD68, CD163 and CD206 in the archived FFPE human perinephric adipose tissue from ccRCC patients. Three pixel-based algorithms, based on either individually optimised thresholding

or consistent maximal and minimal thresholding, were applied to quantify the expression of the CD markers across the whole image and in the segmented cytoplasm compartment. The possible association of macrophage phenotypes and kidney cancer aggressiveness, in particular with regard to distant metastasis of ccRCC, was explored.

5.4 Methods

5.4.1 Study participants

This study received ethics approval from the Metro South Human Research Ethics Committee (HREC/05/QPAH/95; HREC/16/QPAH/353) and utilised archived FFPE perinephric adipose tissue from consenting patients who underwent nephrectomy for renal tumours at the Princess Alexandra Hospital, Brisbane, Australia between June 2013 and September 2017 [236]. Inclusion criteria for the cohort of metastasis are, 1) diagnosis of ccRCC; 2) availability of perinephric adipose tissue with quality suitable for immunofluorescent staining; 3) presence of distant metastasis. The cohort of non-metastasis was established by matching the cohort of metastasis for BMI in the range of 25 to 30 kg/m^2. Moreover, the cohorts of metastasis and non-metastasis were matched as much as possible for gender, age, tumour stage and tumour grade. It was unaccepted in the matching procedure if any participant in the cohort of metastasis was older or diagnosed with more aggressive ccRCC compared to the matched counterpart when the perfect matching was impossible. Participants diagnosed with oncocytoma having available fat tissue constituted the third cohort. A flow chart of participation is displayed in **Fig 5.1**.

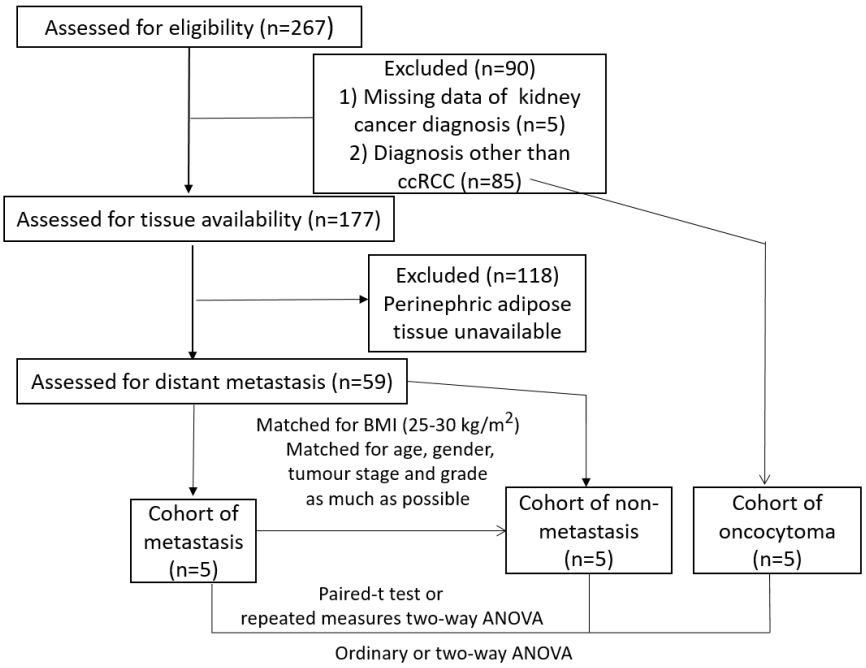

Fig 5.1 Flow chart of participation in the study

Five participants constituted the cohort of metastasis. Another 5 participants who matched for BMI, and matched as much as possible for age, gender, tumour stage and tumour grade, constituted the cohort of non-metastasis. The two cohorts were included in the paired-t test or repeated measures two-way ANOVA; The ccRCC cohorts of metastasis and non-metastasis, and another oncocytoma cohort were included in the ordinary or two-way ANOVA. Abbreviation: ANOVA, analysis of variance; BMI, body mass index; ccRCC, clear cell renal cell carcinoma.

5.4.2 Antibody optimisation

All staining work in this chapter was processed by the core Histology facility at the Translational Research Institute. The perinephric adipose tissue was sequentially stained with 3 primary antibodies. The antibodies were CD163 (clone EDHu-1 mouse monoclonal antibody/mAb, BIO-RAD MCA1853T), CD206 (rabbit polyclonal antibody/pAb, Abcam Ab64693) and CD68 antibody (clone KP1 mouse mAb, Abcam ab955). Antibody-fluorophore pairs were determined based on staining intensities of fluorophores and expression levels of respective antigens. The pairs were: CD163-Rhodamine 6G, CD206-Alexa Fluor 610 and CD68-CY5. The appropriate sequence of applying the primary antibodies in multiplex staining was determined through optimisation trials to make sure the antibody applied earlier was easier to be fully removed than that applied later. Titration of the primary antibody, the incubation time of the secondary antibody and TSA reagent were determined in uniplex DAB IHC (**Fig 5.2**) followed by uniplex immunofluorescent staining to achieve a balance between specific staining patterns and minimised bleed-through. The staining pattern in uniplex immunofluorescent staining is displayed in **Figs 5.3, 5.4 and 5.5.**

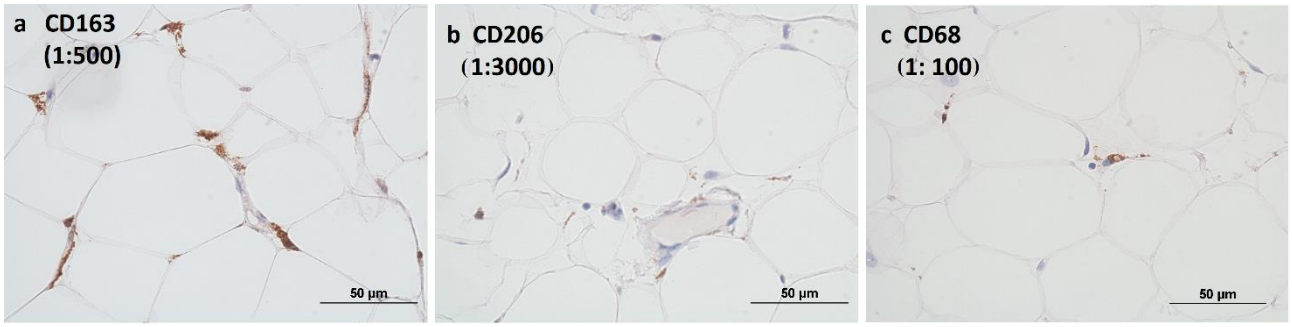

Fig 5.2 DAB staining pattern of the antigens in perinephric adipose tissue

Images were captured at x40 using the Nikon Brightfield microscope. Scale bars = 50 µm. Sub-serial sections from the same block were stained with the CD163 antibody at the dilution ratio of 1:500 (**a**) or stained with the CD206 antibody (1:3000) (**b**) or stained with the CD68 antibody (1:100) (**c**) using Ventana autostainer with Biocare Medical MACH1 Universal Polymer Detection reagents. The expression of CD163 was the most abundant among all three antigens, whereas the staining pattern of CD68 was sporadic.

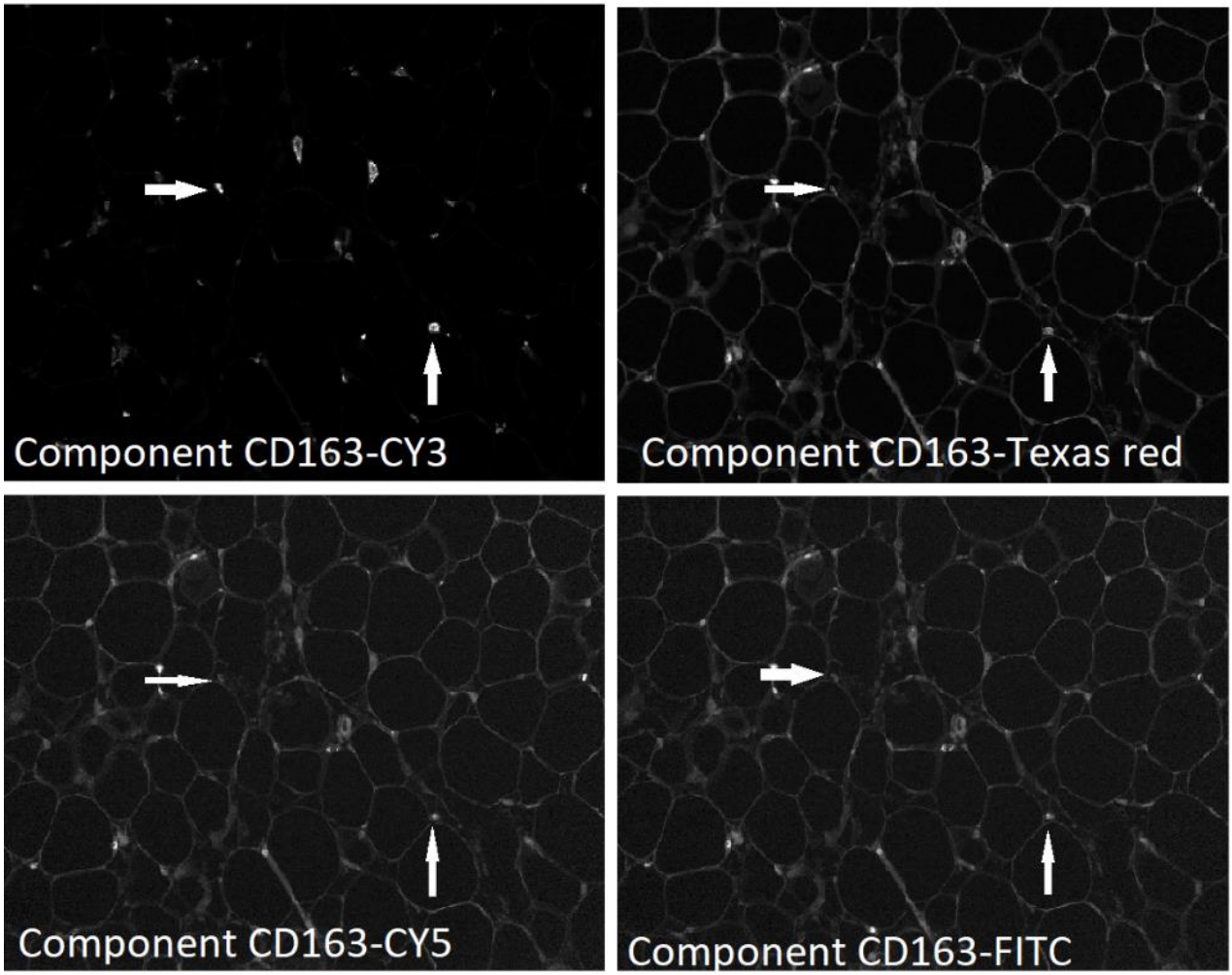

Fig 5.3 Unmixed spectral images of the perinephric adipose tissue stained with CD163 antibody

The slide was incubated with the CD163 antibody (1:500) and scanned with Vectra III multispectral microscopy at ×20 objective (exposure time: 100 ms). Spectra were unmixed using the InForm 2.21 software. Specific staining patterns (bright staining in cell membrane and cytoplasm) of CD163, shown in the channel of cyanine (CY) 3, are labelled with white arrows (upper left). The two arrows are placed in the same location in the Texas Red-spectral unmixed image (upper right), CY5-spectral unmixed image (bottom left) and FITC-spectral unmixed image (bottom right). The distinct fluorescent pattern between the CY3-spectral unmixed image and FITC-spectral unmixed image demonstrated that the fluorescence appearing in the CY3 channel was real staining for CD163 rather than autofluorescence. The disappearance of the CD163-specific staining pattern in Texas Red and CY5-spectral unmixed images demonstrated the CD163 fluorescence labelling did not appear in neighbouring channels.

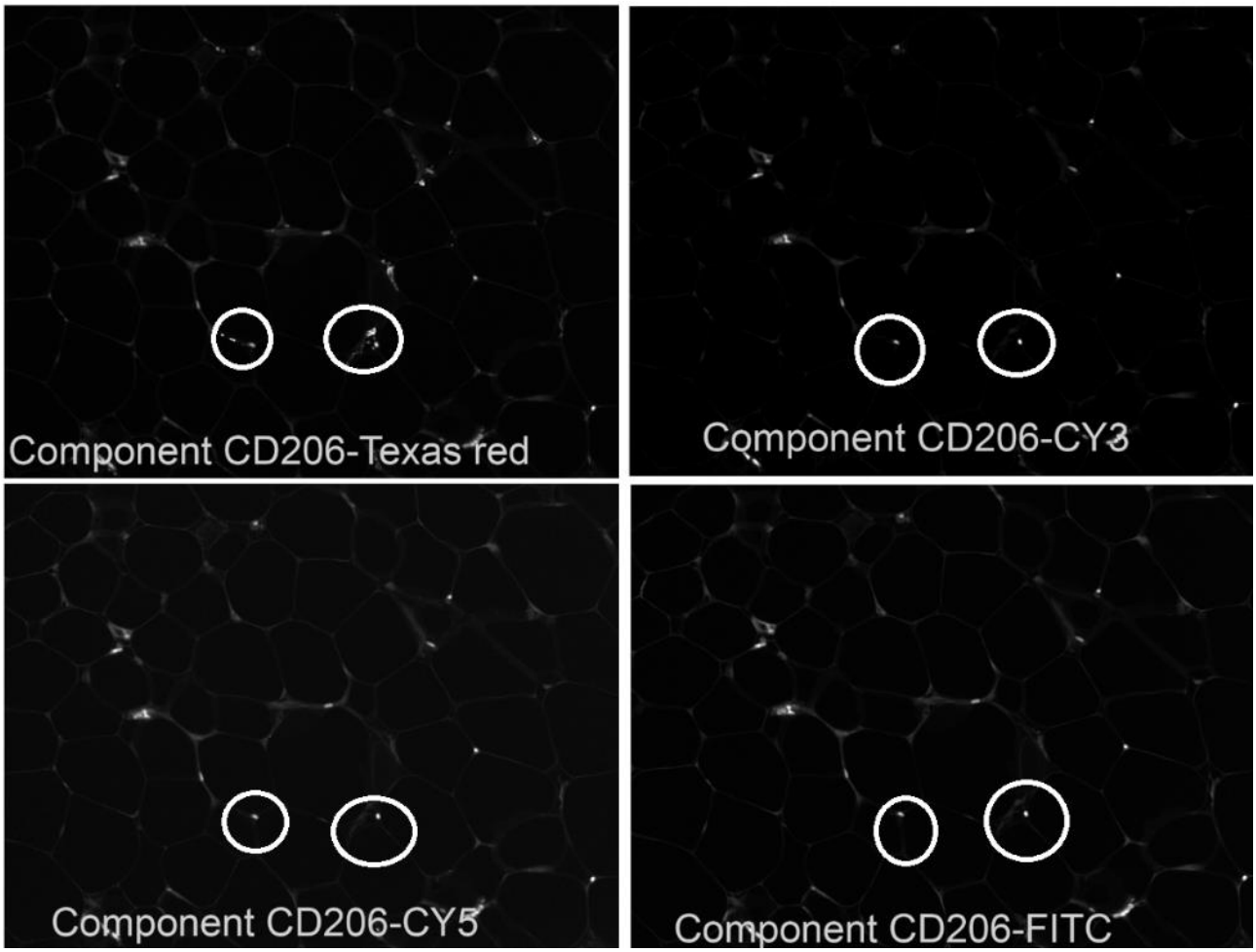

Fig 5.4 Unmixed spectral images of the perinephric adipose tissue stained with CD206 antibody

The slide was incubated with the CD206 antibody (1:3000) and scanned with Vectra III multispectral microscopy at ×20 objective (exposure time: 150 ms). Spectra were unmixed using the InForm 2.21 software. Specific staining patterns (bright tiny dots along the adipocyte cell boarders or filled in the space between adipocytes) of CD206, shown in the channel of Texas Red, are labelled with white circles (upper left). The two circles are placed in the same location in cyanine (CY) 3-spectral unmixed image (upper right), CY5-spectral unmixed image (bottom left) and FITC-spectral unmixed image (bottom right). The distinct fluorescent pattern between the Texas Red-spectral unmixed image and FITC-spectral unmixed image demonstrated the fluorescence appeared in the Texas Red channel was real staining for CD206 rather than autofluorescence. The disappearance of the CD206-specific staining pattern in CY3 and CY5-spectral unmixed images demonstrated the CD206 fluorescence labelling did not appear in neighbouring channels.

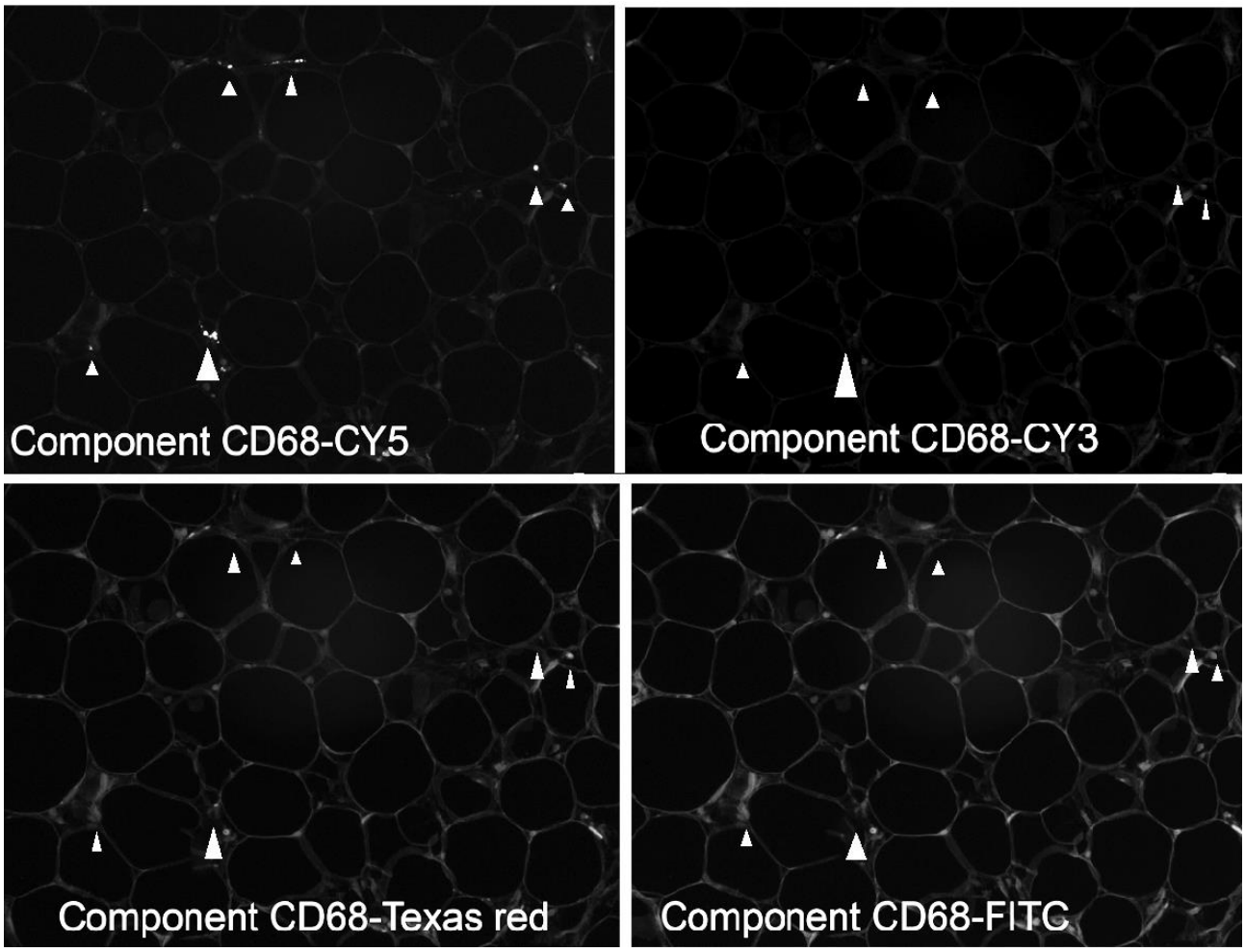

Fig 5.5 Unmixed spectral images of the perinephric adipose tissue stained with CD68 antibody

The slide was incubated with the CD68 antibody (1:100) and scanned with Vectra III multispectral microscopy at ×20 objective (exposure time: 250 ms). Spectra were unmixed using the InForm 2.21 software. Specific staining patterns (sporadic bright dots) of CD68, shown in the channel of cyanine (CY) 5, are labelled with a white arrow heads (upper left). The arrow heads are placed in the same location in CY3-spectral unmixed image (upper right), Texas Red-spectral unmixed image (bottom left) and FITC-spectral unmixed image (bottom right). The distinct fluorescence pattern between the CY5-spectral unmixed image and FITC-spectral unmixed image demonstrated that the fluorescence appearing in the CY5 channel was real staining for CD68 rather than autofluorescence. The disappearance of the CD68-specific staining pattern in CY3 and Texas Red-spectral unmixed images demonstrated that the fluorescence labelling CD68 did not appear in neighbouring channels.

5.4.3 Multiplex immunofluorescent staining

Sections of 4 μm thickness were cut onto Superfrost Plus slides. The multiplex immunofluorescent staining on fresh sections was completed with the Ventana Discovery Ultra autostainer (Leica Instruments, Arizona, USA). To minimise the variability of antibody titres, all slides were processed at the same time. Antigen retrieval was performed on the deparaffinised slides with Cell Conditioning

1 solution (Ventana Medical system 950-124) for 64 min at 95 °C. All slides were first blocked with Discovery Inhibitor (Roche 760-4840) for 8 min. The CD163 primary antibody was applied first at a 1:500 dilution, incubated at 36 °C for 40 min, and visualised with the Discovery Rhodamine 6G kit (Roche 760-244). The secondary antibody (Discovery OmniMap anti-mouse HRP, Ventana Medical systems 760-4310) incubation time was 4 min; TSA reagent incubation time was 8 min. Antibody denaturation was performed with Cell Conditioning 2 solution (Ventana Medical Systems 950-123) for 24 min at 100 °C. Next, the CD206 antibody was applied at a 1:3000 dilution, incubated at 36 °C for 32 min, and visualised with the Discovery Red 610 Kit (Roche 760-245). The secondary antibody (Discovery OmniMap anti-rabbit HRP, Ventana Medical Systems 760-4311) had an incubation time of 4 min; the TSA reagent incubation time was 8 min. Antibody denaturation was again performed with the Cell Conditioning 2 solution for 24 min at 100 °C. Lastly, the CD68 antibody was applied at a 1:100 dilution, incubated at 36 °C for 40 min, and visualised with the Discovery CY5 kit (Roche 760-238). The incubation time for the secondary antibody (Ventana Medical Systems 760-4310) was 16 min; the TSA reagent incubation time was 8 min. The slides were then counterstained with Discovery DAPI (Roche 760-4196), and cover-slipped with Prolong Gold anti-fade reagent (Invitrogen P36930). The invasive edge of human ccRCC FFPE tumour tissue was used as positive control (**Fig 5.6a**) [217, 328]. An example of the perinephric adipose tissue stained with the three primary antibodies is displayed in **Fig 5.6b**. Perinephric adipose tissue without primary antibody, secondary antibody, detection reagents and DAPI, but treated identically to the multiplex staining in terms of steps of antigen retrieval and heat stripping was used as a negative control (**Fig 5.6c**). Perinephric adipose tissue without primary antibody but treated identically to the multiplex staining was used as another negative control (**Fig 5.6d**).

5.4.4 Imaging of fluorescent slides

Upon completion of the multiplex immunofluorescent staining, stained slides were all scanned in one batch using the Vectra III multispectral microscope (PerkinElmer) according to the instructions provided by the manufacturer [329]. The bands of cyanine (CY) 3, CY5, Texas Red and DAPI (used for auto-focusing setting) were chosen to create the protocol of imaging the multispectral fluorescent images. CY3 is closely neighbouring to Rhodamine 6G (the fluorophore used to visualise CD163); Texas Red is closely neighbouring to Alexa Fluo 610 (the fluorophore used to visualise CD206). Hence, the two filters of CY3 and Texas Red were chosen to filter the fluorescent signals of CD163 and CD206, respectively. The exposure time was also optimised and kept consistent over imaging. Images of analysis were sampled from five individual fields randomly chosen on the slide at the ×20 objective. The spectral unmixing of the obtained images (IM3 files) was then processed in the InForm 2.2.1 software. The fluorescence data in each channel were extracted by loading the spectral library

"CY3, CY5, Texas red, DAPI and autofluoresence" (**Fig 5.7**). The autofluorescence spectrum was extracted from a representative unstained sample. After assigning each fluorophore with a specific colour, the multiplexed image was created by combining the individual unmixed images. The fluorescence spectral view of the fluorophores (mentioned above) is displayed in **Appendix 6**.

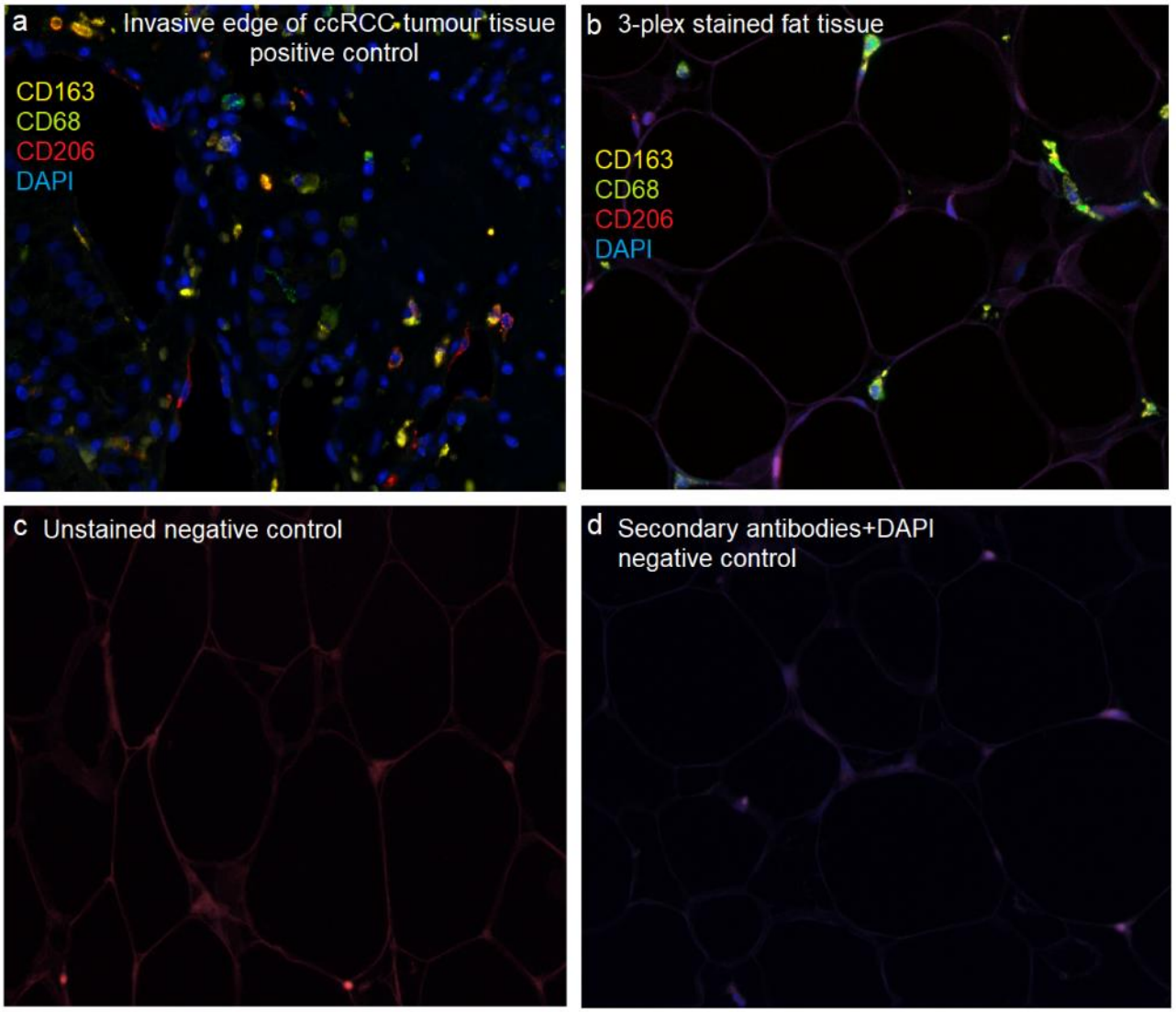

Fig 5.6 Examples of positive control, experimental sample and negative controls

Images were scanned with Vectra III multispectral microscopy at ×20 objective**.** CD163 positive pixels are yellow (exposure time: 100 ms); CD68 positive pixels are green (exposure time: 250 ms); CD206 positive pixels are red (exposure time 150 ms). DAPI-stained nuclei are blue (exposure time: 100 ms). **a** The invasive edge of ccRCC tumour tissue known to express CD163, CD206 and CD68 is positive for all three markers, indicating the staining procedure was working. **b** A representative multiplexed image of the perinephric adipose tissue (experimental sample) which was co-stained with CD163, CD206, CD68 and nuclei is displayed. **c** The non-stained negative control demonstrated there was no CD marker-specific staining caused by the adipose tissue-specific autofluorescence. **d** The negative control without primary antibody demonstrated there was no CD marker-specific staining caused by the secondary antibodies or the detection system.

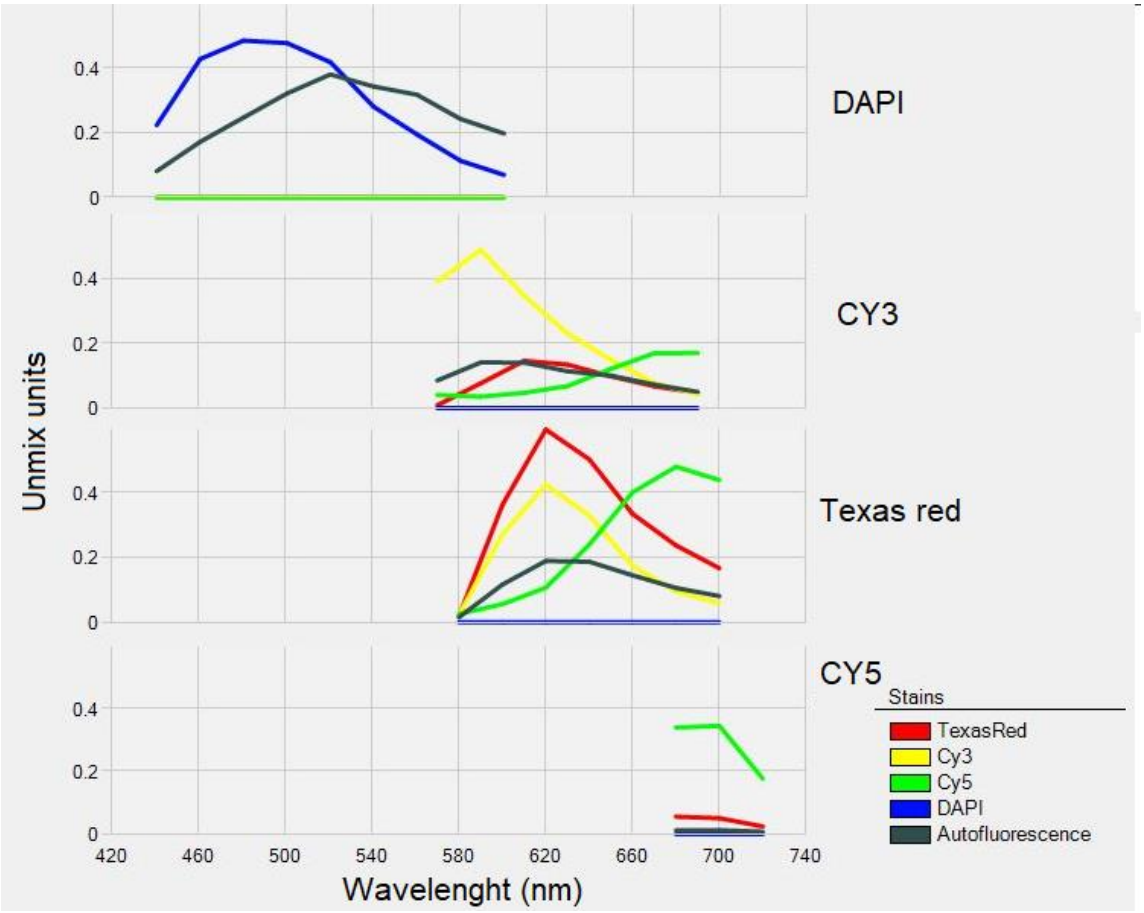

Fig 5.7 Spectral library loaded for spectral unmixing

The spectral segments DAPI, CY3, CY5, Texas Red and autofluorescence had good separation within each of the imaging bands. The Y axis was scaled to the same value, which was the maximal signal value in all of the bands. Abbreviation: CY, cyanine

5.4.5 Image analysis

The expression of each individual CD marker was quantified using the colocalisation and segmentation tool inbuilt in the InForm 2.2.1 image analysis software. The data collecting process was undertaken in a blinded manner by asking a colleague to finish patient de-identification by recoding the images.

5.4.5.1 Colocalisation analysis

Colocalisation is a pixel-based analysis for quantifying percentage of the overlapping components across an image based on the threshold setting for each component [330]. The spectra were chosen based on the colocalisation of interest. The unmixed component in an image was visually thresholded in a greyscale view to generate a binary mask to resemble the specific staining pattern**.** The masked area showing the pattern of autofluorescence was selected as a region of disinterest and excluded from the analysis (**Fig 5.8)**. Except for percentage of colocalised pixels, mean intensity of a

component across the whole image and total intensity of a component in the segmented area were also exported. Upon data collection based on an individual threshold setting, homogeneous maximal and minimal threshold settings were applied to all images again to collect data of the variables mentioned previously. The lower limits of the minimal and maximal thresholds were summarised from the individually-optimised thresholds of all samples (**Table 5.1**). The upper limit was set to be "10" which was beyond the intensity of the brightest pixel that appeared.

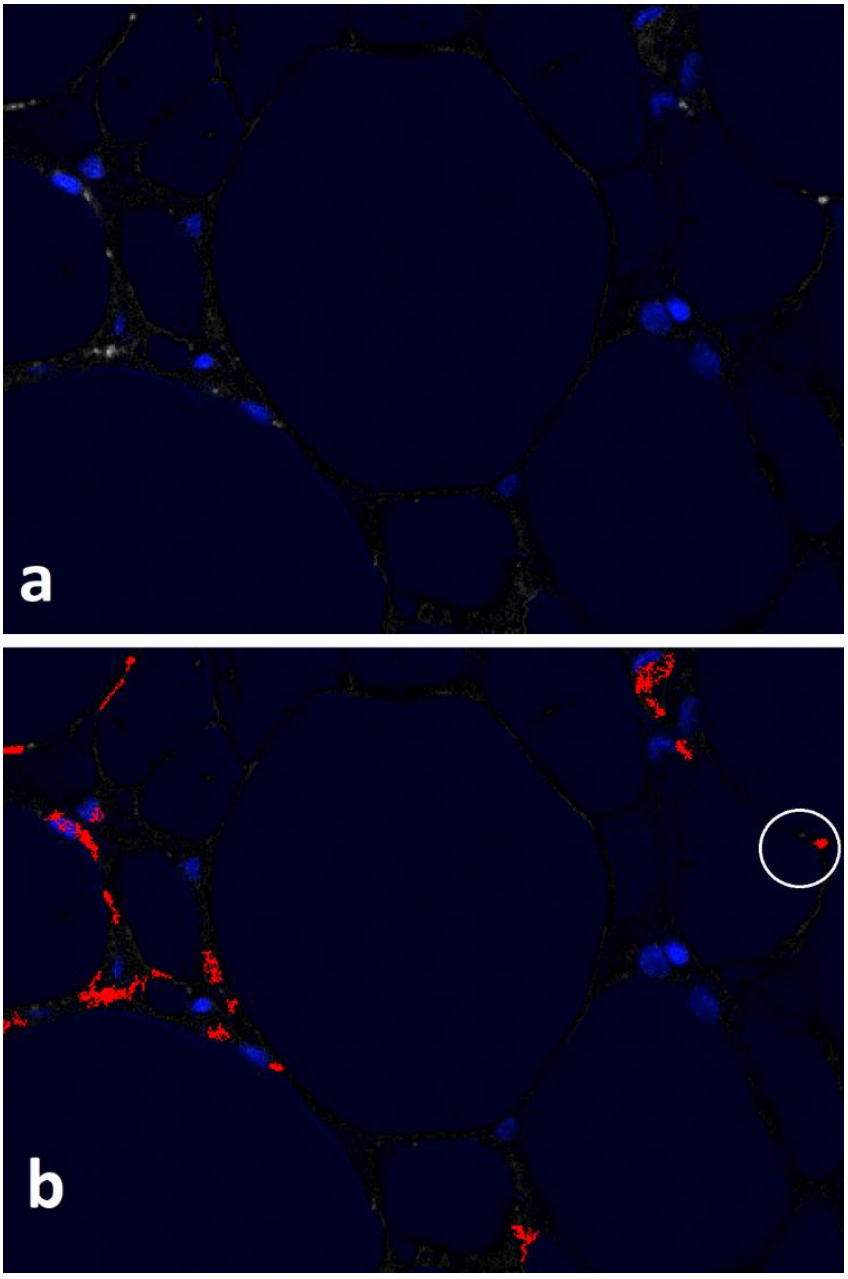

Fig 5.8 Example of generating a mask to segment CD206-positive pixels beyond a threshold

a demonstrates the unmixed staining in Texas Red channel. The white colour represents CD206-positive pixels. The red pixels in **b** were a mask generated by applying a threshold (0.2-10) to resemble the staining pattern in **a**. The white circle demonstrates an excluded autofluorescence-like staining pattern in image analysis.

Table 5.1 Maximal and minimal threshold setting

Minimal thresholding		
CD163-CY3	CD206-Texas Red	CD68-CY5
0.2-10	0.2-10	0.15-10
Maximal thresholding		
CD163-CY3	CD206-Texas Red	CD68-CY5
0.06-10	0.08-10	0.05-10

After applying an individually optimised threshold, the maximal and minimal threshold settings were applied sequentially to all images again to obtain data of interest. Abbreviation: CY, cyanine

5.4.5.2 Cytoplasm segmentation

A nuclear segmentation algorithm and a cytoplasm algorithm were applied to output a cytoplasm mask according to a published protocol with modifications [331]. The positivity of each unmixed component was quantified within the cytoplasm compartment. The process was repeated for all images. The minimal size and typical size of nuclei have been set, respectively, to be 30 pixels and 320 pixels after multiple trials, to make sure DAPI-counterstained nuclei could be recognised as much as possible. The "Split More/Split Less" slider was adjusted to be 3.0 for the purpose of segmenting the nuclei as accurately as possible. The stained cells have heterogeneous staining patterns, with only a portion of the cells demonstrating a typical membrane-like staining pattern (**Fig 5.9a**). To include the positive pixels located in the cellular processes that reach long distances from the nuclei, the outer distance of cytoplasm to nucleus was set to be a fixed 10 pixels (**Fig 5.9b**). To include the positive pixels that may overlap with the nuclear DAPI stain **(Fig 5.9c**), the size of the nuclei was shrunk by 40 %. An example of cytoplasm segmentation followed by nuclear segmentation is displayed in **Fig 5.10**. After segmenting cytoplasm, the positivity of each unmixed component was quantified within the cytoplasm compartment by applying the three threshold settings (individually optimised, maximum and minimum) introduced previously. Simultaneously, the cell counting was exported automatically.

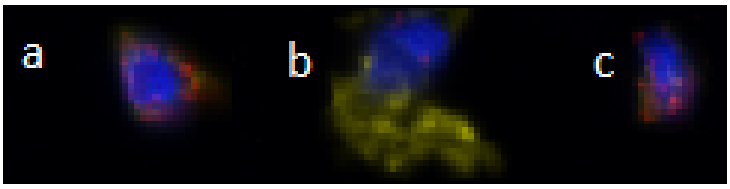

Fig 5.9 Heterogeneous staining patterns of CD markers in cellular compartments

The composite image displays various staining patterns of the CD markers in cellular compartments. **a** demonstrates the stained pixels are found closely around the nucleus. **b** demonstrates the stained cellular processes reach a long distance from the nucleus. **c** demonstrates the stains may overlap with the nuclear DAPI stain.

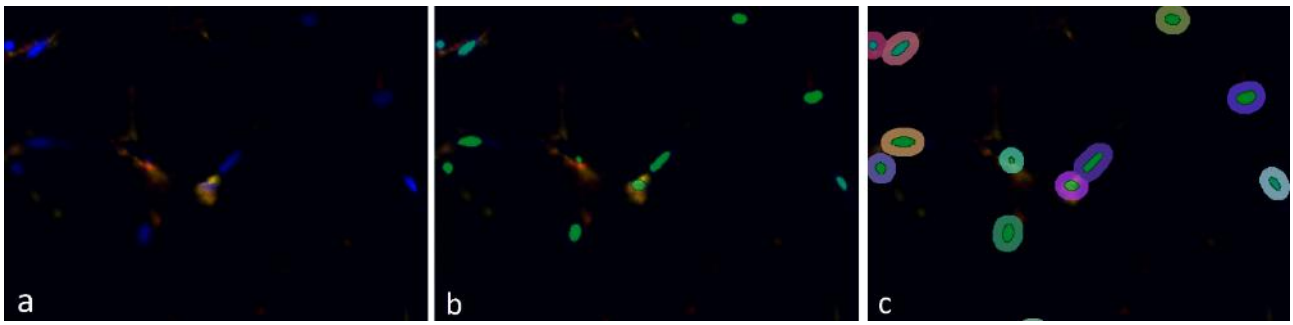

Fig 5.10 Examples of nuclear and cytoplasmic segmentation

a demonstrates the composite multiplexed images of a sample co-stained with the antibodies for CD163, CD206, CD68 and counterstained with DAPI. The green masks in **b** demonstrate the segmented nuclei. The colourful masks in shapes of "doughnuts" around the green nuclear masks demonstrate the segmented cytoplasm in **c**. The positivity of each unmixed component was quantified within the cytoplasmic compartment using three pixel-based algorithms.

5.4.6 Adipocyte size analysis

The volume of adipocytes has close correlation with adipocyte morphology, with small adipocyte volume indicating hyperplastic morphology whereas large adipocyte volume indicating hypertrophic morphology [332]. The size of adipocytes was measured in the same images used for macrophage quantification by excluding adipocytes touching the edge. The quantification was assisted by using the "Adiposoft" tool in the software of Image J, which has been validated in a previous publication [333]. First, an automatic algorithm was applied to extract adipocytes with the minimal and maximal diameter settings being 30 and 300, respectively. Then, the image was further processed in manual edition by deleting adipocytes with inaccurate outlines and adding unrecognised adipocytes. Finally, the area of each adipocyte (output units: pixels) was exported. An example of an image processed by "Adiposoft" is displayed in **Fig 5.11**.

5.4.7 Statistical analysis

Comparisons between groups were made using the paired t-test, one-way ANOVA or two-way ANOVA when appropriate. Two-way ANOVA was conducted to analyse the effect of tumour subtype (three levels: metastatic ccRCC, non-metastatic ccRCC and oncocytoma) and thresholding (three levels: individual, minimal and maximal thresholds) on dependent variables of interest. Repeated measures two-way ANOVA was conducted to analyse the effect of tumour subtype (two levels: metastatic and non-metastatic ccRCC) and thresholding (three levels: individual, minimal and maximal thresholds) on dependent variables of interest. Tukey's or Sidak multiple comparisons were performed after ANOVA if tumour subtype accounted for more than 10 % of total variation of the variables of interest. Cohen's d was calculated to measure the effect size to quantify the difference

between the cohort of metastatic ccRCC and the cohort of non-metastatic ccRCC. $p<0.05$ was considered statistically significant. Statistical analysis was performed using the software GraphPad Prism 7.0.

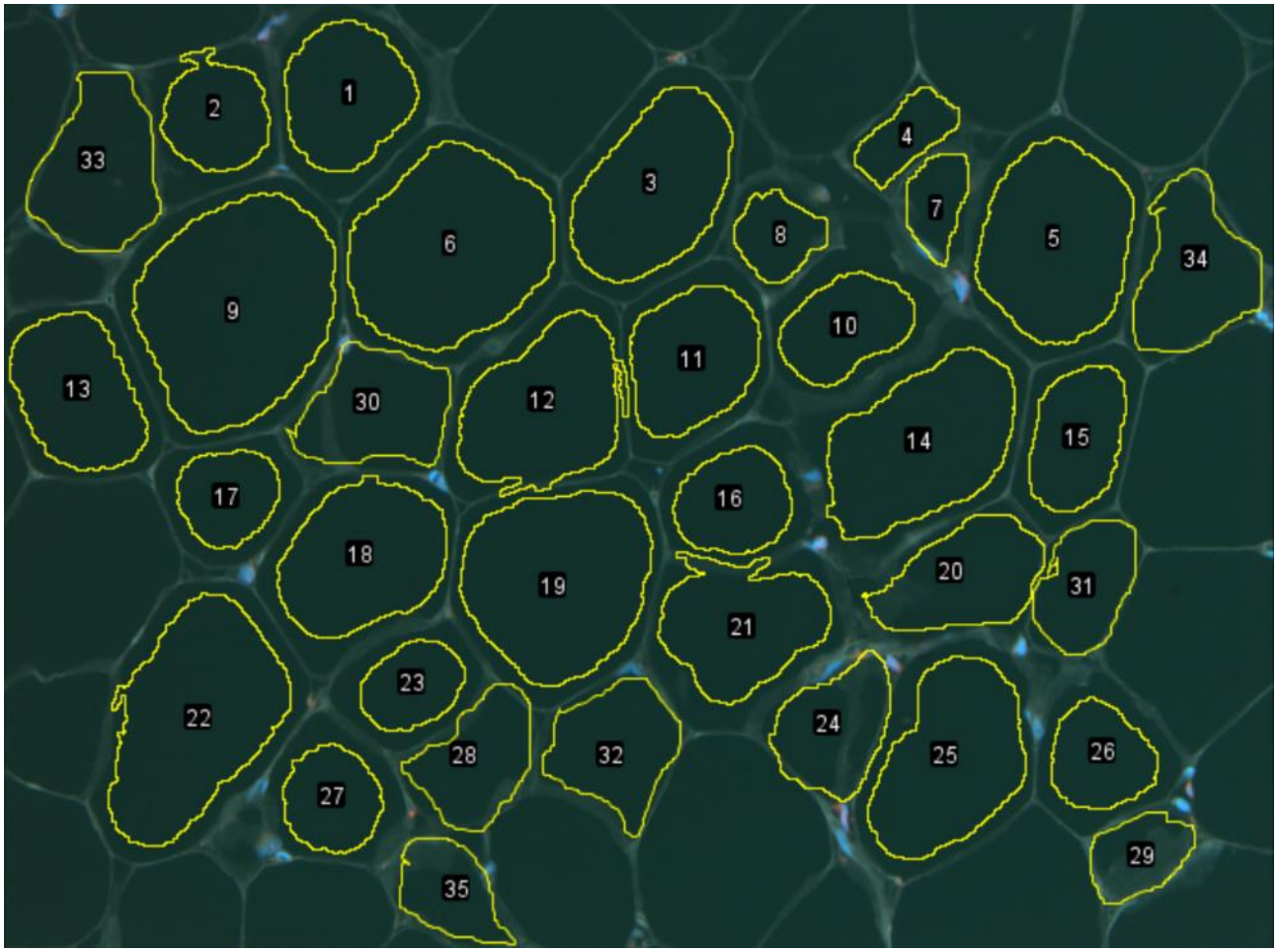

Fig 5.11 Output of an image processed by "Adiposoft"

The outline of adipocytes is highlighted in yellow. Cells that touch the edge of the section were not counted. Area of individual adipocytes was exported automatically.

5.5 Results

5.5.1 Patient characteristics

Two hundred and sixty seven participants recorded in the database were assessed for eligibility. After excluding 90 participants who did not meet the inclusion criteria (missing data about kidney cancer diagnosis n=5, diagnosis other than ccRCC n=85), 177 participants were assessed for tissue availability. 59 participants with perinephric adipose tissue available for IHC were further assessed for the presence of distant metastasis. Five participants with distant metastasis and another 5 participants without distant metastasis who were matched for BMI, and matched as much as possible for gender, age, tumour stage and grade constituted two sets of matched data. A third cohort was made up of 5 participants diagnosed with oncocytoma who had qualified adipose tissue available (**Fig 5.1**). Demographic and pathological diagnostic characteristics of participants in the three cohorts are summarised in **Table 5.2**. Summary of staining results and median size of adipocytes are displayed in **Table 5.3**.

Table 5.2 Characteristics of the study population

ccRCC with distant metastasis						Matched ccRCC without distant metastasis					
ID	Sex	Age	BMI (kg/m^2)	Stage	Grade	ID	Sex	Age	BMI (kg/m^2)	Stage	Grade
125	F	55	25.5	1	2	248	F	54	27.3	*3	2
208	F	69	28.2	3	3	257	*M	62	29.2	3	3
131	M	54	27.4	3	3	206	M	61	26.8	3	3
179	M	39	27.5	3	4	89	M	46	27.5	3	4
186	M	44	28.8	3	2	226	M	*73	28.9	3	2
Oncocytoma											
ID	Sex	Age	BMI (kg/m^2)	Stage#	Grade#						
150	M	76	38.4								
215	M	74	29.4								
219	M	75	25.8								
229	M	75	28.4								
261	F	67	23.6								

Tumours were staged according to the 7th TNM Classification of malignant tumours and graded according to the International Society for Urological Pathology (ISUP) grading system, which were not applicable for oncocytoma. * There was not a perfectly matched participant to join the cohort. Abbreviation: BMI, body mass index; ccRCC, clear cell renal cell carcinoma

Table 5.3 Quantification of the expression of CD markers and size of adipocytes

Variables			ccRCC without metastasis cohort	ccRCC with metastasis cohort	Oncocytoma cohort	#Effect size Non-metastasis vs metastasis (Cohen's d)
Mean intensity of CD206 across the whole image (sd)			0.003 (0.003)	0.012 (0.012)	0.003 (0.003)	1.029
Mean intensity of CD163 across the whole image (sd)			0.004 (0.003)	0.014 (0.016)	0.003 (0.002)	0.869
Mean intensity of CD68 across the whole image (sd)			0.028 (0.036)	0.005 (0.009)	0.045 (0.038)	1.080
Pixel-based segmentation						
CD206	Positivity across the whole image (sd)	Individual thresholding	0.110 % (0.091)	0.828 % (0.857)	0.202 % (0.181)	1.178
		Maximal thresholding	0.088 % (0.089)	0.514 % (0.714)	0.122 % (0.166)	0.837
		Minimal thresholding	0.520 % (0.659)	0.880 % (0.941)	1.016 % (0.712)	0.443
	Total intensity in segmented area (sd)	Individual thresholding	1470.158 (1973.613)	7975.847 (11272.573)	1089.917 (1255.069)	0.804
		Maximal thresholding	1415.126 (1991.658)	7201.080 (10917.030)	918.413 (1270.132)	0.737
		Minimal thresholding	2190.169 (2130.036)	8072.922 (11452.215)	2528.970 (2226.566)	0.714
CD163	Positivity across the whole image (sd)	Individual thresholding	0.342 % (0.288)	0.700 % (0.505)	0.380 % (0.473)	0.871
		Maximal thresholding	0.264 % (0.224)	0.610 % (0.571)	0.214 % (0.196)	0.798
		Minimal thresholding	0.424 % (0.241)	0.848 % (0.679)	0.582 % (0.441)	0.832
	Total intensity in segmented area (sd)	Individual thresholding	4716.107 (4832.116)	18139.962 (21840.452)	1998.078 (2101.384)	0.849
		Maximal thresholding	4528.698 (4700.734)	18802.464 (21223.936)	1604.8669 (1655.004)	0.929
		Minimal thresholding	4878.185 (4681.580)	19332.566 (21356.031)	2414.760 (1912.065)	0.935
CD68	Positivity across the whole image (sd)	Individual thresholding	0.048 % (0.069)	0.672 % (1.015)	0.001 % (0.001)	1.755
		Maximal thresholding	0.018% (0.029)	0.498 % (1.080)	0.072 % (0.129)	0.628
		Minimal thresholding	1.172 % (1.603)	0.964 % (1.574)	2.986 % (2.828)	0.131
	Total intensity in segmented area (sd)	Individual thresholding	181.824 (319.785)	5468.288 (11357.580)	459.783 (860.633)	0.658
		Maximal thresholding	120.404 (219.449)	5211.596 (11493.970)	453.923 (864.356)	0.626
		Minimal thresholding	1819.182 (2390.134)	5933.818 (12289.852)	4021.196 (4444.385)	0.465
CD206/CD163 double positivity across the whole image (sd)		Individual thresholding	0.066 % (0.075)	0.274 % (0.300)	0.064 % (0.095)	0.951
		Maximal thresholding	0.050 % (0.063)	0.202 % (0.246)	0.038 % (0.064)	0.847
		Minimal thresholding	0.120 % (0.103)	0.332 % (0.378)	0.232 % (0.238)	0.765
Cytoplasm segmentation						
		Individual thresholding	1.507 (1.465)	13.111 (17.452)	0.988 (1.112)	0.937

CD206 positive cell numbers in cytoplasm(sd)	Maximal thresholding	0.858 (1.196)	6.256 (9.247)	0.468 (0.735)	0.819
	Minimal thresholding	3.224 (3.471)	16.382 (22.928)	4.029 (5.119)	0.802
CD163 positive cell numbers in cytoplasm (sd)	Individual thresholding	6.783 (7.122)	10.115 (9.205)	3.285 (4.272)	0.405
	Maximal thresholding	3.454 (4.872)	9.282 (9.818)	0.936 (1.004)	0.752
	Minimal thresholding	6.983 (7.079)	14.111 (11.932)	6.242 (3.854)	0.727
CD68 positive cell numbers in cytoplasm (sd)	Individual thresholding	0.365 (0.676)	6.262 (12.860)	0.431 (0.963)	0.648
	Maximal thresholding	0.054 (0.121)	5.980 (13.010)	0.430 (0.962)	0.644
	Minimal thresholding	0.679 (1.375)	12.691 (27.230)	4.103 (5.625)	0.623
CD206/CD163 double positive cell numbers in cytoplasm (sd)	Individual thresholding	1.507 (1.465)	13.111 (17.452)	0.988 (1.112)	0.937
	Maximal thresholding	0.858 (1.196)	6.256 (9.247)	0.468 (0.735)	0.819
	Minimal thresholding	3.224 (3.471)	16.382 (22.928)	4.029 (5.119)	0.802
Median size of adipocytes (sd)*		13434 (2255)	9518 (3153)	13412 (2046)	1.430

All variables regarding expression intensity are displayed in the units of fluorescence counts which had been normalised for exposure and weighted using the method of total weighting.

The effect size was calculated using the online effect size calculator.
http://www.polyu.edu.hk/mm/effectsizefaqs/calculator/calculator.html

* The unit for size of adipocytes was pixel. There were 969, 1108 and 975 adipocytes counted in the cohorts of non-metastatic ccRCC, metastatic ccRCC and oncocytoma, respectively.

Abbreviation: ccRCC, clear cell renal cell carcinoma; sd, standard deviation

5.5.2 Difference of mean intensity of individual CD marker across the whole image between different subytpes of renal tumours

The mean value of CD206 mean intensity across the whole image was higher in metastatic ccRCC perinephric adipose tissue (0.012) compared to non-metastatic ccRCC perinephric adipose tissue (0.003) and oncocytoma perinephric adipose tissue (0.003). However, the differences were not statistically significant (**Figs 5.12 a1-3**). The mean value of CD163 mean intensity across the whole image was higher in metastatic ccRCC perinephric adipose tissue (0.014) compared to non-metastatic ccRCC perinephric adipose tissue (0.004) and oncocytoma perinephric adipose tissue (0.003). However, the differences were not statistically significant (**Figs 5.12 b1-3**). The mean value of CD68 mean intensity across the whole image was lower in metastatic ccRCC perinephric adipose tissue (0.005) compared to non-metastatic ccRCC perinephric adipose tissue (0.028) and oncocytoma perinephric adipose tissue (0.045). However, the differences were not statistically significant (**Figs 5.12 c1-3**).

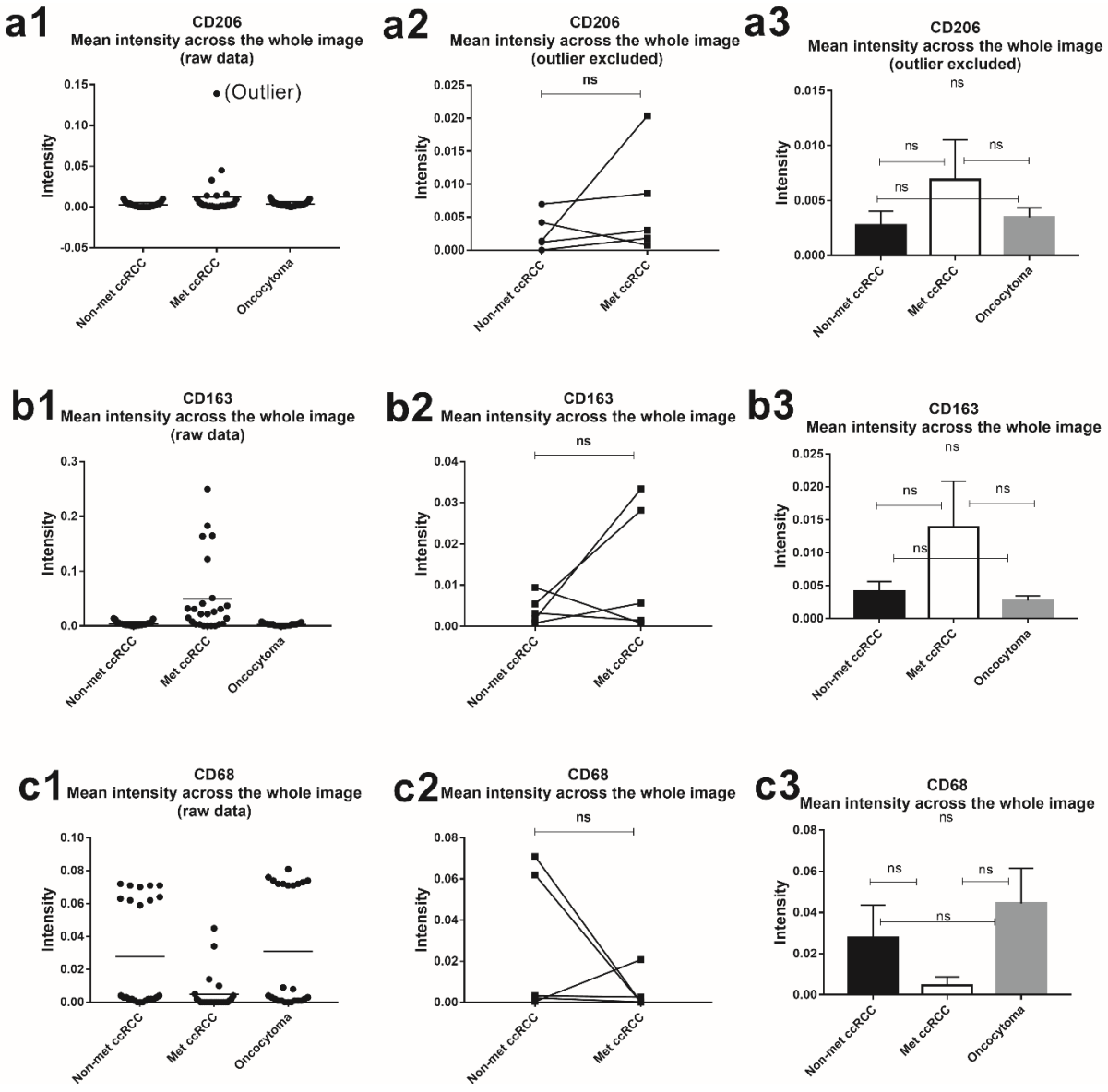

Fig 5.12 Mean intensity of individual CD markers across the whole image

(a1) Scatter plots of the raw data of mean intensity of CD206 across the whole image in ccRCC and oncocytoma; (a2) Scatter plots of the mean value of the mean intensity of CD206 across the whole image in ccRCC (non-met ccRCC vs met ccRCC); (a3) Bar graphs of the mean value of mean intensity of CD206 across the whole image in ccRCC and oncocytoma; (b1) Scatter plots of the raw data of mean intensity of CD163 across the whole image in ccRCC and oncocytoma; (b2) Scatter plots of the mean value of the mean intensity of CD163 across the whole image in ccRCC (non-met ccRCC vs met ccRCC); (b3) Bar graphs of the mean value of mean intensity of CD163 across the whole image in ccRCC and oncocytoma; (c1) Scatter plots of the raw data of mean intensity of CD68 across the whole image in ccRCC and oncocytoma; (c2) Scatter plots of the mean value of the mean intensity of CD68 across the whole image in ccRCC (non-met ccRCC vs met ccRCC); (c3) Bar graphs of the mean value of mean intensity of CD68 across the whole image in ccRCC and oncocytoma; Lines across the raw data indicate mean value. ns, $p>0.05$, paired t-test or Tukey's multiple comparisons after one-way ANOVA. Error bars represent estimated standard errors of the mean. Abbreviation: met, metastatic; ccRCC, clear cell renal cell carcinoma.

5.5.3 Metastatic ccRCC perinephric adipose tissue exhibited higher expression of CD206.

Repeated measures two-way ANOVA was conducted to analyse the association of tumour subtype (two levels: metastatic and non-metastatic ccRCC) and thresholding (three levels: individual, maximal and minimal) with positivity of CD206 across the whole image, total intensity of CD206 in the segmented area and CD206 positive cell number in the cytoplasm. For CD206 positivity (**Fig 5.13 a2**), the interaction effect of the two factors was non-significant, $F(2, 8) = 0.85$, $p = 0.46$, but the effect of thresholding which accounted for 6.08 % of total variation was significant, $F(2, 8) = 5.68$, $p=0.03$. Tumour subtype accounted for 14.29 % of total variation, however the effect was non-significant, $F(1, 4) = 1.55$, $p = 0.28$. Sidak test showed that the positivity of CD206 was higher in metastatic ccRCC compared to non-metastatic ccRCC using individual thresholding ($p = 0.02$), but there were no differences between tumour subtypes when the maximal ($p = 0.20$) or minimal ($p = 0.32$) thresholding were applied. For CD206 total intensity (**Fig 5.13 b2**), the interaction effect was non-significant, $F(2, 8) = 1.05$, $p = 0.39$, but the effect of thresholding was significant, even only accounting for 0.18 % of the total variance, $F(2, 8) = 7.84$, $p = 0.01$. Tumour subtype accounted for 14.97 % of total variation, however the effect was non-significant, $F(1, 4) = 1.60$, $p = 0.28$. Sidak test showed that the total intensity of CD206 was higher in metastatic ccRCC compared to non-metastatic ccRCC using all thresholding ($p < 0.0001$). For CD206 positive cell number (**Fig 5.13 c2**), the interaction effect was non-significant, $F(2, 8) = 1.88$, $p = 0.21$, and the effect of thresholding which accounted for 4.15 % of total variation was non-significant, $F(2, 8) = 3.4$, $p = 0.08$. Tumour subtype accounted for 15.91 % of total variation, however the effect was non-significant, $F(1, 4) = 2.23$, $p=0.21$. Sidak test showed that the positive CD206 cell number in cytoplasm was higher in metastatic ccRCC compared to non-metastatic ccRCC using the individual ($p = 0.01$) and the minimal ($p = 0.007$) thresholding, but there were no differences between tumour subtypes when the maximal ($p = 0.29$) thresholding was applied.

An ordinary two-way ANOVA was conducted to analyse the association of tumour subtype (three levels: metastatic ccRCC, non-metastatic ccRCC and oncocytoma) and thresholding (three levels: individual, maximal and minimal) with positivity of CD206 across the whole image, total intensity of CD206 in the segmented area and CD206 positive cell number in the cytoplasm. For CD206 positivity (**Fig 5.13 a3**), there was not a significant interaction between the two factors, $F(4, 36) = 0.60$, $p = 0.67$, but there was a significant main effect (accounting for 14.45 % of total variation) caused by thresholding, $F(2, 36) = 3.70$, $p = 0.03$. The factor, tumour subtype, accounted for 10.62 % of total variance and yielded an F ratio of $F(2, 36) = 2.72$, $p = 0.08$, indicating a non-significant difference of CD206 positivity between tumour subtypes. Tukey's multiple comparison did not find any significant difference in post hoc testing. For CD206 total intensity (**Fig 5.13 b3**), there was not

a significant interaction between the two factors, F (4, 36) = 0.02, p = 0.99, and the effect caused by thresholding (only accounting for 0.47 % of total variation) was not significant, F (2, 36) = 0.10, p = 0.90. The main factor, tumour subtype (accounting for 19.08 % of total variation), yielded an F ratio of F (2, 36) = 4.28, p = 0.02, indicating a significant difference of CD206 total intensity in segmented area between tumour subtypes. However, Tukey's multiple comparison did not find any significant difference in post hoc testing. For CD206 positive cell number (**Fig 5.13 c3**), there was not a significant interaction between the two factors, F (4, 36) = 0.24, p = 0.91, and the effect caused by thresholding (accounting for 4.15 % of total variation) was not significant, F (2, 36) = 1.00, p = 0.38. The main factor, tumour subtype (accounting for 19.61 % of total variation), yielded an F ratio of F (2, 36) = 4.76, p = 0.01, indicating a significant difference of CD206 positive cell number in cytoplasm between tumour subtypes. However, Tukey's multiple comparison did not find any significant difference in post hoc testing.

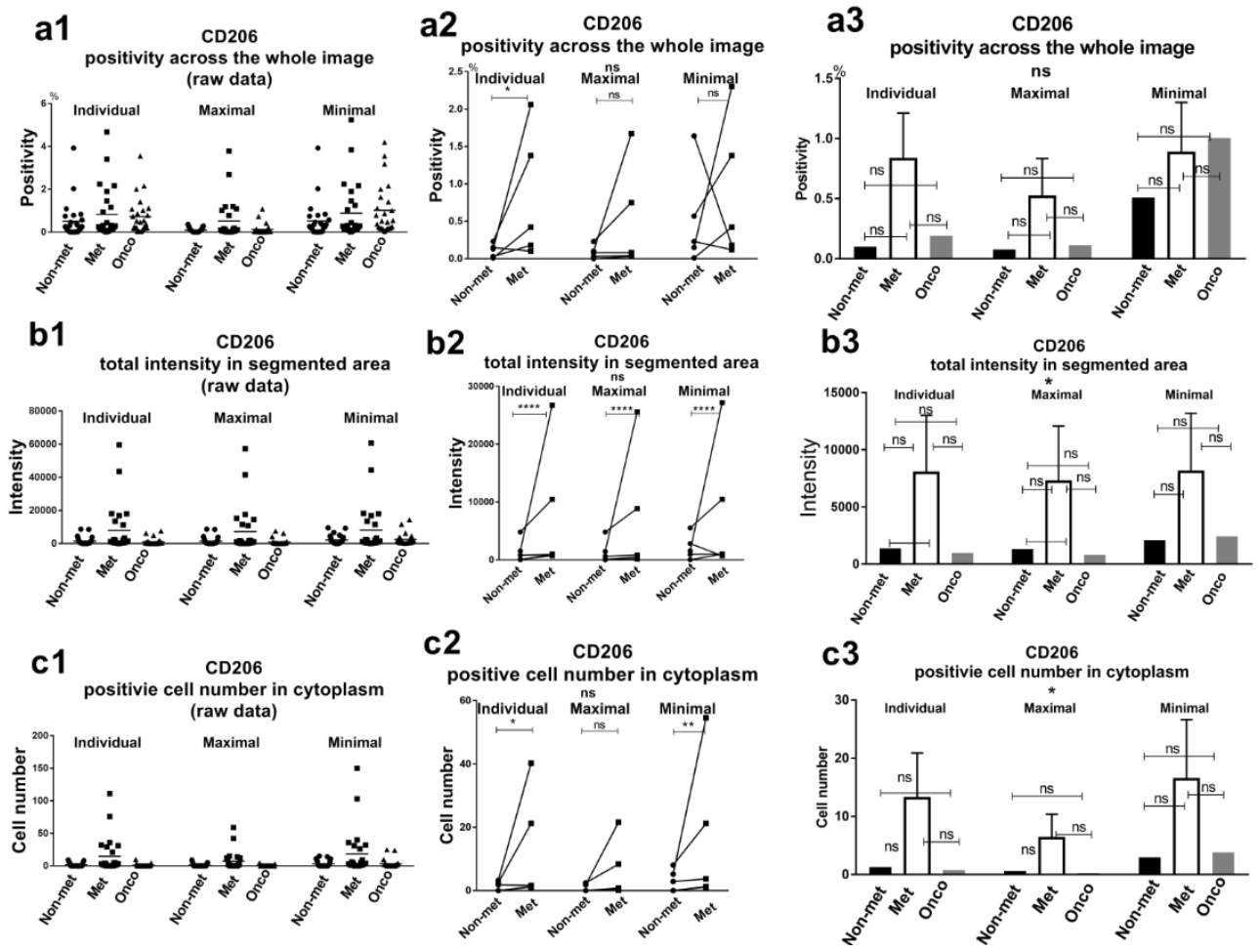

Fig 5.13 CD206 expression

(a1) Scatter plots of the raw data of CD206 positivity in ccRCC and oncocytoma; (a2) Scatter plots of mean value of CD206 positivity in ccRCC (non-met ccRCC vs met ccRCC); (a3) Bar graphs of mean value of CD206 positivity in ccRCC and oncocytoma; (b1) Scatter plots of total intensity of CD206 in segmented area in ccRCC and oncocytoma; (b2) Scatter plots of mean value of total intensity of CD206 in segmented area in ccRCC (non-met ccRCC vs met ccRCC); (b3) Bar graphs of mean value of total intensity of CD206 in segmented area in ccRCC and oncocytoma; (c1) Scatter plots of the raw data of CD206 positive cell number in cytoplasm in ccRCC and oncocytoma; (c2) Scatter plots of the mean value of CD206 positive cell number in cytoplasm in ccRCC (non-met ccRCC vs met ccRCC); (c3) Bar graphs of the mean value of CD206 positive cell number in cytoplasm in ccRCC and oncocytoma; Lines across the raw data indicate mean value. ns, $p>0.05$, *, $p < 0.05$, **, $p < 0.01$, ****, $p < 0.0001$, Sidak test after repeated measures two-way ANOVA or Tukey's multiple comparisons after two-way ANOVA. Error bars represent estimated standard errors of the mean. Abbreviation: met, metastatic; ccRCC, clear cell renal cell carcinoma; onco, oncocytoma.

5.5.4 Metastatic ccRCC perinephric adipose tissue exhibited higher expression of CD163.

Repeated measures two-way ANOVA was conducted to analyse the association of tumour subtype (two levels: metastatic and non-metastatic ccRCC) and thresholding (three levels: individual, maximal and minimal) with positivity of CD163 across the whole image, total intensity of CD163 in the segmented area and CD163 positive cell number in the cytoplasm. For CD163 positivity (**Fig 5.14 a2**), the interaction effect was non-significant, $F(2, 8) = 0.53$, $p = 0.61$, but the effect of thresholding which accounted for 3.22 % of total variation was significant, $F(2, 8) = 7.95$, $p = 0.01$. Tumour subtype accounted for 17.10 % of total variation, however the effect was non-significant, $F(1, 4) = 1.67$, $p = 0.27$. Sidak test showed that the positivity of CD163 was higher in metastatic ccRCC compared to non-metastatic ccRCC using all thresholding ($p < 0.001$). For CD163 total intensity (**Fig 5.14 b2**), the interaction effect was non-significant, $F(2, 8) = 1.22$, $p = 0.35$, and the effect of thresholding which only accounted for 0.03 % of total variation was non-significant, $F(2, 8) = 2.25$, $p=0.17$. Tumour subtype accounted for 20.32 % of total variation, however the effect was non-significant, $F(1, 4) = 1.75$, $p = 0.26$. Sidak test showed that the total intensity of CD163 was higher in metastatic ccRCC compared to non-metastatic ccRCC using all thresholding ($p < 0.0001$). For CD163 positive cell number (**Fig 5.14 c2**), the interaction effect was non-significant, $F(2, 8) = 1.88$, $p = 0.21$, and the effect of thresholding which accounted for 4.15 % of total variation was non-significant, $F(2, 8) = 3.1$, $p=0.10$. Tumour subtype accounted for 10.43 % of total variation, however the effect was non-significant, $F(1, 4) = 0.80$, $p = 0.42$. Sidak test showed that the positive CD163 cell number in cytoplasm was higher in metastatic ccRCC compared to non-metastatic ccRCC using the individual ($p < 0.05$), the maximal ($p < 0.01$), and the minimal ($p < 0.001$) thresholding.

An ordinary two-way ANOVA was conducted to analyse the association of tumour subtype (three levels: metastatic ccRCC, non-metastatic ccRCC and oncocytoma) and thresholding (three levels: individual, maximal and minimal) with positivity of CD163 across the whole image, total intensity of CD163 in the segmented area and CD163 positive cell number in the cytoplasm. For CD163 positivity (**Fig 5.14 a3**), there was not a significant interaction between the two factors, $F(4, 36) = 0.08$, $p = 0.99$, and the effect (accounting for 5.74 % of total variation) caused by thresholding was not significant, $F(2, 36) = 1.31$, $p = 0.28$. The main factor, tumour subtype, accounted for 14.65 % of total variance and yielded an F ratio of $F(2, 36) = 3.34$, $p = 0.05$, indicating a significant difference of CD163 positivity between tumour subtypes. However, Tukey's multiple comparison did not find any significant difference in post hoc testing. For CD163 total intensity (**Fig 5.14 b3**), there was not a significant interaction between the two factors, $F(4, 36) = 0.003$, $p > 0.99$, and effect caused by thresholding (only accounting for 0.04 % of total variation) was not significant, $F(2, 36) = 0.01$, $p = 0.99$. The main factor, tumour subtype (accounting for 29.31 % of total variation), yielded an F ratio

of F (2, 36) = 7.47, p = 0.002, indicating a significant difference of CD163 total intensity in segmented area between tumour subtypes. However, Tukey's multiple comparison did not find any significant difference in post hoc testing. For CD163 positive cell number (**Fig 5.14 c3**), there was not a significant interaction between the two factors, F (4, 36) = 0.10, p = 0.98, and the effect caused by thresholding (accounting for 6.05 % of total variation) was not significant, F (2, 36) = 1.45, p = 0.25. The main factor, tumour subtype (accounting for 18.18 % of total variation), yielded an F ratio of F (2, 36) = 4.37, p = 0.02, indicating a significant difference of CD163 positive cell number in cytoplasm between tumour subtypes. However, Tukey's multiple comparison did not find any significant difference in post hoc testing.

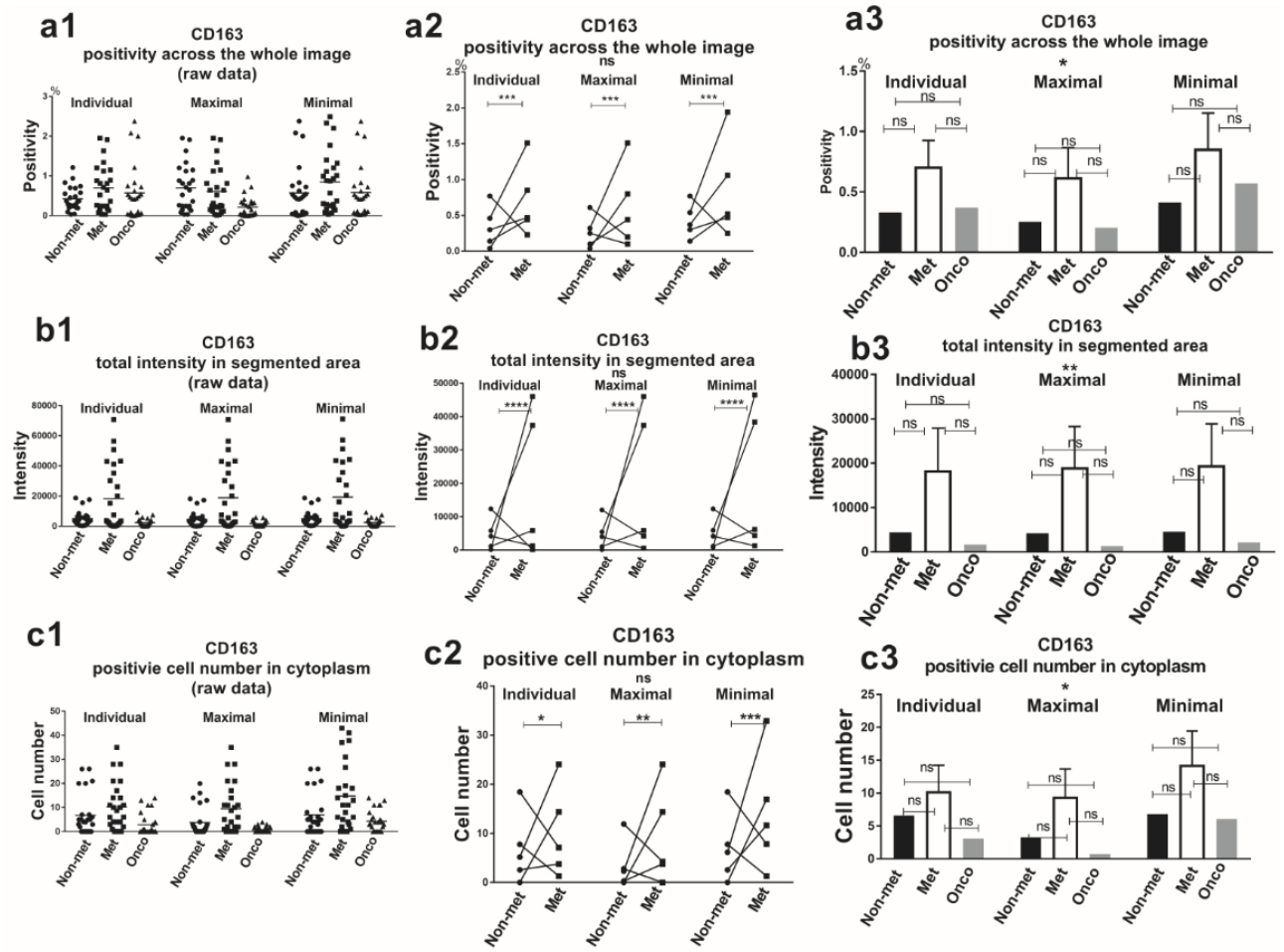

Fig 5.14 CD163 expression

(a1) Scatter plots of the raw data of CD163 positivity in ccRCC and oncocytoma; (a2) Scatter plots of mean value of CD163 positivity in ccRCC (non-met ccRCC vs met ccRCC); (a3) Bar graphs of mean value of CD163 positivity in ccRCC and oncocytoma; (b1) Scatter plots of total intensity of CD163 in segmented area in ccRCC and oncocytoma; (b2) Scatter plots of mean value of total intensity of CD163 in segmented area in ccRCC (non-met ccRCC vs met ccRCC); (b3) Bar graphs of mean value of total intensity of CD163 in segmented area in ccRCC and oncocytoma; (c1) Scatter plots of the raw data of CD163 positive cell number in cytoplasm in ccRCC and oncocytoma; (c2) Scatter plots of the mean value of CD163 positive cell number in cytoplasm in ccRCC (non-met ccRCC vs met ccRCC); (c3) Bar graphs of the mean value of CD163 positive cell number in cytoplasm in ccRCC and oncocytoma; Lines across the raw data indicate mean value. ns, $p>0.05$, *, $p < 0.05$, **, $p < 0.01$, ***, $p < 0.001$, ****, $p < 0.0001$, Sidak test after repeated measures two-way ANOVA or Tukey's multiple comparisons after two-way ANOVA. Error bars represent estimated standard errors of the mean. Abbreviation: met, metastatic; ccRCC, clear cell renal cell carcinoma; onco, oncocytoma.

5.5.5 No difference of CD68 expression in ccRCC perinephric adipose tissue (non-metastatic vs metastatic ccRCC) and oncocytoma perinephric adipose tissue

Repeated measures two-way ANOVA was conducted to analyse the association of tumour subtype (two levels: metastatic and non-metastatic ccRCC) and thresholding (three levels: individual, maximal and minimal) with positivity of CD68 across the whole image, total intensity of CD68 in the segmented area and CD68 positive cell number in the cytoplasm. For CD68 positivity (**Fig 5.15 a2**), the interaction effect was non-significant, $F(2, 8) = 0.80$, $p = 0.48$, but the effect of thresholding which accounted for 11.27 % of total variation was significant, $F(2, 8) = 5.30$, $p = 0.03$. Tumour subtype only accounted for 1.94 % of total variation, and the effect was non-significant, $F(1, 4) = 0.19$, $p = 0.69$. For CD68 total intensity (**Fig 5.15 b2**), the interaction effect was non-significant, $F(2, 8) = 0.68$, $p = 0.53$, but the effect of thresholding was significant, even only accounting for 0.47 % of total variation, $F(2, 8) = 5.08$, $p = 0.04$. Tumour subtype accounted for 9.42 % of total variation, however the effect was non-significant, $F(1, 4) = 0.80$, $p = 0.42$. For CD68 positive cell number (**Fig 5.15 c2**), the interaction effect was non-significant, $F(2, 8) = 0.88$, $p = 0.45$, and the effect of thresholding which accounted for 1.68 % of total variation was non-significant, $F(2, 8) = 1.24$, $p = 0.34$. Tumour subtype accounted for 9.60 % of total variation, and the effect was non-significant, $F(1, 4) = 0.99$, $p = 0.38$.

An ordinary two-way ANOVA was conducted to analyse the association of tumour subtype (three levels: metastatic ccRCC, non-metastatic ccRCC and oncocytoma) and thresholding (three levels: individual, maximal and minimal) with positivity of CD68 across the whole image, total intensity of CD68 in the segmented area and CD68 positive cell number in the cytoplasm. For CD68 positivity (**Fig 5.15 a3**), there was not a significant interaction between the two factors, $F(4, 36) = 1.73$, $p = 0.17$, but the effect of thresholding which accounted for 22.71 % of total variation was significant, $F(2, 36) = 6.54$, $p < 0.01$. Tumour subtype, only accounted for 2.82 % of total variance and yielded an F ratio of $F(2, 36) = 0.81$, $p = 0.45$, indicating there was not a significant difference of CD68 positivity between tumour subtypes. For CD68 total intensity (**Fig 5.15 b3**), there was not a significant interaction between the two factors, $F(4, 36) = 0.08$, $p = 0.99$, and the effect caused by thresholding (accounting for 1.88 % of total variation) was not significant, $F(2, 36) = 0.39$, $p = 0.68$. The factor, tumour subtype (accounting for 9.81 % of total variation), yielded an F ratio of $F(2, 36) = 2.02$, $p = 0.15$, indicating there was not a significant difference of CD68 positive cell number in cytoplasm between tumour subtypes. For CD68 positive cell number (**Fig 5.15 c3**), there was not a significant interaction between the two factors, $F(4, 36) = 0.13$, $p = 0.97$, and effect caused by thresholding (accounting for 2.47 % of total variation) was not significant, $F(2, 36) = 0.52$, $p = 0.60$. The factor, tumour subtype (accounting for 10.52 % of total variation), yielded an F ratio of $F(2, 36) = 2.21$, $p =$

0.12, indicating there was not a significant difference of CD68 positive cell number in cytoplasm between tumour subtypes. Moreover, Tukey's multiple comparison did not find any significant difference in post hoc testing.

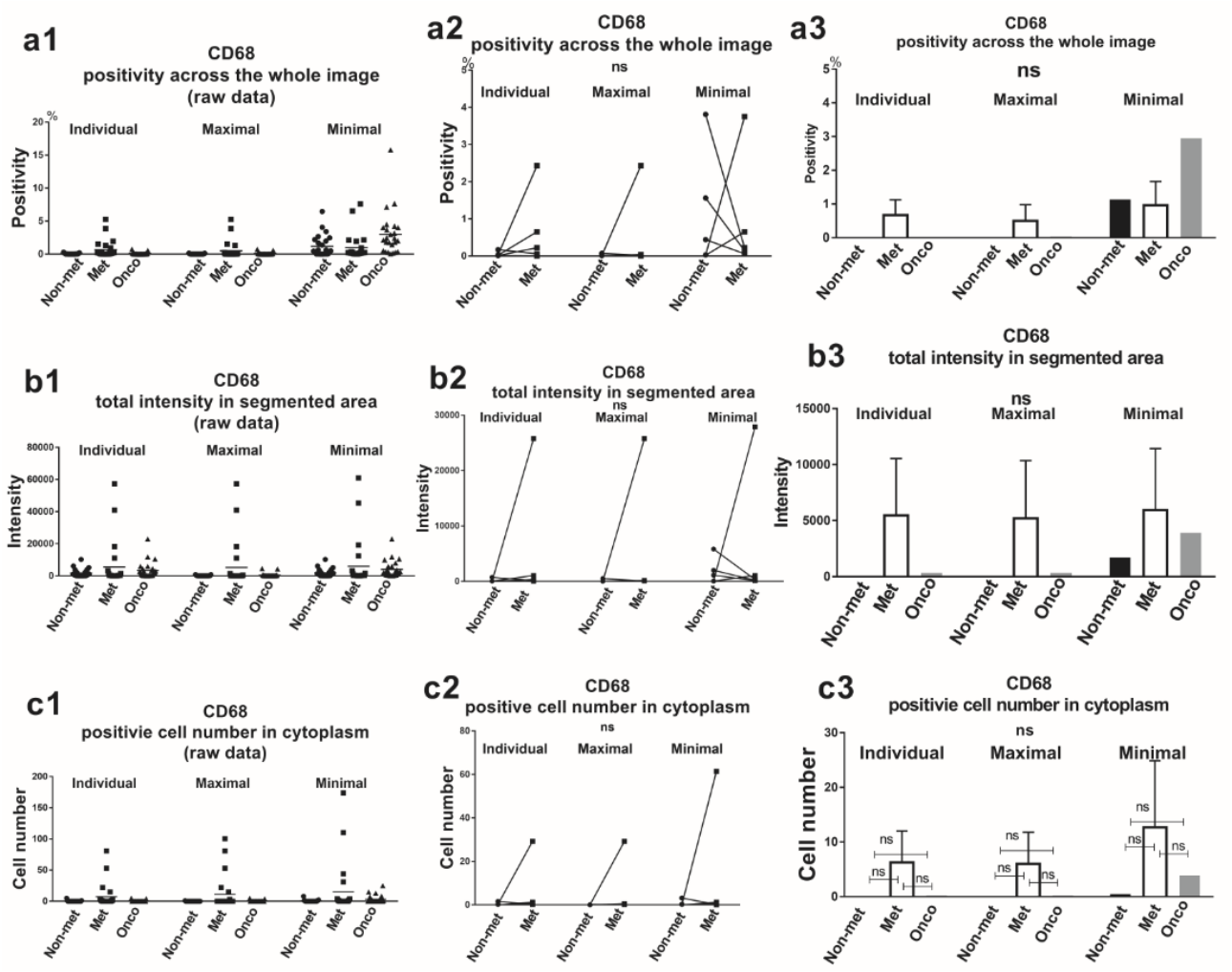

Fig 5.15 CD68 expression

(a1) Scatter plots of the raw data of CD68 positivity in ccRCC and oncocytoma; (a2) Scatter plots of mean value of CD68 positivity in ccRCC (non-met ccRCC vs met ccRCC); (a3) Bar graphs of mean value of CD68 positivity in ccRCC and oncocytoma; (b1) Scatter plots of total intensity of CD68 in the segmented area in ccRCC and oncocytoma; (b2) Scatter plots of mean value of total intensity of CD68 in the segmented area in ccRCC (non-met ccRCC vs met ccRCC); (b3) Bar graphs of mean value of total intensity of CD68 in the segmented area in ccRCC and oncocytoma; (c1) Scatter plots of the raw data of CD68 positive cell number in the cytoplasm in ccRCC and oncocytoma; (c2) Scatter plots of the mean value of CD68 positive cell number in the cytoplasm in ccRCC (non-met ccRCC vs met ccRCC); (c3) Bar graphs of the mean value of CD68 positive cell number in the cytoplasm in ccRCC and oncocytoma; Lines across the raw data indicate mean value. ns, $p>0.05$, Repeated measures two-way ANOVA or Tukey's multiple comparisons after two-way ANOVA. Error bars represent estimated standard errors of the mean. Abbreviation: met, metastatic; ccRCC, clear cell renal cell carcinoma; onco, oncocytoma.

5.5.6 Metastatic ccRCC perinephric adipose tissue exhibited higher expression of CD163/CD206 double positive cells.

Given that metastatic ccRCC exhibited higher expression of CD206 and CD163 when analysing their expression, individually. Repeated measures two-way ANOVA was conducted to analyse the association of tumour subtype (two levels: metastatic and non-metastatic ccRCC) and thresholding with double positivity of CD206/CD163 across the whole image and CD206/CD163 double positive cell number in the cytoplasm. For CD206/CD163 double positivity (**Fig 5.16 a2**), the interaction effect was non-significant, $F(2, 8) = 1.11$, $p = 0.38$, but the effect of thresholding which accounted for 3.17 % of total variation was significant, $F(2, 8) = 4.62$, $p = 0.05$. Tumour subtype accounted for 17.23 % of total variation, however the effect was non-significant, $F(1, 4) = 3.25$, $p = 0.15$. Sidak test showed that the double positivity of CD206/CD163 was higher in metastatic ccRCC compared to non-metastatic ccRCC using all thresholding ($p < 0.01$). For CD206/CD163 double positive cell number (**Fig 5.16 b2**), the interaction effect was non-significant, $F(2, 8) = 1.88$, $p = 0.21$, and the effect of thresholding which accounted for 4.15 % of total variation was non-significant, $F(2, 8) = 3.41$, $p = 0.08$. Tumour subtype accounted for 15.91 % of total variation, however the effect was non-significant, $F(1, 4) = 2.23$, $p = 0.21$. Sidak test showed that the CD206/CD163 double positive cell number in cytoplasm was higher in metastatic ccRCC compared to non-metastatic ccRCC using the individual ($p < 0.05$) and the minimal ($p < 0.01$) thresholding, but there were no differences between tumour subtypes when the maximal thresholding ($p = 0.29$) was applied.

An ordinary two-way ANOVA was conducted to analyse the association of tumour subtype (three levels: metastatic ccRCC, non-metastatic ccRCC and oncocytoma) and thresholding with double positivity of CD206/CD163 across the whole image and CD206/CD163 double positive cell number in the cytoplasm. For CD206/CD163 double positivity (**Fig 5.16 a3**), there was not a significant interaction between the two factors, $F(4, 36) = 0.17$, $p = 0.95$, and the effect caused by thresholding (accounting for 6.81 % of total variation) was not significant, $F(2, 36) = 1.61$, $p = 0.21$. The main factor, tumour subtype, accounted for 15.51 % of total variance and yielded an F ratio of $F(2, 36) = 3.66$, $p = 0.04$, indicating a significant difference of CD206/CD163 double positivity between tumour subtypes. However, Tukey's multiple comparison did not find any significant difference in post hoc testing. For CD206/CD163 double positive cell number (**Fig 5.16 b3**), there was not a significant interaction between the two factors, $F(4, 36) = 0.24$, $p = 0.91$, and the effect caused by thresholding (accounting for 4.15 % of total variation) was not significant, $F(2, 36) = 1.01$, $p = 0.38$. The main factor, tumour subtype (accounting for 19.61 % of total variation), yielded an F ratio of $F(2, 36) = 4.76$, $p = 0.01$, indicating a significant difference of CD206/CD163 double positive cell number in

cytoplasm between tumour subtypes. However, Tukey's multiple comparison did not find any significant difference in post hoc testing.

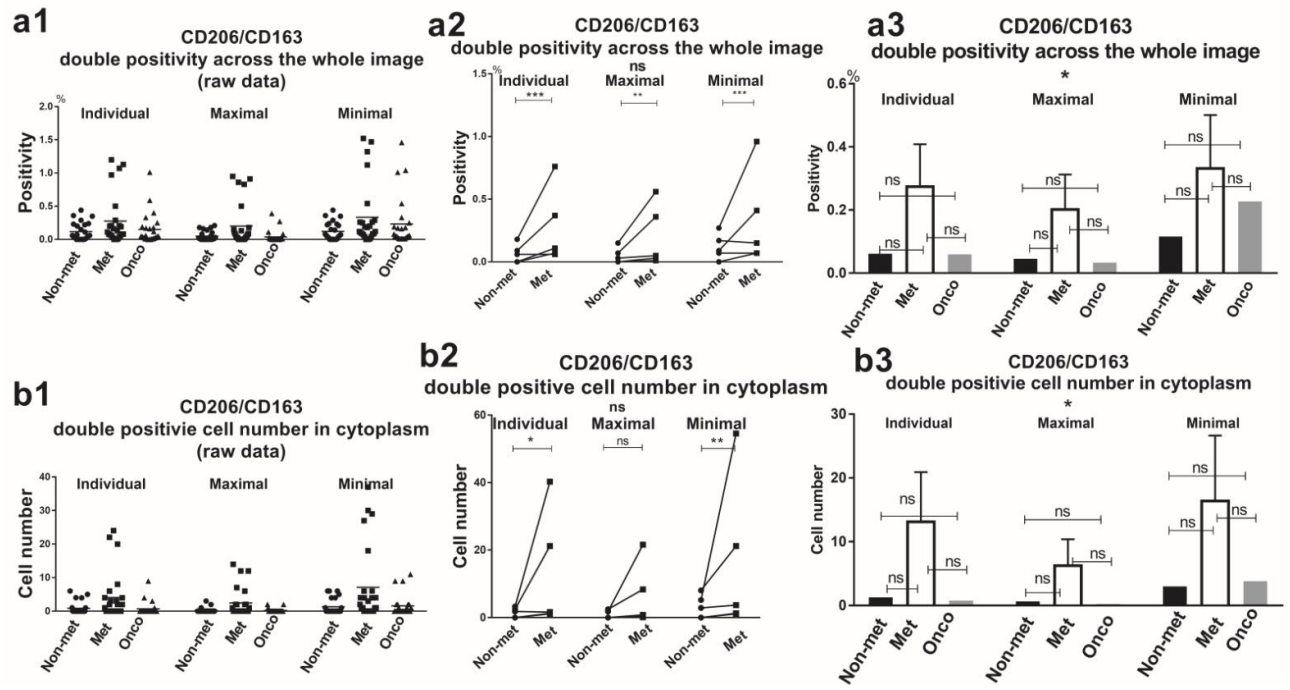

Fig 5.16 Colocalising expression of CD206/CD163

(a1) Scatter plots of the raw data of CD206/CD163 double positivity in ccRCC and oncocytoma; (a2) Scatter plots of mean value of CD206/CD163 double positivity in ccRCC (non-met ccRCC vs met ccRCC); (a3) Bar graphs of mean value of CD206/CD163 double positivity in ccRCC and oncocytoma; (b1) Scatter plots of the raw data of CD206/CD163 double positive cell number in the cytoplasm in ccRCC and oncocytoma; (b2) Scatter plots of the mean value of CD206/CD163 double positive cell number in the cytoplasm in ccRCC (non-met ccRCC vs met ccRCC); (c3) Bar graphs of the mean value of CD206/CD163 double positive cell number in the cytoplasm in ccRCC and oncocytoma; Lines across the raw data indicate mean value. ns, $p>0.05$, *, $p < 0.05$, **, $p < 0.01$, ***, $p < 0.001$, Sidak test after repeated measures two-way ANOVA or Tukey's multiple comparisons after two-way ANOVA. Error bars represent estimated standard errors of the mean. Abbreviation: met, metastatic; ccRCC, clear cell renal cell carcinoma; onco, oncocytoma.

5.5.7 Metastatic ccRCC exhibited smaller size of adipocytes.

Four out of the five participants in the cohort of metastatic ccRCC exhibited smaller median size of adipocytes compared to their counterparts in the cohort of non-metastatic ccRCC, even the difference from the paired-t test was not significant (**Fig 5.17 b**). The mean value of the median size of adipocytes was smaller in metastatic ccRCC perinephric adipose tissue (9518 pixels) compared to non-metastatic ccRCC perinephric adipose tissue (13434 pixels) and oncocytoma perinephric adipose tissue (13412 pixels), and the differences between groups were statistically significant. However, Tukey's multiple comparison did not find any significant difference in post hoc testing (**Fig 5.17 c**).

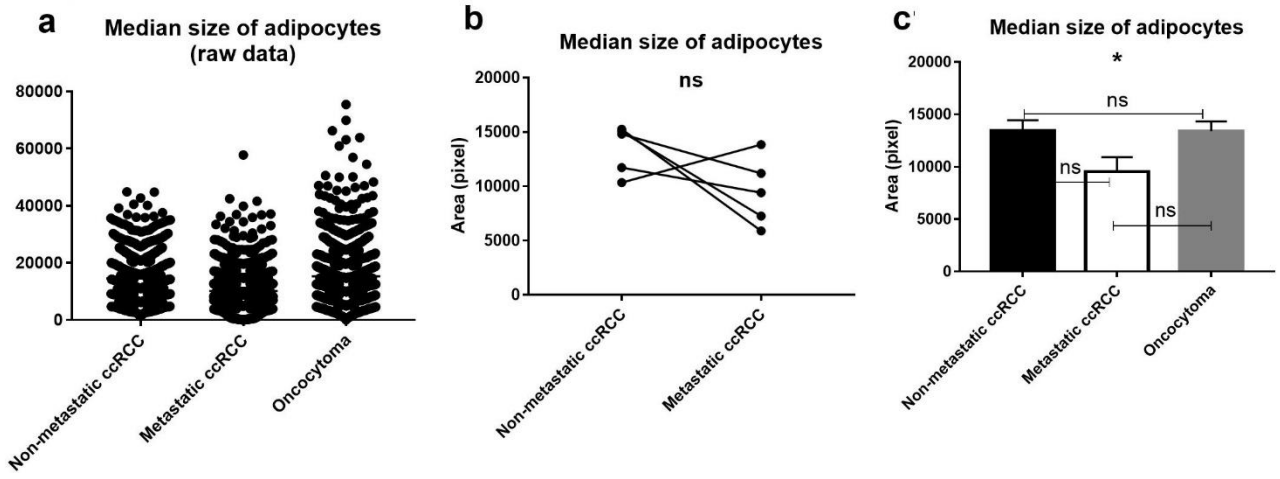

Fig 5.17 Median size of adipocytes

(a) Scatter plots of raw data of median size of adipocytes in ccRCC and oncocytoma; (b) Scatter plots of mean value of median size of adipocytes in ccRCC (non-met ccRCC vs met ccRCC); (c) Bar graphs of mean value of median size of adipocytes in ccRCC and oncocytoma; ns, $p>0.05$, * $p<0.05$, paired t-test or Tukey's multiple comparisons after one-way ANOVA. Error bars represent estimated standard errors.

5.6 Discussion

This is the first study using the multiplex immunofluorescence and digital analysis approaches to profile the immune phenotypes of macrophages in human perinephric adipose tissue. Based on the analysis of all the outcome variables that related to the expressive levels of the CD markers, it was found that almost all of the ccRCC samples with distant metastases expressed higher levels of CD206 and CD163, compared to the matched ccRCC samples without distant metastases, using all three thresholding. Similarly, compared to the cohort of oncocytoma which is a benign subtype of renal tumour, the cohort of ccRCC with distant metastasis exhibited higher mean expressive levels of CD206 and CD163. However, compared to the relatively small difference caused by the factor of tumour subtypes, which in most cases accounted for less than 10 % of the total variation of the CD68 expression, the effects caused by the factor of thresholding cannot be ignored. Hence, there is not enough evidence to deduce that the expression of CD68 varies between different subtypes of renal tumours with distinct aggressiveness. Moreover, it was found that there would possibly be a negative association between median sizes of adipocytes in the perinephric adipose tissue with the aggressiveness of renal tumours, as evidenced by smaller sizes measured in ccRCC samples with distant metastasis compared to the ccRCC cohort without distant metastasis and the oncocytoma cohort.

A team from Fudan University in Shanghai had investigated the prognostic value of macrophage phenotypes in ccRCC tumour tissue [217]. They discovered that an M2 phenotype in tumour tissue characterised by high CD206 and low CD11c expression was an independent prognostic factor for shorter ccRCC-specific survival. However, they did not find any prognostic potential for CD68. Consistent with their findings, CD68 expression in perinephric adipose tissue in the present study did not show a stable trend of variation between different subtypes of renal tumours, however CD206 expressive levels varied between different subtypes of renal tumours, with the most aggressive subtype, metastatic ccRCC, demonstrating the highest expression. The kidney cancer-specific prognostic value of macrophage immune profiles had never been investigated in kidney cancer-associated adipose tissue. However, relevant research questions had been addressed in breast cancer. For example, similar to the finding in this study that metastatic ccRCC exhibited higher expression of CD163, it was reported that high CD163 expression in the adipose stroma of breast cancer independently predicted shorter cancer-specific survival [210]. However, unlike the result in another study based in the US, which found a prognostic potential for CD68 in discriminating invasive (high expression) and benign (low expression) breast tumours [213], CD68 expression levels in the perinephric adipose tissue in this present study did not show any discriminative potential for metastatic and non-metastatic ccRCC. The discrepancy may be due to different quantification

methods: subjective semi-quantitative evaluation was applied in the previous study, whereas objective digital quantification was applied in this present study based on three thresholding.

As a pilot experiment, this study provided valuable information, such as effect size and standard deviation, which is an important reference to decide optimal sample size in future studies to obtain adequate statistical power [334]. Taking the CD206/CD163 double positivity measured under the individual thresholding as an example, at least 15 paired samples are required when choosing a type 1 error (α) of 0.05 and a type 2 error (β) of 0.1 in the two-tailed paired-t test, using the following formula: "$N = [(z_{\alpha/2}+z_{\beta})\sigma/\delta]^2$", where the standard deviation of the paired difference (σ) = 0.3, the mean difference (δ) = 0.208, $z_{\alpha/2} = 1.96$, $z_{\beta} = 1.282$, N = paired sample number [335]. Given that only 5 paired samples were included to compare the difference between non-metastatic and metastatic ccRCC, there is a possibility that the "large" effect size of most outcome variables related to the expression of CD206 and CD163 (according to the Cohen's d value in **Table 5.3)** observed in this study might be caused by random variation [336]. However, the results reflected the expression of two different M2 markers and their colocalisation information. Additionally, the outcomes which were measured using various methods (i.e. mean intensity across the whole image, positivity across the whole image, total intensity in the segmented area and positive cell number in the cytoplasm) and under three thresholding were mostly consistent. Moreover, the trend that more aggressive ccRCC exhibited higher expression of M2 markers had been confirmed in previous relevant studies (**Table 1.2, Chapter 1**). Hence, a statistically significant difference between groups is likely to be detected within a larger sample size.

Another important finding in this study is that metastatic ccRCC adipose tissue exhibited smaller size of adipocytes compared to non-metastatic ccRCC and oncocytoma adipose tissue. Given that BMI, and age are important confounding factors when assessing the size of adipocytes, participants in the cohort of non-metastatic and metastatic ccRCC were matched for BMI and age initially [337]. Hence, the size differences in this case indicated that the metastatic ccRCC associated perinephric adipose tissue was undergoing more active cachexia related remodelling, such as fibrosis, adipocyte atrophy and browning [338]. It is unclear the association between this phenomenon and the other observation that increased infiltration of M2 macrophages in metastatic ccRCC adipose tissue. One possible mechanism is that M2 macrophages disrupted normal ECM structure in the cancer microenvironment through secreting MMP 9, which facilitated the invasion of renal tumours [339]. Monocyte-specific MMP-9 knock-out mice model could be established to assess the contribution of M2 macrophages in cancer metastasis. A recent study has revealed that recruited macrophages in the adipose tissue can functionally mediate lipid metabolism in obesity [222]. From the view of cancer metabolism, macrophages in the perinephric adipose tissue may be involved in the process of disrupting the

metabolic homeostasis in the adipose tissue therefore assisting the energy requirement of the neighboring cancer cells. Metabolomic profiling of macrophages in the tumour-associated adipose tissue could be a future direction to unveil the interaction of cancer metabolism and metastasis.

5.7 Conclusion

For the first time, this study confirmed in the perinephric adipose tissue that high expression of M2 macrophages may be associated with a high chance of metastasis, which is a prevalent paradigm. Metastasis-associated perinephric adipose tissue may undergo cachexia-related remodelling as indicated by the smaller size of adipocytes observed in metastasis-associated perinephric adipose tissue. How the crosstalk between macrophages and tumour-associated adipose tissue affects the progression of cancer can be explored from the view of lipid metabolism in future studies.

Chapter 6

Discussion and future directions

6.1 Overview

Accumulating evidence indicates there is a close interplay between adipose tissue biology and kidney cancer development. For example, obesity is an established risk factor for developing kidney cancer. Paradoxically, obese patients may have a better prognosis for kidney cancer. Of note, the most common subtype of kidney cancer, ccRCC, is characterised by lipid accumulation in cancer cells. However, roles of adipose tissue microenvironment remain elusive in kidney cancer.

The thesis explored GRP78 expression and macrophage immune phenotypes in human perinephric adipose tissue in an attempt to define their potential prognostic values for ccRCC, particularly with regard to metastasis. Additionally, a novel and cost-effective liquid overlay-based technique was applied to establish a 3D model to mimic the ER stress-activated perinephric adipose tissue microenvironment. Thereafter, macrophage behaviour, including migration/invasion and polarisation, was investigated in a co-culture system which included adipocyte spheroids and cancer cells.

There were 7 major findings:

1) GRP78 expression was not upregulated in ccRCC tissue compared to the adjacent normal kidney;

2) High ER stress levels in perinephric adipose tissue might be associated with a lower chance of developing metastasis in ccRCC;

3) The liquid overlay-based technique cost-effectively generated functional adipocyte spheroids that secreted adiponectin, MCP-1 and IL-8, and were responsive to the ER stress activator, tunicamycin;

4) Tunicamycin blocked the migration of the murine macrophage cell line Raw 264.7 towards adipocyte spheroids in an MCP-1 independent manner;

5) M1 macrophages differed from M2 macrophages in invasion capacity towards adipocyte spheroids, with invasive behaviour only observed for M2 macrophages;

6) The presence of M1 macrophages inhibited the invasion of KHOS and 786-0 cancer cell lines;

7) Metastatic ccRCC perinephric adipose tissue exhibited higher expression of CD206 and CD163 compared to the matched non-metastatic ccRCC samples.

The comprehensive discussions provided following the major findings in **Chapters 2** to **5** will not be reiterated in this chapter. Instead, some considerations have emerged from the results and these may help better understand the topics or advance the approaches for future research. These topics will be discussed in greater depth in the present discussion and future directions Chapter. Future directions

will be raised by reflecting limitations of the studies that were included in the thesis or by referring to other methodologies that have recently been published and applied in relevant research.

6.2 Discussion

6.2.1 Tissue heterogeneity will affect image analysis.

The findings in **Chapter 2** demonstrated GRP78 expression in ccRCC tumour tissue was not a valuable risk stratification marker of ccRCC. Neither the staining intensity based quantification nor the proportion of positive pixel based quantification detected a significate upregulation of GRP78 expression in ccRCC tumour tissue compared with the adjacent normal renal tissue, in contrast to what had been published previously [37]. To minimise the bias caused by heterogeneity between ccRCC tumour tissue and normal renal tissue, tissue compartments that may demonstrate a weak staining pattern of GRP78 or are impossible to stain, such as glomeruli, fibrosis and tubular lumen space, were manually eliminated from image analysis. Hence, the results faithfully reflected the very small difference in GRP78 expression between ccRCC tumour tissue and normal renal tissue, with little impact of tissue heterogeneity (**Table 2.2, Chapter 2**). Failure to account for tissue heterogeneity may, therefore, introduce bias when comparing the proportion of positively stained areas in different tissue types. However, the physiological or pathological conditions may also introduce bias relating to tissue heterogeneity even if there is only one type of tissue involved in analysis. For example, the statistically significant inverse association observed between BMI and proportion of positive pixels (correlation coefficient= - 0.20, $p = 0.02$) was contrary to the notion that ER stress can be caused by obesity (**Fig 2.8C, Chapter 2**) [340]. However, such a trend was observed when staining intensity was used to quantify the expression of GRP78, though the coefficient was small and insignificant (**Fig 2.8D, Chapter 2**). Further comparison between the staining patterns in tissues originated from two representative participants suggested that larger adipocytes for participants with higher BMI may leave the cellular stainable area smaller, because lipid was washed away during staining processing (**Figs 2.8A** and **2.8B**, **Chapter 2**). Hence, the change in adipose tissue morphology under obese conditions needs to be considered when performing image analysis.

6.2.2 Why did the topic progress from ER stress to macrophage behaviour?

A metastatic discrimination potential was found for GRP78 expression in perinephric adipose tissue, with one unit increase in average grey value of GRP78 staining (negatively associated with staining intensity) poorly ($p = 0.07$) correlating with a 17 % increased probability of ccRCC being diagnosed with metastasis (**Fig 2.5E, Chapter 2**). The result indicated that high ER stress levels in perinephric adipose tissue may exert protective functions by preventing metastasis in ccRCC. However, due to the small number of participants diagnosed with metastasis by pathologists according to the TNM staging system (n=9), no covariate was introduced in the logistic regression model to adjust potential bias. Hence, the role as a ccRCC metastatic indicator for ER stress level in perinephric adipose tissue is uncertain. A 3D culture model was therefore established to study the role of the ER stress-activated

adipose tissue microenvironment in kidney cancer metastasis (**Chapter 3**). Considering recent studies have demonstrated the contributions of TAM on metastasis and relevant mechanisms had never been addressed from the view of ER stress, the thesis then focused on the effects of an ER stress activated adipose tissue microenvironment on macrophage behaviour, especially for macrophage polarisation and migration (**Chapter 4**).

6.2.3 Adiponectin might protect adipocytes against the ER stress.

It was hypothesised in **Chapter 3** that increasing numbers of adipocyte spheroids maintained in a single well would cause ER stress due to a rapid consumption of nutrients. However, compared with 5 spheroid states, average mRNA expression of GRP78 (**Fig 3.11a2**) and sXBP1 (**Fig 3.11b2**) were lower in 20 spheroid states. The mechanism might be related to a protective role of adiponectin against ER stress. It had been reported that the lipolysis mediated by ER stress may help maintain the metabolism homeostasis in conditions of nutrient deprivation [341]. The saturated fatty acids released from adipocytes activated the pro-apoptotic ATF2-CHOP cascade of UPR and decreased synthesis of proteins [342, 343]. Deng *et al.* have found that adiponectin rescued the apoptosis in palmitate acid mediated ER stress through activating the PPARα-AMP activated protein kinase (AMPK)-protein kinase C (PKC) signaling pathway, which suppressed the activation of ATF2 [285]. Given that the concentration of total adiponectin in the conditioned medium increased with increasing adipocyte spheroid numbers, the ER stress caused by nutrient deprivation might be compromised (**Fig 3.10a1**). Investigating the fatty acid profiles when the same numbers of spheroids (e.g. 20) are maintained in the starvation medium and in the adipocyte maintenance medium would help to understand whether nutrient deprivation would influence the lipolysis of adipocytes. A comparison of UPR components with or without addition of the adiponectin neutralising antibody would help to clarify whether adiponectin is responsible for the blunted response to ER stress.

6.2.4 The mechanism underlying the unchanged M2 macrophage phenotype upon tunicamycin stimulation remains elusive.

Given that ER stress levels in perinephric adipose tissue may be negatively associated with the likelihood of developing metastasis in ccRCC and that an M2-like macrophage phenotype may favour cancer metastasis, it was hypothesised that ER stress could induce the M1 phenotype skew for M2 macrophages [293, 298]. However, results from flow cytometry analysis demonstrated that no dose response related upregulation of M1 markers or downregulation of M2 markers was observed in M2 macrophages upon tunicamycin treatment at concentrations from 2 to 4 μg/mL (**Fig 4.6, Chapter 4**). Considering M2 macrophages may be vulnerable to high doses of tunicamycin, with 97.5 % cell death observed upon exposure to 5 μg/mL of tunicamycin in a pilot experiment, no further increases in the dose were used for the purpose of augmenting the level of ER stress. The short exposure time (24 h)

to tunicamycin might be a limitation to the conclusion drawn that tunicamycin was unlikely to trigger reprograming of M2 macrophages to the M1 phenotype. However, Tarique and his colleagues found that macrophage polarisation induced by cytokine stimuli was reversible, with the phenotype profiles dramatically changed over resting polarised macrophages in cytokine-free medium [295]. Considering that 24 h is normally enough for an effective stimulus [e.g. toll like receptor (TLR)-3] to induce an evident M1 skew for M2 macrophages, investigation of the polarising effect of prolonged exposure to low dose of tunicamycin was not undertaken, thereby avoiding the bias caused by a spontaneous reverse of macrophage phenotype [344]. It was recently published that another ER stress activator, palmitate acid, induced the M1 phenotype shift of M2 macrophages through activating the PERK- eIF2α signaling pathway, which is a shared downstream cascade of UPR that can be activated by tunicamycin [345]. It would be informative to screen the secretory profiles and expression of ER stress associated proteins in M2 macrophages upon tunicamycin stimulation, considering contrary regulatory roles for macrophage phenotypes were found between palmitate acid and tunicamycin.

6.2.5 Limitations of the 3D models in the thesis

The established 3D co-culture model introduced in **Chapter 4** included cancer cell lines, M1 or M2 macrophages, adipocyte spheroids and a polycarbonate membrane coated with growth factor reduced basement membrane matrix. Adipocyte spheroids were separated from other cells by the transwell inserts, allowing indirect interactions between components on either side of the filter. The model fits in the setting of most cases of kidney cancer, in which renal tumours are not grown directly in the adipose stroma, like breast cancer. However, the involvement of the exogenous ECM which was extracted from Engelbreth-Holm-Swarm mouse sarcoma did not resemble the heterogeneous microenvironment of ccRCC [346]. Supplementation of cytokines that have been known to induce macrophage phenotype modulations made the co-culture system more controllable. However, it did not allow the effects of the perinephric adipose tissue on the polarisation and filtration of PBMC derived monocytes to be monitored directly. Although it is known that the established adipocyte spheroids could secrete adipokines and are responsive to ER stress stimulus (**Chapter 3**), a continuous functional assessment was lacking in the co-culture system. Even though the macrophage immune phenotypes in perinephric adipose tissue have been profiled in **Chapter 5**, continuous monitoring has not been done to evaluate whether a model of TAM residing in adipocyte spheroids can be recreated by long-term co-culture. Even with the limitations in the existing models, they are compatible to different screening systems and can be easily adapted by incorporating different cell types. One of the relevant approaches will be introduced in the section of 6.3.3.

6.2.6 Limitations of the adipocyte spheroids differentiated *in vitro*

Although intracellular unilocular lipid droplets (**Fig 3.5c**) and functional adiponectin secretion (**Fig 3.5d**) were observed in the adipocyte spheroids differentiated using the liquid overlay-based technique, the adipocyte spheroids differentiated *in vitro* may present different characteristics compared to the mature adipocytes residing in the perinephric adipose tissue. Adipocyte differentiation is mediated by multiple factors [347, 348]. Hence, variabilities in cultural conditions can affect the phenotype of the induced adipocytes. For example, the physiological adipogenic differentiation happens under a specific oxygen tension (8-9 %) [349]. It was reported that the high oxygen level in the incubator (21 %) would inhibit the adipogenic differentiation of MSC and the mechanism was related to an activated gene expression of *p53* [350]. Additionally, exposure of the high oxygen atmosphere induced a pro-inflammatory microenvironment, as evidenced by increased levels of reactive oxygen species and proinflammatory cytokines (e.g. IL-6 and IL-beta) being measured in the conditioned medium of ASC grown *in vitro* [349]. It has recently been noted that the growth hormone has antiadipogenic function via activating Wnt signaling [348, 351]. Supplementation with the growth hormone in the culture medium of MSC at a physiological concentration (5 ng/mL) could downregulate the expression of CCAAT/enhancer-binding protein alpha (C/EBPα, an adipogenic gene) while upregulating osteogenic genes, such as osterix and osteoprotegrin [352]. It should be noted that, in this thesis, 10 % FBS was supplemented in the adipogenic differentiation medium. FBS may contain some non-tested hormones that may affect the process of adipogenesis in an unknown manner [353, 354].

6.3 Future directions

6.3.1 Targeting cellular based ER stress profiles in perinephric adipose tissue

The routine IHC analysis across the whole image may be affected by tissue heterogeneity when comparing the expression of biomarkers in different tissue types. It is cumbersome to tailor the image for the purpose of eliminating compartments that may bias the results. Segmentation of cellular compartment-based single-cell analysis in FFPE tissue has provided a solution, in which individual cells are segmented to obtain cellular or subcellular quantification of biomarkers of interest [355]. However, DAPI counterstain based nuclear segmentation has limitations when applied to detect ER stress markers in live cell imaging, since the dye affects UPR signaling [356]. Considering that the extent of literature reporting relevant applications in human FFPE tissue is limited, it would be worth investigating the cellular based ER stress profiles in perinephric adipose tissue using either uniplex or multiplex IHC. Similar research questions, such as the association between ER stress levels and cancer aggressiveness, could be addressed by profiling the expression of other ER stress markers of interest, such as CHOP and eIF2α, in individual cells.

6.3.2 Targeting lipid metabolism in ccRCC diagnosis and treatment

Thanks to the increasing awareness of cancer screening, many cases of small renal masses (less than 4 cm in diameter) are diagnosed incidentally [357]. Developing non-invasive diagnostic techniques to detect reliable prognostic markers for small renal masses is important, since these would help discriminate malignancies that have a high chance of metastasis. Simultaneously, the new diagnostic techniques would minimise overtreatment of patients who would have a better prognosis without ablation surgery [358]. Except for a macroscopic cellular accumulation of lipids, altered lipid metabolism exists in ccRCC [359]. Lipidomic signatures may provide useful information for ccRCC diagnosis. For example, compared to the normal renal tissue, ccRCC tumour tissue is characterised by increased levels of cholesterol esters, ether-type phospholipids and triacylglycerols, and decreased levels of polyunsaturated fatty acids and most phospholipids [360]. Given that the secretory profile of adipocytes co-cultured with cancer cells was not screened in this present project, future research is encouraged to map the lipid metabolism in the ccRCC tumour tissue as well as in perinephric adipose tissue using the novel imaging modalities, such as nuclear magnetic resonance spectroscopy, which can provide non-invasive tools to visualise alterations in lipid metabolism in vivo [361]. Relevant data can help us better understand the fat-tumour interplay from the view of lipid metabolism. It was reported that upregulation of fatty acid synthase (FAS) in ccRCC tissue was associated positively with ccRCC aggressiveness [362]. Treatment with the FAS inhibitor. C75, impaired the cell viability and invasiveness of ccRCC cell lines [363]. Hence, targeting lipid metabolism is a promising strategy for finding novel synergistic treatments for metastatic ccRCC.

6.3.3 Adapting the 3D culture model by incorporating cancer-associated fibroblasts

ccRCC is a highly vascularised solid tumour characterised by various degrees of intratumoural fibrosis, with potential impacts on cancer aggressiveness [364]. Cancer-associated fibroblasts (CAF) may have a protumoural role by supporting tumourigenesis, angiogenesis, EMT and metastasis [365]. Compared to normal fibroblasts, CAF secrete more components of ECM, such as collagens and MMP [366, 367]. Given that CAF is an important tumour stromal component, replacing the commercial Matrigel in the co-culture system with CAF may facilitate study of the effects of the ccRCC tumour microenvironment on macrophage polarisation and invasion. Sofia and colleagues designed a 3D model with direct interactions of CAF, primary monocytes and lung cancer cell lines, which were encapsulated in alginate and maintained for 3 weeks in suspension cell culture under continuous stirring [368]. They found that the model recreated the structure of tumour tissue with collagen fibres intercalating cancer cells. Moreover, without addition of exogenous cytokines, the secretory profiles of the co-culture system promoted an M2-like phenotype. In this co-culture system, CAF and monocytes were encapsulated with the tumour spheroids simultaneously. It would be of interest to

first build tumour spheroids with ECM accumulation, then monitor the invasion of monocytes into spheroids in real-time, and finally profile the macrophage immune phenotypes in spheroids. Given that the properties of CAF and their impacts on cancer development may vary between individuals, it would be valuable to record the volume of the spheroids over time and analyse the association of macrophage behaviour with the quantity of cytokines present in the conditioned medium, such as GM-CSF, CSF-1, IL-8, MCP-1, VEGF, TNF-α and MMP-9.

6.3.4 Applying single-cell technologies to unravel intratumoural heterogeneity

The tumour microenvironment is heterogeneous, with cell-cell interactions influencing the cancer progression. For example, it was reported in **Chapter 4** that the presence of M1 macrophages inhibited the invasion of cancer cells, whereas the effects of M2 macrophages varied between KHOS (**Fig 4.12c**) and 786-0 (**Fig 4.13c**) cell lines. It is unclear whether the inhibited invasion in the presence of M1 macrophages was due to a phagocytic effect or the interactions of cancer cells and M2 macrophages promoted the process of EMT in cancer cells. Applying single-cell RNA sequencing will enable detecting the holistic shift of the transcriptional features after modulating the cell composition in the co-culture system, therefore uncovering potential mechanisms underlying the distinct cellular behaviour [369]. By combining single-cell RNA sequencing with high-throughput digital imaging of RNA fluorescence in situ hybridization (FISH), the findings in in vitro models can be translated into patient samples, providing distributional information of those functional "units" across the tissue [370]. The spatial information can be further translated into risk predictive models for cancers. For example, combining single-cell RNA sequencing and FISH techniques, a group from Harvard has successfully used the spatial localisation of EMT and proliferative cell composition in primary and liver metastatic sites of pancreatic ductal adenocarcinoma to risk stratify patients [371].

6.3.5 Targeting adipose tissue to restore metabolic homeostasis in cachexia

Associated with poor cancer survival, cachexia is characterised by ≥ 5 % weight loss and functional abnormalities including a hypermetabolic state, anaemia, tissue wasting and systemic inflammation [338]. Adipose tissue undergoes dramatic remodelling during cancer cachexia, including browning, adipocyte atrophy and increased fibrotic and inflammatory infiltration [372]. Adipose tissue has a great impact on the metabolism of cancer cells under cachexia. Huang et al. found that the process of adipogenesis in the adipose tissue was suppressed in an adipocyte-specific SQSTM1 ablated mouse model bearing prostate cancer, serving to save nutrition and energy to profit the demand of cancer progression. SQSTM1 is the gene encoding an autophagy-associated protein, P62. The mechanism was related to downregulated mTORC1 and PPAR α in adipocytes and an inverse upregulated profile in cancer cells [150]. It would be promising to modulate nutrient-utilising pathways in the adipose tissue to reverse the metabolic profiles that favour the growth of cancer cells. The importance of

adipose tissue-associated macrophages in maintaining the metabolic homeostasis in adipose tissue has been underestimated. Using single-cell based techniques, a functional subset of adipose tissue-associated macrophages (CD9 and CD36 double positive) has been recently found. Recruited from circulating monocytes, the macrophages were also positive for triggering receptor expressed on myeloid cells 2 (Trem2) and conservatively expressed a genomic signature involved in lipid metabolism and endocytosis, including LIPA, CTSB, CTSL, FABP4, FABP5, LGAL3, CD9 and CD36. Functional analysis demonstrated that Trem2 expressing macrophages were key mediators in lipid metabolism upon loss of adipose tissue homeostasis in obesity [222]. Future research is warranted to profile the TREM2 signaling pathways in cachexia-associated adipose tissue to find potential drivers for the metabolic abnormalities in cachexia. The information yielded from these studies may facilitate novel drug design targeting cachexia.

6.3.6 Exploring the mechanism underlying the "obesity paradox" in kidney cancer

Fig 5.17 demonstrated that the perinephric adipose tissue sampled from metastatic ccRCC exhibited smaller adipocytes (measured by median size) than those from non-metastatic ccRCC and benign renal tumours. Given that the histological phenotype of the perinephric adipose tissue is characterised by multilocular brown adipocytes interspersing with unilocular white adipocytes, the result shown in **Fig 5.17** could also be interpreted as the most aggressive ccRCC have fewer unilocular white adipocytes in the perinephric adipose tissue, which may be a sign of active fat browning [132]. If the perinephric adipose tissue of obese individuals is less "brownable" than its counterpart in lean individuals, the blunted tumour-associated adipose tissue remodelling, under obesity, could be a mechanism that explains the "obesity paradox" in kidney cancer. Further research is needed to elucidate the different content of brown adipocytes or brown fat precursor cells in perinephric adipose tissue of obese and lean individuals under a healthy status. Research mapping the whole-body BAT composition is available, however kidney tissue-specific data are missing [373]. Screening the process of BAT activation, vasculature remodelling and metabolic state within the perinephric adipose tissue in obese and lean subjects should provide their relevance in tumourigenesis. Furthermore, it would be necessary to elucidate whether the metabolic crosstalk between adipocytes and cancer cells exhibits a different profile when investigated in an obese or a lean microenvironment. If proved to be a cause of kidney cancer-associated cachexia or metastasis, targeting the browning of perinephric adipose tissue is promising in suppressing the progression of aggressive kidney cancer.

6.4 Conclusions

This thesis broadly explored the role of the adipose tissue microenvironment in kidney cancer, particularly focusing on using the perinephric adipose tissue. In addition to risk stratifying ccRCC patients using the IHC profiles of ER stress biomarkers and macrophage immunophenotypes, the thesis established a 3D co-culture model to investigate macrophage behaviour in the adipose tissue microenvironment. Many interesting findings have been discovered. Some are contrary to previous publications (e.g. no difference of GRP78 expression was observed between tumour tissue and normal renal tissue in ccRCC compared with Fu *et al.* who found increased GRP78 expression in tumour tissue [37]; ER stress did not upregulate with increasing numbers of adipocyte spheroids compared with Klingelhutz *et al.* who found the opposite [258]), and some have confirmed prevalent paradigms (e.g. ER stress upregulated with increasing BMI; co-culture of mature adipocytes promoted an M2 phenotype skew in unpolarised macrophages; M2 macrophages exhibited stronger invasive capacity than M1 macrophages and the mechanism was related to distinct integrin expression levels between M1 and M2 macrophages). There are still some novel observations that cannot be fully and convincingly interpreted, based on the limited exploration of the mechanisms (e.g. Tunicamycin blocked the migration of Raw 267.4 cells; the presence of M1 macrophages inhibited the invasion of cancer cell lines, whereas the presence of M2 macrophages exerted contrary effects on the invasion of KHOS and 786-0 cancer cell lines). Thus, there is an urgent need to identify the regulatory mechanisms that drive those behaviours of adipose tissue-associated macrophages and to understand the fat-cancer interplay in determining the metastasis of ccRCC. Although lipid metabolism is beyond the scope of the thesis, it is associated with macrophage behaviour, adipose tissue homeostasis and cancer progression, and therefore can become the focus of future studies. Adipose tissue is a “treasure box”. Combining routine cell culture with advanced sequencing and imaging techniques would no doubt help better understand the molecular mechanisms underlying the association of adipose tissue with cancer progression. In line with the planned goals, the thesis has resulted in development of understanding the heterogeneity of the adipose tissue microenvironment and its functions in ccRCC progression.

References

[1] C. Himbert, M. Delphan, D. Scherer, L.W. Bowers, S. Hursting, C.M. Ulrich. Signals from the adipose microenvironment and the obesity-cancer link-A systematic review, (2017), Cancer Prev Res (Phila), 10 (9), p. 494-506.
[2] B. Lauby-Secretan, C. Scoccianti, D. Loomis, Y. Grosse, F. Bianchini, K. Straif. Body fatness and cancer-Viewpoint of the IARC Working Group, (2016), N Engl J Med, 375 (8), p. 794-798.
[3] Y. Choi, B. Park, B.C. Jeong, S.I. Seo, S.S. Jeon, H.Y. Choi, H.O. Adami, J.E. Lee, H.M. Lee. Body mass index and survival in patients with renal cell carcinoma: a clinical-based cohort and meta-analysis, (2013), Int J Cancer, 132 (3), p. 625-634.
[4] I. Almendros, A. Gileles-Hillel, A. Khalyfa, Y. Wang, S.X. Zhang, A. Carreras, R. Farré, D. Gozal. Adipose tissue macrophage polarization by intermittent hypoxia in a mouse model of OSA: Effect of tumor microenvironment, (2015), Cancer Lett, 361 (2), p. 233-239.
[5] N.K. Sharma, S.K. Das, A.K. Mondal, O.G. Hackney, W.S. Chu, P.A. Kern, N. Rasouli, H.J. Spencer, A. Yao-Borengasser, S.C. Elbein. Endoplasmic reticulum stress markers are associated with obesity in nondiabetic subjects, (2008), J Clin Endocrinol Metab., 93 (11), p. 4532-4541.
[6] N. Kawasaki, R. Asada, A. Saito, S. Kanemoto, K. Imaizumi. Obesity-induced endoplasmic reticulum stress causes chronic inflammation in adipose tissue, (2012), Sci Rep, 2 p. 799.
[7] V. Beral, D. Bull, J. Green, G. Reeves. Ovarian cancer and hormone replacement therapy in the Million Women Study, (2007), Lancet, 369 (9574), p. 1703-1710.
[8] The American Cancer Society Medical and Editorial Content Team. Can kidney cancer be found early? https://www.cancer.org/cancer/kidney-cancer/detection-diagnosis-staging/detection.html (Accessed on 1/08/2017).
[9] R.H. Thompson, M.A. Ordonez, A. Iasonos, F.P. Secin, B. Guillonneau, P. Russo, K. Touijer. Renal cell carcinoma in young and old patients-Is there a difference?, (2008), J Urol., 180 (4), p. 1262-1266.
[10] F. Bray, J. Ferlay, I. Soerjomataram, R.L. Siegel, L.A. Torre, A. Jemal. Global cancer statistics 2018: GLOBOCAN estimates of incidence and mortality worldwide for 36 cancers in 185 countries, (2018), CA Cancer J Clin, 68 (6), p. 394-424.
[11] M.B. Atkins, T.K. Choueiri. Epidemiology, pathology, and pathogenesis of renal cell carcinoma https://www-uptodate-com.ezproxy.library.uq.edu.au/contents/epidemiology-pathology-and-pathogenesis-of-renal-cell-carcinoma?source=see_link (Accessed on 5/03/2019).
[12] B.I. Rini, S.C. Campbell, B. Escudier. Renal cell carcinoma, (2009), Lancet, 373 (9669), p. 1119-1132.
[13] J.L. Ericsson, R. Seljelid, S. Orrenius. Comparative light and electron microscopic observations of the cytoplasmic matrix in renal carcinomas, (1966), Virchows Arch Pathol Anat Physiol Klin Med, 341 (3), p. 204-223.

[14] C.J. Ricketts, A.A. De Cubas, H. Fan, C.C. Smith, M. Lang, E. Reznik, R. Bowlby, E.A. Gibb, R. Akbani, R. Beroukhim, D.P. Bottaro, T.K. Choueiri, R.A. Gibbs, A.K. Godwin, S. Haake, A.A. Hakimi, E.P. Henske, J.J. Hsieh, T.H. Ho, R.S. Kanchi, B. Krishnan, D.J. Kwiatkowski, W. Lui, M.J. Merino, G.B. Mills, J. Myers, M.L. Nickerson, V.E. Reuter, L.S. Schmidt, C.S. Shelley, H. Shen, B. Shuch, S. Signoretti, R. Srinivasan, P. Tamboli, G. Thomas, B.G. Vincent, C.D. Vocke, D.A. Wheeler, L. Yang, W.Y. Kim, A.G. Robertson, P.T. Spellman, W.K. Rathmell, W.M. Linehan. The cancer genome atlas comprehensive molecular characterization of renal cell carcinoma, (2018), Cell Rep, 23 (12), p. 3698.

[15] G. Guangwu, G. Yaoting, G. Shengjie, T. Aifa, H. Xueda, H. Yi, J. Wenlong, L. Zesong, H. Minghui, S. Liang, S. Pengfei, S. Xiaojuan, Z. Xiaokun, Y. Sangming, L. Chaozhao, W. Shengqing, Z. Fangjian, C. Chao, Z. Jialou, L. Xianxin, J. Minghan, Z. Liang, Y. Rui, H. Peide, C. Jing, J. Tao, L. Xiao, W. Yong, Z. Jing, J. Zhimao, W. Renhua, W. Song, F. Fan, Z. Zhongfu, L. Lin, Y. Ruilin, L. Xingwang, W. Haibo, Y. Weihua, Z. Xia, L. Yuchen, P. Huanhuan, J. Binghua, F. Qingxin, L. Cailing, X. Jun, L. Jingxiao, K. Karsten, L. Yingrui, Z. Xiuqing, L. Songgang, W. Jian, Y. Huanming, C. Zhiming, W. Jun. Frequent mutations of genes encoding ubiquitin-mediated proteolysis pathway components in clear cell renal cell carcinoma, (2011), Nat. Genet., 44 (1), p. 17.

[16] S. Nabi, E.R. Kessler, B. Bernard, T.W. Flaig, E.T. Lam. Renal cell carcinoma: a review of biology and pathophysiology, (2018), F1000Res, 7 p. 307-307.

[17] W. Du, L. Zhang, A. Brett-Morris, B. Aguila, J. Kerner, C.L. Hoppel, M. Puchowicz, D. Serra, L. Herrero, B.I. Rini, S. Campbell, S.M. Welford. HIF drives lipid deposition and cancer in ccRCC via repression of fatty acid metabolism, (2017), Nat Commun, 8 (1), p. 1769.

[18] S.B. Yadlapalli, D. Shi, U. Vaishampayan, Renal cell carcinoma: clinical presentation, staging, and prognostic factors, in: P.N. Lara, E. Jonasch (Eds.), Kidney cancer: principles and practice, Springer Cham, 2015, p. 105-121.

[19] J. Shen, Z. Chen, Q. Zhuang, M. Fan, T. Ding, H. Lu, X. He. Prognostic value of serum lactate dehydrogenase in renal cell carcinoma: A systematic review and meta-analysis, (2016), PloS one, 11 (11), p. e0166482-e0166482.

[20] R.J. Motzer, M. Mazumdar, J. Bacik, W. Berg, A. Amsterdam, J. Ferrara. Survival and prognostic stratification of 670 patients with advanced renal cell carcinoma, (1999), J Clin Oncol, 17 (8), p. 2530-2540.

[21] N. Kroeger, W. Xie, J.L. Lee, G.A. Bjarnason, J.J. Knox, M.J. Mackenzie, L. Wood, S. Srinivas, U.N. Vaishamayan, S.Y. Rha, S.K. Pal, T. Yuasa, F. Donskov, N. Agarwal, C.K. Kollmannsberger, M.H. Tan, S.A. North, B.I. Rini, T.K. Choueiri, D.Y. Heng. Metastatic non-clear cell renal cell carcinoma treated with targeted therapy agents: characterization of survival outcome

and application of the International mRCC Database Consortium criteria, (2013), Cancer, 119 (16), p. 2999-3006.
[22] R. Pichler, E. Compérat, T. Klatte, M. Pichler, W. Loidl, L. Lusuardi, M. Schmidinger. Renal cell carcinoma with sarcomatoid features: Finally new therapeutic hope?, (2019), Cancers, 11 (3), p. 422.
[23] Y. Wang, H. Wang, Q. Zhao, Y. Xia, X. Hu, J. Guo. PD-L1 induces epithelial-to-mesenchymal transition via activating SREBP-1c in renal cell carcinoma, (2015), Med Oncol, 32 (8), p. 212.
[24] U. Kucuk, E.E. Pala, O. Sezer, E. Caki, U. Bayol, R.T. Divrik. Significance of TNM staging, demographic and histologic features in predicting the prognosis of renal cell carcinoma, (2015), Acta Chir Belg, 115 (3), p. 202-207.
[25] V. Ficarra, G. Novara, M. Iafrate, L. Cappellaro, E. Bratti, F. Zattoni, W. Artibani. Proposal for reclassification of the TNM staging system in patients with locally advanced (pT3-4) renal cell carcinoma according to the cancer-related outcome, (2007), Eur Urol, 51 (3), p. 722-729; discussion 729-731.
[26] American Cancer Society. Cancer Facts & Figures 2019 https://www.cancer.org/content/dam/cancer-org/research/cancer-facts-and-statistics/annual-cancer-facts-and-figures/2019/cancer-facts-and-figures-2019.pdf (Accessed on 14/09/2019).
[27] L. Yang, B.F. Drake, G.A. Colditz. Obesity and other cancers, (2016), J Oncol, 34 (35), p. 4231-4237.
[28] N. Donin, A. Pantuck, P. Klopfer, P. Bevan, B. Fall, J. Said, A. Belldegrun, K. Chamie. Body mass index and survival in a prospective randomized trial of localized high-risk renal cell carcinoma, (2016), Cancer Epidemiol Biomarkers Prev, 25 (9), p. 1326-1332.
[29] W.K. Lee, S.K. Hong, S. Lee, C. Kwak, J.J. Oh, C.W. Jeong, Y.J. Kim, S.H. Kang, S.H. Hong, S.-S. Byun. Prognostic value of body mass index according to histologic subtype in nonmetastatic renal cell carcinoma: A large cohort analysis, (2015), Clin Genitourin Cancer, 13 (5), p. 461-468.
[30] H.W. Lee, B.C. Jeong, S.I. Seo, S.S. Jeon, H.M. Lee, H.Y. Choi, H.G. Jeon. Prognostic significance of visceral obesity in patients with advanced renal cell carcinoma undergoing nephrectomy, (2015), Int J Urol, 22 (5), p. 455-461.
[31] G. Kaneko, A. Miyajima, K. Yuge, S. Yazawa, R. Mizuno, E. Kikuchi, M. Jinzaki, M. Oya. Visceral obesity is associated with better recurrence-free survival after curative surgery for Japanese patients with localized clear cell renal cell carcinoma, (2015), Jpn J Clin Oncol, 45 (2), p. 210-216.
[32] R. Mizuno, A. Miyajima, T. Hibi, A. Masuda, T. Shinojima, E. Kikuchi, M. Jinzaki, M. Oya. Impact of baseline visceral fat accumulation on prognosis in patients with metastatic renal cell carcinoma treated with systemic therapy, (2017), Med Oncol, 34 (4), p. 47.

[33] Y.H. Park, J.K. Lee, K.M. Kim, H.R. Kook, H. Lee, K.B. Kim, S. Lee, S.S. Byun, S.E. Lee. Visceral obesity in predicting oncologic outcomes of localized renal cell carcinoma, (2014), J Urol., 192 (4), p. 1043-1049.
[34] M. Sun, A. Larcher, P.I. Karakiewicz. Optimal first-line and second-line treatments for metastatic renal cell carcinoma: current evidence, (2014), Int J Nephrol Renovasc Dis, 7 p. 401-407.
[35] T.K. Choueiri, D.J. Figueroa, A.P. Fay, S. Signoretti, Y. Liu, R. Gagnon, K. Deen, C. Carpenter, P. Benson, T.H. Ho, L. Pandite, P. De Souza, T. Powles, R.J. Motzer. Correlation of PD-L1 tumor expression and treatment outcomes in patients with renal cell carcinoma receiving sunitinib or pazopanib: Results from COMPARZ, a randomized controlled trial, (2015), Clin Cancer Res, 21 (5), p. 1071-1077.
[36] M. Weinstock, D. McDermott. Targeting PD-1/PD-L1 in the treatment of metastatic renal cell carcinoma, (2015), Ther Adv Urol., 7 (6), p. 365-377.
[37] W. Fu, X. Wu, J. Li, Z. Mo, Z. Yang, W. Huang, Q. Ding. Upregulation of GRP78 in renal cell carcinoma and its significance, (2010), Urology, 75 (3), p. 603-607.
[38] K. von Schwarzenberg, S.A. Held, A. Schaub, K.M. Brauer, A. Bringmann, P. Brossart. Proteasome inhibition overcomes the resistance of renal cell carcinoma cells against the PPARgamma ligand troglitazone, (2009), Cell Mol Life Sci., 66 (7), p. 1295-1308.
[39] L. Westrate, J. Lee, W. Prinz, G. Voeltz. Form follows function: The importance of endoplasmic reticulum shape, (2015), Annu Rev Biochem, 84 p. 791-811.
[40] A. Patrizia, S. Afshin, Endoplasmic reticulum stress in health and disease, Springer Netherlands, Dordrecht, 2012.
[41] M. Bergeron, P. Gaffiero, G. Thiery. Segmental variations in the organization of the endoplasmic reticulum of the rat nephron: A stereomicroscopic study, (1987), Cell Tissue Res, 247 (1), p. 215-225.
[42] H. Pavenstadt, W. Kriz, M. Kretzler. Cell biology of the glomerular podocyte, (2003), Physiol Rev, 83 (1), p. 253-307.
[43] D. Drummond, C. Wilke. The evolutionary consequences of erroneous protein synthesis, (2009), Nat Rev Genet, 10 (10), p. 715-724.
[44] P. Walter, D. Ron. The unfolded protein response: from stress pathway to homeostatic regulation, (2011), Science (New York, N.Y.), 334 (6059), p. 1081.
[45] A. Fink. Protein aggregation: folding aggregates, inclusion bodies and amyloid, (1998), Fold Des, 3 (1), p. R9-R23.
[46] F. Hartl, M. Hayer-Hartl. Molecular chaperones in the cytosol: from nascent chain to folded protein, (2002), Science (New York, N.Y.), 295 (5561), p. 1852.

[47] H. Saibil. Chaperone machines for protein folding, unfolding and disaggregation, (2013), Nat Rev Mol Cell Biol, 14 (10), p. 630-642.
[48] R. Mattoo, S. Sharma, S. Priya, A. Finka, P. Goloubinoff. Hsp110 is a bona fide chaperone using ATP to unfold stable misfolded polypeptides and reciprocally collaborate with Hsp70 to solubilize protein aggregates, (2013), J Biol Chem., 288 (29), p. 21399-21411.
[49] B. Bukau, A. Horwich. The Hsp70 and Hsp60 chaperone machines, (1998), Cell, 92 (3), p. 351-366.
[50] G. Zavilgelsky, V. Kotova, M. Mazhul, I. Manukhov. Role of Hsp70 (DnaK-DnaJ-GrpE) and Hsp100 (ClpA and ClpB) chaperones in refolding and increased thermal stability of bacterial luciferases in Escherichia coli cells, (2002), Biochemistry (Mosc), 67 (9), p. 986-992.
[51] S. Sharma, P. De los Rios, P. Christen, A. Lustig, P. Goloubinoff. The kinetic parameters and energy cost of the Hsp70 chaperone as a polypeptide unfoldase, (2010), Nat Chem Biol, 6 (12), p. 914-920.
[52] A. Ruggiano, O. Foresti, P. Carvalho. ER-associated degradation: Protein quality control and beyond, (2014), J Cell Biol, 204 (6), p. 869.
[53] S. Clerc, C. Hirsch, D. Oggier, P. Deprez, C. Jakob, T. Sommer, M. Aebi. Htm1 protein generates the N-glycan signal for glycoprotein degradation in the endoplasmic reticulum, (2009), J Cell Biol, 184 (1), p. 159-172.
[54] C. Hirsch, R. Gauss, S.C. Horn, O. Neuber, T. Sommer. The ubiquitylation machinery of the endoplasmic reticulum, (2009), Nature, 458 (7237), p. 453.
[55] T. Satoh, Y. Chen, D. Hu, S. Hanashima, K. Yamamoto, Y. Yamaguchi. Structural basis for oligosaccharide recognition of misfolded glycoproteins by OS-9 in ER-associated degradation, (2010), Mol cell, 40 (6), p. 905-916.
[56] R. Gauss, E. Jarosch, T. Sommer, C. Hirsch. A complex of Yos9p and the HRD ligase integrates endoplasmic reticulum quality control into the degradation machinery, (2006), Nat Cell Biol, 8 (8), p. 849-854.
[57] D. Voges, P. Zwickl, W. Baumeister. The 26S proteasome: a molecular machine designed for controlled proteolysis, (1999), Annu Rev Biochem, 68 p. 1015-1068.
[58] L. Hendershot. The mammalian endoplasmic reticulum as a sensor for cellular stress, (2002), Cell Stress Chaperones, 7 (2), p. 222-229.
[59] A. Bertolotti, Y. Zhang, L. Hendershot, P.H. Heather, R. David. Dynamic interaction of BiP and ER stress transducers in the unfolded-protein response, (2000), Nat Cell Biol, 2 (6), p. 326.
[60] J. Shen, X. Chen, L. Hendershot, R. Prywes. ER stress regulation of ATF6 localization by dissociation of BiP/GRP78 binding and unmasking of Golgi localization signals, (2002), Dev Cell, 3 (1), p. 99-111.

[61] X. Chen, J. Shen, R. Prywes. The luminal domain of ATF6 senses endoplasmic reticulum (ER) stress and causes translocation of ATF6 from the ER to the Golgi, (2002), J Biol Chem., 277 (15), p. 13045-13052.
[62] Y. Adachi, K. Yamamoto, T. Okada, H. Yoshida, A. Harada, K. Mori. ATF6 is a transcription factor specializing in the regulation of quality control proteins in the endoplasmic reticulum, (2008), Cell Struct Funct, 33 (1), p. 75-89.
[63] B. Teske, T. Baird, R. Wek. Methods for analyzing eIF2 kinases and translational control in the unfolded protein response, (2011), Methods Enzymol, 490 p. 333-356.
[64] T. Baird, L. Palam, M. Fusakio, J. Willy, C.M. Davis, J.N. McClintick, T.G. Anthony, R.C. Wek. Selective mRNA translation during eIF2 phosphorylation induces expression of IBTKα, (2014), Mol Bio Cell, 25 (10), p. 1686-1697.
[65] Y. Li, Y. Guo, J. Tang, J. Jiang, Z. Chen. New insights into the roles of CHOP-induced apoptosis in ER stress, (2014), Acta Biochim Biophys Sin, 46 (8), p. 629-640.
[66] M. Choy, P. Yusoff, I. Lee, J. Newton, Catherine W. Goh, R. Page, S. Shenolikar, W. Peti. Structural and Functional Analysis of the GADD34:PP1 eIF2α Phosphatase, (2015), Cell Rep, 11 (12), p. 1885-1891.
[67] A. Hinnebusch, K. Natarajan. Gcn4p, a master regulator of gene expression, is controlled at multiple levels by diverse signals of starvation and stress, (2002), Eukaryot Cell, 1 (1), p. 22-32.
[68] J. Brewer, L. Hendershot, C. Sherr, J. Diehl. Mammalian unfolded protein response inhibits cyclin D1 translation and cell-cycle progression, (1999), Proc Natl Acad Sci U S A, 96 (15), p. 8505-8510.
[69] C. Piperi, C. Adamopoulos, A. Papavassiliou. XBP1: A pivotal transcriptional regulator of glucose and lipid metabolism, (2016), Trends Endocrinol Metab, 27 (3), p. 119-122.
[70] F. Brozzi, S. Gerlo, F. Grieco, M. Juusola, A. Balhuizen, S. Lievens, C. Gysemans, M. Bugliani, C. Mathieu, P. Marchetti, J. Tavernier, D.L. Eizirik. Ubiquitin D regulates IRE1alpha/c-Jun N-terminal kinase (JNK) protein-dependent apoptosis in pancreatic beta cells, (2016), J Biol Chem., 291 (23), p. 12040-12056.
[71] D. Nakamura, A. Tsuru, K. Ikegami, Y. Imagawa, N. Fujimoto, K. Kohno. Mammalian ER stress sensor IRE1β specifically down-regulates the synthesis of secretory pathway proteins, (2011), FEBS Lett, 585 (1), p. 133-138.
[72] Y. Imagawa, A. Hosoda, S. Sasaka, A. Tsuru, K. Kohno. RNase domains determine the functional difference between IRE1α and IRE1β, (2008), FEBS Lett, 582 (5), p. 656-660.
[73] M. Martino, L. Jones, B. Brighton, C. Ehre, L. Abdulah, C.W. Davis, D. Ron, W.K. O'Neal, C.M.P. Ribeiro. The ER stress transducer IRE1β is required for airway epithelial mucin production, (2013), Mucosal Immunol, 6 (3), p. 639-654.

[74] A. Tsuru, N. Fujimoto, S. Takahashi, M. Saito, D. Nakamura, M. Iwano, T. Iwawaki, H. Kadokura, D. Ron, K. Kohno. Negative feedback by IRE1beta optimizes mucin production in goblet cells, (2013), Proc Natl Acad Sci USA, 110 (8), p. 2864-2869.
[75] J. Kim, I. Tchernyshyov, G. Semenza, C. Dang. HIF-1-mediated expression of pyruvate dehydrogenase kinase: a metabolic switch required for cellular adaptation to hypoxia, (2006), Cell Metab, 3 (3), p. 177-185.
[76] D. Hanahan, R. Weinberg. Hallmarks of cancer: The next generation, (2011), Cell, 144 (5), p. 646-674.
[77] C. Koumenis. ER stress, hypoxia tolerance and tumor progression, (2006), Curr Mol Med, 6 (1), p. 55-69.
[78] N. Badiola, C. Penas, A. Miñano-Molina, B. Barneda-Zahonero, R. Fadó, G. Sánchez-Opazo, J.X. Comella, J. Sabriá, C. Zhu, K. Blomgren, C. Casas, J. Rodríguez-Alvarez. Induction of ER stress in response to oxygen-glucose deprivation of cortical cultures involves the activation of the PERK and IRE-1 pathways and of caspase-12, (2011), Cell Death Dis, 2 (4), p. e149.
[79] R. Shiu, J. Pouyssegur, I. Pastan. Glucose depletion accounts for the induction of two transformation-sensitive membrane proteinsin Rous sarcoma virus-transformed chick embryo fibroblasts, (1977), Proc Natl Acad Sci U S A, 74 (9), p. 3840-3844.
[80] D. Schewe, J. Aguirre-Ghiso. ATF6alpha-Rheb-mTOR signaling promotes survival of dormant tumor cells in vivo, (2008), Proc Natl Acad Sci USA, 105 (30), p. 10519-10524.
[81] Y. Hazari, A. Bashir, E. Haq, K. Fazili. Emerging tale of UPR and cancer: an essentiality for malignancy, (2016), Tumor Biol, 37 (11), p. 14381-14390.
[82] M. Bi, C. Naczki, M. Koritzinsky, D. Fels, J. Blais, N. Hu, H. Harding, I. Novoa, M. Varia, J. Raleigh, D. Scheuner, R.J. Kaufman, J. Bell, D. Ron, B.G. Wouters, C. Koumenis. ER stress-regulated translation increases tolerance to extreme hypoxia and promotes tumor growth, (2005), Embo J, 24 (19), p. 3470-3481.
[83] H. Tsai, Y. Yang, A. Wu, C. Yang, Y.P. Liu, Y.H. Jan, C.H. Lee, Y.W. Hsiao, C.T. Yeh, C.N. Shen, P.J. Lu, M.S. Huang, M. Hsiao. Endoplasmic reticulum ribosome-binding protein 1 (RRBP1) overexpression is frequently found in lung cancer patients and alleviates intracellular stress-induced apoptosis through the enhancement of GRP78, (2013), Oncogene, 32 (41), p. 4921-4931.
[84] Kim JY, Heo SH, Song IH, Park IA, Kim YA, Gong G, L. HJ. Activation of the PERK-eIF2 pathway is associated with tumor-infiltrating lymphocytes in HER2-positive breast cancer, (2016), Anticancer Res, 36 (6), p. 2705-2711.
[85] D. Ryan, S. Carberry, Á. Murphy, A. Lindner, J. Fay, S. Hector, N. McCawley, O. Bacon, C.G. Concannon, E.W. Kay, D.A. McNamara, J.H.M. Prehn. Calnexin, an ER-induced protein, is a

prognostic marker and potential therapeutic target in colorectal cancer, (2016), J Transl Med Epidemiol, 14 (1),
[86] X. Shen, Y. Xue, Y. Si, Q. Wang, Z. Wang, J. Yuan, X. Zhang. The unfolded protein response potentiates epithelial-to-mesenchymal transition (EMT) of gastric cancer cells under severe hypoxic conditions, (2015), Med Oncol, 32 (1), p. 1-7.
[87] Z. Niu, M. Wang, L. Zhou, L. Yao, Q. Liao, Y. Zhao. Elevated GRP78 expression is associated with poor prognosis in patients with pancreatic cancer, (2015), Sci Rep, 5 p. 16067.
[88] M. Shuda, N. Kondoh, N. Imazeki, K. Tanaka, T. Okada, K. Mori, A. Hada, M. Arai, T. Wakatsuki, O. Matsubara, N. Yamamoto, M. Yamamoto. Activation of the ATF6, XBP1 and GRP78 genes in human hepatocellular carcinoma: a possible involvement of the ER stress pathway in hepatocarcinogenesis, (2003), J Hepatol, 38 (5), p. 605-614.
[89] F. Al-Rawashdeh, P. Scriven, I. Cameron, P. Vergani, L. Wyld. Unfolded protein response activation contributes to chemoresistance in hepatocellular carcinoma, (2010), Eur J Gastroenterol Hepatol, 22 (9), p. 1099-1105.
[90] M. Storm, X. Sheng, Y. Arnoldussen, F. Saatcioglu. Prostate cancer and the unfolded protein response, (2016), Oncotarget, 7 (33), p. 54051-54066.
[91] J. Liu, M. Xiao, J. Li, D. Wang, Y. He, J. He, F. Gao, L. Mai, Y. Li, Y. Liang, Y. Liu, X. Zhong. Activation of UPR signaling pathway is associated with the malignant progression and poor prognosis in prostate cancer, (2017), Prostate, 77 (3), p. 274-281.
[92] A. Shimizu, K. Kaira, M. Yasuda, T. Asao, O. Ishikawa. Clinical and pathological significance of ER stress marker (BiP/GRP78 and PERK) expression in malignant melanoma, (2017), Pathol Oncol Res, 23 (1), p. 111-116.
[93] L. Lin, S. Lin, H. Chou. Role of asparagine synthetase in doxorubicin-induced resistance, (2013), Biomarkers and Genomic Medicine, 5 (3), p. 100-102.
[94] J. Cubillos-Ruiz, P. Silberman, M. Rutkowski, S. Chopra, A. Perales-Puchalt, M. Song, S. Zhang, Sarah E. Bettigole, D. Gupta, K. Holcomb, Lora H. Ellenson, T. Caputo, A.-H. Lee, Jose R. Conejo-Garcia, Laurie H. Glimcher. ER stress sensor XBP1 controls anti-tumor immunity by disrupting dendritic cell homeostasis, (2015), Cell, 161 (7), p. 1527-1538.
[95] F. Buontempo, E. Orsini, A. Lonetti, A. Cappellini, F. Chiarini, C. Evangelisti, C. Evangelisti, F. Melchionda, A. Pession, A. Bertaina, F. Locatelli, J. Bertacchini, L.M. Neri, J.A. McCubrey, A.M. Martelli. Synergistic cytotoxic effects of bortezomib and CK2 inhibitor CX-4945 in acute lymphoblastic leukemia: Turning offthe prosurvival ER chaperone BIP/Grp78 and turning on the proapoptotic NF-κB, (2016), Oncotarget, 7 (2), p. 1323-1340.

[96] Y. Zhong, Y. Zhang, P. Wang, H. Gao, C. Xu, H. Li. V8 induces apoptosis and the endoplasmic reticulum stress response in human multiple myeloma RPMI 8226 cells via the PERK-eIF2alpha-ATF4 signaling pathway, (2016), Oncol Lett, 12 (4), p. 2702-2709.
[97] L. Epple, R. Dodd, A. Merz, A. Dechkovskaia, M. Herring, B.A. Winston, A.M. Lencioni, R.L. Russell, H. Madsen, M. Nega, N.L. Dusto, J. White, D.D. Bigner, C.V. Nicchitta, N.J. Serkova, M.W. Graner. Induction of the unfolded protein response drives enhanced metabolism and chemoresistance in glioma cells, (2013), PloS one, 8 (8), p. e73267.
[98] M. Ni, H. Zhou, S. Wey, P. Baumeister, A. Lee. Regulation of PERK signaling and leukemic cell survival by a novel cytosolic isoform of the UPR regulator GRP78/BiP, (2009), PloS one, 4 (8),
[99] S. Krishn, S. Kaur, L. Smith, S. Johansson, M. Jain, A. Patel, S.K. Gautam, M.A. Hollingsworth, U. Mandel, H. Clausen, W.C. Lo, W.T.L. Fan, U. Manne, S.K. Batra. Mucins and associated glycan signatures in colon adenoma-carcinoma sequence: Prospective pathological implication(s) for early diagnosis of colon cancer, (2016), Cancer Lett, 374 (2), p. 304-314.
[100] Y. Jiang, Y. Zhou, Y. Zheng, H. Guo, L. Gao, P. Chen, D. Feng, R. Qi, X. Li, Y. Chang, F.F. Chu, Q. Gao. Expression of inositol-requiring enzyme 1β is downregulated in colorectal cancer, (2017), Oncol Lett, 13 (3), p. 1109-1118.
[101] F. Osorio, S. Tavernier, E. Hoffmann, Y. Saeys, L. Martens, J. Vetters, I. Delrue, R. De Rycke, E. Parthoens, P. Pouliot, T. Iwawaki, S. Janssens, B.N. Lambrecht. The unfolded-protein-response sensor IRE-1[alpha] regulates the function of CD8[alpha]+ dendritic cells, (2014), Nat Immunol, 15 (3), p. 248-257.
[102] J. Cubillos-Ruiz, S. Bettigole, L. Glimcher. Molecular pathways: Immunosuppressive roles of IRE1a-XBP1 Signaling in dendritic cells of the tumor microenvironment, (2016), Clin Cancer Res, 22 (9), p. 2121-2126.
[103] M. Shah, G. Schwartz. Cell cycle-mediated drug resistance: an emerging concept in cancer therapy, (2001), Clin Cancer Res, 7 (8), p. 2168-2181.
[104] A. Bianchi, S. Fischer, A. Robles, E. Rinchik, C. Conti. Overexpression of cyclin D1 in mouse skin carcinogenesis, (1993), Oncogene, 8 (5), p. 1127-1133.
[105] N. Arber, H. Hibshoosh, S. Moss, T. Sutter, Y. Zhang, M. Begg, S. Wang, I.B. Weinstein, P.R. Holt. Increased expression of cyclin D1 is an early event in multistage colorectal carcinogenesis, (1996), Gastroenterology, 110 (3), p. 669-674.
[106] E. Youssef, T. Hasuma, Y. Morishima, N. Takada, H. Osugi, M. Higashino, S. Otani, S. Fukushima. Overexpression of cyclin D1 in rat esophageal carcinogenesis model, (1997), Jpn J Cancer Res, 88 (1), p. 18-25.
[107] R. Donnellan, R. Chetty. Cyclin D1 and human neoplasia, (1998), Mol Pathol, 51 (1), p. 1.

[108] M. Drobnjak, I. Osman, H. Scher, M. Fazzari, C. Cordon-Cardo. Overexpression of cyclin D1 is associated with metastatic prostate cancer to bone, (2000), Clin Cancer Res., 6 (5), p. 1891-1895.
[109] O. Gautschi, D. Ratschiller, M. Gugger, D. Betticher, J. Heighway. Cyclin D1 in non-small cell lung cancer: a key driver of malignant transformation, (2007), Lung cancer, 55 (1), p. 1-14.
[110] K. Matsuo, M. Gray, D. Yang, S. Srivastava, P.B. Tripathi, L.A. Sonoda, E.-J. Yoo, L. Dubeau, A.S. Lee, Y.G. Lin. The endoplasmic reticulum stress marker, glucose-regulated protein-78 (GRP78) in visceral adipocytes predicts endometrial cancer progression and patient survival, (2012), Gynecol Oncol,
[111] F. Xia, J. Xu, P. Zhang, Y. Zhang, Q. Zhang, Z. Chao, F. Wang. Glucose-regulated protein 78 and heparanase expression in oral squamous cell carcinoma: correlations and prognostic significance, (2014), World J Surg Oncol, 12 p. 121.
[112] S. Daneshmand, M. Quek, E. Lin, C. Lee, R.J. Cote, D. Hawes, J. Cai, S. Groshen, G. Lieskovsky, D.G. Skinner, A.S. Lee, J. Pinski. Glucose-regulated protein GRP78 is up-regulated in prostate cancer and correlates with recurrence and survival, (2007), Hum Pathol, 38 (10), p. 1547-1552.
[113] Lim S, Park SG, Yoo JH, Park YM, Kim HJ, Jang KT, Cho JW, Yoo BC, Jung GH, P. CK. Expression of heat shock proteins （HSP27, HSP60, HSP70, HSP90,GRP78, GRP94） in hepatitis B virus-related hepatocellular carcinomas and dysplastic nodules, (2005), World J Gastroenterol, 11 (14), p. 2072-2079.
[114] Q. Wang, Z. He, J. Zhang, Y. Wang, T. Wang, S. Tong, L. Wang, S. Wang, Y. Chen. Overexpression of endoplasmic reticulum molecular chaperone GRP94 and GRP78 in human lung cancer tissues and its significance, (2005), Cancer Detect Prev, 29 (6), p. 544-551.
[115] L. Zhuang, R. Scolyer, C. Lee, S. McCarthy, W.A. Cooper, X.D. Zhang, J.F. Thompson, P. Hersey. Expression of glucose-regulated stress protein GRP78 is related to progression of melanoma, (2009), Histopathology, 54 (4), p. 462-470.
[116] R. Langer, M. Feith, J. Siewert, H. Wester, H. Hoefler. Expression and clinical significance of Glucose Regulated Proteins GRP78 (BiP) and GRP94 (GP96) in human adenocarcinomas of the esophagus, (2008), BMC Cancer, 8 p. 70-70.
[117] K. Uematsu, S. Ogata, K. Nakanishi, S. Hiroi, S. Tominaga, S. Aida, T. Kawai. Glucose-regulated protein 78 expression in urothelial carcinoma of the upper urinary tract, (2010), BJU Int, 106 (6), p. 873-878.
[118] V. Pellegrinelli, S. Carobbio, A. Vidal-Puig. Adipose tissue plasticity: how fat depots respond differently to pathophysiological cues, (2016), Diabetologia, 59 (6), p. 1075-1088.

[119] N. Ouchi, J.L. Parker, J.J. Lugus, K. Walsh. Adipokines in inflammation and metabolic disease, (2011), Nat Rev Immunol, 11 (2), p. 85-97.
[120] K. Shimada, T. Miyazaki, H. Daida. Adiponectin and atherosclerotic disease, (2004), Clin Chim Acta., 344 (1-2), p. 1-12.
[121] N. Ouchi, A. Higuchi, K. Ohashi, Y. Oshima, N. Gokce, R. Shibata, Y. Akasaki, A. Shimono, K. Walsh. Sfrp5 is an anti-inflammatory adipokine that modulates metabolic dysfunction in obesity, (2010), Science (New York, N.Y.), 329 (5990), p. 454-457.
[122] H. Selye, P.S. Timiras. Participation of 'Brown Fat' Tissue in the Alarm Reaction, (1949), Nature, 164 (4174), p. 745-746.
[123] W. Aherne, D. Hull. Brown adipose tissue and heat production in the newborn infant, (1966), The Journal of pathology and bacteriology, 91 (1), p. 223-234.
[124] T. Ito, Y. Tanuma, M. Yamamoto, C. Yokochi. The Occurrence of Brown Adipose Tissue in Perirenal Fat in Japanese, (1975), Archivum histologicum japonicum, 38 (1), p. 43-70.
[125] Y. Tanuma, M. Ohata, T. Ito, C. Yokochi. Possible Function of Human Brown Adipose Tissue as Suggested by Observation on Perirenal Brown Fats from Necropsy Cases of Variable Age Groups, (1976), Archivum histologicum japonicum, 39 (2), p. 117-145.
[126] F. Villarroya, A. Gavaldà-Navarro, M. Peyrou, J. Villarroya, M. Giralt. The Lives and Times of Brown Adipokines, (2017), Trends Endocrinol Metab, 28 (12), p. 855-867.
[127] J.E. Silva, P.R. Larsen. Adrenergic activation of triiodothyronine production in brown adipose tissue, (1983), Nature, 305 (5936), p. 712-713.
[128] G. Gaich, J.Y. Chien, H. Fu, L.C. Glass, M.A. Deeg, W.L. Holland, A. Kharitonenkov, T. Bumol, H.K. Schilske, D.E. Moller. The effects of LY2405319, an FGF21 analog, in obese human subjects with type 2 diabetes, (2013), Cell Metab, 18 (3), p. 333-340.
[129] K.D. Nguyen, Y. Qiu, X. Cui, Y.P. Goh, J. Mwangi, T. David, L. Mukundan, F. Brombacher, R.M. Locksley, A. Chawla. Alternatively activated macrophages produce catecholamines to sustain adaptive thermogenesis, (2011), Nature, 480 (7375), p. 104-108.
[130] S. Kralisch, A. Hoffmann, N. Klöting, A. Frille, H. Kuhn, M. Nowicki, S. Paeschke, A. Bachmann, M. Blüher, M.Z. Zhang, R.C. Harris, M. Stumvoll, M. Fasshauer, T. Ebert. The brown fat-secreted adipokine neuregulin 4 is decreased in human and murine chronic kidney disease, (2019), Eur J Endocrinol, 181 (2), p. 151-159.
[131] Z. Chen, G.X. Wang, S.L. Ma, D.Y. Jung, H. Ha, T. Altamimi, X.Y. Zhao, L. Guo, P. Zhang, C.R. Hu, J.X. Cheng, G.D. Lopaschuk, J.K. Kim, J.D. Lin. Nrg4 promotes fuel oxidation and a healthy adipokine profile to ameliorate diet-induced metabolic disorders, (2017), Mol Metab, 6 (8), p. 863-872.

[132] F.G. Shellock, M.S. Riedinger, M.C. Fishbein. Brown adipose tissue in cancer patients: possible cause of cancer-induced cachexia, (1986), J Cancer Res Clin Oncol, 111 (1), p. 82-85.
[133] M.A.V. Cavagnari, T.D. Silva, M.A.H. Pereira, L.J. Sauer, D. Shigueoka, S.S. Saad, K. Barão, C.C.D. Ribeiro, N.M. Forones. Impact of genetic mutations and nutritional status on the survival of patients with colorectal cancer, (2019), BMC Cancer, 19 (1),
[134] G.S. Naik, S.S. Waikar, A.E.W. Johnson, E.I. Buchbinder, R. Haq, F.S. Hodi, J.D. Schoenfeld, P.A. Ott. Complex inter-relationship of body mass index, gender and serum creatinine on survival: Exploring the obesity paradox in melanoma patients treated with checkpoint inhibition, (2019), J Immunother Cancer, 7 (1),
[135] M. Ebadi, L. Martin, S. Ghosh, C.J. Field, R. Lehner, V.E. Baracos, V.C. Mazurak. Subcutaneous adiposity is an independent predictor of mortality in cancer patients, (2017), Br J Cancer, 117 (1), p. 148-155.
[136] J.A. Vaitkus, F.S. Celi. The role of adipose tissue in cancer-associated cachexia, (2017), Exp Biol Med (Maywood), 242 (5), p. 473-481.
[137] E.E. Calle, R. Kaaks. Overweight, obesity and cancer: epidemiological evidence and proposed mechanisms, (2004), Nat Rev Cancer, 4 (8), p. 579-591.
[138] L.A. Zúñiga, W.J. Shen, B. Joyce-Shaikh, E.A. Pyatnova, A.G. Richards, C. Thom, S.M. Andrade, D.J. Cua, F.B. Kraemer, E.C. Butcher. IL-17 regulates adipogenesis, glucose homeostasis, and obesity, (2010), Journal of immunology (Baltimore, Md. : 1950), 185 (11), p. 6947-6959.
[139] Y.S. Yoon, A.R. Kwon, Y.K. Lee, S.W. Oh. Circulating adipokines and risk of obesity related cancers: A systematic review and meta-analysis, (2019), Obes Res Clin Pract,
[140] S.I. Grivennikov, M. Karin. Dangerous liaisons: STAT3 and NF-kappaB collaboration and crosstalk in cancer, (2010), Cytokine Growth Factor Rev, 21 (1), p. 11-19.
[141] F. Colotta, P. Allavena, A. Sica, C. Garlanda, A. Mantovani. Cancer-related inflammation, the seventh hallmark of cancer: Links to genetic instability, (2009), Carcinogenesis, 30 (7), p. 1073-1081.
[142] Product Information [PDF on Internet]. Sigma, [cited 31th May 2019] Available from: https://www.sigmaaldrich.com/content/dam/sigma-aldrich/docs/Sigma/Product_Information_Sheet/1/10771pis.pdf,
[143] B.R. Seo, P. Bhardwaj, S. Choi, J. Gonzalez, R.C. Andresen Eguiluz, K. Wang, S. Mohanan, P.G. Morris, B. Du, X.K. Zhou, L.T. Vahdat, A. Verma, O. Elemento, C.A. Hudis, R.M. Williams, D. Gourdon, A.J. Dannenberg, C. Fischbach. Obesity-dependent changes in interstitial ECM mechanics promote breast tumorigenesis, (2015), Science translational medicine, 7 (301), p. 301ra130.

[144] N.L. Springer, N.M. Iyengar, R. Bareja, A. Verma, M.S. Jochelson, D.D. Giri, X.K. Zhou, O. Elemento, A.J. Dannenberg, C. Fischbach. Obesity-Associated Extracellular Matrix Remodeling Promotes a Macrophage Phenotype Similar to Tumor-Associated Macrophages, (2019), Am J Pathol, 189 (10), p. 2019-2035.
[145] T. Okumura, K. Ohuchida, S. Kibe, C. Iwamoto, Y. Ando, S. Takesue, H. Nakayama, T. Abe, S. Endo, K. Koikawa, M. Sada, K. Horioka, N. Mochidome, M. Arita, T. Moriyama, K. Nakata, Y. Miyasaka, T. Ohtsuka, K. Mizumoto, Y. Oda, M. Hashizume, M. Nakamura. Adipose tissue-derived stromal cells are sources of cancer-associated fibroblasts and enhance tumor progression by dense collagen matrix, (2019), Int J Cancer, 144 (6), p. 1401-1413.
[146] B.A. Dirat, L. Bochet, G. Escourrou, P. Valet, C. Muller. Unraveling the obesity and breast cancer links: a role for cancer-associated adipocytes?, (2010), Endocrine development, 2010 (19), p. 45-52.
[147] M.N. Duong, A. Geneste, F. Fallone, X. Li, C. Dumontet, C. Muller. The fat and the bad: Mature adipocytes, key actors in tumor progression and resistance, (2017), Oncotarget, 8 (34), p. 57622-57641.
[148] B. Dirat, L. Bochet, M. Dabek, D. Daviaud, S. Dauvillier, B. Majed, Y.Y. Wang, A. Meulle, B. Salles, S. Le Gonidec, I. Garrido, G. Escourrou, P. Valet, C. Muller. Cancer-associated adipocytes exhibit an activated phenotype and contribute to breast cancer invasion, (2011), Cancer Res, 71 (7), p. 2455-2465.
[149] S. Beloribi-Djefaflia, S. Vasseur, F. Guillaumond. Lipid metabolic reprogramming in cancer cells, (2016), Oncogenesis, 5 (1), p. e189-.
[150] J. Huang, A. Duran, M. Reina-Campos, T. Valencia, E.A. Castilla, T.D. Muller, M.H. Tschop, J. Moscat, M.T. Diaz-Meco. Adipocyte p62/SQSTM1 Suppresses Tumorigenesis through Opposite Regulations of Metabolism in Adipose Tissue and Tumor, (2018), Cancer cell, 33 (4), p. 770-784.e776.
[151] J.C. Zarif, J.A. Baena-Del Valle, J.L. Hicks, C.M. Heaphy, I. Vidal, J. Luo, T.L. Lotan, J.E. Hooper, W.B. Isaacs, K.J. Pienta, A.M. De Marzo. Mannose receptor–positive macrophage infiltration correlates with prostate cancer onset and metastatic castration-resistant disease, (2019), Eur Urol Oncol, 2 (4), p. 429-436.
[152] J.M. Cathcart, A. Banach, A. Liu, J. Chen, M. Goligorsky, J. Cao. Interleukin-6 increases matrix metalloproteinase-14 (MMP-14) levels via down-regulation of p53 to drive cancer progression, (2016), Oncotarget, 7 (38), p. 61107-61120.
[153] S.J. Cutler, J.D. Doecke, I. Ghazawi, J. Yang, L.R. Griffiths, K.J. Spring, S.J. Ralph, A.S. Mellick. Novel STAT binding elements mediate IL-6 regulation of MMP-1 and MMP-3, (2017), Sci Rep, 7

[154] S.I. Daas, B.R. Rizeq, G.K. Nasrallah. Adipose tissue dysfunction in cancer cachexia, (2018), J Cell Physiol., 234 (1), p. 13-22.
[155] J. Han, Q. Meng, L. Shen, G. Wu. Interleukin-6 induces fat loss in cancer cachexia by promoting white adipose tissue lipolysis and browning, (2018), Lipids Health Dis, 17 (1), p. 14.
[156] M.J. Alves, R.G. Figuerêdo, F.F. Azevedo, D.A. Cavallaro, N.I.P. Neto, J.D.C. Lima, E. Matos-Neto, K. Radloff, D.M. Riccardi, R.G. Camargo, P.S.M. De Alcântara, J.P. Otoch, M.L.B. Junior, M. Seelaender. Adipose tissue fibrosis in human cancer cachexia: The role of TGFβ pathway, (2017), BMC Cancer, 17 (1),
[157] N.L. Springer, N.M. Iyengar, R. Bareja, A. Verma, M. Jochelson, D.D. Giri, X.K. Zhou, O. Elemento, A.J. Dannenberg, C. Fischbach. Obesity-associated extracellular matrix remodeling promotes a macrophage phenotype similar to tumor-associated macrophages, (2019), Am J Pathol, 189 (10), p. 2019-2035.
[158] I.A. Potapova, G.R. Gaudette, P.R. Brink, R.B. Robinson, M.R. Rosen, I.S. Cohen, S.V. Doronin. Mesenchymal stem cells support migration, extracellular matrix invasion, proliferation, and survival of endothelial cells in vitro, (2007), Stem cells (Dayton, Ohio), 25 (7), p. 1761-1768.
[159] N. Maishi, K. Hida. Tumor endothelial cells accelerate tumor metastasis, (2017), Cancer Sci, 108 (10), p. 1921-1926.
[160] B.G. Rowan, J.M. Gimble, M. Sheng, M. Anbalagan, R.K. Jones, T.P. Frazier, M. Asher, E.A. Lacayo, P.L. Friedlander, R. Kutner, E.S. Chiu. Human adipose tissue-derived stromal/stem cells promote migration and early metastasis of triple negative breast cancer xenografts, (2014), PloS one, 9 (2), p. e89595.
[161] Y. Pan, X. Hui, R.L. Chong Hoo, D. Ye, C.Y. Cheung Chan, T. Feng, Y. Wang, K.S. Ling Lam, A. Xu. Adipocyte-secreted exosomal microRNA-34a inhibits M2 macrophage polarization to promote obesity-induced adipose inflammation, (2019), J Clin Invest., 129 (2), p. 834-849.
[162] Z. Zhang, P.E. Scherer. Adipose tissue: The dysfunctional adipocyte - a cancer cell's best friend, (2018), Nat Rev Endocrinol, 14 (3), p. 132-134.
[163] D.G. Johns, L. LeVoci, M. Krsmanovic, M. Lu, G. Hartmann, S. Xu, S.P. Wang, Y. Chen, T. Bateman, R.O. Blaustein. Characterization of Anacetrapib Distribution into the Lipid Droplet of Adipose Tissue in Mice and Human Cultured Adipocytes, (2019), Drug Metab Dispos, 47 (3), p. 227-233.
[164] X. Sheng, J.H. Parmentier, J. Tucci, H. Pei, O. Cortez-Toledo, C.M. Dieli-Conwright, M.J. Oberley, M. Neely, E. Orgel, S.G. Louie, S.D. Mittelman. Adipocytes Sequester and Metabolize the Chemotherapeutic Daunorubicin, (2017), Molecular cancer research : MCR, 15 (12), p. 1704-1713.
[165] P.A. Thompson, G.L. Rosner, K.K. Matthay, T.B. Moore, L.R. Bomgaars, K.J. Ellis, J. Renbarger, S.L. Berg. Impact of body composition on pharmacokinetics of doxorubicin in children:

a Glaser Pediatric Research Network study, (2009), Cancer Chemother Pharmacol, 64 (2), p. 243-251.
[166] J. Kim, J.-S. Bae. Tumor-associated macrophages and neutrophils in tumor microenvironment, (2016), Mediators Inflamm, 2016 p. 6058147-6058147.
[167] A.R. Poh, M. Ernst. Targeting macrophages in cancer: From bench to bedside, (2018), Front Oncol, 8 p. 49-49.
[168] D. Hashimoto, A. Chow, C. Noizat, P. Teo, M.B. Beasley, M. Leboeuf, C.D. Becker, P. See, J. Price, D. Lucas, M. Greter, A. Mortha, S.W. Boyer, E.C. Forsberg, M. Tanaka, N. van Rooijen, A. Garcia-Sastre, E.R. Stanley, F. Ginhoux, P.S. Frenette, M. Merad. Tissue-resident macrophages self-maintain locally throughout adult life with minimal contribution from circulating monocytes, (2013), Immunity, 38 (4), p. 792-804.
[169] A. Aderem, D.M. Underhill. Mechanisms of phagocytosis in macrophages, (1999), Annu Rev Immunol, 17 p. 593-623.
[170] R.D. Stout, K. Bottomly. Antigen-specific activation of effector macrophages by IFN-gamma producing (Th1) T-cell clones-failure of IL-4 producing (Th2) T cell clones to activate effector function in macrophages, (1989), J. Immunol., 142 (3), p. 760-765.
[171] E. Peranzoni, J. Lemoine, L. Vimeux, V. Feuillet, S. Barrin, C. Kantari-Mimoun, N. Bercovici, M. Guérin, J. Biton, H. Ouakrim, F. Régnier, A. Lupo, M. Alifano, D. Damotte, E. Donnadieu. Macrophages impede CD8 T cells from reaching tumor cells and limit the efficacy of anti-PD-1 treatment, (2018), Proc Natl Acad Sci U S A, 115 (17), p. E4041-E4050.
[172] L. Bingle, C.E. Lewis, K.P. Corke, M.W. Reed, N.J. Brown. Macrophages promote angiogenesis in human breast tumour spheroids in vivo, (2006), Br J Cancer, 94 (1), p. 101-107.
[173] F. Moroni, E. Ammirati, G.D. Norata, M. Magnoni, P.G. Camici. The role of monocytes and macrophages in human atherosclerosis, plaque neoangiogenesis, and atherothrombosis, (2019), Mediators Inflamm, 2019 p. 7434376.
[174] B.K. Surmi, A.H. Hasty. Macrophage infiltration into adipose tissue: initiation, propagation and remodeling, (2008), Future Lipidol, 3 (5), p. 545-556.
[175] D.A. Hume, K.M. Irvine, C. Pridans. The mononuclear phagocyte system: The relationship between monocytes and macrophages, (2019), Trends Immunol, 40 (2), p. 98-112.
[176] D.A.D. Munro, J. Hughes. The origins and functions of tissue-resident macrophages in kidney development, (2017), Front Physiol, 8 p. 837.
[177] J.F. Charles, A.O. Aliprantis. Osteoclasts: more than 'bone eaters', (2014), Trends Mol Med, 20 (8), p. 449-459.
[178] R. van Furth, Z.A. Cohn. The origin and kinetics of mononuclear phagocytes, (1968), J Exp Med., 128 (3), p. 415-435.

[179] E. Gomez Perdiguero, K. Klapproth, C. Schulz, K. Busch, M. de Bruijn, H.R. Rodewald, F. Geissmann. The origin of tissue-resident macrophages: When an erythro-myeloid progenitor is an erythro-myeloid progenitor, (2015), Immunity, 43 (6), p. 1023-1024.
[180] C. Schulz, E.G. Perdiguero, L. Chorro, H. Szabo-Rogers, N. Cagnard, K. Kierdorf, M. Prinz, B. Wu, S.E.W. Jacobsen, J.W. Pollard, J. Frampton, K.J. Liu, F. Geissmann. A lineage of myeloid cells independent of myb and hematopoietic stem cells, (2012), Science (New York, N.Y.), 336 (6077), p. 86.
[181] M. Kurashige, M. Kohara, K. Ohshima, S. Tahara, Y. Hori, S. Nojima, N. Wada, J.-i. Ikeda, K. Miyamura, M. Ito, E. Morii. Origin of cancer-associated fibroblasts and tumor-associated macrophages in humans after sex-mismatched bone marrow transplantation, (2018), Commun Biol, 1 (1), p. 131.
[182] B.-Z. Qian, J.W. Pollard. Macrophage diversity enhances tumor progression and metastasis, (2010), Cell, 141 (1), p. 39-51.
[183] A. Mantovani, A. Sica. Macrophages, innate immunity and cancer: balance, tolerance, and diversity, (2010), Curr Opin Immunol, 22 (2), p. 231-237.
[184] D.S. Hong, L.S. Angelo, R. Kurzrock. Interleukin-6 and its receptor in cancer, (2007), Cancer, 110 (9), p. 1911-1928.
[185] G. Gopinathan, C. Milagre, O.M.T. Pearce, L.E. Reynolds, K. Hodivala-Dilke, D.A. Leinster, H. Zhong, R.E. Hollingsworth, R. Thompson, J.R. Whiteford, F. Balkwill. Interleukin-6 stimulates defective angiogenesis, (2015), Cancer Res, 75 (15), p. 3098-3107.
[186] S. Akira, T. Kishimoto. Role of interleukin-6 in macrophage function, (1996), Curr Opin Hematol, 3 (1), p. 87-93.
[187] J. Mauer, B. Chaurasia, J. Goldau, M.C. Vogt, J. Ruud, K.D. Nguyen, S. Theurich, A.C. Hausen, J. Schmitz, H.S. Brönneke, E. Estevez, T.L. Allen, A. Mesaros, L. Partridge, M.A. Febbraio, A. Chawla, F.T. Wunderlich, J.C. Brüning. Signaling by IL-6 promotes alternative activation of macrophages to limit endotoxemia and obesity-associated resistance to insulin, (2014), Nat Immunol, 15 (5), p. 423-430.
[188] M.S. Han, D.Y. Jung, C. Morel, S.A. Lakhani, J.K. Kim, R.A. Flavell, R.J. Davis. JNK expression by macrophages promotes obesity-induced insulin resistance and inflammation, (2013), Science (New York, N.Y.), 339 (6116), p. 218-222.
[189] A. Mercalli, I. Calavita, E. Dugnani, A. Citro, E. Cantarelli, R. Nano, R. Melzi, P. Maffi, A. Secchi, V. Sordi, L. Piemonti. Rapamycin unbalances the polarization of human macrophages to M1, (2013), Immunology, 140 (2), p. 179-190.
[190] P.M. Aponte, A. Caicedo. Stemness in cancer: Stem cells, cancer stem cells, and their microenvironment, (2017), Stem Cells Int, 2017 p. 5619472.

[191] F. Guilloton, G. Caron, C. Ménard, C. Pangault, P. Amé-Thomas, J. Dulong, J. De Vos, D. Rossille, C. Henry, T. Lamy, O. Fouquet, T. Fest, K. Tarte. Mesenchymal stromal cells orchestrate follicular lymphoma cell niche through the CCL2-dependent recruitment and polarization of monocytes, (2012), Blood, 119 (11), p. 2556-2567.
[192] J. Huang, M.T. Diaz-Meco, J. Moscat. The macroenviromental control of cancer metabolism by p62, (2018), Cell Cycle, 17 (17), p. 2110-2121.
[193] M.-Y. Song, S.H. Kim, G.-H. Ryoo, M.-K. Kim, H.-N. Cha, S.-Y. Park, H.P. Hwang, H.C. Yu, E.J. Bae, B.-H. Park. Adipose sirtuin 6 drives macrophage polarization toward M2 through IL-4 production and maintains systemic insulin sensitivity in mice and humans, (2019), Exp Mol Med, 51 (5), p. 56.
[194] H.R. Ali, L. Chlon, P.D.P. Pharoah, F. Markowetz, C. Caldas. Patterns of immune infiltration in breast cancer and their clinical implications: A gene-expression-based retrospective study, (2016), PLoS Med, 13 (12),
[195] X. Li, W. Yao, Y. Yuan, P. Chen, B. Li, J. Li, R. Chu, H. Song, D. Xie, X. Jiang, H. Wang. Targeting of tumour-infiltrating macrophages via CCL2/CCR2 signalling as a therapeutic strategy against hepatocellular carcinoma, (2017), Gut, 66 (1), p. 157-167.
[196] F.O. Martinez, S. Gordon, M. Locati, A. Mantovani. Transcriptional profiling of the human monocyte-to-macrophage differentiation and polarization: new molecules and patterns of gene expression, (2006), J Immunol., 177 (10), p. 7303-7311.
[197] L. Cassetta, S. Fragkogianni, A.H. Sims, A. Swierczak, L.M. Forrester, H. Zhang, D.Y.H. Soong, T. Cotechini, P. Anur, E.Y. Lin, A. Fidanza, M. Lopez-Yrigoyen, M.R. Millar, A. Urman, Z. Ai, P.T. Spellman, E.S. Hwang, J.M. Dixon, L. Wiechmann, L.M. Coussens, H.O. Smith, J.W. Pollard. Human tumor-associated macrophage and monocyte transcriptional landscapes reveal cancer-specific reprogramming, biomarkers, and therapeutic targets, (2019), Cancer cell, 35 (4), p. 588-602.
[198] Y. Wu, J. Wei, X. Chen, Y. Qin, R. Mao, J. Song, Y. Fan. Comprehensive transcriptome profiling in elderly cancer patients reveals aging-altered immune cells and immune checkpoints, (2019), Int J Cancer, 144 (7), p. 1657-1663.
[199] B.H. Joshi, P. Leland, S. Lababidi, F. Varrichio, R.K. Puri. Interleukin-4 receptor alpha overexpression in human bladder cancer correlates with the pathological grade and stage of the disease, (2014), Cancer Med, 3 (6), p. 1615-1628.
[200] G. Gallina, L. Dolcetti, P. Serafini, C. De Santo, I. Marigo, M.P. Colombo, G. Basso, F. Brombacher, I. Borrello, P. Zanovello, S. Bicciato, V. Bronte. Tumors induce a subset of inflammatory monocytes with immunosuppressive activity on CD8+ T cells, (2006), J Clin Inves, 116 (10), p. 2777-2790.

[201] M. Thorn, P. Guha, M. Cunetta, N.J. Espat, G. Miller, R.P. Junghans, S.C. Katz. Tumor-associated GM-CSF overexpression induces immunoinhibitory molecules via STAT3 in myeloid-suppressor cells infiltrating liver metastases, (2016), Cancer Gene Ther, 23 p. 188.
[202] C. Lin, H. He, H. Liu, R. Li, Y. Chen, Y. Qi, Q. Jiang, L. Chen, P. Zhang, H. Zhang, H. Li, W. Zhang, Y. Sun, J. Xu. Tumour-associated macrophages-derived CXCL8 determines immune evasion through autonomous PD-L1 expression in gastric cancer, (2019), Gut,
[203] A. Mantovani, M. Locati. Macrophage metabolism shapes angiogenesis in tumors, (2016), Cell Metab, 24 (5), p. 653-654.
[204] F. Valverde Lde, A. Pereira Tde, R.B. Dias, V.S. Guimaraes, E.A. Ramos, J.N. Santos, C.A. Gurgel Rocha. Macrophages and endothelial cells orchestrate tumor-associated angiogenesis in oral cancer via hedgehog pathway activation, (2016), Tumour Biol., 37 (7), p. 9233-9241.
[205] M. Wenes, M. Shang, M. Di Matteo, J. Goveia, R. Martin-Perez, J. Serneels, H. Prenen, B. Ghesquiere, P. Carmeliet, M. Mazzone. Macrophage metabolism controls tumor blood vessel morphogenesis and metastasis, (2016), Cell Metab, 24 (5), p. 701-715.
[206] L.R. Sanchez, L. Borriello, D. Entenberg, J.S. Condeelis, M.H. Oktay, G.S. Karagiannis. The emerging roles of macrophages in cancer metastasis and response to chemotherapy, (2019), J Leukoc Biol, 106 (2), p. 259-274.
[207] A. Jablonska-Trypuc, M. Matejczyk, S. Rosochacki. Matrix metalloproteinases (MMPs), the main extracellular matrix (ECM) enzymes in collagen degradation, as a target for anticancer drugs, (2016), J Enzyme Inhib Med Chem., 31 (sup1), p. 177-183.
[208] V. Pelekanou, F. Villarroel-Espindola, K.A. Schalper, L. Pusztai, D.L. Rimm. CD68, CD163, and matrix metalloproteinase 9 (MMP-9) co-localization in breast tumor microenvironment predicts survival differently in ER-positive and -negative cancers, (2018), Breast Cancer Res, 20 (1),
[209] H. Jeong, I. Hwang, S.H. Kang, H.C. Shin, S.Y. Kwon. Tumor-associated macrophages as potential prognostic biomarkers of invasive breast cancer, (2019), J Breast Cancer, 22 (1), p. 38-51.
[210] Y.J. Cha, E.S. Kim, J.S. Koo. Tumor-associated macrophages and crown-like structures in adipose tissue in breast cancer, (2018), Breast Cancer Res Treat, 170 (1), p. 15-25.
[211] K. Esbona, Y. Yi, S. Saha, M. Yu, R.R. Van Doorn, M.W. Conklin, D.S. Graham, K.B. Wisinski, S.M. Ponik, K.W. Eliceiri, L.G. Wilke, P.J. Keely. The presence of cyclooxygenase 2, tumor-associated macrophages, and collagen alignment as prognostic markers for invasive breast carcinoma patients, (2018), Am J Pathol, 188 (3), p. 559-573.
[212] J.M. Carter, T.L. Hoskin, M.A. Pena, R. Brahmbhatt, S.J. Winham, M.H. Frost, M. Stallings-Mann, D.C. Radisky, K.L. Knutson, D.W. Visscher, A.C. Degnim. Macrophagic "crown-like structures" are associated with an increased risk of breast cancer in benign breast disease, (2018), Cancer Prev Res (Phila), 11 (2), p. 113-119.

[213] Y. Morita, R. Zhang, M. Leslie, S. Adhikari, N. Hasan, I. Chervoneva, H. Rui, T. Tanaka. Pathologic evaluation of tumor-associated macrophage density and vessel inflammation in invasive breast carcinomas, (2017), Oncol Lett, 14 (2), p. 2111-2118.
[214] S. Garvin, H. Oda, L.G. Arnesson, A. Lindström, I. Shabo. Tumor cell expression of CD163 is associated to postoperative radiotherapy and poor prognosis in patients with breast cancer treated with breast-conserving surgery, (2018), J Cancer Res Clin Oncol, 144 (7), p. 1253-1263.
[215] T.A. Klingen, Y. Chen, H. Aas, E. Wik, L.A. Akslen. Tumor-associated macrophages are strongly related to vascular invasion, non-luminal subtypes, and interval breast cancer, (2017), Hum Pathol, 69 p. 72-80.
[216] W.J. Zhang, X.H. Wang, S.T. Gao, C. Chen, X.Y. Xu, Q. sun, Z.H. Zhou, G.Z. Wu, Q. Yu, G. Xu, Y.Z. Yao, W.X. Guan. Tumor-associated macrophages correlate with phenomenon of epithelial-mesenchymal transition and contribute to poor prognosis in triple-negative breast cancer patients, (2018), J Surg Res, 222 p. 93-101.
[217] L. Xu, Y. Zhu, L. Chen, H. An, W. Zhang, G. Wang, Z. Lin, J. Xu. Prognostic value of diametrically polarized tumor-associated macrophages in renal cell carcinoma, (2014), Ann Surg Oncol, 21 (9), p. 3142-3150.
[218] C. Lan, X. Huang, S. Lin, H. Huang, Q. Cai, T. Wan, J. Lu, J. Liu. Expression of M2-polarized macrophages is associated with poor prognosis for advanced epithelial ovarian cancer, (2013), Technol Cancer Res Treat, 12 (3), p. 259-267.
[219] C. Luchini, J. Cros, A. Pea, C. Pilati, N. Veronese, B. Rusev, P. Capelli, A. Mafficini, A. Nottegar, L.A.A. Brosens, M. Noë, G.J.A. Offerhaus, P. Chianchiano, G. Riva, P. Piccoli, C. Parolini, G. Malleo, R.T. Lawlor, V. Corbo, N. Sperandio, M. Barbareschi, M. Fassan, L. Cheng, L.D. Wood, A. Scarpa. PD-1, PD-L1, and CD163 in pancreatic undifferentiated carcinoma with osteoclast-like giant cells: expression patterns and clinical implications, (2018), Hum Pathol, 81 p. 157-165.
[220] S. Hiratsuka, K. Nakamura, S. Iwai, M. Murakami, T. Itoh, H. Kijima, J.M. Shipley, R.M. Senior, M. Shibuya. MMP9 induction by vascular endothelial growth factor receptor-1 is involved in lung-specific metastasis, (2002), Cancer cell, 2 (4), p. 289-300.
[221] L. Liu, Y. Ye, X. Zhu. MMP-9 secreted by tumor associated macrophages promoted gastric cancer metastasis through a PI3K/AKT/Snail pathway, (2019), Biomed Pharmacother, 117 p. 109096.
[222] D.A. Jaitin, L. Adlung, C.A. Thaiss, A. Weiner, B. Li, H. Descamps, P. Lundgren, C. Bleriot, Z. Liu, A. Deczkowska, H. Keren-Shaul, E. David, N. Zmora, S.M. Eldar, N. Lubezky, O. Shibolet, D.A. Hill, M.A. Lazar, M. Colonna, F. Ginhoux, H. Shapiro, E. Elinav, I. Amit. Lipid-associated

macrophages control metabolic homeostasis in a Trem2-dependent manner, (2019), Cell, 178 (3), p. 686-698.e614.
[223] E.L. Mills, L.A. O'Neill. Reprogramming mitochondrial metabolism in macrophages as an anti-inflammatory signal, (2016), Eur J Immunol, 46 (1), p. 13-21.
[224] P. Zheng, Q. Luo, W. Wang, J. Li, T. Wang, P. Wang, L. Chen, P. Zhang, H. Chen, Y. Liu, P. Dong, G. Xie, Y. Ma, L. Jiang, X. Yuan, L. Shen. Tumor-associated macrophages-derived exosomes promote the migration of gastric cancer cells by transfer of functional Apolipoprotein E, (2018), Cell Death Dis, 9 (4), p. 434.
[225] G.S. Getz, C.A. Reardon. Apoprotein E as a lipid transport and signaling protein in the blood, liver, and artery wall, (2009), J Lipid Res, 50 Suppl (Suppl), p. S156-S161.
[226] D.A. Lawson, K. Kessenbrock, R.T. Davis, N. Pervolarakis, Z. Werb. Tumour heterogeneity and metastasis at single-cell resolution, (2018), Nat Cell Biol, 20 (12), p. 1349-1360.
[227] H. Axelson, E. Fredlund, M. Ovenberger, G. Landberg, S. Pahlman. Hypoxia-induced dedifferentiation of tumor cells--a mechanism behind heterogeneity and aggressiveness of solid tumors, (2005), Semin Cell Dev Biol, 16 (4-5), p. 554-563.
[228] B.A. Smith, N.G. Balanis, A. Nanjundiah, K.M. Sheu, B.L. Tsai, Q. Zhang, J.W. Park, M. Thompson, J. Huang, O.N. Witte, T.G. Graeber. A human adult stem cell signature marks aggressive variants across epithelial cancers, (2018), Cell Reports, 24 (12), p. 3353-3366.e3355.
[229] P. Tiwari, A. Blank, C. Cui, K.Q. Schoenfelt, G. Zhou, Y. Xu, G. Khramtsova, F. Olopade, A.M. Shah, S.A. Khan, M.R. Rosner, L. Becker. Metabolically activated adipose tissue macrophages link obesity to triple-negative breast cancer, (2019), J Exp Med., 216 (6), p. 1345-1358.
[230] V.F. Muglia, A. Prando. Renal cell carcinoma: histological classification and correlation with imaging findings, (2015), Radiol Bras, 48 (3), p. 166-174.
[231] T. Li, J. Chen, Y. Jiang, X. Ning, S. Peng, J. Wang, Q. He, X. Yang, K. Gong. Multilocular cystic renal cell neoplasm of low malignant potential: A series of 76 cases, (2016), Clin Genitourin Cancer, 14 (6), p. e553-e557.
[232] R.R. Fowler C. The indeterminate renal mass, (2001), Imaging, (13), p. 27-43.
[233] J.H. Van Drie. Protein folding, protein homeostasis, and cancer, (2011), Chin J Cancer, 30 (2), p. 124-137.
[234] H.D. Patel, M.H. Johnson, P.M. Pierorazio, S.M. Sozio, R. Sharma, E. Iyoha, E.B. Bass, M.E. Allaf. Diagnostic accuracy and risks of biopsy in the diagnosis of a renal mass suspicious for localized renal cell carcinoma: Systematic review of the literature, (2016), J Urol., 195 (5), p. 1340-1347.

[235] C. EE, K. Rudolf. Overweight, obesity and cancer: epidemiological evidence and proposed mechanisms, (2004), Nat Rev Cancer, 4 (8), p. 579.
[236] R.J. Ellis, S.J. Del Vecchio, K.L. Ng, E.P. Owens, J.S. Coombes, C. Morais, R.S. Francis, S.T. Wood, G.C. Gobe. The correlates of kidney dysfunction-Tumour Nephrectomy Database (CKD-TUNED) Study: protocol for a prospective observational Study, (2017), Asian Pac J Cancer Prev, 18 (12), p. 3281-3285.
[237] A. Vegiopoulos, M. Rohm, S. Herzig. Adipose tissue: between the extremes, (2017), EMBO J, 36 (14), p. 1999-2017.
[238] B. Delahunt, J.C. Cheville, G. Martignoni, P.A. Humphrey, C. Magi-Galluzzi, J. McKenney, L. Egevad, F. Algaba, H. Moch, D.J. Grignon, R. Montironi, J.R. Srigley. The International Society of Urological Pathology (ISUP) grading system for renal cell carcinoma and other prognostic parameters, (2013), Am J Surg Pathol, 37 (10), p. 1490-1504.
[239] J. Schindelin, I. Arganda-Carreras, E. Frise, V. Kaynig, M. Longair, T. Pietzsch, S. Preibisch, C. Rueden, S. Saalfeld, B. Schmid, J.Y. Tinevez, D.J. White, V. Hartenstein, K. Eliceiri, P. Tomancak, A. Cardona. Fiji: an open-source platform for biological-image analysis, (2012), Nat Methods, 9 (7), p. 676-682.
[240] J. Shu, G.E. Dolman, J. Duan, G. Qiu, M. Ilyas. Statistical colour models: an automated digital image analysis method for quantification of histological biomarkers, (2016), Biomed Eng Online, 15 p. 46.
[241] G.K. Rangan, G.H. Tesch. Quantification of renal pathology by image analysis, (2007), Nephrology (Carlton), 12 (6), p. 553-558.
[242] Labno. Basic Intensity Quantification with ImageJ https://www.unige.ch/medecine/bioimaging/files/1914/1208/6000/Quantification.pdf (Accessed on 28/09/2018).
[243] W.L. Clapp, B.P. Croker, Histology for Pathologists, 4 ed., Wolters Kluwer Health, 2012.
[244] M. Moras, S.D. Lefevre, M.A. Ostuni. From erythroblasts to mature red blood cells: Organelle clearance in mammals, (2017), Front Physiol, 8 p. 1076.
[245] Y. Kim, Q. Lin, P.M. Glazer, Z. Yun. Hypoxic tumor microenvironment and cancer cell differentiation, (2009), Curr Mol Med, 9 (4), p. 425-434.
[246] E.R. Pereira, K. Frudd, W. Awad, L.M. Hendershot. Endoplasmic reticulum (ER) stress and hypoxia response pathways interact to potentiate hypoxia-inducible factor 1 (HIF-1) transcriptional activity on targets like vascular endothelial growth factor (VEGF), (2014), J Bio chem, (1083-351X (Electronic)),
[247] A. Samali, U. FitzGerald, S. Deegan, S. Gupta. Methods for monitoring endoplasmic reticulum stress and the unfolded protein response, (2010), Int J Cell Biol, 2010 p. 11.

[248] C.M. Oslowski, F. Urano. Measuring ER stress and the unfolded protein response using mammalian tissue culture system, (2011), Methods Enzymol, 490 p. 71-92.
[249] H.J. Clarke, J.E. Chambers, E. Liniker, S.J. Marciniak. Endoplasmic reticulum stress in malignancy, (2014), Cancer cell, 25 (5), p. 563-573.
[250] M.L. Batista, Jr., F.S. Henriques, R.X. Neves, M.R. Olivan, E.M. Matos-Neto, P.S. Alcantara, L.F. Maximiano, J.P. Otoch, M.J. Alves, M. Seelaender. Cachexia-associated adipose tissue morphological rearrangement in gastrointestinal cancer patients, (2016), J Cachexia Sarcopenia Muscle., 7 (1), p. 37-47.
[251] M.M. Ibrahim. Subcutaneous and visceral adipose tissue: structural and functional differences, (2010), Obes Rev., 11 (1), p. 11-18.
[252] K.N. Frayn. Adipose tissue as a buffer for daily lipid flux, (2002), Diabetologia, 45 (9), p. 1201-1210.
[253] B. Guiu, J.M. Petit, F. Bonnetain, S. Ladoire, S. Guiu, J.P. Cercueil, D. Krausé, P. Hillon, C. Borg, B. Chauffert, F. Ghiringhelli. Visceral fat area is an independent predictive biomarker of outcome after first-line bevacizumab-based treatment in metastatic colorectal cancer, (2010), Gut, 59 (3), p. 341-347.
[254] L. Frese, P.E. Dijkman, S.P. Hoerstrup. Adipose tissue-derived stem cells in regenerative medicine, (2016), Transfus Med Hemother, 43 (4), p. 268-274.
[255] A.N. Cebeci, A. Guven, L.I. Kuru. Perinephric adipose tissue thickness in relation to blood pressure, plasma apelin and C-reactive protein levels in obese adolescents, (2016), Minerva Endocrinol, 41 (2), p. 166-174.
[256] C. Chen, W. He, J. Huang, B. Wang, H. Li, Q. Cai, F. Su, J. Bi, H. Liu, B. Zhang, N. Jiang, G. Zhong, Y. Zhao, W. Dong, T. Lin. LNMAT1 promotes lymphatic metastasis of bladder cancer via CCL2 dependent macrophage recruitment, (2018), Nat Commun, 9 (1), p. 3826.
[257] B.-X. Liu, W. Sun, X.-Q. Kong. Perirenal fat: A unique fat pad and potential target for cardiovascular disease, (2018), Angiology, 70 (7), p. 584-593.
[258] A.J. Klingelhutz, F.A. Gourronc, A. Chaly, D.A. Wadkins, A.J. Burand, K.R. Markan, S.O. Idiga, M. Wu, M.J. Potthoff, J.A. Ankrum. Scaffold-free generation of uniform adipose spheroids for metabolism research and drug discovery, (2018), Sci Rep, 8 (1), p. 523.
[259] N. Amirpour, S. Razavi, E. Esfandiari, B. Hashemibeni, M. Kazemi, H. Salehi. Hanging drop culture enhances differentiation of human adipose-derived stem cells into anterior neuroectodermal cells using small molecules, (2017), Int J Dev Neurosci, 59 p. 21-30.
[260] Y.-H. Wang, J.-Y. Wu, P.-J. Chou, C.-H. Chen, C.-Z. Wang, M.-L. Ho, J.-K. Chang, M.-L. Yeh, C.-H. Chen. Characterization and evaluation of the differentiation ability of human adipose-

derived stem cells growing in scaffold-free suspension culture, (2014), Cytotherapy, 16 (4), p. 485-495.
[261] W. Metzger, D. Sossong, A. Bachle, N. Putz, G. Wennemuth, T. Pohlemann, M. Oberringer. The liquid overlay technique is the key to formation of co-culture spheroids consisting of primary osteoblasts, fibroblasts and endothelial cells, (2011), Cytotherapy, 13 (8), p. 1000-1012.
[262] M.J. Lerman, J. Lembong, S. Muramoto, G. Gillen, J.P. Fisher. The evolution of polystyrene as a cell culture material, (2018), Tissue Eng Part B Rev., 24 (5), p. 359-372.
[263] T.A. Ulrich, A. Jain, K. Tanner, J.L. MacKay, S. Kumar. Probing cellular mechanobiology in three-dimensional culture with collagen–agarose matrices, (2010), Biomaterials, 31 (7), p. 1875-1884.
[264] N. Naderi, C. Wilde, T. Haque, W. Francis, A.M. Seifalian, C.A. Thornton, Z. Xia, I.S. Whitaker. Adipogenic differentiation of adipose-derived stem cells in 3-dimensional spheroid cultures (microtissue): implications for the reconstructive surgeon, (2014), J Plast Reconstr Aesthet Surg, 67 (12), p. 1726-1734.
[265] M.J. Lee, S.K. Fried. Optimal protocol for the differentiation and metabolic analysis of human adipose stromal cells, (2014), Methods Enzymol, 538 p. 49-65.
[266] M.D. Lane, B.C. Reed, P.R. Clements. Insulin receptor synthesis and turnover in differentiating 3T3-L1 preadipocytes, (1981), Proc Natl Acad Sci USA, 77 (1), p. 285-289.
[267] R. Lillie, L. Ashburn. Supersaturated solutions of fat stains in dilute isopropanol for demonstration of acute fatty degeneration not shown by Herxheimer's technique, (1943), Arch Pathol, 36 p. 432-440.
[268] C.-S. Lin, Z.-C. Xin, J. Dai, T.F. Lue. Commonly used mesenchymal stem cell markers and tracking labels: Limitations and challenges, (2013), Histol Histopathol, 28 (9), p. 1109-1116.
[269] T. Egeland, R. Steen, H. Quarsten, G. Gaudernack, Y.C. Yang, E. Thorsby. Myeloid differentiation of purified CD34+ cells after stimulation with recombinant human granulocyte-monocyte colony-stimulating factor (CSF), granulocyte-CSF, monocyte-CSF, and interleukin-3, (1991), Blood, 78 (12), p. 3192-3199.
[270] M.L. Gimeno, F. Fuertes, A.E. Barcala Tabarrozzi, A.I. Attorressi, R. Cucchiani, L. Corrales, T.C. Oliveira, M.C. Sogayar, L. Labriola, R.A. Dewey, M.J. Perone. Pluripotent nontumorigenic adipose tissue-derived muse cells have immunomodulatory capacity mediated by transforming growth factor-beta1, (2017), Stem Cells Transl Med, 6 (1), p. 161-173.
[271] M. Azim, H. Surani. Glycoprotein synthesis and inhibition of glycosylation by tunicamycin in preimplantation mouse embryos: Compaction and trophoblast adhesion, (1979), Cell, 18 (1), p. 217-227.

[272] S.G. de la Cadena, K. Hernandez-Fonseca, I. Camacho-Arroyo, L. Massieu. Glucose deprivation induces reticulum stress by the PERK pathway and caspase-7- and calpain-mediated caspase-12 activation, (2014), Apoptosis., 19 (3), p. 414-427.
[273] A.L. Aulthouse, E. Freeh, S. Newstead, A.L. Stockert. Part 1: A novel model for three-dimensional culture of 3T3-L1 preadipocytes stimulates spontaneous cell differentiation independent of chemical induction typically required in monolayer, (2019), Nutr Metab Insights, 12
[274] E. Carletti, A. Motta, C. Migliaresi, Scaffolds for tissue engineering and 3D cell culture, in: J.W. Haycock (Ed.) 3D cell culture: Methods and protocols, Humana Press, Totowa, NJ, 2011, p. 17-39.
[275] G.R. Hajer, T.W. van Haeften, F.L.J. Visseren. Adipose tissue dysfunction in obesity, diabetes, and vascular diseases, (2008), Eur Heart J, 29 (24), p. 2959-2971.
[276] S.L. Deshmane, S. Kremlev, S. Amini, B.E. Sawaya. Monocyte chemoattractant protein-1 (MCP-1): an overview, (2009), J Interferon Cytokine Res., 29 (6), p. 313-326.
[277] H. Kanda, S. Tateya, Y. Tamori, K. Kotani, K.-i. Hiasa, R. Kitazawa, S. Kitazawa, H. Miyachi, S. Maeda, K. Egashira, M. Kasuga. MCP-1 contributes to macrophage infiltration into adipose tissue, insulin resistance, and hepatic steatosis in obesity, (2006), J Clin Inves, 116 (6), p. 1494-1505.
[278] B.B. Moore, S.L. Kunkel. Attracting attention: Discovery of IL-8/CXCL8 and the birth of the chemokine field, (2019), J Immunol., 202 (1), p. 3.
[279] J.M. Bruun, S.B. Pedersen, B. Richelsen. Regulation of interleukin 8 production and gene expression in human adipose tissue in vitro, (2001), J Clin Endocrinol Metab., 86 (3), p. 1267-1273.
[280] A.K. Mondal, S.K. Das, V. Varma, G.T. Nolen, R.E. McGehee, S.C. Elbein, J.Y. Wei, G. Ranganathan. Effect of endoplasmic reticulum stress on inflammation and adiponectin regulation in human adipocytes, (2012), Metab Syndr Relat Disord., 10 (4), p. 297-306.
[281] J. Yin, L. Gu, Y. Wang, N. Fan, Y. Ma, Y. Peng. Rapamycin improves palmitate-induced ER stress/NF kappa B pathways associated with stimulating autophagy in adipocytes, (2015), Mediators Inflamm, 2015 p. 272313.
[282] P.L. Marjon, E.V. Bobrovnikova-Marjon, S.F. Abcouwer. Expression of the pro-angiogenic factors vascular endothelial growth factor and interleukin-8/CXCL8 by human breast carcinomas is responsive to nutrient deprivation and endoplasmic reticulum stress, (2004), Mol Cancer., 3 p. 4.
[283] S.R. Jones, S. Carley, M. Harrison. An introduction to power and sample size estimation, (2003), Emerg Med J., 20 (5), p. 453-458.
[284] A. Khakurel, P.H. Park. Globular adiponectin protects hepatocytes from tunicamycin-induced cell death via modulation of the inflammasome and heme oxygenase-1 induction, (2018), Pharmacol Res., 128 p. 231-243.

[285] Z. Liu, L. Gan, T. Wu, F. Feng, D. Luo, H. Gu, S. Liu, C. Sun. Adiponectin reduces ER stress-induced apoptosis through PPARα transcriptional regulation of ATF2 in mouse adipose, (2016), Cell Death Dis, 7 (11), p. e2487-e2487.
[286] A.B. Engin, A. Engin, I.I. Gonul. The effect of adipocyte-macrophage crosstalk in obesity-related breast cancer, (2019), J Mol Endocrinol, 62 (3), p. R201-R222.
[287] A. Shapouri-Moghaddam, S. Mohammadian, H. Vazini, M. Taghadosi, S.A. Esmaeili, F. Mardani, B. Seifi, A. Mohammadi, J.T. Afshari, A. Sahebkar. Macrophage plasticity, polarization, and function in health and disease, (2018), J Cell Physiol., 233 (9), p. 6425-6440.
[288] C.N. Lumeng, J.B. DelProposto, D.J. Westcott, A.R. Saltiel. Phenotypic switching of adipose tissue macrophages with obesity is generated by spatiotemporal differences in macrophage subtypes, (2008), Diabetes, 57 (12), p. 3239-3246.
[289] K. Ohashi, J.L. Parker, N. Ouchi, A. Higuchi, J.A. Vita, N. Gokce, A.A. Pedersen, C. Kalthoff, S. Tullin, A. Sams, R. Summer, K. Walsh. Adiponectin promotes macrophage polarization toward an anti-inflammatory phenotype, (2010), J Biol Chem., 285 (9), p. 6153-6160.
[290] D. Thomas, C. Apovian. Macrophage functions in lean and obese adipose tissue, (2017), Metabolism, 72 p. 120-143.
[291] K. Liu, E. Zhao, G. Ilyas, G. Lalazar, Y. Lin, M. Haseeb, K.E. Tanaka, M.J. Czaja. Impaired macrophage autophagy increases the immune response in obese mice by promoting proinflammatory macrophage polarization, (2015), Autophagy, 11 (2), p. 271-284.
[292] J.M. Brown, L. Recht, S. Strober. The promise of targeting macrophages in cancer therapy, (2017), Clin Cancer Res, 23 (13), p. 3241-3250.
[293] K. Shen, D.A. Vesey, R.J. Ellis, S.J. Del Vecchio, Y. Cho, A. Teixeira-Pinto, M.A. McGuckin, D.W. Johnson, G.C. Gobe. GRP78 expression in tumor and perinephric adipose tissue is not an optimal risk stratification marker for clear cell renal cell carcinoma, (2019), PloS one, 14 (1), p. e0210246.
[294] L. Ziegler-Heitbrock, P. Ancuta, S. Crowe, M. Dalod, V. Grau, D.N. Hart, P.J. Leenen, Y.J. Liu, G. MacPherson, G.J. Randolph, J. Scherberich, J. Schmitz, K. Shortman, S. Sozzani, H. Strobl, M. Zembala, J.M. Austyn, M.B. Lutz. Nomenclature of monocytes and dendritic cells in blood, (2010), Blood, 116 (16), p. e74-80.
[295] A.A. Tarique, J. Logan, E. Thomas, P.G. Holt, P.D. Sly, E. Fantino. Phenotypic, functional, and plasticity features of classical and alternatively activated human macrophages, (2015), Am J Respir Cell Mol Biol, 53 (5), p. 676-688.
[296] J. Partridge. Migration of human mesenchymal stem cells using corning fluoroblok cell culture inserts [PDF on Internet]. https://www.corning.com/media/worldwide/cls/documents/CLS-DL-CC-054%20REV1%20DL.pdf (accessed on 28/05/2019),

[297] S. Nakajima, V. Koh, L.F. Kua, J. So, L. Davide, K.S. Lim, S.H. Petersen, W.P. Yong, A. Shabbir, K. Kono. Accumulation of CD11c+CD163+ adipose tissue macrophages through upregulation of intracellular 11beta-HSD1 in human obesity, (2016), J Immunol., 197 (9), p. 3735-3745.
[298] S.R. Nielsen, M.C. Schmid. Macrophages as key drivers of cancer progression and metastasis, (2017), Mediators Inflamm., 2017 p. 9624760-9624760.
[299] Z. Zhang, Z. Wang, H. Ren, M. Yue, K. Huang, H. Gu, M. Liu, B. Du, M. Qian. P2Y(6) agonist uridine 5'-diphosphate promotes host defense against bacterial infection via monocyte chemoattractant protein-1-mediated monocytes/macrophages recruitment, (2011), J Immuno 186 (9), p. 5376-5387.
[300] N.P. Podolnikova, Y.S. Kushchayeva, Y. Wu, J. Faust, T.P. Ugarova. The role of integrins αMβ2 (Mac-1, CD11b/CD18) and αDβ2 (CD11d/CD18) in macrophage fusion, (2016), Am J Pathol, 186 (8), p. 2105-2116.
[301] G. Luo, Y. He, X. Yu. Bone marrow adipocyte: An intimate partner with tumor cells in bone metastasis, (2018), Front Endocrinol, 9 p. 339.
[302] P. Suraj, R.P. Hanumantha, H.M. William, C.G. Bradley, F.P. Maria. Diffuse marrow involvement in metastatic osteosarcoma: An unusual presentation, (2017), J Oncol Pract, 13 (6), p. 401-403.
[303] Edge SB, Byrd DR, Compton CC, Fritz AG, Greene FL, Trotti A, G. G, AJCC cancer staging manual. 7th ed. New York: Springer, Verlag, 2010.,
[304] M.G.S. Boels, A. Koudijs, M.C. Avramut, W.M.P.J. Sol, G. Wang, A.M. van Oeveren-Rietdijk, A.J. van Zonneveld, H.C. de Boer, J. van der Vlag, C. van Kooten, D. Eulberg, B.M. van den Berg, D.H.T. Ijpelaar, T.J. Rabelink. Systemic monocyte chemotactic protein-1 inhibition modifies renal macrophages and restores glomerular endothelial glycocalyx and barrier function in diabetic nephropathy, (2017), Am J Pathol, 187 (11), p. 2430-2440.
[305] W. Xuan, Q. Qu, B. Zheng, S. Xiong, G.H. Fan. The chemotaxis of M1 and M2 macrophages is regulated by different chemokines, (2015), J Leukoc Biol, 97 (1), p. 61-69.
[306] B.B. Moore, L. Murray, A. Das, C.A. Wilke, A.B. Herrygers, G.B. Toews. The role of CCL12 in the recruitment of fibrocytes and lung fibrosis, (2006), Am J Respir Cell Mol Biol, 35 (2), p. 175-181.
[307] A.A. Preobrazhensky, S. Dragan, T. Kawano, M.A. Gavrilin, I.V. Gulina, L. Chakravarty, P.E. Kolattukudy. Monocyte chemotactic protein-1 receptor CCR2B is a glycoprotein that has tyrosine sulfation in a conserved extracellular N-terminal region, (2000), J Immuno, 165 (9), p. 5295-5303.

[308] P. Mandal, B.T. Pratt, M. Barnes, M.R. McMullen, L.E. Nagy. Molecular mechanism for adiponectin-dependent M2 macrophage polarization: link between the metabolic and innate immune activity of full-length adiponectin, (2011), J Biol Chem., 286 (15), p. 13460-13469.
[309] Z. Tan, N. Xie, H. Cui, D.R. Moellering, E. Abraham, V.J. Thannickal, G. Liu. Pyruvate dehydrogenase kinase 1 participates in macrophage polarization via regulating glucose metabolism, (2015), J Immuno, 194 (12), p. 6082-6089.
[310] K. Cui, C.L. Ardell, N.P. Podolnikova, V.P. Yakubenko. Distinct migratory properties of M1, M2, and resident macrophages are regulated by αDβ2 and αMβ2 integrin-mediated adhesion, (2018), Front in Immunol, 9 (2650),
[311] T. Chanmee, P. Ontong, K. Konno, N. Itano. Tumor-associated macrophages as major players in the tumor microenvironment, (2014), Cancers, 6 (3), p. 1670-1690.
[312] J.B. Wyckoff, Y. Wang, E.Y. Lin, J.F. Li, S. Goswami, E.R. Stanley, J.E. Segall, J.W. Pollard, J. Condeelis. Direct visualization of macrophage-assisted tumor cell intravasation in mammary tumors, (2007), Cancer Res, 67 (6), p. 2649-2656.
[313] S.P. Weisberg, D. McCann, M. Desai, M. Rosenbaum, R.L. Leibel, A.W. Ferrante. Obesity is associated with macrophage accumulation in adipose tissue, (2003), J Clin Inves, 112 (12), p. 1796-1808.
[314] D.A. Chistiakov, M.C. Killingsworth, V.A. Myasoedova, A.N. Orekhov, Y.V. Bobryshev. CD68/macrosialin: not just a histochemical marker, (2017), Lab Inves, 97 (1), p. 4-13.
[315] J.T. Beranek. CD68 is not a macrophage-specific antigen, (2005), Ann Rheum Dis, 64 (2), p. 342.
[316] E. Kunisch, R. Fuhrmann, A. Roth, R. Winter, W. Lungershausen, R. Kinne. Macrophage specificity of three anti-CD68 monoclonal antibodies (KP1, EBM11, and PGM1) widely used for immunohistochemistry and flow cytometry, (2004), Ann Rheum Dis, 63 (7), p. 774-784.
[317] E.R. Andreeva, I.M. Pugach, A.N. Orekhov. Subendothelial smooth muscle cells of human aorta express macrophage antigen in situ and in vitro, (1997), Atherosclerosis, 135 (1), p. 19-27.
[318] M.M. Van Den Heuvel, C.P. Tensen, J.H. Van As, T.K. Van Den Berg, D.M. Fluitsma, C.D. Dijkstra, E.A. Döpp, A. Droste, F.A. Van Gaalen, C. Sorg, P. Högger, R.H.J. Beelen. Regulation of CD163 on human macrophages: Cross-linking of CD163 induces signaling and activation, (1999), J Leukoc Biol, 66 (5), p. 858-866.
[319] M.B. Maniecki, A. Etzerodt, B.P. Ulhøi, T. Steiniche, M. Borre, L. Dyrskjøt, T.F. Ørntoft, S.K. Moestrup, H.J. Møller. Tumor-promoting macrophages induce the expression of the macrophage-specific receptor CD163 in malignant cells, (2012), Int J Cancer, 131 (10), p. 2320-2331.

[320] B.O. Fabriek, R. van Bruggen, D.M. Deng, A.J. Ligtenberg, K. Nazmi, K. Schornagel, R.P. Vloet, C.D. Dijkstra, T.K. van den Berg. The macrophage scavenger receptor CD163 functions as an innate immune sensor for bacteria, (2009), Blood, 113 (4), p. 887-892.
[321] E. Sierra-Filardi, M.A. Vega, P. Sanchez-Mateos, A.L. Corbi, A. Puig-Kroger. Heme Oxygenase-1 expression in M-CSF-polarized M2 macrophages contributes to LPS-induced IL-10 release, (2010), Immunobiology, 215 (9-10), p. 788-795.
[322] R.A. Ezekowitz, K. Sastry, P. Bailly, A. Warner. Molecular characterization of the human macrophage mannose receptor: demonstration of multiple carbohydrate recognition-like domains and phagocytosis of yeasts in Cos-1 cells, (1990), J Exp Me, 172 (6), p. 1785-1794.
[323] F. Sallusto, M. Cella, C. Danieli, A. Lanzavecchia. Dendritic cells use macropinocytosis and the mannose receptor to concentrate macromolecules in the major histocompatibility complex class II compartment: downregulation by cytokines and bacterial products, (1995), J Exp Me, 182 (2), p. 389-400.
[324] H. He, J. Xu, C.M. Warren, D. Duan, X. Li, L. Wu, M.L. Iruela-Arispe. Endothelial cells provide an instructive niche for the differentiation and functional polarization of M2-like macrophages, (2012), Blood, 120 (15), p. 3152-3162.
[325] J. Kalra, J. Baker. Multiplex immunohistochemistry for mapping the tumor microenvironment, (2017), Methods Mol Biol., 1554 p. 237-251.
[326] E.C. Stack, C. Wang, K.A. Roman, C.C. Hoyt. Multiplexed immunohistochemistry, imaging, and quantitation: A review, with an assessment of Tyramide signal amplification, multispectral imaging and multiplex analysis, (2014), Methods, 70 (1), p. 46-58.
[327] R. von Wasielewski, M. Mengel, S. Gignac, L. Wilkens, M. Werner, A. Georgii. Tyramine amplification technique in routine immunohistochemistry, (1997), J Histochem Cytochem., 45 (11), p. 1455-1459.
[328] C. Ma, H. Horlad, K. Ohnishi, T. Nakagawa, S. Yamada, S. Kitada, T. Motoshima, T. Kamba, T. Nakayama, N. Fujimoto, M. Takeya, Y. Komohara. CD163-positive cancer cells are potentially associated with high malignant potential in clear cell renal cell carcinoma, (2018), Med Mol Morphol., 51 (1), p. 13-20.
[329] Vectra 3 Quantitative Pathology Imaging System User's Manual https://www.perkinelmer.com/Content/LST_Software_Downloads/Vectra-User-Manual-3-0-3.pdf (Accessed on 07/10/2019).
[330] InForm User Manual https://www.google.com.au/url?sa=t&rct=j&q=&esrc=s&source=web&cd=1&ved=2ahUKEwjKxe72rs_kAhWb7HMBHYENBsYQFjAAegQIBhAC&url=https%3A%2F%2Fwww.perkinelmer.com

%2FContent%2FLST_Software_Downloads%2FinFormUserManual_2_3_0_rev1.pdf&usg=AOvVaw1nc1ZF9rice3BDiGjwfFg6 (Accessed on 07/10/2019).
[331] J. Saylor, Z. Ma, H.S. Goodridge, F. Huang, A.E. Cress, S.J. Pandol, S.L. Shiao, A.C. Vidal, L. Wu, N.G. Nickols, A. Gertych, B.S. Knudsen. Spatial mapping of myeloid cells and macrophages by multiplexed tissue Staining, (2018), Front Immunol., 9 p. 2925.
[332] E. Arner, P.O. Westermark, K.L. Spalding, T. Britton, M. Rydén, J. Frisén, S. Bernard, P. Arner. Adipocyte turnover: Relevance to human adipose tissue morphology, (2010), Diabetes, 59 p. 105-109.
[333] M. Galarraga, J. Campión, A. Muñoz-Barrutia, N. Boqué, H. Moreno, J.A. Martínez, F. Milagro, C. Ortiz-de-Solórzano. Adiposoft: automated software for the analysis of white adipose tissue cellularity in histological sections, (2012), J Lipid Res, 53 (12), p. 2791-2796.
[334] G.M. Sullivan, R. Feinn. Using effect size-or why the p value ss not enough, (2012), J Grad Med Educ., 4 (3), p. 279-282.
[335] Sample Size for Paired t Test https://www.statsdirect.com/help/sample_size/paired_t_test.htm (Accessed on 30/09/2019).
[336] A. Hackshaw. Small studies: strengths and limitations, (2008), Eur Respir J., 32 (5), p. 1141-1143.
[337] V. van Harmelen, T. Skurk, K. Rohrig, Y.M. Lee, M. Halbleib, I. Aprath-Husmann, H. Hauner. Effect of BMI and age on adipose tissue cellularity and differentiation capacity in women, (2003), Int J Obes Relat Metab Disord., 27 (8), p. 889-895.
[338] A.E. Utech, E.M. Tadros, T.G. Hayes, J.M. Garcia. Predicting survival in cancer patients: the role of cachexia and hormonal, nutritional and inflammatory markers, (2012), J Cachexia Sarcopenia Muscle., 3 (4), p. 245-251.
[339] M. Lech, H.J. Anders. Macrophages and fibrosis: How resident and infiltrating mononuclear phagocytes orchestrate all phases of tissue injury and repair, (2013), Biochimica et biophysica acta, 1832 (7), p. 989-997.
[340] M.J. Pagliassotti, P.Y. Kim, A.L. Estrada, C.M. Stewart, C.L. Gentile. Endoplasmic reticulum stress in obesity and obesity-related disorders: An expanded view, (2016), Metabolism, 65 (9), p. 1238-1246.
[341] J. Deng, S. Liu, L. Zou, C. Xu, B. Geng, G. Xu. Lipolysis response to endoplasmic reticulum stress in adipose cells, (2012), J Biol Chem., 287 (9), p. 6240-6249.
[342] B.D. Perry, J.A. Rahnert, Y. Xie, B. Zheng, M.E. Woodworth-Hobbs, S.R. Price. Palmitate-induced ER stress and inhibition of protein synthesis in cultured myotubes does not require Toll-like receptor 4, (2018), PloS one, 13 (1), p. e0191313.

[343] J. Haywood, R.R. Yammani. Free fatty acid palmitate activates unfolded protein response pathway and promotes apoptosis in meniscus cells, (2016), Osteoarthritis Cartilage., 24 (5), p. 942-945.
[344] A. Vidyarthi, N. Khan, T. Agnihotri, S. Negi, D.K. Das, M. Aqdas, D. Chatterjee, O.R. Colegio, M.K. Tewari, J.N. Agrewala. TLR-3 stimulation skews M2 macrophages to M1 through IFN-alpha\beta signaling and restricts tumor progression, (2018), Front Immunol., 9 p. 1650.
[345] F. Yang, Y. Liu, H. Ren, G. Zhou, X. Yuan, X. Shi. ER-stress regulates macrophage polarization through pancreatic EIF-2alpha kinase, (2019), Cell Immunol, 336 p. 40-47.
[346] S. Futaki, Y. Hayashi, M. Yamashita, K. Yagi, H. Bono, Y. Hayashizaki, Y. Okazaki, K. Sekiguchi. Molecular basis of constitutive production of basement membrane components. Gene expression profiles of Engelbreth-Holm-Swarm tumor and F9 embryonal carcinoma cells, (2003), J Biol Chem., 278 (50), p. 50691-50701.
[347] T. Rharass, S. Lucas. High Glucose Level Impairs Human Mature Bone Marrow Adipocyte Function Through Increased ROS Production, (2019), Front Endocrinol, 10: 607. Published online doi: 10.3389/fendo.2019.00607
[348] S. Bolamperti, F. Guidobono, A. Rubinacci, I. Villa. The role of growth hormone in mesenchymal stem cell commitment, (2019), Int J Mol Sci, 20 (21), p. 5264.
[349] G. Tirza, I. Solodeev, M. Sela, I. Greenberg, M. Pasmanik-Chor, E. Gur, N. Shani. Reduced culture temperature attenuates oxidative stress and inflammatory response facilitating expansion and differentiation of adipose-derived stem cells, (2020), Stem Cell Res Ther., 11 (1), p. 35.
[350] S.V. Boregowda, V. Krishnappa, J.W. Chambers, P.V. Lograsso, W.T. Lai, L.A. Ortiz, D.G. Phinney. Atmospheric oxygen inhibits growth and differentiation of marrow-derived mouse mesenchymal stem cells via a p53-dependent mechanism: implications for long-term culture expansion, (2012), Stem cells (Dayton, Ohio), 30 (5), p. 975-987.
[351] S.E. Ross, N. Hemati, K.A. Longo, C.N. Bennett, P.C. Lucas, R.L. Erickson, O.A. MacDougald. Inhibition of adipogenesis by Wnt signaling, (2000), Science (New York, N.Y.), 289 (5481), p. 950-953.
[352] S. Bolamperti, M. Signo, A. Spinello, G. Moro, G. Fraschini, F. Guidobono, A. Rubinacci, I. Villa. GH prevents adipogenic differentiation of mesenchymal stromal stem cells derived from human trabecular bone via canonical Wnt signaling, (2018), Bone, Jul (112), p. 136-144.
[353] S.W. Yau, V.C. Russo, I.J. Clarke, F.R. Dunshea, G.A. Werther, M.A. Sabin. IGFBP-2 inhibits adipogenesis and lipogenesis in human visceral, but not subcutaneous, adipocytes, (2015), Int J Obes (Lond), 39 (5), p. 770-781.

[354] M. Fasshauer, J. Klein, S. Kralisch, M. Klier, U. Lossner, M. Bluher, R. Paschke. Growth hormone is a positive regulator of adiponectin receptor 2 in 3T3-L1 adipocytes, (2004), FEBS Lett, 558 (1-3), p. 27-32.
[355] M.J. Gerdes, C.J. Sevinsky, A. Sood, S. Adak, M.O. Bello, A. Bordwell, A. Can, A. Corwin, S. Dinn, R.J. Filkins, D. Hollman, V. Kamath, S. Kaanumalle, K. Kenny, M. Larsen, M. Lazare, Q. Li, C. Lowes, C.C. McCulloch, E. McDonough, M.C. Montalto, Z. Pang, J. Rittscher, A. Santamaria-Pang, B.D. Sarachan, M.L. Seel, A. Seppo, K. Shaikh, Y. Sui, J. Zhang, F. Ginty. Highly multiplexed single-cell analysis of formalin-fixed, paraffin-embedded cancer tissue, (2013), Proc Natl Acad Sci U S A, 110 (29), p. 11982-11987.
[356] A. Nougarede, C. Tesniere, J. Ylanko, R. Rimokh, G. Gillet, D.W. Andrews. Improved IRE1 and PERK pathway sensors for multiplex endoplasmic reticulum stress assay reveal stress response to nuclear dyes used for image segmentation, (2018), Assay Drug Dev Technol., 16 (6), p. 350-360.
[357] D.D. Buethe, P.E. Spiess. Current management considerations for the incidentally detected small renal mass, (2013), Cancer Control., 20 (3), p. 211-221.
[358] M.A.S. Jewett, A. Zuniga. Renal tumor natural history: The rationale and role for active surveillance, (2008), Urol Clin North Am, 35 (4), p. 627-634.
[359] J.H. Pinthus, K.F. Whelan, D. Gallino, J.P. Lu, N. Rothschild. Metabolic features of clear-cell renal cell carcinoma: mechanisms and clinical implications, (2011), Can Urol Assoc J., 5 (4), p. 274-282.
[360] K. Saito, E. Arai, K. Maekawa, M. Ishikawa, H. Fujimoto, R. Taguchi, K. Matsumoto, Y. Kanai, Y. Saito. Lipidomic signatures and associated transcriptomic profiles of clear cell renal cell carcinoma, (2016), Sci Rep, 6 p. 28932-28932.
[361] S.B. Thakur, J.V. Horvat, I. Hancu, O.M. Sutton, B. Bernard‐Davila, M. Weber, J.H. Oh, M.A. Marino, D. Avendano, D. Leithner. Quantitative in vivo proton MR spectroscopic assessment of lipid metabolism: Value for breast cancer diagnosis and prognosis, (2019), J Magn Reson Imaging,
[362] A. Horiguchi, T. Asano, T. Asano, K. Ito, M. Sumitomo, M. Hayakawa. Fatty acid synthase over expression is an indicator of tumor aggressiveness and poor prognosis in renal cell carcinoma, (2008), J Urol., 180 (3), p. 1137-1140.
[363] A. Horiguchi, T. Asano, T. Asano, K. Ito, M. Sumitomo, M. Hayakawa. Pharmacological inhibitor of fatty acid synthase suppresses growth and invasiveness of renal cancer cells, (2008), J Urol., 180 (2), p. 729-736.
[364] J.W. Joung, H.K. Oh, S.J. Lee, Y.A. Kim, H.J. Jung. Significance of intratumoral fibrosis in clear cell renal cell carcinoma, (2018), J Pathol Transl Med, 52 (5), p. 323-330.

[365] N.I. Nissen, M. Karsdal, N. Willumsen. Collagens and cancer associated fibroblasts in the reactive stroma and its relation to cancer biology, (2019), J Exp Clin Cancer Res., 38 (1), p. 115.
[366] D. Pankova, Y. Chen, M. Terajima, M.J. Schliekelman, B.N. Baird, M. Fahrenholtz, L. Sun, B.J. Gill, T.J. Vadakkan, M.P. Kim, Y.H. Ahn, J.D. Roybal, X. Liu, E.R. Parra Cuentas, J. Rodriguez, Wistuba, II, C.J. Creighton, D.L. Gibbons, J.M. Hicks, M.E. Dickinson, J.L. West, K.J. Grande-Allen, S.M. Hanash, M. Yamauchi, J.M. Kurie. Cancer-associated fibroblasts induce a collagen cross-link switch in tumor Stroma, (2016), Mol Cancer Res., 14 (3), p. 287-295.
[367] Q. Cui, B. Wang, K. Li, H. Sun, T. Hai, Y. Zhang, H. Kang. Upregulating MMP-1 in carcinoma-associated fibroblasts reduces the efficacy of Taxotere on breast cancer synergized by Collagen IV, (2018), Oncol Lett, 16 (3), p. 3537-3544.
[368] S.P. Rebelo, C. Pinto, T.R. Martins, N. Harrer, M.F. Estrada, P. Loza-Alvarez, J. Cabecadas, P.M. Alves, E.J. Gualda, W. Sommergruber, C. Brito. 3D-3-culture: A tool to unveil macrophage plasticity in the tumour microenvironment, (2018), Biomaterials, 163 p. 185-197.
[369] E. Shapiro, T. Biezuner, S. Linnarsson. Single-cell sequencing-based technologies will revolutionize whole-organism science, (2013), Nat Rev Genet, 14 p. 618.
[370] E. Querido, L. Dekakra-Bellili, P. Chartrand. RNA fluorescence in situ hybridization for high-content screening, (2017), Methods, 126 p. 149-155.
[371] M. Ligorio, S. Sil, J. Malagon-Lopez, L.T. Nieman, S. Misale, M. Di Pilato, R.Y. Ebright, M.N. Karabacak, A.S. Kulkarni, A. Liu, N. Vincent Jordan, J.W. Franses, J. Philipp, J. Kreuzer, N. Desai, K.S. Arora, M. Rajurkar, E. Horwitz, A. Neyaz, E. Tai, N.K.C. Magnus, K.D. Vo, C.N. Yashaswini, F. Marangoni, M. Boukhali, J.P. Fatherree, L.J. Damon, K. Xega, R. Desai, M. Choz, F. Bersani, A. Langenbucher, V. Thapar, R. Morris, U.F. Wellner, O. Schilling, M.S. Lawrence, A.S. Liss, M.N. Rivera, V. Deshpande, C.H. Benes, S. Maheswaran, D.A. Haber, C. Fernandez-Del-Castillo, C.R. Ferrone, W. Haas, M.J. Aryee, D.T. Ting. Stromal microenvironment shapes the intratumoral architecture of pancreatic cancer, (2019), Cell, 178 (1), p. 160-175.e127.
[372] J. Argilés, B. Stemmler, F. López-Soriano, S. Busquets. Inter-tissue communication in cancer cachexia, (2019), Nat Rev Endocrinol, 15 (1), p. 9-20.
[373] B.P. Leitner, S. Huang, R.J. Brychta, C.J. Duckworth, A.S. Baskin, S. McGehee, I. Tal, W. Dieckmann, G. Gupta, G.M. Kolodny, K. Pacak, P. Herscovitch, A.M. Cypess, K.Y. Chen. Mapping of human brown adipose tissue in lean and obese young men, (2017), Proc Natl Acad Sci U S A, 114 (32), p. 8649-8654.

Appendices

Appendix 1. Summary of antibodies and live/dead cell dye for flow cytometry analysis

Antibody	Names of antibodies or dye	Company (Cat. No.)	Dilution
	APC Mouse Anti-Human CD105	BD (562408)	1:20
	PerCP-Cy5.5 Mouse Anti-Human CD90	BD (561557)	1:20
	PE Rat anti-SSEA-3	BD (5602337)	1:5
	PE Mouse Anti-Human CD16	BD (555407)	1:100
	APC Mouse Anti-Human CD14	BD (555399)	1:100
	PerCP Cy5.5 Mouse Anti-Human CD14	BD (550787)	1:50
	APC Mouse Anti-Human CD11b	BioLegend (301309)	1:20
	PE Mouse Anti-Human CD18	BioLegend (374707)	1:20
	FITC Mouse Anti-Human CD209	BD (551264)	1: 20
	BV480 Mouse Anti-Human CD86	BD (566131)	1:50
	BV786 Mouse Anti-Human CD80	BD (564159)	1: 50
	PE Mouse Anti-Human CD163	BD (556018)	1: 20
	APC Mouse Anti-Human CD206	BD (550889)	1:20
	BV421 Mouse Anti-Human CD200 Receptor	BD (566344)	1: 100
Live/dead dye	DAPI	Invitrogen (D1306)	0.2 µg/mL
	FVS700	BD (564997)	1:3000
	Live/dead Aqua	Invitrogen (L34957)	1:500

Appendix 2. Recipe for making the Kaiser glycerine-jelly aqueous mounting medium

Distilled water	80 mL
Glycerine	20 mL
Gelatine	3 g
Chromic potassium sulphate	0.2 g

Chromic potassium sulphate was dissolved in 30 mL of distilled water. Gelatine was dissolved in 50 mL of warm distilled water. Chromic potassium sulphate and gelatine solutions were mixed and glycerine was added. The pH was tested with an indicator and neutralised with sodium bicarbonate solution to pH 7.0. The recipe was kindly provided by Dr Clay Winterford (QIMR Berghofer Medical Research Institute, Brisbane).

Appendix 3 List of gene-specific primers for q-rtPCR

Target mRNA	Sequence	Size (bp)
GRP78 (human)	F: GCCTGTATTTCTAGACCTGCC	150
	R: TTCATCTTGCCAGCCAGTTG	
GRP78 (mouse)	F: TGCTGCTAGGCCTGCTCCGA	237
	R: CGACCACCGTGCCCACATCC	
sXBP1 (human and mouse)	F: GAGTCCGCAGCAGGTGC	102
	R: CAAAAGGATATCAGACTCAGAATCTGAA	
APM-1 (human)	F: GCAGAGATGGCACCCCTG	80
	R: GGTTTCACCGATGTCTCCCT	
MCP-1 (human)	F: TGTCCCAAAGAAGCTGTGATC	84
	R: GGAATCCTGAACCCACTTCTG	
IL-8 (human)	F: TGCAGCTCTGTGTGAAGGTGCAG	145
	R: TGTGTTGGCGCAGTGTGGTCC	
18sRNA (human)	F: GTAACCCGTTGAACCCCATT	151
	R: CAAAAGGATATCAGACTCAGAATCTGAA	
β-actin (mouse)	F: AGCACTGTGTTGGCATAGAGGTC	102
	R: CTTCTTGGGTATGGAATCCTGTG	

Appendix 4 Agarose gel electrophoresis of q-rtPCR products

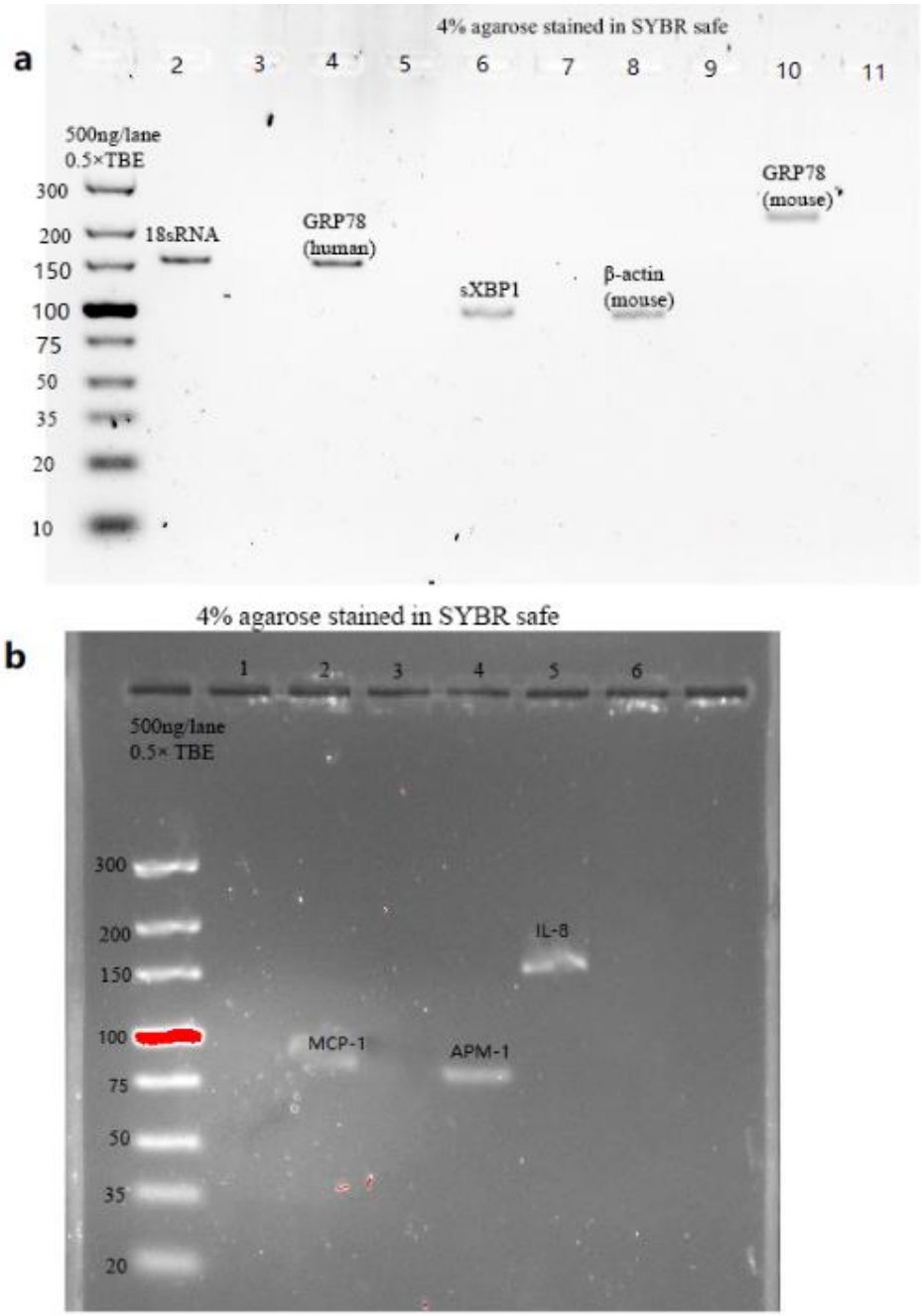

a and **b** demonstrate the electrophoretic gels of q-rtPCR products (names labelled in gels), which were photographed by BIO-RAD Gel Doc XR. 500 ng of the DNA ladders in the range of 10 bp to 300 bp were added. DNA was separated in 4 % agarose TBE buffer stained with SYBR safe. Bands did not appear in the NRT controls (lanes 3, 5, 7, 9 and 11 for **a**; lanes 1, 3 and 6 for **b**), indicating the DNA contamination presented in RNA preparation was negligible. The specificity of the PCR products for all primers was confirmed by the presence of predicted band sizes demonstrated in the gels (**Appendix 3**).

Abbreviations: NRT, no reverse transcriptase control; q-rtPCR, quantitative real-time polymerase chain reaction; TBE, Tris/Borate/Ethylenediaminetetraacetic acid

Appendix 5 Summary of ingredients in the culture media used in generation of M1/M2 macrophages

Culture medium	Ingredients	Catalogue number
Macrophage differentiation medium	CSF-1 (50 ng/mL)	BioLegend 574802
M1 induction medium	LPS (20 ng/mL)	Sigma L2654
	INF- γ (20 ng/mL)	BioLegend 570202
M2 induction medium	IL-4 (20 ng/mL)	BioLegend 574002
	IL-13 (20 ng/mL)	BioLegend 571102

RPMI-1640 was applied as the base medium. All culture media contained 10 % heat inactivated FBS and 1 % penicillin/streptomycin. Abbreviations: CSF, colony stimulating factor; IL, interleukin; INF, interferon; LPS, lipopolysaccharide.

Appendix 6 Fluorescence spectral overview

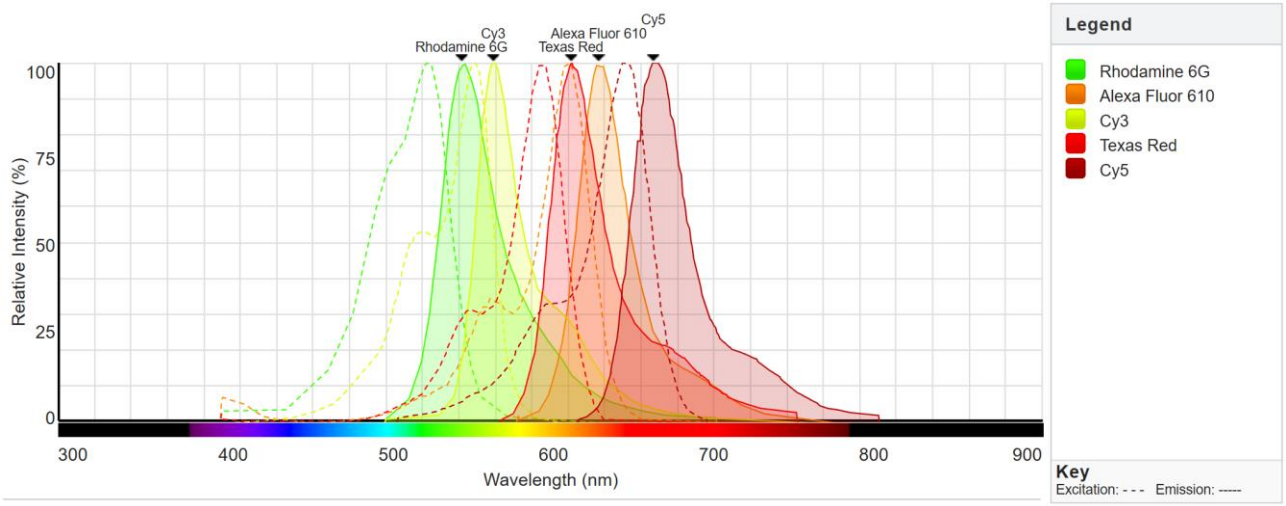

The filters cyanine 3 (Cy3) and Texas-Red were chosen to build the imaging protocol for the Vectra III multispectral slide scanner as alternatives for Rhodamine 6G (CD163-linked fluorophore) and Alexa Fluor 610 (CD206-linked fluorophore), which were not built into the instrument.